Spring 5-6-2022

Fabrication of Particulates for Detecting Trace Level Analytes in Water Using Optical Spectroscopy and for Developing Thermoelectric Materials

Mohammed Nayeem Ibnul
University of Maine, mohammed.ibnul@maine.edu

FABRICATION OF PARTICULATES FOR DETECTING TRACE LEVEL ANALYTES IN WATER USING OPTICAL SPECTROSCOPY AND FOR DEVELOPING THERMOELECTRIC MATERIALS

By

Mohammed Nayeem Ibnul

B.Sc. University of Dhaka, 2014

A DISSERTATION

Submitted in Partial Fulfillment of the

Requirements for the Degree of

Doctor of Philosophy

(in Chemistry)

The Graduate School

The University of Maine

May 2022

Advisory Committee:

Dr. Carl P. Tripp, Professor of Chemistry, Advisor

Dr. Alice Bruce, Professor of Chemistry

Dr. William Gramlich, Associate Professor of Chemistry

Dr. Douglas Bousfield, Professor of Chemical Engineering

Dr. Mark Wells, Professor of Marine Science

FABRICATION OF PARTICULATES FOR DETECTING TRACE LEVEL ANALYTES IN WATER USING OPTICAL SPECTROSCOPY AND FOR DEVELOPING THERMOELECTRIC MATERIALS

By Mohammed Nayeem K. Ibnul

Dissertation Advisor: Dr. Carl P. Tripp

An Abstract of the Dissertation Presented
in Partial Fulfillment of the Requirements for the
Degree of Doctor of Philosophy
(in Chemistry)
May 2022

The underlying concepts developed in this thesis involve particulate fabrication of known size using a bottom-up synthesis or a top-down milling process. This bottom-up approach was used for detection of analytes in water. Conventional UV-Vis spectroscopic based detection methods require target analytes to be soluble or have enough vapor pressure for analysis in the gas phase. We achieved an order in magnitude improvement in the detection limit over the standard molybdenum blue method for phosphate and arsenate by conversion of target analytes present in solution to a solid for quantification by UV-Vis and IR spectroscopy. Furthermore, by recording a visible and infrared spectrum on the same membrane, we were able to selectively determine both phosphate and arsenate. This is not possible using the standard molybdenum blue method.

We also developed generalized approach involved the precipitation of polyatomic anions with simple monoatomic cations. We demonstrated this concept with the detection of free and weak acid dissociative (WAD) cyanide in water. In our method, cyanide ions are precipitated with silver ions and then captured on an IR transparent membrane. Key to our approach was the use of an ^{13}CN spiked addition to achieve detection limits below the 0.2 mgL^{-1} level. Furthermore,

we were able to distinguish between free and WAD cyanide by using a spiked addition of sodium sulfide. The sulfide freed the cyanide from the WAD compounds enabling detection of this fraction of cyanide by our method.

Using a tops-down approach we generated bismuth telluride nanoparticles for thermoelectric power generation. The “as received” bismuth telluride ingots were ball milled in the presence of the cationic polymer PADAMAc which prevented particle aggregation during the milling process. By adjusting the milling conditions, we were able to control the particle size of the particulate to a small as 40 nm in diameter. Sintering pellets of the particulates below the melting point resulted in voids that scattered the thermal radiation. As a result, we show that adjusting particle size and sintering temperature could be viable strategies for developing TE material.

ACKNOWLEDGEMENTS

I'd like to thank my advisor, Professor Dr. Carl P. Tripp, for all of his assistance, support, guidance, feedback, and encouragement throughout my graduate studies.

I would also like to thank my advisory committee members, Professor Dr. Alice Bruce, Associate Professor Dr. William Gramlich, Professor Dr. Douglas Bousfield and Professor Dr. Mark Wells for all of their invaluable assistance, constructive feedback, discussions, ideas, and advice throughout my Ph.D. work. I'd like to thank all of my collaborators, particularly Professor Dr. Robert Lad from the Frontier Institute for Research in Sensor Technologies (FIRST) and Dr. Travis Wallace from the Maine Maritime Academy (MMA), for their valuable assistance, discussions, ideas, and advice on the thermoelectrics project.

Special thanks and gratitude to Mrs. Carol Tripp for her support in reviewing the manuscripts and the thesis.

Many thanks to all of the Carl Tripp Research Group members, particularly Sabrina, Sfoog, Pradnya, Rihab, and Alyson, for their help and feedback on the research, seminars, presentations, and manuscripts.

I'd like to thank my wife, Nashra Nisha, for her unending encouragement and for keeping me on track so that I could achieve my goal. I'd also like to thank my parents and family members for their unwavering faith in me.

Thank you, University of Maine, for providing me with pleasant, wonderful memories, and unforgettable experiences throughout my life!

TABLE OF CONTENTS

LIST OF FIGURES

LIST OF TABLES

CHAPTER 1: INTRODUCTION

1.1. Overview

The overall goal of my research is to develop infrared and UV-vis spectroscopic methods to detect and quantify chemical species in water matrices. Commercial labs devoted to measuring chemical species in water use a variety of methods and equipment that are approved by the Environmental Protection Agency (EPA)[1]. Many of these involve specific chemical reactions and measurement of a unique response (change in conductivity, pH, color, turbidity, alkalinity etc.)[2–7]. Methods that provide a wider range of chemical identification and quantification are typically based on GC/MS for organics, ICP/MS and AAS for metals [8–11]. Despite the rich information content for identification and quantification of both organic and inorganic species in water, infrared spectroscopic based methods are not used and FTIR spectrometers are rarely present in commercial labs devoted to water analysis. On the other hand, this represents a tremendous opportunity to introduce IR spectroscopic methods to this community. For this to occur, the key will be to develop simple and easy sampling approaches that circumvent the many hurdles with IR analysis of species in water.

The biggest hurdle for IR spectroscopic detection of chemical species is the opacity of water. In transmission measurements in water, the entire infrared region of the spectrum is essentially opaque when the pathlength of the cell exceeds 25 μm. Even for the strongest absorbing species, this narrow pathlength puts a lower level of detection in the parts per thousand level which is much higher than the parts per million to parts per trillion required by most EPA standards. Although attenuated total reflection (ATR) has alleviated much of the

tedious sample preparation for IR studies in aqueous media, it does not circumvent the fundamental opacity of water and hence, does not lead to lower detection limits. Thus, any approach that uses IR spectroscopy will require some extraction of target analytes from water or concentration of these analytes in water.

Both extraction and concentration methods are standard pre-sampling methods in analytical methods used for detecting species in water. It is common to use a membrane or packed column to concentrate the target analyte from water and then elute the analyte from the membrane or column into a smaller volume of water or into an alternative solvent to present this to a Gas chromatography- Mass spectrometry (GS-MS) or Inductive coupled plasma- Mass spectrometry (ICP-MS). An obvious solution would be to apply the same pre-sampling extraction and concentration methods, elute the analyte and record an IR spectrum. However, this would offer little advantage and would be, at best, an incremental change to the current GC/MS or ICP/MS methods.

One of the attributes of IR spectroscopy is its versatility, in that a spectrum can be obtained for gases, liquids, or solids. It is the ability to record spectra of solids that is key to this thesis work. Typically, when presented with a solid in analytical chemistry, the first thing one does is to dissolve the solid into a liquid or convert it to the gas phase for quantification. An infrared spectroscopic based approach enables the complete opposite approach. In other words, our idea is: if it is a gas, convert it to a solid; if it is in a liquid, extract and convert it to a solid; if it is a solid, then extract and record a spectrum. If we now take this to the next level and apply it to the use of membranes, there are key advantages if one could record a spectrum directly on

the membrane. This, in turn, requires a membrane that is transparent in the IR spectral region. Once collected on the membrane, there would be no need to elute the analyte from the membrane for analysis. This not only simplifies the pre-sampling methods as one avoids determining extraction efficiencies, but it also opens new avenues for sampling. For example, in the traditional use of membranes, one requires the target analyte to partition out of the solution on the membrane but to not bind strongly, as the analyte will need to be extracted later. This, in turn, involves knowledge of partition functions and other complicating factors. However, if analysis occurs directly on the membrane, the target analyte could be irreversibly bound through strong electrostatic bonds, covalent bonds, etc. This opens a variety of new detection methodologies that we name collectively as "material enabled spectroscopies (MES)".

The Tripp group first demonstrated MES, with the detection of Fe^{3+} in seawater, using a siderophore tethered to a Si wafer[12]. When placed in water containing Fe^{3+}, the siderophore selectively binds the Fe^{3+}, leading to a change in the IR spectrum, as shown in Figure 1.1. From the intensity of the Fe-O band at 560 cm^{-1}, they demonstrated a detection level of 2 parts per trillion Fe^{3+} with samples taken from the Pacific Ocean off the coast of Alaska. While the preferred substrate would be a porous membrane, the Si wafer as a platform demonstrated two key elements; detection of very low levels of a metal ion that itself has no IR bands, and circumvention of the opacity issue with water. To achieve a low parts per trillion detection level, the Si wafers were immersed in a beaker containing 1L of ocean water, then the sample was stirred for 24 hours to ensure complete capture of all Fe^{3+} in the 1L sample. The Si wafers were removed from the water and dried. Then an absorbance spectrum was recorded in transmission mode through the wafer.

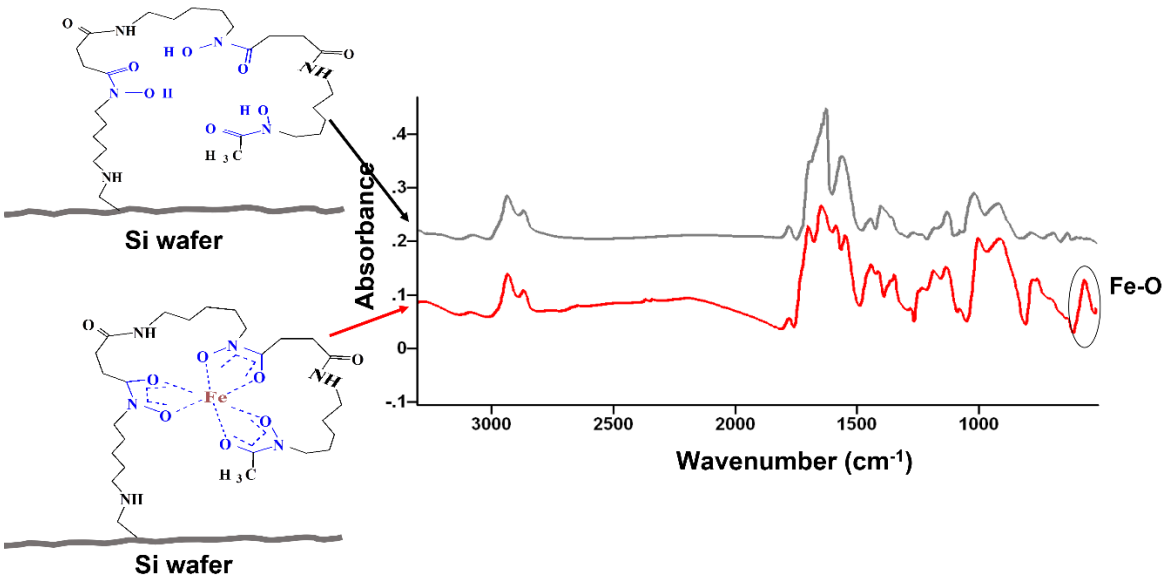

Figure 1.1. IR spectra of a siderophore (DFB) attached to a mesoporous silica layer on top of a silicon wafer and after exposure of the wafer to a solution containing Fe^{3+} [12].

Hg^{2+} was also detected using a Si wafer. However, in this case, the Hg^{2+} was not captured by the Si wafer but rather, the Hg^{2+} catalyzed the conversion of a semicarbizide covalently attached onto a Si wafer to an oxadiazole via the reaction shown in Figure 1.2[13]. Unique IR bands were observed for the oxadiazole and detection levels at the low ppb level were achieved. However, as with the detection of Fe^{3+}, a long incubation time of 24 hours in a stirred beaker was required to achieve these low detection levels.

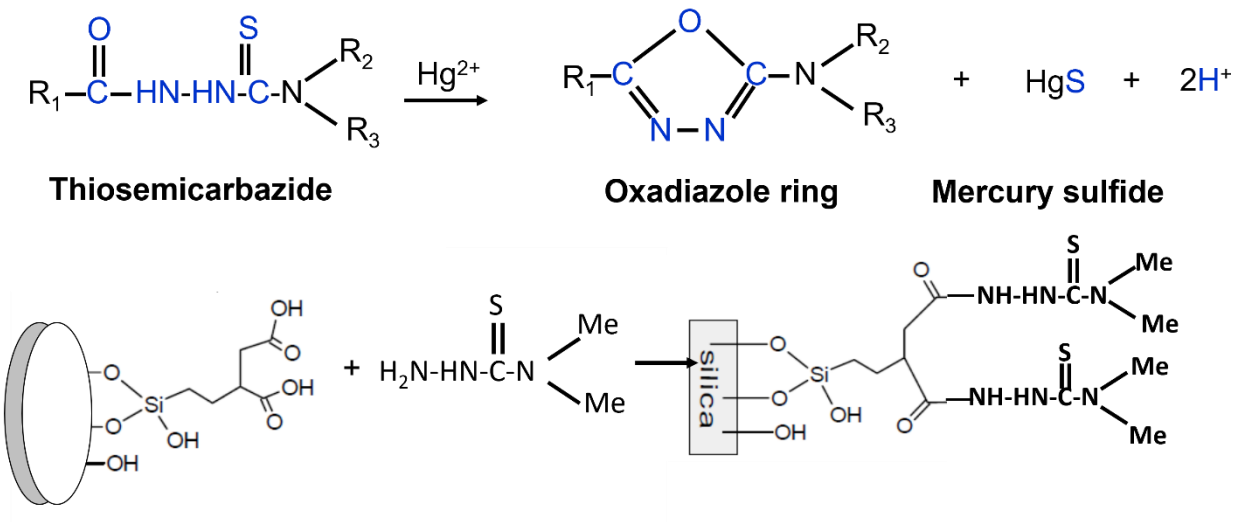

Figure 1.2. Reaction of a thiosemicarbazide with Hg^{2+} to form an oxadiazole ring. Surface reactions leading to a thiosemicarbazide, attached to a mesoporous silica film, deposited on a Si wafer[13].

To overcome the long incubation times, work centered on tethering the siderophore or semicarbizide to an IR transparent membrane. The IR transparent membranes were obtained from Orono Spectral Solutions Inc. While this enabled rapid contact of the Fe^{3+} and Hg^{2+} by way of the torturous pathway of the water passing through the membrane, the amount of Fe^{3+} and Hg^{2+} bound to the membrane were found to be sensitive to flow rate and varied with the type of water matrix. This is because of the short contact time of the Fe^{3+} and Hg^{2+} with the tethered moieties to allow for the capture of the Fe^{3+} by the siderophore or for the Hg^{2+} to catalyze the formation of the oxadiazole ring. For example, a fully saturated membrane holds about 30 µL of water and thus, at the typical flow rates of 2 mL/min[14], the contact time of the Fe^{3+} or Hg^{2+} inside the membrane is about 0.9 seconds[14].

For detection of oil and grease in water, as described in the ASTM method D7575 developed by Orono Spectral Solutions[15], or the detection of water in oils as reported by Saleh

and Tripp[14][16], the short contact times within the membranes were not an issue, as 100% of the target analyte was captured. In both cases, the target analyte existed as droplets stabilized in the solvent. When these suspensions were flowed through the membrane, the droplets burst upon contact with the fibers and the target molecules adsorb onto the membrane.

The challenge remained in how to capture analytes that were soluble in water. Saleh and Tripp developed two approaches to address this problem. In one case, particulate adsorbates were added to a stirred suspension containing the target analyte. In the second case, particulate particles were added that chemically react with the target molecule to form a new compound. Both concepts were demonstrated with the detection of water in oils. For the adsorbate approach, particles of $CuSO_4$ were added to the oil. The water adsorbed strongly to the $CuSO_4$ particles, forming the monohydrate, $CuSO_4.H_2O$. An IR spectrum of the captured particles on the membrane produced a unique water bending mode at 1720 cm^{-1}[17]. In the second case, particles of CaO were added to the oil. Here, the CaO was converted to $Ca(OH)_2$ by reaction with water. A unique OH band due to $Ca(OH)_2$ was observed at 3645 cm^{-1}[16]. Since particles were used, the time for adsorption or reaction is avoided because the suspensions were stirred for 30 minutes or longer. After the reaction was complete, a 10 ml aliquot of the stirred suspension was then passed through the membrane at a flow rate of 2 mL/min. The particles were of sufficient size (> 0 .5 um diameter) to be captured on the 0.45 µm pore sized membranes.

The work described in this thesis builds on the use of the transparent membranes and deviates from the previous studies in two key concepts. The first concept involves using membranes that are transparent in the UV-vis spectral region. We have found that membranes

used for the IR spectroscopic studies become transparent in the visible spectral region when filled with water. Thus, the membranes do not have to be dried before measuring a UV-vis spectrum which has implications for simplifying the sampling approach and improving the detection limits for many of the current UV-vis based methods. Furthermore, the ability to record UV-Vis and IR spectra of the same sample provides a route to achieve additional selectivity in our methods. The second concept involves the use of reactions with target analytes to form precipitates that then can be captured on the membrane. This differs from our previous work that involved adsorption or reaction with existing particles, whereas here, we are performing reactions to form particles.

1.1.1. UV-vis detection of analytes

Figure 1.3 shows essential elements in the classical approach for using UV-vis spectroscopy in detecting an analyte in water. A water sample containing the target analyte at concentration c, is placed in a fixed pathlength cell or cuvette of 0.1-10 cm in length. The cuvette is place in the sample compartment of the spectrometer and a spectrum in transmission mode is recorded. A reference spectrum is typically prerecorded through the cuvette containing water or placing a cuvette containing water in the reference beam s when recording a sample spectrum using a dual beam dispersive spectrometer[18].

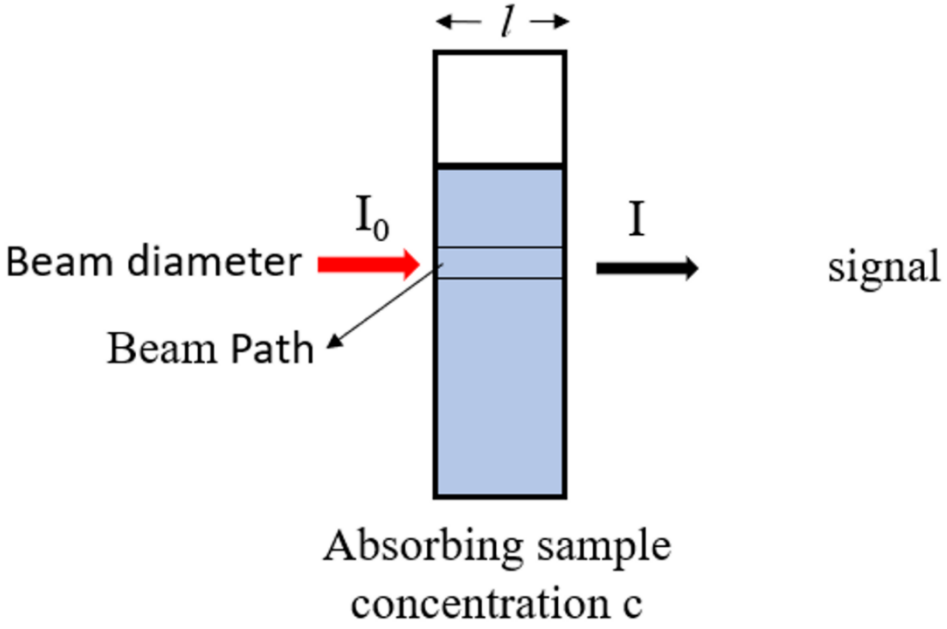

Figure 1.3. UV-Vis spectroscopic measurement in transmission mode using a fixed pathlength cuvette.

The quantification of the analyte is determined from the Beer-Lambert Law shown in Equation 1.1.

$$A = \epsilon\, c\, l \qquad 1.1$$

In the Beer-Lambert law, *A* is absorbance (unitless), ε is the molar absorption coefficient for the height or area of a band due to the analyte in solution (Mol L^{-1} cm^{-1}), *l* is the pathlength of the cuvette (1-10 cm), and c is the concentration of the analyte or molecule in the solution (mol/L)[19][20]. For UV-vis spectroscopy, the height of the band is almost exclusively used. The molar absorption coefficient is a constant, which is the measurement of how efficiently an analyte absorbs light at a specific wavelength. From Equation 1.1, the concentration of the analyte in solution is directly proportional to the height of the band in absorbance units. From

the known molar absorbance coefficient, pathlength of the cuvette, and measurement of the peak height in absorbance units, the concentration of the analyte is calculated.

When distilling the Beer's Law relationship down to its essence, it is the number of molecules in the light beam that determines the absorbance peak height. Increasing the concentration of the analyte in solution or the pathlength of the cell leads to an increase in the number of molecules in the light beam and hence, an increase in the band intensity. However, as shown in Figure 1.2, most of the molecules in the cuvette are not in the beam path and therefore, do not contribute to the intensity of the absorption peak. Consider a sample size of 1L. Typically, a 1 cm cuvette holds about 3 mL of the 1L sample or 0.3% of the total molecules in the beaker. Now the beam diameter in a fiber optic-based UV- Vis spectrometer is about 4 mm in diameter and thus, only about 4.3% of the molecules in the cuvette are in the beam area. Thus, only about 0.013% of the total molecules in the 1L container are sampled by the light beam.

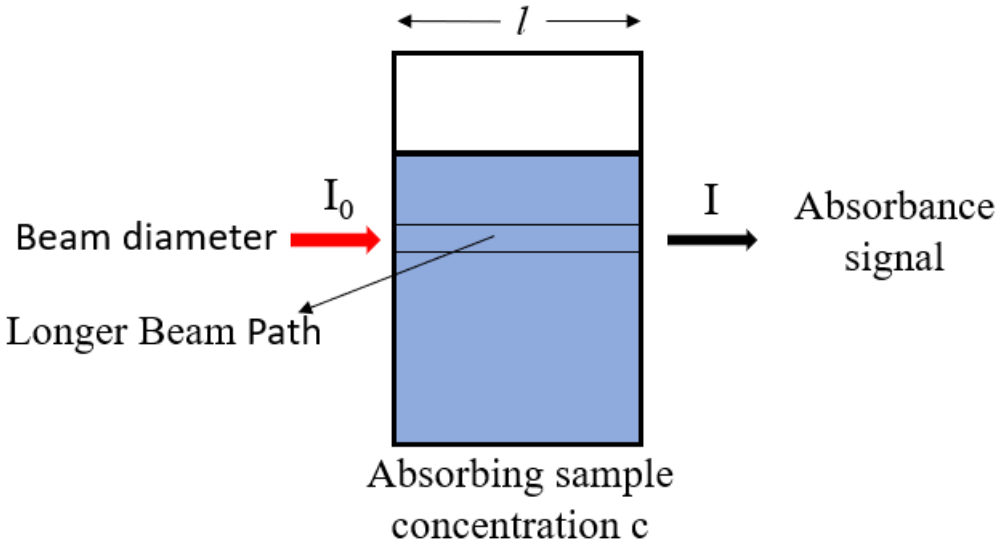

Figure 1.4. Using a longer pathlength cell increases the peak absorbance value for the analyte in the UV-Vis spectrum.

The primary avenue to improve the detection limit of UV-vis spectroscopy is to increase the pathlength of the cuvette. However, practical limitations and cost typically limit the pathlength of cuvettes to 10 cm which is typically not sufficient to detect concentrations in the low ppb or sub ppb range. Sometimes, even a 10 cm pathlength cell is not sufficient to observe a peak when the concentration of phosphate is less than 7 μg L^{-1} [21]. In these cases, approaches to concentrate the analyte in solution or automated flow injection analysis are used to improve the detection limit[22][23].

1.1.2. Conversion of liquid analytes into solid precipitates

Our approach is to convert the dissolved analyte to solid particles, collect the particles on a membrane and record a visible spectrum through the membrane. The advantage of converting the analyte to a solid is that it is possible to have a higher amount of analyte in the light beam of the spectrometer. Recall when we estimated that only 0.013% of the entire analyte species in a 1L sample would be probed by the spectrometer light beam using a standard 1 cm cuvette. If we convert all the analytes in a 1 L sample to particles and process the full liter of the suspension through a 4 mm diameter membrane, then the light beam would pass through all the particles. This, in theory, would lower the detection limit by almost 4 orders in magnitude. However, this improvement is not attainable for a variety of reasons. First, the Beer's Law relationship becomes nonlinear over a large dynamic range. In essence, the absorption of the light beam by the first layer of particles would lower the light intensity impinging on the next layer of particles and so on. Furthermore, as we show below, passing the 1 L sample through a 4 mm diameter membrane is not practical. Typically, a flow rate of 2 mL/min is possible through a 13 mm diameter membrane. Reducing the diameter to 4 mm would lower the maximum flow rate to

0.2 mL/min would then require 83 hours to process the entire 1L. Our experience is that the membrane would become plugged within the first3-5 minutes and certainly long before reaching the 83-hour mark. Given all the various trade-offs, we find, in general, an improvement of between 1 and 2 orders in magnitude in the detection limits using a membrane can be achieved.

1.1.3. Quantitation using a membrane and transmission spectroscopy

In the membrane approach, there is no fixed pathlength *l*. In the thin film approximation, the peak intensity in absorbance units is proportional to the concentration of the analyte times the pathlength *(c * l)*, which is the mass of the analyte per area of the membrane and for the method, has units of mg or μg/cm^2. Thus, Equation 1.1 becomes:

$$A = \epsilon \times \left(\frac{\mu g}{cm^2}\right) \qquad 1.2$$

The extinction coefficient with units of cm^2/μg is used in Equation 1.2 instead of the standard molar extinction coefficient mol L^{-1} cm^{-1} that is used in Equation 1.1. When under-sampling the entire membrane surface, the uniformity of the particulate film over the membrane is important. In our case, the membranes are 13 mm in diameter, and the visible beam is approximately 4 mm in diameter. Hence, the membrane is under-sampled. It is important to have a uniform particulate film so that the mass/area measured in the beam area is representative of the mass collected over the entire area of the membrane.

Using the known extinction coefficient derived from a Beer's Law plot, the mass of the analyte $M_{analyte}$ on the membrane can be determined as shown in Equation 1.3 and 1.4:

$$M_{analyte} = \frac{A \times \ area\ of\ the\ membrane\ (cm^2)}{\epsilon\ (\frac{cm^2}{ug})} \quad 1.3$$

From this, the concentration of the analyte in the solution is calculated in terms of mgL^{-1} or μgL^{-1} :

$$C_{analyte} = \frac{M_{analyte(mg\ or\ \mu g)}}{V\ (mL)} \quad 1.4$$

where V is the volume of the sample suspension passed through the membrane.

From Equation 1.3, the absorbance is proportional to $M_{analyte}$ collected on the membrane and inversely proportional to the area of the membrane. Thus, the detection limit will depend on the volume of the sample passed through the membrane and the diameter of the membrane.

1.1.4. Transparent membranes

The major issue with performing transmission spectroscopy results from scattering of the incident light by the solid analyte particles and the membrane. Figure 1.5 shows that the membrane is opaque in the visible range but becomes transparent after being wetted with water, allowing a visible spectrum to be recorded through the membrane in transmission mode.

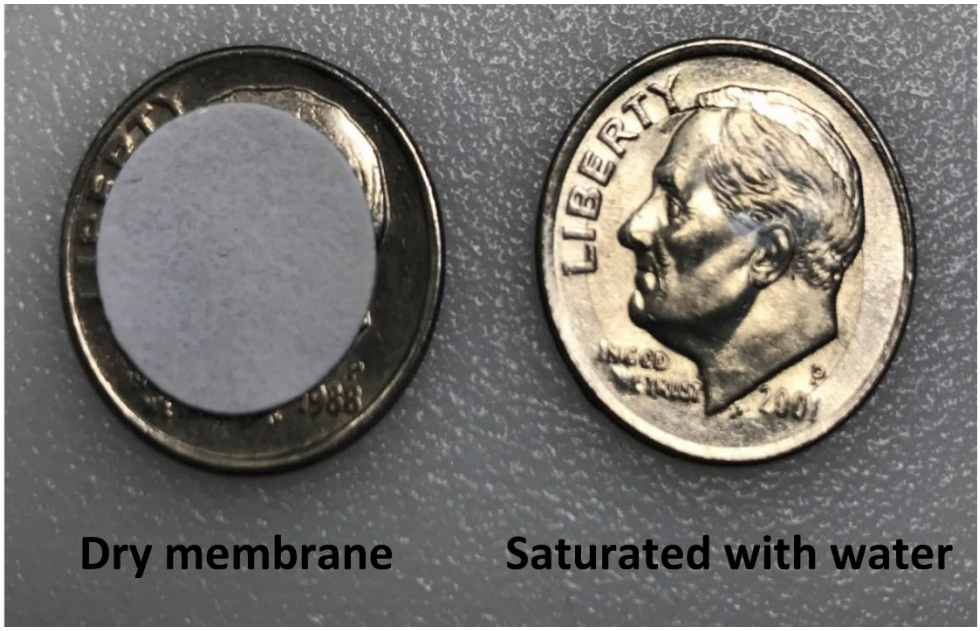

Figure 1.5. A dry membrane and a membrane fully saturated with water.

The membrane's transparency is due to a refractive index matching between the membrane material and the water. The polytetrafluorethylene membrane has a refractive index of 1.38. The dry membrane is opaque in the visible region of the spectrum because the pores of the membrane are filled with air which has a refractive index of 1.003. The refractive index mismatch between the membrane material and pores scatters the radiation, rendering the membrane opaque in the visible region. However, when the membrane is filled with water (refractive index = 1.33), the refractive index mismatch is such that the light experiences very little scattering and the membrane becomes clear. As we show in this thesis, the same effect occurs with loading particles on the surface. Most inorganic particles have refractive indexes between 1.35 and 1.5. When the particles cover the surface of the membrane and saturated with water, the refractive index matching leads to little, if any, scattering of the visible light, regardless of the particle size.

1.2.1. Target analytes: Phosphate and arsenate

We selected the detection of phosphate and arsenate to demonstrate the concept of particulate formation and capture on a transparent membrane for analysis by visible spectroscopy. Phosphorus is one of the main nutrients for plants and crops, thus, used extensively in fertilizers. However, agricultural runoff leads to an increase in the growth of algae and other aquatic plants in the water systems. Continuous presence of such nutrients causes uncontrollable growth of algae in the ecosystem. At the end of the algae life cycle, they consume oxygen, which leads to depletion of dissolved oxygen in freshwater bodies. Thus, phosphorus in the form of phosphates are a key environmental pollutant that contributes to the eutrophication of water resources, such as rivers, lakes, ponds, and streams. [24][25]. Excess phosphate has caused a surge of atmospheric, water, and human health complications around the globe, and controlling nutrient pollution has become a major task for the countries[26]. According to the EPA, 40% of our nation's rivers and streams have elevated concentrations of phosphorus. The main source of such high levels of phosphorus is the fertilizer and animal waste that tends to leach from the farms[26].

Arsenic, on the other hand, is a toxic element that has been identified as a human carcinogen [27–30]. It naturally occurs in soil, sediments, surface water, and groundwater. Arsenic is very mobile and prevalent in organic and inorganic forms with multiple oxidation states. According to the World Health Organization (WHO) and the Environmental Protection Agency (EPA), the permissible limit of arsenic in drinking water is 10 $\mu g L^{-1}$. Given their environmental and health impact, the necessity to monitor both phosphate and arsenate concentrations in water systems has been of paramount importance.

1.2.1.1. Phosphorus classification

Phosphorus tends to exist in a variety of forms in water, such as orthophosphate, metaphosphate, pyrophosphate, particulate phosphate, and organic bound phosphate. Thus, the detection of the total phosphorus becomes a complex process and, as a result, it is extremely difficult to monitor the total phosphorus concentration in water[31–33]. Pretreatment processes, such as digestion or oxidation, are typically used to convert all forms of phosphorus into orthophosphate for a quantitative detection. Thus, measurement of orthophosphate or phosphate is the most common approach to monitor the concentration of phosphorus in water systems [34–36].

Orthophosphate is the dissolved inorganic form and the most available form of phosphorus in water. Other dissolved inorganic forms are polyphosphates or metaphosphates[37][38]. There is also dissolved organic phosphate, which mostly comes from nucleic acids, proteins or organic pesticides[39]. The particulate phosphorus is the fraction that can be filtered using a 0.2- or 0.45-micron filter. Figure 1.6 shows the various forms of phosphorus that are found in the natural water systems and the subsequent treatments for determination of the phosphorus concentration.

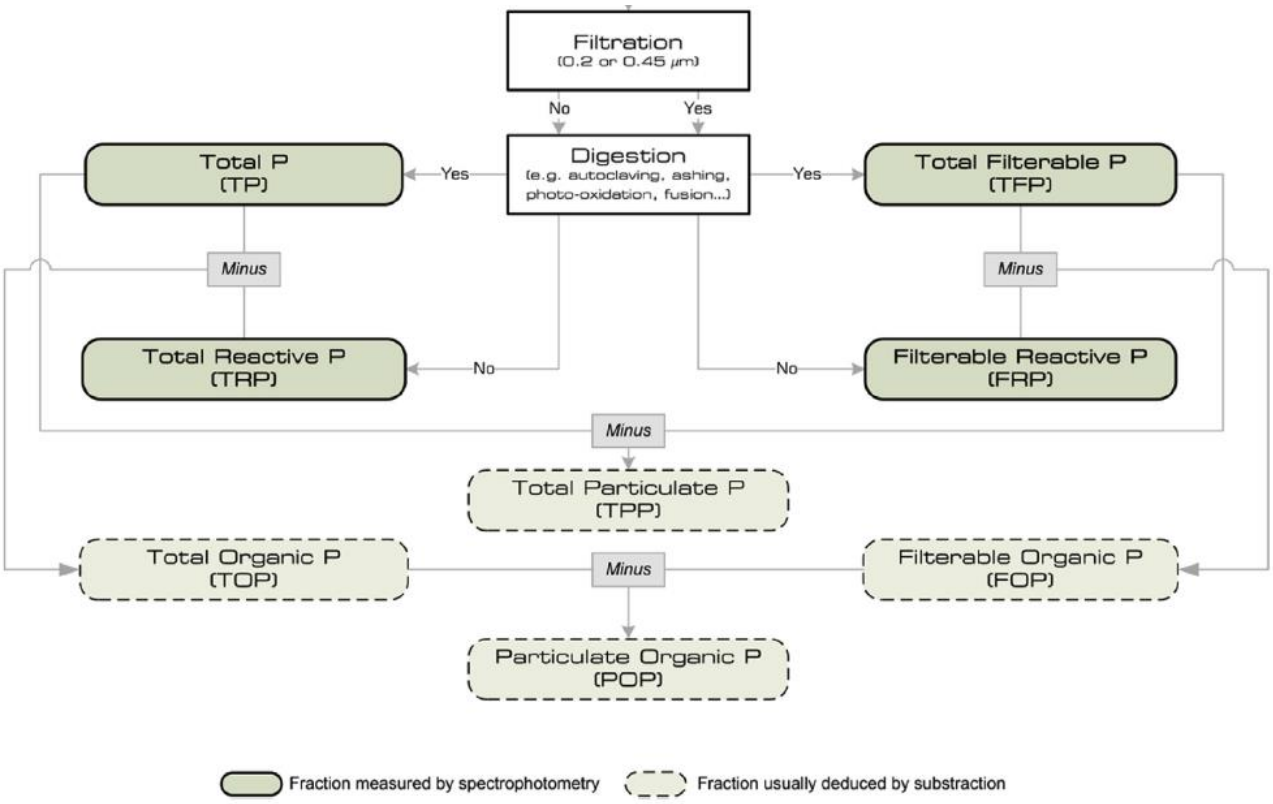

Figure 1.6. Approach for differentiating various phosphorus species in water. Reproduced with permission from Elsevier[38].

1.2.1.2. Arsenic classification

Arsenic can be found in both inorganic and organic forms in natural water systems. The inorganic forms are oxides of the trivalent arsenite, As (III) and the pentavalent arsenate, As (V). The organic forms of arsenic prevalent in the environment are the monomethylarsinic acid (MMAA) and the dimethylarsinic acid (DMAA)[40]. However, both of the organic forms can be converted into the inorganic arsenate (V) under oxidizing conditions[41]. The concentration of the inorganic arsenics is often much higher than the organic arsenics in natural waters, such as rivers and lakes. Regarding the two oxides, the concentration of arsenate dominants over arsenite[42][43]. The arsenite is also oxidized by atmospheric O_2 to form arsenate[44].

As with orthophosphate, arsenate reacts in the molybdenum blue method[38]. Therefore, arsenate is considered as an interference for the detection of molybdenum reactive phosphate using the molybdenum blue method[45]. Arsenite, on the other hand, does not from the molybdenum blue complex[46][45].

1.2.2. Molybdenum blue method for detection of phosphate

The molybdenum blue method is the most common and widely used method for the determination of dissolved reactive phosphate in water[47–49]. However, the molybdenum blue method is not limited to phosphate ions, as both arsenate and silicate ions also undergo the molybdenum blue reaction[38]. Phosphate, arsenate and silicate concentrations in fresh oligotrophic waters are typically in the range of 1-500 μgL^{-1}. However, silicate does not form a blue molybdate complex in water at concentrations below 5.0 mgL^{-1}. As a result, silicate interference in the measurement of phosphate levels can be ignored in most samples. However, the molybdenum blue reaction occurs at phosphate and arsenate concentrations in the μgL^{-1} range in water. As a result, additional steps are required to isolate the arsenate and phosphate from the sample before determination of the phosphate concentration.

In the molybdenum blue method, both phosphate and arsenate react with molybdenum (VI) under the acidic condition to form the Keggin structured 12-molybdophosphoric acid (12-MPA, Reaction 1.1) and 12-molydoarsenoric acid (12-MAsA, Reaction 1.2). The 12-MPA and 12-MAsA are then reduced to form the blue anionic phosphomolybdenum blue (PMB, Reaction 1.3) and arsenomolybdenum blue (AsMB, Reaction 1.4) species[50–52]. The sample is then placed in a cuvette and a visible spectrum is recorded. Depending on the type of reductant used, the blue

anionic PMB or AsMB produce an intense band in the range of 700-900 nm, and the typical molar extinction coefficients for PMB and AsMB are between 10000-28000 L mol^{-1} cm^{-1} [49][53], as shown in Figure 1.8.

$$PO_4^{3-} + 12MoO_4^{2-} + 27H^+ \rightarrow H_3PO_4(MoO_3)_{12} + 12H_2O \quad 1.1$$

12-MPA

$$H_3PO_4(MoO_3)_{12} + \text{Reductant} \rightarrow [H_4PMo(VI)_8Mo(V)_4O_{40}]^{3-} \quad 1.2$$

PMB

$$AsO_4^{3-} + 12MoO_4^{2-} + 27H^+ \rightarrow H_3AsO_4(MoO_3)_{12} + 12H_2O \quad 1.3$$

12-MAsA

$$H_3AsO_4(MoO_3)_{12} + \text{Reductant} \rightarrow [H_4AsMo(VI)_8Mo(V)_4O_{40}]^{3-} \quad 1.4$$

AsAMB

Acid and molybdate concentrations are critical for the synthesis of heteropoly acid and subsequent reduction to the blue-colored PMB and AsMB species. Phosphate and arsenate, like other tetrahedral anions, generate the $[X^{n+}Mo_{12}O_{40}]^{\beta-}$ Keggin ions, where X is the heteroatom of interest. The Keggin species is known as 12-molybdophosphoric acid in the case of phosphate (12-MPA) and 12-molydoarsenoric acid for arsenate[54]. Figure 1.7 depicts the structure of the Keggin ion $[PMo_{12}O_{40}]^{3-}$, which forms in an acidic environment and generates a stable product for spectroscopic phosphate detection[50].

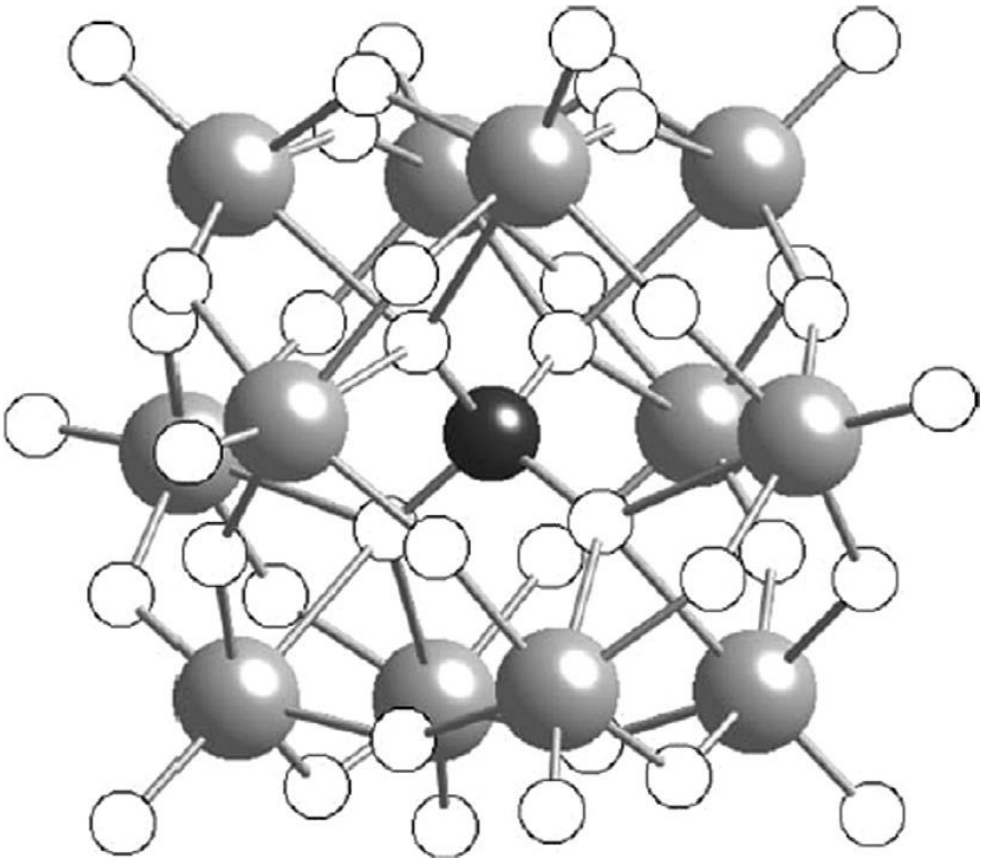

Figure 1.7. The Structure of the Keggin ion $[PMo_{12}O_{40}]^{3-}$. The black, grey, and white spheres show the phosphorus, molybdenum, and oxygen atoms. Reproduced with permission from the Royal Society of Chemistry[50].

The d-d electron transfer between the Mo (V) and Mo (VI) species is responsible for the two bands shown in Figure 1.8. The PMB's strong inter valence charge transfer (IVCT) band, which appears between 800-900 nm, has a molar extinction coefficient between 26000-34000 L mol^{-1} cm^{-1}. The shoulder band in the 650-720 nm range has a molar extinction coefficient of 10000 L mol^{-1} cm^{-1}.

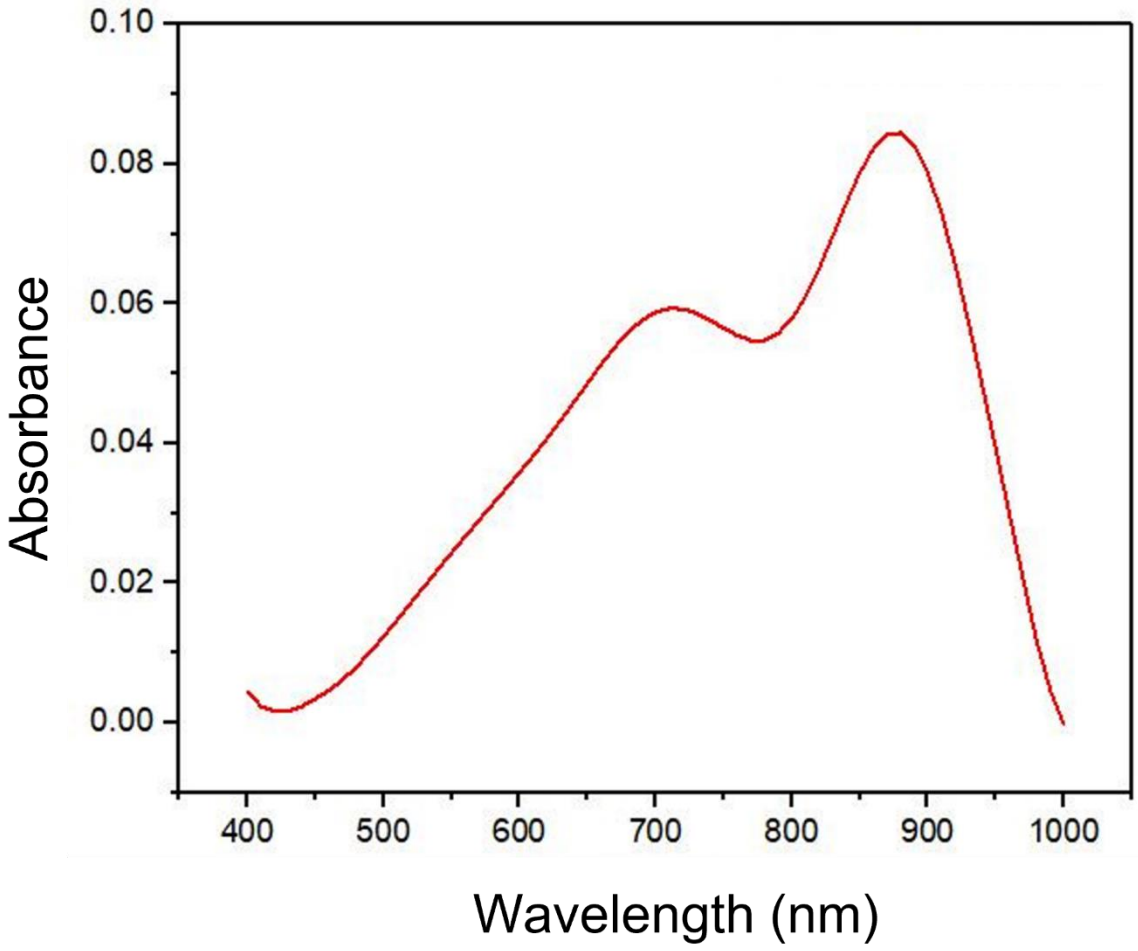

Figure 1.8. A visible spectrum of the PMB species recorded using a 1 cm cuvette.

While a variety of chemicals have been used to reduce the MPA and MAsA into PMB and AsMB, the EPA approved method for the detection of phosphate uses $SnCl_2$ or ascorbic acid, coupled with antimony, as a reductant [55–57]. However, ascorbic acid is the most widely used reductant because the use of antimony as a catalyst accelerates the rate of reduction of 12-MPA to PMB more quickly than $SnCl_2$[17,18]. When using ascorbic acid, the antimony incorporates into the PMB structure and is converted into Sb_2PMB or PAMB [49]. The use of ascorbic acid with antimony does not require heating, which is needed when using $SnCl_2$ as the reductant. In addition, formation of the blue-colored PAMB species is achieved within 10 min with ascorbic

acid, whereas typical times using $SnCl_2$ are much longer. The formation of a blue anionic AsAMB species with arsenate shows a similar band at 880-890 nm when ascorbic acid is used as the reductant, as shown in Figure 1.9.

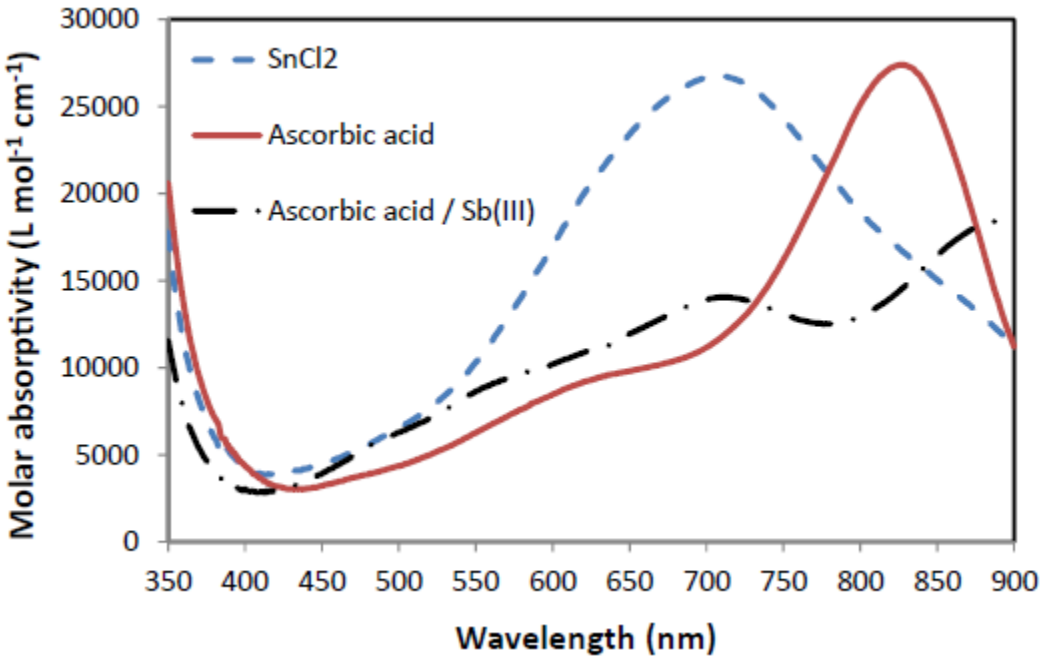

Figure 1.9. The molar absorptivity as a function of wavelength for PAMB species generated using three different reductants. Reproduced with permission from Elsevier[49].

The molybdenum blue method, as described in APHA 4500-PE, can achieve a detection limit of 30 μgL^{-1} phosphate (10 μgL^{-1} phosphorus) in freshwater using a 5 cm pathlength cuvette [59]. Lowering the detection limit below 30 μgL^{-1} requires alternative sampling methods. Gimbert *et al*. have obtained a detection limit of 1 μgL^{-1} phosphate in water using flow injection equipped with a 1 m liquid waveguide capillary cell and $SnCl_2$ as a reducing agent[21][22]. Asaoka et al. have achieved a detection limit of 0.15 μgL^{-1} phosphate by using high-performance liquid chromatography coupled with solid-state extraction[60]. In this method, preconcentration of the PAMB ions was achieved by precipitating PAMB ions with a surfactant and entrapping the

precipitate on a silane column. The precipitate was then eluted with an acetonitrile/water solvent and the intensity of the band from the eluent was recorded at 872 nm to determine the phosphate concentration.

While arsenate (V) and phosphate are indistinguishable by the molybdenum blue method, arsenite(III) does not produce the blue colored complex. As a result, other techniques are used to measure arsenic concentrations in water. The standard methods for the detection of total arsenic (V+III) in water are hydride generation atomic absorption spectroscopy (HG-AAS), as described in APHA method 3114B, induced coupled plasma- mass spectroscopy (ICP-MS), as described in APHA method 3125, and the silver diethyldithiocarbamate method, as described in APHA method 3500-AsB[59,61,62]. The above methods can achieve detection limits of 1-5 μgL^{-1} arsenic in water. However, the standard methods have their own drawbacks. For example, the toxic AsH_3 is formed when using the silver diethyldithiocarbamate method, whereas the HG-AAS and ICP-MS methods require expensive instrumentation and a skilled operator. As a result, developing an approach to measure arsenic using the molybdenum blue method would be an desirable alternative to the current methods.

There have been efforts to address the selective determination of arsenate (V) in the presence of phosphate using the molybdenum blue method. One of the most widely used approaches for the selective detection of arsenate (V), arsenite (III) and phosphate using the molybdenum blue method was developed by Johnson and Pilson [63]. The key concept of this approach is that arsenate(V) and phosphate both form a blue heteropolymolybdate complex that absorbs in the visible region, whereas arsenite (III) shows no absorption with the molybdenum

blue method. Hence, dissolved total arsenic can be quantified by determining the difference in absorbance between a sample that is pre-treated to oxidize arsenite (III) into arsenate(V) (absorbance due to P and total As) and a second sample as arsenate(V) reduced to arsenite (III) (absorbance from P only). Using this approach, Tsang *et al.* were able to achieve a detection limit of 1 μgL^{-1} of total arsenic in the presence of phosphate using sodium dithionite as a reducing agent[64]. Other modifications of the molybdenum blue method for the detection of arsenic involve the preconcentrating of the phosphate or arsenate (V) over a soluble membrane using organic solvents[65,66]. Okazaki et al. achieved a 10 μgL^{-1} detection limit for arsenic by concentrating the arsenate (V) over a soluble membrane and by removing the interfering phosphate over a calcium carbonate column[67]. Asaoka et al. used a solid-phase membrane extraction process to obtain a detection limit of 0.80 μgL^{-1} phosphate in water was reported. This was achieved by preconcentrating the PAMB species in solution over a soluble membrane [68]. In this approach, PAMB ions were converted into a solid precipitate by charge neutralization with a cationic surfactant CTAB.

1.3.1. Target analyte: Cyanide

As with Asaoka et al., our work for detecting phosphate and arsenate was done by forming a precipitate with the large molybdenum clusters. The reason we required a molybdenum cluster is because of the need to have formation of a visible color. However, the concept of a reaction to form a precipitate could be applied to the infrared spectral region and in this case, the approach could be simplified to forming simple salts with the polyatomic anion of interest. To demonstrate this concept, we had chosen cyanide as the target analyte because

the cyanide ion forms precipitates with a number of cations and produces a sharp and intense infrared band in a region where few other species absorb.

Cyanide (CN^-) in water is a highly poisonous blood agent with a maximum allowed concentration in drinking water in the United States of 0.2 mgL^{-1} [69]. This limit is lower in the European Union (0.05 mgL^{-1}). In mineral water, the limit is 0.07 mgL^{-1} [70][71]; which is also the limit of cyanide in drinking water established by the World Health Organization [72]. In natural waters, the acceptable limit for cyanide is lower than the drinking water. The permissible limit of cyanide in natural water is 0.035 mgL^{-1} on a 24-hour average and should never exceed 0.052 mgL^{-1} at any time, as severe toxicity to marine life can occur at 0.03 mgL^{-1} [73].

The above regulations refer to free cyanide (CN^-) in water, as cyanide can form many complexes with metal ions present in water. Cyanides form strong complexes with cations, such as Fe^{3+}, Au^{2+} and Co^{2+}, as well as weak acid dissociate (WAD) cyanides with cations, such as Cu^{2+}, Ni^{2+} and Zn^{2+}. Each of these complexes have their own toxicity, but by far, the most toxic form of cyanide for humans and aquatic life is the CN^- [74]. Even the amount of CN^- in water can vary. For example, the pKa of HCN is 9.2 and thus, loss of the volatile HCN can occur under acidic conditions.

The complex nature of the cyanide species in water has led to numerous methods to measure total cyanide, WAD cyanide and CN^- and these methods often require elaborate sample pretreatment steps. For example, in ASTM D7237 (or EPA 4500- CN^- methods B and C), HCN gas is liberated as a continuous stream from a sample at pH 6.0. The CN^- is then separated using gas dialysis at room temperature. Another pretreatment method involves manual gas reflux

distillation, where HCN gas is liberated and then absorbed using a NaOH scrubber to separate the CN^- from the HCN, as described in the EPA method 9016 or 4500-CN^- method C. Quantification of the CN^- is then accomplished using semi-automated colorimetry, where the CN^- is converted into cyanogen chloride by reacting it with chloramine-T. This cyanogen chloride then reacts with pyridine and barbituric acid to produce a red-colored complex in the solution with a band at 590-610 nm, as described in EPA 4500- CN^- method E [75]. The dynamic range of detection for EPA 4500-CN^- is from 0.005 to 0.5 mgL^{-1}.

Another approach to measure CN^- is EPA-approved method 4500-CN^- D. In this case, the CN^- is titrated using silver nitrate to form a stable $Ag(CN)_2^-$ complex in solution (see Reaction 1). Once all the CN^- is bound with Ag^+, the excess Ag^+ then forms a complex with p-dimethylaminobenzylidene rhodanine, resulting in a change in color from yellow to light pink. Before forming the complex, the rhodanine indicator exhibits an absorbance peak at 450 nm, and after reaching the end point, the band shifts to 490 nm. Thus, from the amount of silver nitrate added to reach the endpoint, the concentration of the CN^- is determined. Further addition of the Ag^+ results in the formation of AgCN precipitate in the solution as shown in Reaction 1.5 and 1.6.

$$Ag^+ + 2CN^- \rightarrow Ag(CN)_2^- \qquad 1.5$$

$$Excess\ Ag^+ + Rhodanine\ (Yellow) \rightarrow Ag^+ - Rhodanine\ complex\ (Pink)$$

$$450\ nm \qquad\qquad 490\ nm$$

$$Ag^+ + Ag(CN)_2^- \rightarrow 2AgCN \qquad 1.6$$

The method has a detection limit of 1.0 mgL^{-1} CN^- in water. However, the accuracy of this method in measuring CN^- in an unknown sample is highly matrix specific and vulnerable to interference

at all pH values. Apart from the interference of cations that complex the CN^-, which is a problem for measuring total cyanide, the method is also susceptible to interference due to the presence of anions, such as S^{2-} or $S_2O_3^{2-}$, in a matrix sample. This is because the method relies of the fate of the Ag^+ ion, and both S^{2-} and $S_2O_3^{2-}$ form Ag_2S and $Ag_2S_2O_3^{2-}$ precipitates with the Ag^+ in solution. Ag_2S also is a dark black precipitate which masks the pink color of the Ag^+-rhodanine complex, making it impossible to obtain the band at 490 nm. Similarly, $S_2O_3^{2-}$ reacts with the silver ions to form an $Ag(S_2O_3)^{3-}{}_2$ complex and causes over estimation of cyanide in the samples(see Reaction 1.7 and 1.8).

$$2Ag^+ + S^{2-} \rightarrow Ag_2S_{(s)} \quad 1.7$$

$$Ag^+ + 2S_2O_3^{2-} \rightarrow Ag(S_2O_3)_2^{3-}{}_{(aq)} \quad 1.8$$

As a result, CN^- solutions must be pre-treated with Pb(II) to remove the S^{2-} or $S_2O_3^{2-}$ ions from the solution before the rhodanine titration method can be used. Therefore, depending on the type of ions present in the matrix sample, the use of the $AgNO_3$ titration method can become ineffective or lead to positive or negative bias of CN^- in the sample.

1.4.1. Organization of the thesis

In Chapter 2, we describe a solventless approach that improves on the approach developed by Asaoka et al. The method shown in Figure 1.10, eliminated the need for solvent extraction and achieved a lower detection limit. CTAB was added to the PAMB and AsAMB ions to form PAMB and the AsAMB particles. The particles in the suspension are then collected into a syringe and a fixed volume of suspension is then passed through a transparent membrane. A Visible spectrum is recorded in transmission mode with the beam passing through the membrane

as shown in Figure 1.10. From the intensity of the band at 700 nm, the concentration of the phosphate and arsenate in the samples were determined.

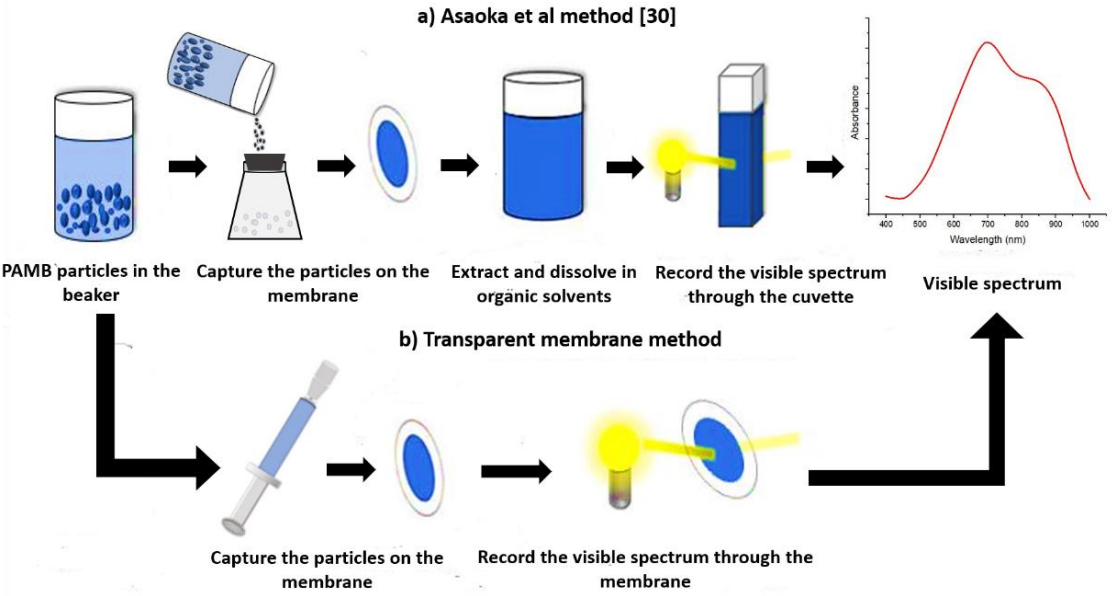

Figure 1.10. (a) The Aosaki method[30] for detection of phosphate and (b) our method, based on spectroscopic measurement of PAMB or AsAMB particles deposited on a transparent membrane in the visible region of the spectrum.

One of the major drawbacks of the molybdenum blue method is its inability to distinguish between phosphate and arsenate. In Chapter 3, we describe an approach to achieve selective detection of phosphate and arsenate. The elements of the approach are shown in Figure 1.11. The key to this method resides in the membrane being transparent in both the visible and infrared spectral regions. As a result, the same membrane, containing both the PAMB and AsAMB particles that were used to record a visible spectrum, is simply dried and then used to record an infrared spectrum in transmission mode. The intensity of an IR band unique to arsenate and located at 879 cm^{-1} is used to measure the arsenate concentration in the sample mixture. Once the arsenate concentration is determined, the contribution of arsenate to the overall

intensity of the band at 700 nm in the visible spectrum can be calculated. The difference in intensity of the 700 nm band is then used to compute the concentration of phosphate in the sample. Thus, by recording a visible and infrared spectrum directly through the same membrane, we achieve the advantage of lower detection levels by concentrating the phosphate and arsenate directly in the beam of the spectrometer, as well as obtaining the selective measurement of phosphate and arsenate concentrations.

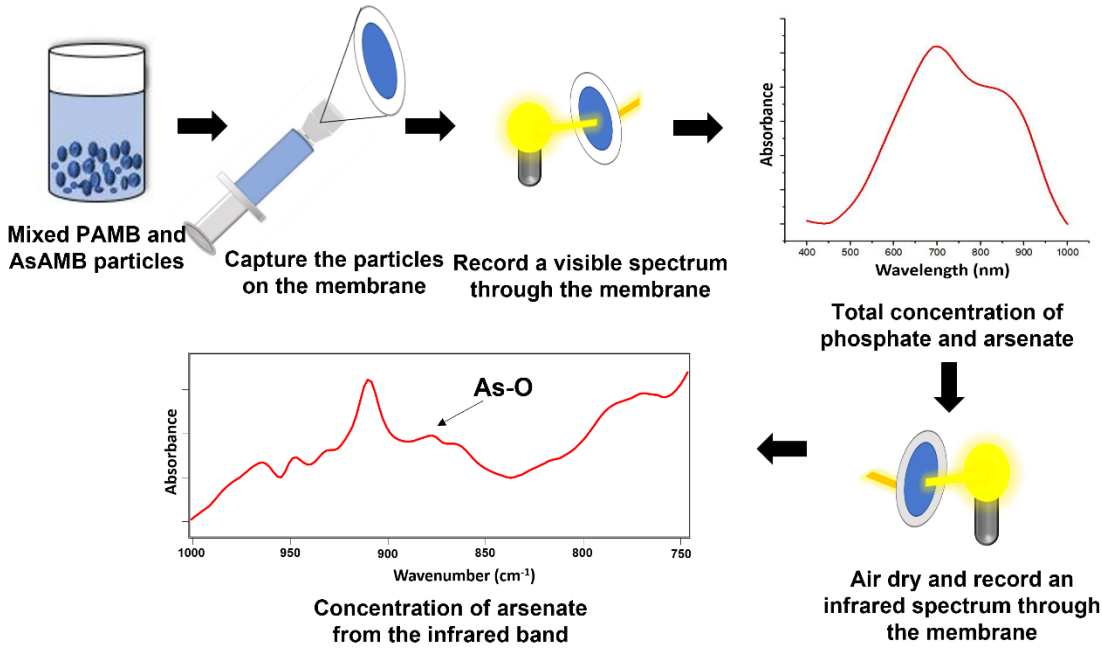

$$\text{Total concentration of phosphate and arsenate} - \text{Concentration of arsenate} = \text{Concentration of phosphate}$$

Figure 1.11. The Vis/IR method for the selective detection of phosphate and arsenate in water by the MBM.

The concept of precipitation of a molybdate complex described in Chapters 2 and 3 laid the foundation for the concept that was investigated in Chapter 4. As described in Chapter 3, the challenge in detecting arsenate and phosphate by IR spectroscopy was from the strong IR bands due to CTAB and the molybdate ions obscuring the IR bands due to phosphate and arsenate. The

idea in Chapter 4 is to eliminate both CTAB and molybdate from the process and to develop a simpler, and more general approach, involving the precipitation of polyatomic anions with simple monoatomic cations. In Chapter 4, this concept is demonstrated with the detection of free and bound cyanide in water. The approach capitalizes on the underlying chemistry of the EPA method 4500-CN^- D, used currently to detect cyanide in water. Specifically, our approach is not based on a titration with Ag^+ to reach an endpoint used in method 4500-CN^- D, but rather the formation of an AgCN precipitate with the addition of excess Ag^+ ions. The concept is illustrated in Figure 1.12. In our approach, the AgCN precipitates that form in the beaker are then captured onto an IR transparent membrane by passing a fixed volume of sample through the membrane filter assembly. The membrane is then air dried and an infrared spectrum is recorded in transmission mode. The captured AgCN particles produce a strong and narrow CN stretching mode at 2165 cm^{-1} and from the intensity this band, the concentration of the CN^- in the water is determined.

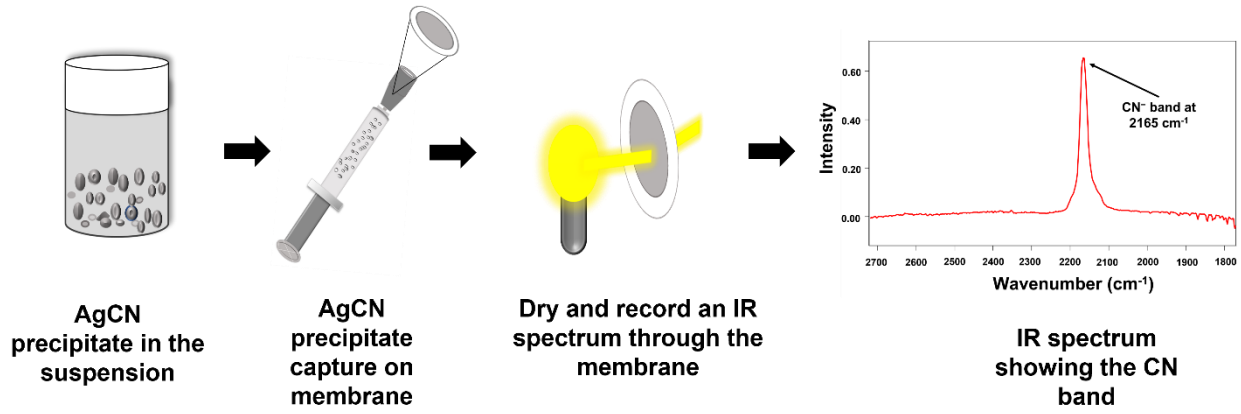

Figure 1.12. The method recording the IR spectrum of AgCN precipitate through a membrane to determine and quantify CN^- concentration in water using the CN^- band intensity at 2165 cm^{-1}.

We note that the methods developed for detection of analytes in water represent a "proof of concept" and not a full-blown method development that would meet ASTM or EPA

standards. In order to meet these standards, the methods would have to be extended to more diverse matrices and involve analysis done by multiple certified labs.

CHAPTER 2: A SOLVENTLESS METHOD FOR DETECTING TRACE LEVEL PHOSPHATE AND ARSENATE IN WATER USING A TRANSPARENT MEMBRANE AND VISIBLE SPECTROSCOPY

2.1. Introduction

Phosphate is a significant environmental pollutant leading to the eutrophication of oligotrophic water resources, such as rivers, lakes, ponds, and streams[24][25]. It has been well established that the presence of an increased amount of phosphate in the ecosystem causes rapid growth of algae, which subsequently leads to eutrophication or a "dead zone" for aquatic lives[76]. On the other hand, arsenic is an extremely toxic element and is classified as a human carcinogenic substance[27–30]. It naturally occurs in soil, sediments, surface water, and groundwater. Arsenic is very mobile and prevalent in organic and inorganic forms with multiple oxidation states[77]. The two most common forms of arsenic in water are arsenic (V) and arsenic (III) oxides. According to the World Health Organization (WHO) and the Environmental Protection Agency (EPA), the permissible limit of arsenic in drinking water is 10 μgL^{-1}[78][79]. Given their environmental and health impact, the necessity to monitor both phosphate and arsenate concentrations in water systems has been of paramount importance.

The most common method for the detection of phosphate in water is the molybdenum blue method, proposed by Murphy and Riley, which is approved by the APHA[1][48][59]. However, the molybdenum blue method is not selective to phosphate ions, as both arsenate and silicate ions also do the molybdenum blue reaction like phosphate. The typical

1 APHA- American Public Health Association

concentrations of phosphate, arsenate, and silicate in fresh oligotrophic waters are in the range of 1-500 μgL^{-1}. However, silicate is not measured below 5.0 mgL^{-1} in water by the molybdenum blue reaction and thus, the interference by silicate in the measurement of targeted phosphate levels can be neglected in most samples. But the molybdenum blue reaction occurs at μgL^{-1} concentrations for phosphate and arsenate in water. Hence, additional steps are needed to first isolate the arsenate and phosphate from the sample for detection using the molybdenum blue method.

In the molybdenum blue method, both phosphate and arsenate react with molybdenum (VI) under the acidic condition to form the Keggin structured, 12-molybdophosphoric acid (12-MPA, Reaction 2.1) and 12-molybdoarsenoric acid (12-MAsA, Reaction 2.2). The 12-MPA and 12-MAsA are then reduced to form the blue anionic phosphomolybdenum blue (PMB, Reaction 2.3) and arsenomolybdenum blue (AsMB, Reaction 2.4) species[49,66,80,81]. The sample is then placed in a cuvette and a Visible spectrum is recorded. Depending on the type of reductant used, the blue anionic PMB[2] or AsMB[3] produce an intense band in the range of 700-900 nm, and the typical molar extinction coefficients for PMB and AsMB are between 10000-28000 L mol^{-1} cm^{-1} [49].

2 PMB- phosphomolybdenum blue

3 AsMB-arsenomolybdenum blue

$$PO_4^{3-} + 12MoO_4^{2-} + 27H^+ \rightarrow H_3PO_4(MoO_3)_{12} + 12H_2O \quad 2.1$$

12-MPA

$$H_3PO_4(MoO_3)_{12} + \text{Reductant} \rightarrow [H_4PMo(VI)_8Mo(V)_4O_{40}]^{3-} \quad 2.2$$

PMB

$$AsO_4^{3-} + 12MoO_4^{2-} + 27H^+ \rightarrow H_3AsO_4(MoO_3)_{12} + 12H_2O \quad 2.3$$

12-MAsA

$$H_3AsO_4(MoO_3)_{12} + \text{Reductant} \rightarrow [H_4AsMo(VI)_8Mo(V)_4O_{40}]^{3-} \quad 2.4$$

AsAMB

While a variety of chemicals have been used to reduce the MPA and MAsA into PMB and AsMB, the EPA approved method for the detection of phosphate uses $SnCl_2$ or ascorbic acid coupled with antimony as reductant [55–57]. However, ascorbic acid is the most widely used reductant because the use of antimony as a catalyst accelerates the rate of reduction of 12-MPA to PMB more quickly than $SnCl_2$[17,18]. In the ascorbic acid method, the antimony incorporates into the PMB structure and is converted into Sb_2PMB or PAMB4[49]. The use of ascorbic acid with antimony does not require heating as needed for the $SnCl_2$ method and the formation of blue-colored PAMB species is achieved within 10 min. A strong band near 880-890 nm with a distinct shoulder at 710 nm is observed in the Visible spectrum. The formation of a blue anionic

4 PAMB-phosphoantimonylmolybdenum blue

AsAMB species with arsenate shows a similar band at 880-890 nm when ascorbic acid is used as the reductant.

The standard molybdenum blue method, as described in APHA 4500-PE, can achieve a detection limit of 30 μgL^{-1} phosphate (10 μgL^{-1} phosphorus) in freshwater using a 5 cm pathlength cuvette[59]. Lowering the detection limit below 30 μgL^{-1} requires alternative sampling methods. Gimbert et al. have obtained a detection limit of 1 μgL^{-1} phosphate in water using a flow injection method equipped with a 1 m liquid waveguide capillary cell and $Sncl_2$ as a reducing agent[21][22]. Asaoka et al. have achieved a detection limit of 0.15 μgL^{-1} phosphate by using high-performance liquid chromatography coupled with solid-state extraction[60]. In this method, preconcentration of the PAMB ions was achieved by precipitating PAMB ions with a surfactant and entrapping the precipitate on a silane column. The precipitate was then eluted with an acetonitrile/water solvent and the intensity of the band from the eluent was recorded at 872 nm to determine the phosphate concentration. Thus, the detection of sub μgL^{-1} phosphate in water requires complex techniques and expensive instruments.

Since arsenate(V) and phosphate are indistinguishable by the molybdenum blue method and arsenite(III) does not produce the blue colored complex with the molybdenum blue method like arsenate(V). Other techniques are typically used to measure arsenic concentrations in water. The standard methods for the detection of total arsenic (V+III) in water are hydride generation atomic absorption spectroscopy (HG-AAS), as described in APHA method 3114B, induced coupled plasma- mass spectroscopy (ICP-MS), as described in APHA method 3125, and silver diethyldithiocarbamate method, as described in APHA method 3500-AsB[59,61,62]. The above

methods can achieve detection limits of 1-5 μgL^{-1} arsenic in water. However, the application of these methods can be limited due to the formation of toxic AsH_3, as in the silver diethyldithiocarbamate method. The HG-AAS and ICP-MS both require expensive instrumentation and a skilled operator, which makes it difficult to do on-site testing. Therefore, the simple, cost-effective nature of the molybdenum blue method has attracted a lot of attention for the detection of arsenate in water.

Given the ease of the molybdenum blue chemistry for the detection of arsenate, there have been efforts to address the selective determination of arsenate (V) in the presence of phosphate using the molybdenum blue method. However, the selective detection of arsenate (V) requires solving the problem of insufficient sensitivity and phosphate interference. One of the most widely used approaches for the selective detection of arsenate (V), arsenite (III), and phosphate using the molybdenum blue method is a scheme described by Johnson and Pilson [63]. The key concept of this scheme is that arsenate(V) and phosphate both form a blue heteropolymolybdate complex that absorbs in the Visible region, whereas, arsenite (III) shows no absorption with the molybdenum blue method. Hence, dissolved total arsenic can be quantified by determining the difference in absorbance between a sample that is pre-treated to oxidize arsenite into arsenate(V) (absorbance due to P and total As) and a second sample as arsenate(V) reduced to arsenite(III) (absorbance from P only). Using this scheme, Tsang et al. were able to achieve a detection limit of 1 μgL^{-1} of total arsenic in the presence of phosphate using sodium dithionite as a reducing agent[64]. Other modifications of the molybdenum blue method for the detection of arsenic involve the preconcentrating of the phosphate or arsenate (V) over a soluble membrane using organic solvents[65,66]. Okazaki et al. achieved a 10 μgL^{-1} detection limit for

arsenic by concentrating the arsenate(V) over a soluble membrane and by removing the interfering phosphate over a calcium carbonate column [67].

Recently, using this solid-phase membrane extraction process, a detection limit of 0.80 μgL^{-1} phosphate in water was reported. This was achieved by preconcentrating the PAMB species in solution over a soluble membrane[68]. In this approach, PAMB ions were converted into a solid precipitate by charge neutralization with a cationic surfactant CTAB. (Reaction 2.5).

$$[Sb2H_4PMo(VI)_8Mo(V)_4O_{40}]^{3-} + 3[H_3C(CH_2)_{15}N^+(CH_3)_3]Br^- \rightarrow \text{PAMB particles} \qquad 2.5$$

PAMB ions CTAB

The solid PAMB particles in suspension were captured by passing 50-100 mL of the suspension through a membrane. The PAMB precipitate was then dissolved from the membrane by using 10-20 mL of solvent, such as methanol, ethanol, and acetonitrile. Hence, the PAMB was concentrated by a factor of 10, as the volume of solvent used to dissolve the precipitate was 10 times lower than the volume of the suspension passed through the membrane. This, in turn, led to 10 times increase in the intensity of the band at 690 nm when recording a Visible spectrum through a cuvette. However, this method required the use of organic solvents, and calibration was required to determine the extraction efficiency for the solvent.

The approach we developed builds on the concept of forming a precipitate but has the advantage that a solvent is not needed to dissolve the blue precipitate. The differences in the approach described in the work of Asaoka et al and the transparent membrane method are shown in Figure 2.1 [30]. In our method, the CTAB was dissolved in water and added to the volumetric flasks containing the PAMB ions to form PAMB particles. The PAMB particles in the

suspension are then collected into a syringe and passed through a transparent membrane. There is no need to extract and dissolve the particles back into the solution as a visible spectrum is recorded directly through the membrane in transmission mode. Thus, by recording a spectrum directly on a transparent membrane, we achieve the advantage of lower detection levels by concentrating the phosphate directly in the beam of the spectrometer. The method is quantitative, providing concentration values of phosphate in water equal to the standard molybdenum blue method with a lower detection limit of 0.64 μgL^{-1} phosphate in water (n=4). Furthermore, we show that this method could be used for arsenate detection down to 4.8 μgL^{-1} in water.

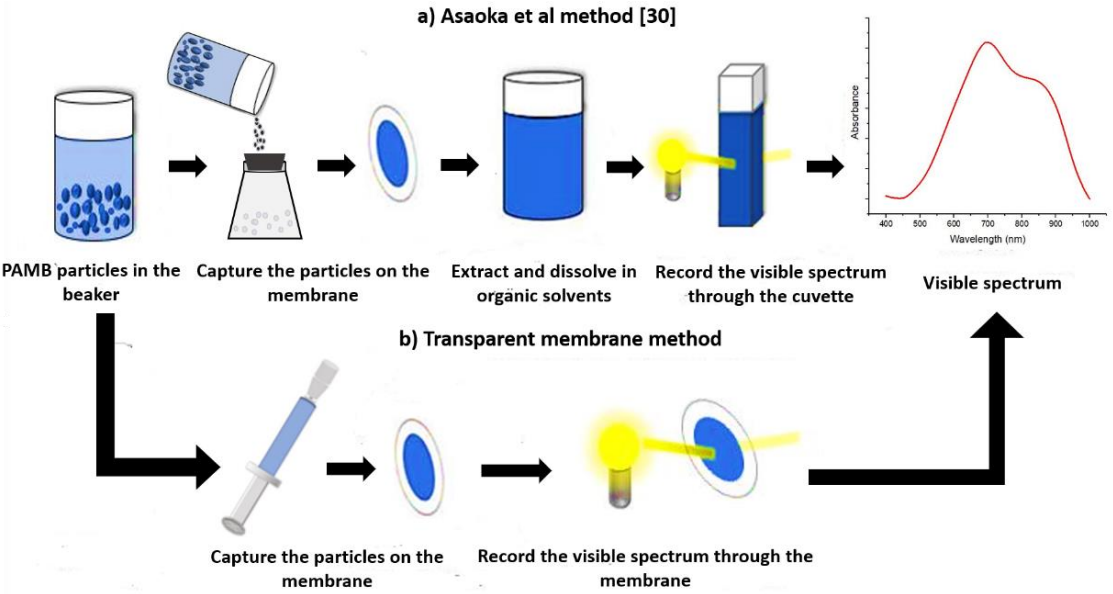

Figure 2.1. (a) The formation and the capture of the PAMB or AsAMB particles over a membrane, followed by extraction and post concentrating, to record the Visible spectrum using a 5-10 cm cuvette; (b) The proposed method of collecting the Visible spectrum of the PAMB or AsAMB particles directly through the membrane for quantification.

2.2. Experimental

2.2.1. Materials

All glassware was first washed with phosphate-free (Tergajet) detergent powder in deionized water (18 MΩ), then acid washed with a warm 10% HCl solution and dried in the oven at 105 °C for 1 hour before use. Reagent grade ammonium molybdate heptahydrate $(NH_4)_6Mo_7O_{24}$), potassium antimonyl tartrate ($C_8H_{10}K_2O_{15}Sb_2$), L-ascorbic acid, cetyltrimethylammonium bromide (CTAB) (364.45 g/mol), analytical grade monopotassium dihydrogen phosphate (KH_2PO_4), and sodium arsenate dibasic heptahydrate (Na_2HAsO_4. $7H_2O$) were purchased from Sigma Aldrich. The Visible transparent membranes and the membrane housings (0.10 µm /13 mm and 0.45 µm/13 mm) were obtained from Orono Spectral Solutions Inc. The details of the membrane assembly are described elsewhere [82].

2.2.2. Standard solutions

Polyethylene volumetric flasks were used to prepare the phosphate and arsenate standard solutions. The volumetric flasks were washed using the same protocol as the glassware and were dried at room temperature before use. The stock solutions of 100 mgL^{-1} phosphate and arsenate were prepared by dissolving 0.144±0.005 g of monobasic potassium dihydrogen phosphate and 0.224±0.005 g of sodium arsenate dibasic heptahydrate into 1000 mL of deionized water in a volumetric flask. Standard phosphate and arsenate solutions of 0.25-500 μgL^{-1} were freshly prepared by serial dilution of the stock solution. A 1 mL sample of the stock solution was transferred to a 100 mL volumetric flask and was filled up to the mark with water to make the 1 mgL^{-1} phosphate and arsenate stock solutions. Then 0.25 mL of the 1 mgL^{-1} solutions were transferred to a 25 mL polyethylene volumetric flask and brought to the mark with deionized

water to make the 10 μgL^{-1} standard solutions. Similarly, 25-50 mL standard solutions of 0.5, 1, 5, and 25, 50, and 100 μgL^{-1} were prepared. All the standard solutions were made at room temperature and stored at 21°C.

2.2.3. Formation of the molybdenum reagent

The experimental procedures for the standard molybdenum blue method (APHA 4500-PE) to generate the PAMB solution with phosphate were followed[59]. In brief, a greenish-yellow reagent solution was prepared by mixing 50 mL of 2.5 M H_2SO_4 with 5 mL of potassium antimonyl tartrate ($C_8H_{10}K_2O_{15}Sb_2$) for 45 seconds and then adding 0.60 g ammonium molybdate heptahydrate $(NH_4)_6Mo_7O_{24}$) dissolved in 15 mL of water. This was followed by the addition of 30 mL of 0.10 M L-ascorbic acid. The solution was stored at room temperature and was stable for 4 hours[59]. The formation of the PAMB solution was carried out by adding 2 mL of the greenish-yellow reagent to 25 mL samples of the freshly prepared phosphate solution. The combined solution was stirred at 21°C for 20 min, leading to the formation of the PAMB anionic species, as shown in Reactions 1.1 and 1.2. 2 mL of that greenish-yellow reagent was also added to 25 mL of DI water to make a reference blank.

2.2.4. Formation of the PAMB suspension with the CTAB

This PAMB solution was used to measure the amount of phosphate, as described in method APHA 4500-PE and a Visible spectrum of the PAMB solution was recorded with a 1 cm cuvette with a blank solution as a reference. The same PAMB solution was also used for the membrane-based method. The first step was to form the PAMB particles with the PAMB ions in the solution by the addition of the cationic surfactant, CTAB. A 0.1 w/v % CTAB in water solution

was made by dissolving 0.1 g CTAB in 100 mL of water. The amount of CTAB solution added to the PAMB solution was chosen to have a minimum of 10 times CTAB to phosphate mole ratio to ensure complete precipitation of the PAMB ions from the solution. A volume of 0.25, 0.5, and 1 mL of the 0.1 w/v % CTAB solution was added to the 25 mL PAMB solution for phosphate concentrations less than 25 μgL^{-1}, 25 to 100 μgL^{-1}, and greater than 100 μgL^{-1}. Similarly, 0.25 to 1.0 mL of a 0.10 w/v% CTAB solution was added to 25 mL of a blank solution to form the blank suspension (no PAMB) for use in recording the reference spectrum. The PAMB particles in suspension were sonicated for 20 min and diluted 10-fold to measure the average particle size on a Malvern 3000 HSA zeta sizer.

2.2.5. Recording the visible spectra through the membrane

The Visible spectra of the captured particles on the membrane were recorded using an Ocean Optics USB 2000+ UV-Vis spectrometer equipped with an ocean optics DH-2000 NIR Halogen light source. The spectra were recorded in transmission mode through the wetted membrane containing the PAMB particles to maintain the transparency of the light beam through the membrane. A fully wetted membrane containing reference blank particles was used as a reference spectrum for samples containing 50-500 μgL^{-1} phosphate. For phosphate concentrations of 0.5-50 μgL^{-1}, the peak intensity at 700 nm PAMB particles was determined by subtracting the peak intensity recorded from the spectrum of the blank particles recorded directly through the membrane.

Formation of the PAMB suspension often resulted in the settling of the PAMB particles to the bottom of the beaker. However, the particles do not stick to the surface beaker and can be

easily re-dispersed by re-stirring the suspension. There was no trace of blue-colored precipitate observed on the sidewall of the glass beaker or polyethylene volumetric flask, even after 36 h of stirring. The suspension was re-dispersed using a magnetic stir bar at 400 rpm as shown in Figure 2.2.

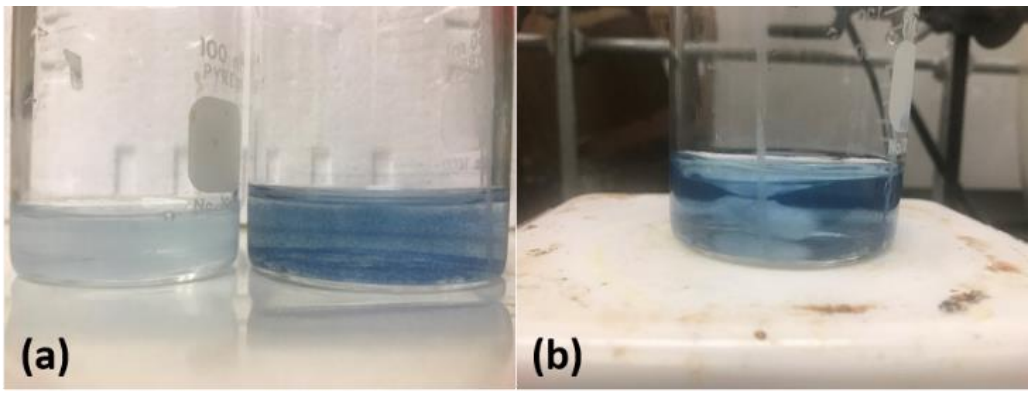

Figure 2.2. (a) The formation of blue colloidal PAMB particles in the beaker after the addition of the CTAB to the PAMB solution. (b) The PAMB suspension was stirred at 400 rpm to make a uniform distribution of the particles and disperse the aggregates before collecting 3-12 mL suspension with the syringe to pass it through the membrane.

A 3-12 mL sample was extracted from a continuously stirred PAMB suspension using a Luer™ lock syringe. The syringe was then connected to the Luer™ lock of the membrane assembly. The assembly was held vertically, and the suspension was pushed by hand through the assembly at a rate of 1-2 mL/min. Pushing the suspension vertically through the membrane from below resulted in a uniform distribution of the PAMB particles on the membrane. While passing the PAMB suspension through the membrane, blue particles were not observed on the sidewall of the syringe. However, particles could be trapped in the tip area. The following control experiment was performed to confirm that there were no particles deposited on the syringe wall or trapped in the tip area. First, 3 mL of a PAMB suspension generated from a 500 μgL^{-1} phosphate solution was drawn into a 3 mL new disposable syringe, and the suspension was then

passed through a 13 mm membrane. Once fully discharged, the same syringe was then filled with 3 mL of DI water. The syringe was shaken and then the water was passed through a new 13 mm membrane. This rinsing step was repeated 3 times. Using these multiple washing steps would result in the collection of any PAMB particles deposited on the wall and around the tip area of the syringe. A visible spectrum was then recorded through the membrane and no band at 700 nm was observed, indicating that little, if any PAMB particles are deposited in the syringe.

Nevertheless, in an abundance of caution to avoid any cross-contamination, we used a new disposable syringe for each measurement. However, the membrane assembly, O-rings, and metal screens were reused and, although we did not detect any residual particles trapped on these components, they were cleaned after each measurement with DI water and wiped with Kim wipes to remove any trace of precipitated particles on the assembly.

2.2.6. Formation of the AsAMB suspension

Formation of the blue AsAMB particles using 5-100 μgL^{-1} of 25 mL arsenate solution was carried out following the same procedures used for generating PAMB suspensions. A sample containing 6-12 mL of the AsAMB suspension was passed through the membrane and a Visible spectrum was recorded. Similarly, 6-12 mL of the blank suspension was passed through a membrane and a blank spectrum was recorded. A wetted membrane was used as the reference spectrum for recording the visible spectrum of the AsAMB particles and the blank. The spectrum obtained for the blank was then subtracted from the AsAMB spectrum and then the intensity of the band at 700 nm was measured.

2.2.7. Environmental sample analysis

Water samples were collected from the Orono municipal tap water and the shallows of the Stillwater River, Orono, Maine during June, July, and August. The collected samples were passed through a 0.45 µm pore size polyvinylidene membrane to remove the undissolved particulate phosphate or arsenate from the water samples. All samples were processed using the procedures described above to form the suspensions using the tap and river water and Visible spectra were recorded after passing 3-12 mL of the suspensions through a membrane and similarly, a blank spectrum was subtracted to measure the intensity of the band at 700 nm for the matrices.

2.3. Results and discussion

2.3.1. Qualitative aspects of the method

Figure 2.3a and Figure 2.3b show the Visible spectra of the membrane before and after wetting with water. The reference spectrum for these two curves was an open beam.

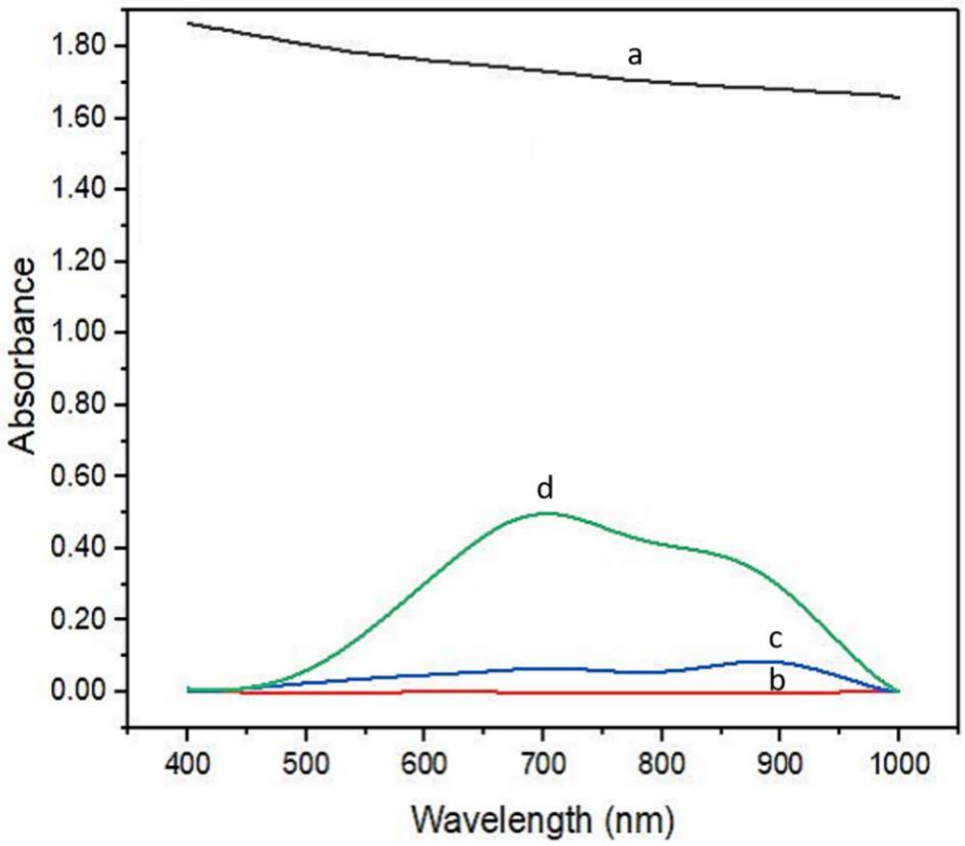

Figure 2.3: The Visible spectra of the membranes were recorded (a) before and (b) after wetting with water. (c) The spectrum of the PAMB ions of 500 μgL^{-1} phosphate solution was measured with a 1 cm cuvette, following the standard molybdenum blue method. (d) The visible spectrum of the precipitated PAMB particles captured on a membrane by passing 3 mL of the PAMB suspension generated using the same 500 μgL^{-1} phosphate solution.

In Figure 2.3a, the Visible spectrum of the non-wetted membrane has a background absorbance value of about 1.78 at 700 nm (1.6% transmittance). This low transmission is due to the scattering of the light as the membrane is white and not transparent by the eye. When wetted with water as shown in Figure 2.3b, the membrane becomes clear, and the Visible spectrum has an absorbance value of 0.01 at 700 nm (98 % transmittance). This increase in throughput from 1.6% to 98% transmittance is due to refractive index matching between the water-filled pores

and the membrane which demonstrates that for recording spectra the membrane must remain wetted with the water.

Figure 2.3c shows the baseline-corrected spectrum obtained for a 500 µgL-1 phosphate solution using the standard molybdenum blue method and a 1 cm cuvette. Figure 2.3d shows the baseline-corrected spectrum obtained for the same 500 μgL^{-1} phosphate solution, as measured using the membrane-based method. In this case, the volume of the PAMB suspension passed through the membrane was 3 mL. Note that the peak is located at 700 nm in Figure 2.3d, compared to 880 nm found in Figure 2.3c. This observation is consistent with the spectra obtained by Asaoka[30] and this blue shift is likely due to the charge neutralization of the PAMB ions with CTAB. This shift to 700 nm is desirable, as it enables the use of low-cost Visible spectrometers that have a cutoff at 900 nm. Also, note that the intensity of the band at 700 nm in Figure 2.3d is a factor of 4.5 times higher than the band at 880 nm in Figure 2.3c. This aspect will be discussed in the sub section 2.3.2.2. entitled “Detection limit”.

We were concerned that transparency through the membrane will be reduced after collecting the PAMB and AsAMB particles, as the particles could lead to scattering of the light. We anticipated that the level of scattering would be dependent on the size of the PAMB and AsAMB particles. However, we found that the level of scattering observed when the particles are deposited on the membrane surface had little if any dependence on the particle size. The background slope underneath the peak at 700 nm shows little if any change for the collection of particles that are 5 µm in diameter, compared to particles of 0.5 µm diameter as shown in Figure

2.4. Once adsorbed on the membrane, the particles form a uniform film that is independent of particle size, and it is the formation of that film that leads to a low level of light scattering.

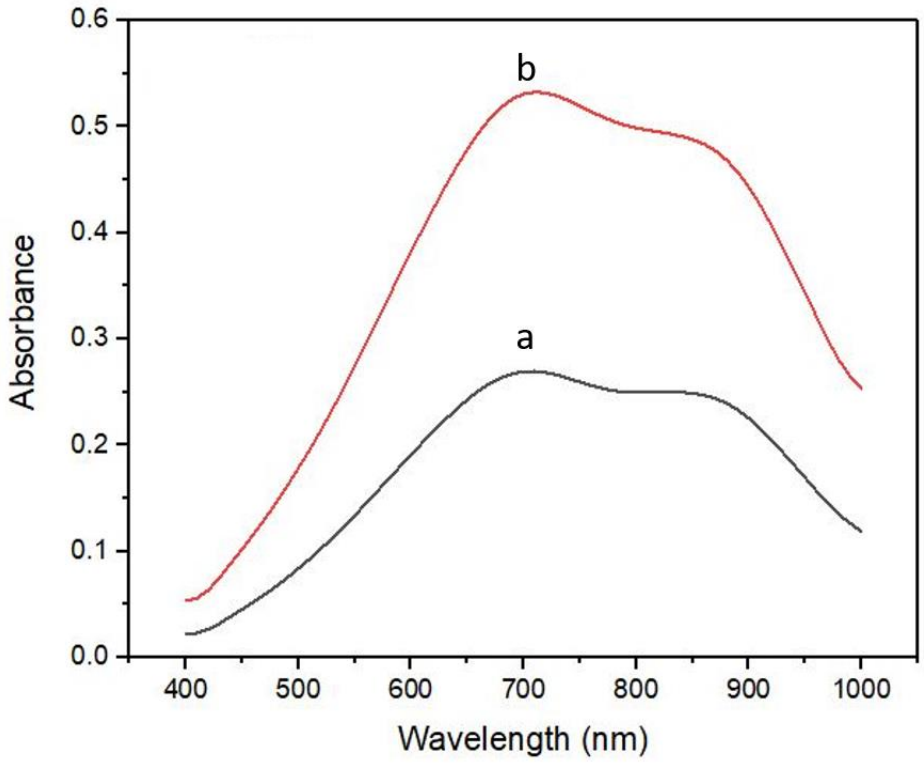

Figure 2.4: The visible spectra of two different sized PAMB particles (a) 0.5 µm and (b) 5.0 µm recorded directly through the membrane surface showing no light scattering under the 700 nm band. No baseline correction was used for either spectrum.

While the particle size of 5 µm or smaller does not lead to scattering issues, there is a lower limit imposed on the particle size due to the pore size of the membrane. We anticipated that some of the particles having an average size of 0.5 µm would pass through the membrane size of 0.45 µm used in this work. However, we found that the effluent was clear, which indicated otherwise. A Visible spectrum of the effluent was measured in a 1 cm path length cuvette using the blank reagent as the reference. No band between 600-900 nm was observed as shown in Figure 2.5.

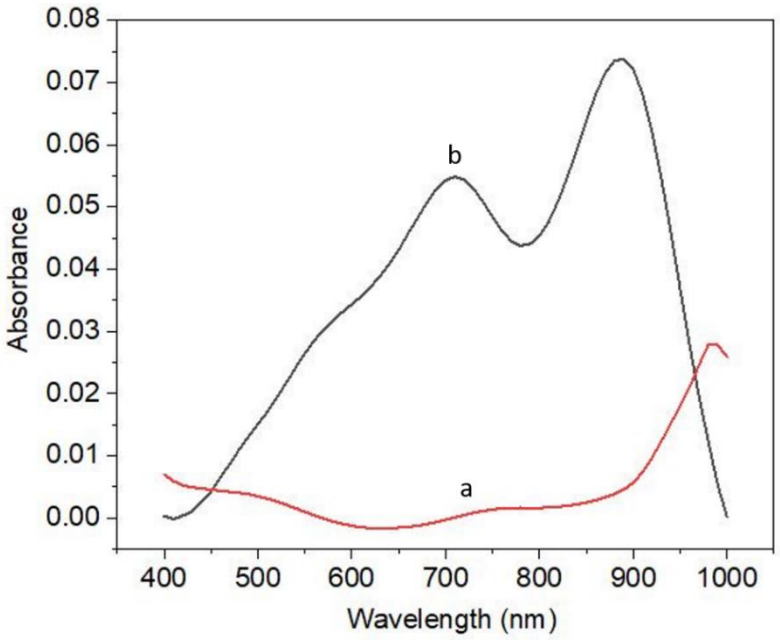

Figure 2.5. (a) Visible spectrum of a 400 μgL^{-1} phosphate solution measured using the standard molybdenum blue method with a 1 cm cuvette. (b) The visible spectrum of the effluent was recorded using a 1 cm cuvette, collected after passing 6 mL of PAMB suspension through the membrane generated using the same 400 μgL^{-1} phosphate solution.

This was further confirmed by passing 3-12 mL of PAMB suspension generated from 0.5-50 μgL^{-1} phosphate solution through 13 mm diameter 0.1 µm and 0.45 µm pore size membranes. The intensity of the 700 nm band was plotted against the captured mass of phosphate per area of the membrane as shown in Figure 2.6. The intensity of the 700 nm band was consistent on both pore size membranes for a captured mass of phosphate per membrane area, which shows that both membranes captured an equal number of PAMB particles. However, a 0.45 µm pore membrane is preferred over a 0.1 µm pore membrane, as it can tolerate higher flow rates of 1-2 mL/min versus 0.5 mL/min for the 0.1 µm membrane. Therefore, only 0.45 µm membranes were used during the development of the method.

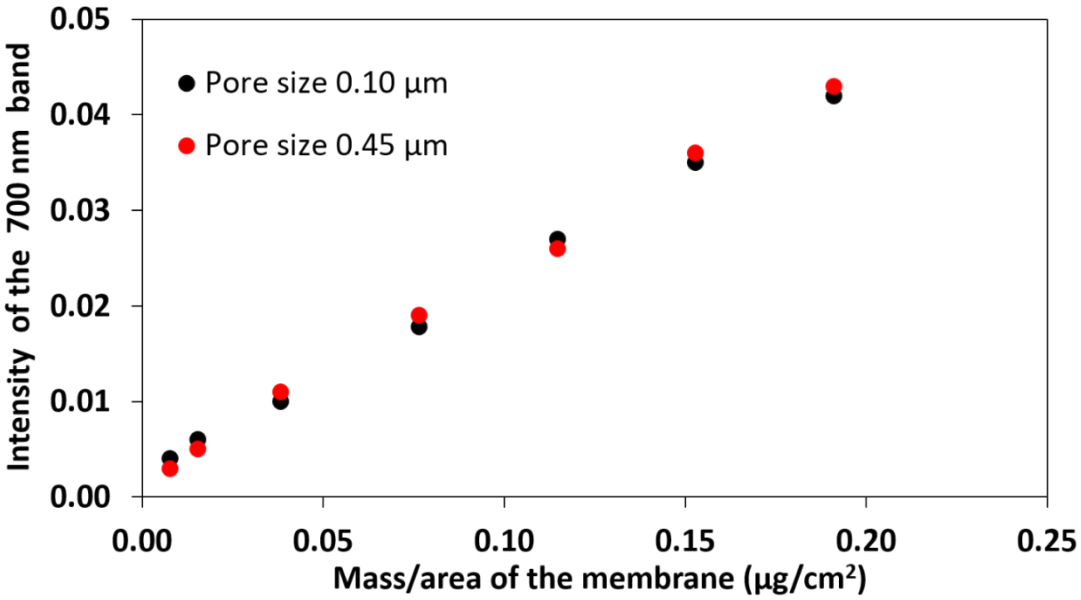

Figure 2.6. The plot of the intensity of the 700 nm band against the mass of phosphate was captured per area of the 0.10 and 0.45 µm pore membranes. This was obtained by passing 3-12 mL of the PAMB suspensions through the membrane generated from 0.5-50 μgL^{-1} phosphate solution.

Even though the 0.45 µm pore membrane captured particles ranging from 0.5 to 5 µm with flow rates of 1-2 mL/min, the smaller 0.5 µm particles were preferred, as the size of the PAMB particles impacts the volume of suspension that can be processed. When the particle size is in the range of 0.50-2 µm, we have found that up to 12-18 mL of the PAMB particulate suspension can be passed through the membrane with uniform distribution of the particles on the membrane. Whereas, when the particle diameters are around 5 µm, a maximum of 3-9 mL of the PAMB suspension can be passed through the membrane. Above this volume, a non-uniform distribution of the PAMB particles on the membrane occurs as shown in Figure 2.7. This is due to the blockage of the pores on the membrane by the larger particles, leading to the nonuniform passage of the fluid through the membrane. Also, the average flow rate of the PAMB suspension

through the membrane decreases from 2 mL/min to 0.5 mL/min, with an increase in particle size from 0.5 to 5 um.

Figure 2.7. The photograph image of the (a) Non-uniform distribution of PAMB particles obtained after passing 12 mL of PAMB suspension of 100 μgL^{-1} phosphate solution through a 0.45 µm pore membrane. (b) Uniform distribution of PAMB particles was obtained over the membrane after passing 6 mL PAMB suspension of the same 100 ppb phosphate solution through a 0.45 µm pore membrane.

The size of the PAMB particles is important to achieve a uniform layer over the membrane and hence, the next step was to determine the parameters that control the particle size. The formation of the particles in the PAMB solution is due to the addition of the CTAB, as the cationic CTAB charge neutralizes the anionic PAMB ions in the solution. Therefore, the change in particle size from 0.50 µm to 5 µm is dependent on the amount of CTAB added to the PAMB solution. When 0.25, 0.50, and 1 mL of a 0.1% w/v CTAB in water was added to a standard 25 mL PAMB solution of 10 μgL^{-1} phosphate, the size of the PAMB particles in the suspension increased from 0.50 µm to 5 µm shown in Figure 2.8.

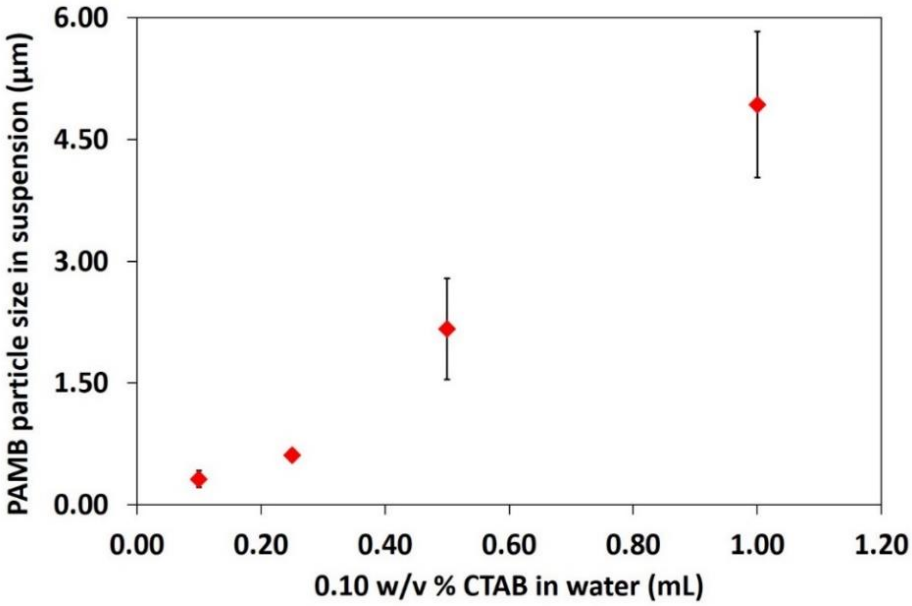

Figure 2.8. Average PAMB particle size distribution for different volumes of 0.1% w/v CTAB in water added to a 25 mL PAMB solution of 10 μgL^{-1} phosphate and measured followed by sonicating for 20 min. The error bars indicate the standard deviation. (n=3).

The increase in the particle size with increasing CTAB concentration is caused by the aggregation of the smaller PAMB particles. As the added CTAB volume in the PAMB solution was increased from 0.25 mL to 1 mL of 0.1% w/v CTAB, the time to form visible particles in the suspension was also reduced to 10 min from 30 min. However, lowering the CTAB amount to less than 0.25 mL resulted in a particle size smaller than 0. 45 µm and thus, a portion of the particles passed through the membrane. Therefore, to ensure a 100% capture of the particles on the membrane, the minimum volume of CTAB was maintained at 0.25 mL. We selected this amount of CTAB so that a minimum phosphate/CTAB mole ratio of 10:1 was maintained, to ensure complete neutralization and precipitation of the PAMB present in the solution. For the 500 μgL^{-1} phosphate sample, this ratio was 5:1.

2.3.2. Quantitative aspects of the transparent membrane method

In transmission spectroscopy, the peak intensity in absorbance units is proportional to the concentration of the sample analyte in solution, as described by the Beer- Lambert's relationship:

$$A = \epsilon\, c\, l \qquad 2.1$$

where A is the absorbance of the analyte at λ_{max}, ϵ is the molar extinction coefficient in mol L^{-1} cm^{-1}, c is the concentration of the analyte in the solution in mol/L, and l is the path length or the cuvette length in cm.

In the membrane approach, there is no fixed path length *l*. The peak intensity in absorbance units is proportional to the concentration of the analyte times the pathlength *(c * l)*, which is the mass of the analyte per area of the membrane and for the work in this paper, has units of µg/ cm^2. Thus, Equation.2.1 is then rewritten as:

$$A = \epsilon \times (\frac{\mu g}{cm^2}) \qquad 2.2$$

Thus, the extinction coefficient with units of cm^2/µg is used in Equation.2 instead of the standard molar extinction coefficient mol L^{-1} cm^{-1} that is used in Equation. 1.

Thus, the extinction coefficient for the band at 700 nm was determined for the PAMB particles. Suspensions of the PAMB particles using standard 0.5-500 µgL^{-1} phosphate solutions were prepared and 3-12 mL of the PAMB suspension were passed through the 13 mm diameter membranes. Then a Visible spectrum was recorded, and the Beer's Law plot of band intensity at 700 nm versus the captured mass of phosphate/per area of the membrane was constructed for 0.5-500 µgL^{-1} phosphate as shown in Figure 2.9.

The intensity of the band at 700 nm for each phosphate concentration was measured 4 different times with 4 different membranes. A linear Beer's Law relationship provides the slope as the extinction coefficient and has a value of 0.223±0.007 $cm^2/\mu g$. The calibration curve shows linearity with the R^2 value of 0.997 over the range of 0.5 μgL^{-1} to 500 μgL^{-1} phosphate. The plotted error bars are the standard deviation (n=4). The average % relative standard deviation (%RSD) of 6 different concentrations for the regression model was found to be 10%.

It is common in most analytical methods to generate a calibration plot where a signal is calibrated using known concentrations of sample analytes. In our case, we are not using a calibration plot but rather a Beer's law plot because the amount of phosphate captured on the membrane is close to 100%. The effluent, after passing each suspension through a membrane, was clear, devoid of any particulates. Furthermore, the Visible spectrum of the effluent showed no presence of PAMB ions as shown in Figure 2.5. Hence, the slope is a measure of the extinction coefficient and not a calibration constant.

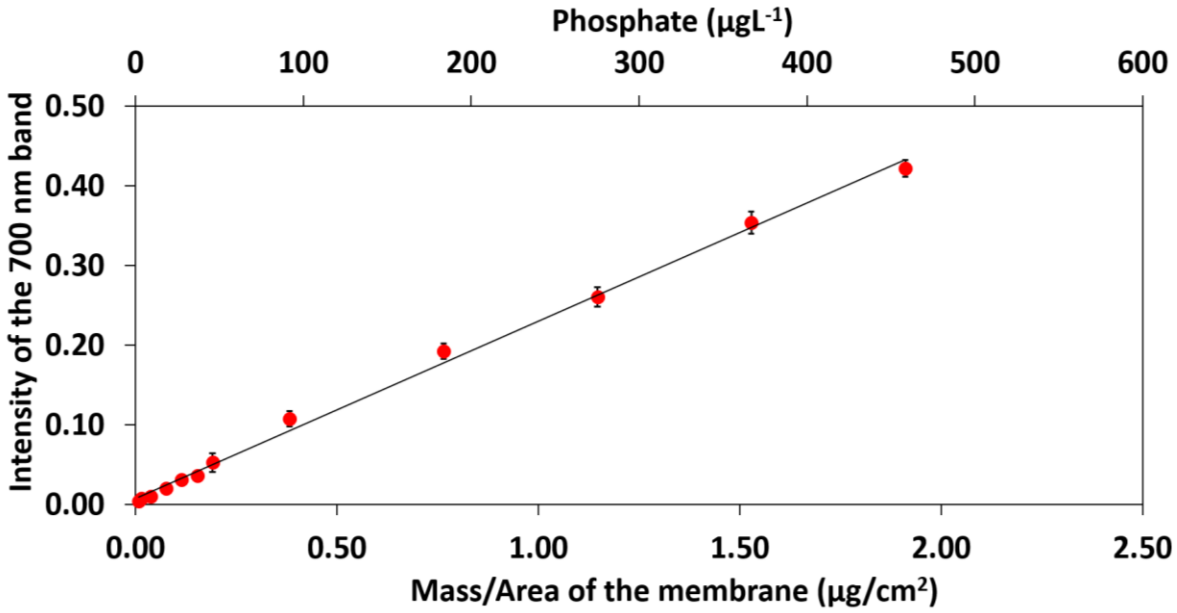

Figure 2.9. Beer's law plot of the 700 nm band intensity as a function of the mass of the PAMB particles captured per area of a 13 mm membrane. The error bars are plotted as the standard deviation where n= 4. The secondary x-axis is the concentration of phosphate defined by passing 3-12 mL of PAMB suspension generated from 0.5-500 μgL^{-1} phosphate solution through the 13 mm membranes.

Therefore, the uniformity of the particulate film over the membrane is very crucial. Since the Visible beam is approximately 4 mm in diameter, the membrane is under-sampled. Thus, it is important to have a uniform particulate film so that the mass/area measured in the beam area is representative of the mass/area across the entire membrane. We note that during the method development, multiple spectra were collected for each sample by rotating and changing the position of the wet membrane in the light beam to ascertain the uniformity of the PAMB particles over the membrane surface. The spot to spot the difference in intensity was about 5%. We also note that a non-uniform film would result in lower precision and as shown in Figure 2.7, the average relative standard deviation was 10%. Hence, the uniformity of the particulate film was not an issue.

Thus, using the known extinction coefficient derived from Figure 2.9, the mass of the phosphate $M_{phosphate}$ on the membrane can be calculated:

$$M_{phosphate} = \frac{A \times \ area\ of\ the\ membrane\ (cm^2)}{\epsilon\ (\frac{cm^2}{ug})} \quad 2.3$$

Then, the concentration of the phosphate in the solution is calculated in terms of μgL^{-1} :

$$C_{phosphate} = \frac{M_{phosphate(\mu g)}}{V\ (mL)} \quad 2.4$$

where V is the volume of the PAMB suspension passed through the membrane.

From Equation.3, the intensity of the 700 nm band is proportional to $M_{phosphate}$ collected on the membrane and inversely proportional to the area of the membrane. Thus, the detection limit will depend on the volume of the sample passed through the membrane and the diameter of the membrane. In this work, we use a 13 mm diameter membrane, and the active diameter was found to be 10 mm due to the use of a Teflon™ O-ring as a seal inside the membrane holder. Thus, the active area was calculated to be 0.785 cm^2.

Then we compared the accuracy of the membrane method with the standard molybdenum blue method. Phosphate concentrations over the range of 100-500 μgL^{-1} were determined using the standard molybdenum blue method (APHA 4500-PE) and the membrane method. Separate samples of 100-500 μgL^{-1} phosphate are measured 3 times with a 1 cm cuvette for the standard method. The same samples are used to form PAMB particles for measurement by the membrane method with the 13 mm membranes. A weighted least square regression for the comparison gave a slope of 0.977±0.017 with an R^2 value of 0.997 as shown in Figure 2.10.

The error in the slope is the standard deviation (n=5). The slope value near 1 shows that the values obtained for the concentration of phosphate from the two methods are the same and that the membrane captured the PAMB particles formed in solution. The highest %RSD is 11% for the 100 μgL^{-1} sample and the average %RSD of all samples is 7%. The low %RSD obtained shows that the mass per unit area of the membrane is uniform from the membrane to the membrane. Thus, we obtained both high precision and accuracy for the membrane-based method.

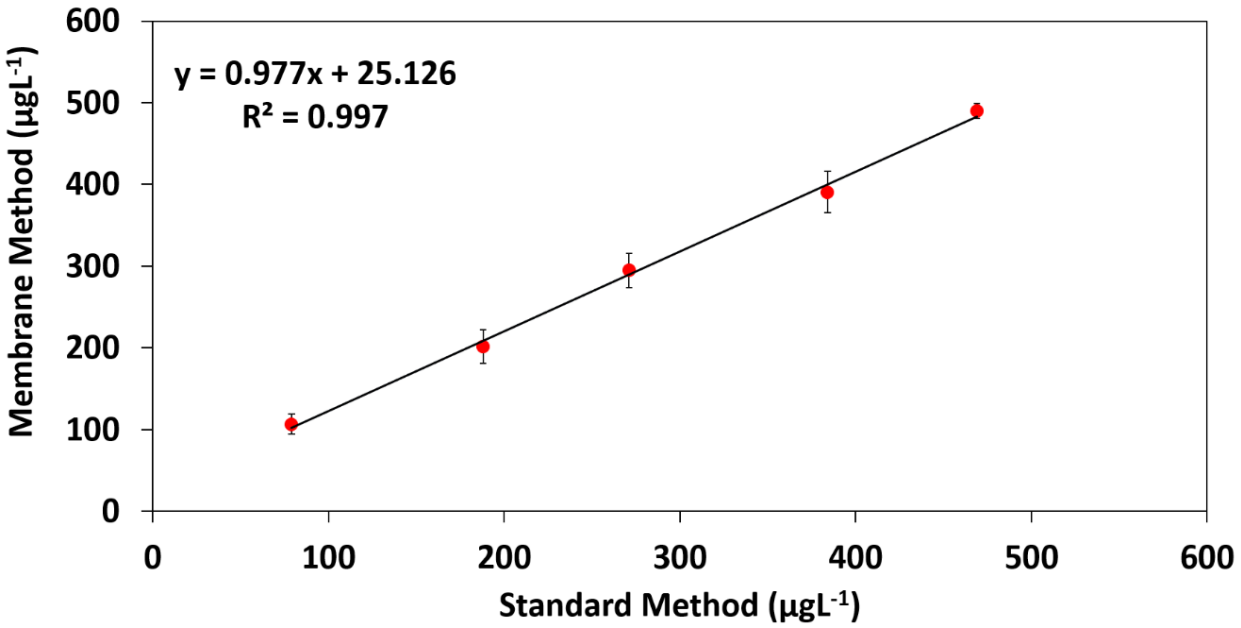

Figure 2.10: The plot of concentration of phosphate measured using the standard molybdenum blue method (1 cm cuvette) versus the transparent membrane method with a 13 mm membrane and passing 3-6 mL of the suspension volume generated using 100-500 μgL^{-1} phosphate solution. The error bars represent the standard deviation, (n=4).

2.3.2.1. Analysis of the environmental samples

The concentration of phosphate in the shallows of the Stillwater River, Orono, and in the Orono Municipal tap water was determined using the membrane method. Hoi wever, the concentrations were not determined using the standard molybdenum blue method because the concentration of phosphate in river water and tap water was below the 100 μgL^{-1} detection limit

using a 1 cm cuvette. Thus, a matrix spike test was performed with the Stillwater River and Orono Municipal tap samples. Visible spectra for both the membrane and standard method (high concentration spike) were recorded using the spiked samples. A 5 times dilution of the river and the tap water was done for the low concentration spike analysis (10 μgL^{-1} phosphate). The amount of phosphate in the diluted river and tap water was determined only using the membrane method. The concentration of the phosphate in all the spiked samples was measured using the membrane method and the % recovery of phosphate in spiked samples was determined. The measured concentrations and % recovery of phosphate in the spiked samples are given in Table 2.1.

Table 2.1: Matrix spike analysis of the water samples collected from the Stillwater River and Orono Municipal tap.

Samples	Matrix Spike (μgL^{-1})	[5]River and tap water (μgL^{-1})	[6]Standard Method (μgL^{-1})	Membrane Method (μgL^{-1})	% Recovery (membrane method)	SD, membrane method (μgL^{-1})
Stillwater river	10	17± 2 (5 times dilution)	-	26	86	5
Tap water	10	17± 2 (5 times dilution)	-	25	83	2
Stillwater river	50	58±5	-	108	99	7
Tap water	50	60±2	-	110	103	10
Stillwater river	200	58	244	247	94	14
Tap water	200	60	258	252	96	12
Stillwater river	500	58	545	541	97	14
Tap water	500	60	563	553	99	10

From Table 2.1 it can be observed that the membrane method showed an average of 95% phosphate recovery, compared to the standard method. This high percent recovery validates the method to use for detecting phosphate in the rivers, lakes, and ponds where the concentration of phosphate is in the range of 1- 500 μgL^{-1}. Thus, the good precision and accuracy of the spiked samples validate the method for use with environmental samples.

[5] Measured using the membrane method (n=3)
[6] With a 1cm cuvette

2.3.2.2. Detection limit

The detection limit for the membrane method was found to be 0.64 μgL^{-1} phosphate for 4 replicates with a 98% confidence interval. In the standard molybdenum blue method, the amount of molybdenum reagent is typically 500-50000 times in excess of the phosphate concentration of 0.5-500 μgL^{-1}. This is to ensure that all the phosphate in the solution is converted into PAMB ions. However, the excess molybdenum also results in the formation of the blank polymolybdate clusters. Depending on the pH and the extent of reduction, the clusters are referred to as the 'big wheel cluster' $[Mo_{154}O_{462}H_{14}(H_2O)_{70}]^{14-}$ or 'blue lemon cluster' $[H_xMo_{368}O_{1032}(H_2O)_{240}(SO_4)_{48}]^{48-}$ and are much larger than the Keggin structure ($PMo_{12}O_{40}^{3-}$) that forms with phosphate [51,83,84] These large blank clusters also produce a broad band centered at 870-890 nm (referred to as the blank) that is identical to the peak obtained with PAMB ions. Thus, the contribution to the overall intensity of the band at 870-890 nm from the blank needs to be determined. Failure to account for the clusters can lead to an overestimation of the phosphate concentration in the water sample as mentioned by several authors [22,34,60,85]. In the standard method, the signal from the blank at 870-890 nm is corrected by using a blank solution to record the reference spectrum. Moreover, The signal from the blank solutions also has an important effect on the detection limit. As the phosphate concentration approaches the detection limit, the difference in signal from the blank reference decreases, and extracting this difference with enough precision becomes difficult.

However, this level of excess molybdenum regent is also used in our membrane method. When the CTAB solution is added to the PAMB solution, the polymolybdate clusters also precipitate and are captured on the membrane along with the PAMB particles. The

polymolybdate clusters have an absorption band around 700 nm and thus, the contribution to the overall intensity of the band at 700 nm from the blank polymolybdate particles must also be accounted for in our membrane method. We showed earlier that the concentration of CTAB is an important factor to control particle size. We also find that the CTAB concentration affects the intensity of the band around 670-700 nm obtained from the captured blank polymolybdate particles.

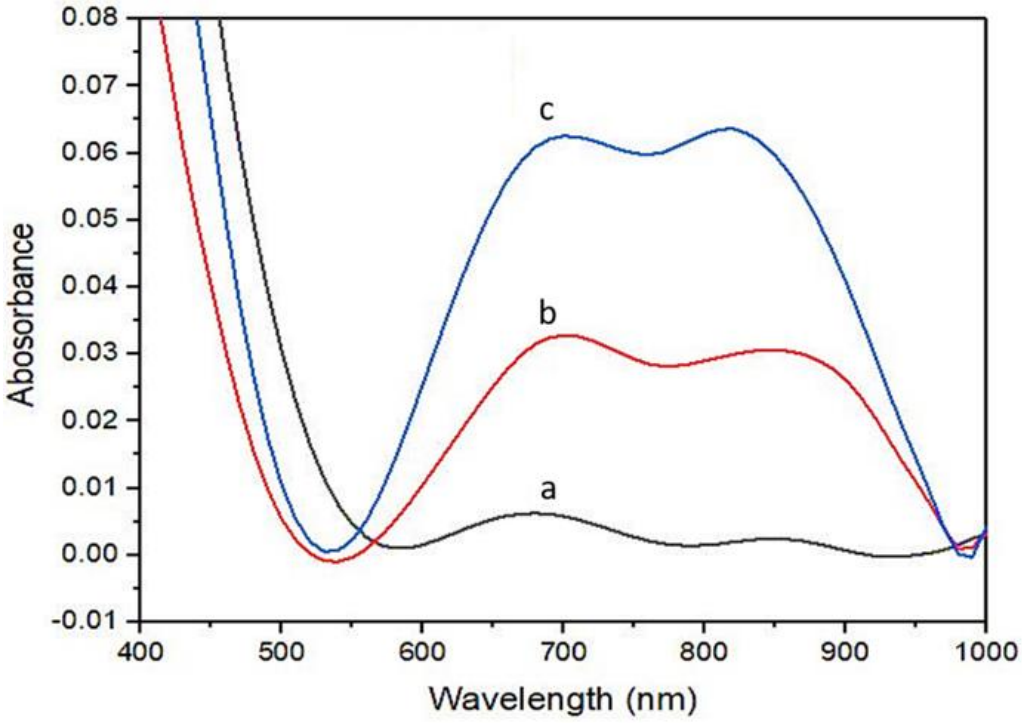

Figure 2.11. Visible spectra of the blank polymolybdate particles were recorded directly through the 13 mm membrane. The particles were captured by passing 12 mL of blank suspension formed by adding (a) 0.25 mL, (b) 0.50 mL and (c) 1.0 mL of 0.1% w/v CTAB in water to the 25 mL blank solutions.

Figure 2.11. shows the Visible spectra of the blank polymolybdate particles recorded directly through the membrane by varying the amounts of 0.1% w/v CTAB solution from 0.25-1 mL, added to a 25 mL blank solution, and passing 12 mL of that suspension. In all cases, the blank polymolybdate particles show a peak around-700 nm with a shoulder around 820 nm. As the

volume of CTAB increased from 0.25 mL to 1 mL, the intensity of the 700 bands also increased from 0.007 to 0.062 absorbance units. Further increase of the CTAB volume to 1.5 mL did not cause any increase in the intensity of the 700 nm band. Thus, a fraction of the excess big wheel clusters is precipitated at 0.25 mL and 0.50 mL of 0.1% w/v CTAB in water. However, with 1 mL of CTAB, all the clusters present were precipitated from the solution phase.

Even though the addition of 0.25 and 0.50 mL of 0.1% w/v CTAB resulted in a fraction of the polymolybdate ions to precipitate, these volumes precipitated all PAMB ions for the phosphate solutions. In Figure 2.9, the linearity across the entire concentration range of 0.5 to 500 μgL^{-1} phosphate was achieved, even though the volume of CTAB solution used below 50 μgL^{-1} phosphate was not enough to precipitate all the blank polymolybdate ions. The blank polymolybdate clusters, such as the big wheel $[Mo_{154}O_{462}H_{14}(H_2O)_{70}]^{14-}$ or the blue lemon $[H_xMo_{368}O_{1032}(H_2O)_{240}(SO_4)_{48}]^{48-}$, possess a large negative charge. Therefore, they require more CTAB for complete neutralization of negative charge to precipitate the ions from the solution, compared to the PAMB $Sb_2[H_4PMo(VI)_8Mo(V)_4O_{40}]^{3-}$ ions, which have a 3- charge and are neutralized with lower amounts of CTAB. Thus, this leads to an improvement in the detection limit because, at low CTAB (0.25 mL of 0.1% w/v CTAB) concentrations, only a small fraction of the large blank polymolybdate ions are precipitated from the solution, compared to the full precipitation of the PAMB ions. Therefore, as the concentration of the CTAB goes down the contrast between the signal from the PAMB particles and the blank polymolybdate particles captured over the membrane increases, allowing to record a Visible spectrum.

However, the question remains as, how much CTAB should be added to precipitate all the PAMB from the solution, as this could differ from the amount needed to form submicron-sized particulates. At sub μgL^{-1} levels, the amount of molybdenum blue reagent is almost 4.0×10^4 fold excess, compared to the phosphate concentration in solution. At this level of excess reagent, the band at 700 nm arising from the blank is about 10-20% in intensity to that obtained for the phosphate. We did not explore the idea of using a lower amount of molybdenum reagent, as the detection of sub μgL^{-1} levels phosphate is well below the 20-30 μgL^{-1} range of the EPA approved detection limit of phosphate in water. Also, as the blank intensity varies from sample to sample, the error in subtracting the blank leads to lower precision. At sub μgL^{-1} concentration, the corresponding blank intensity can show a 10-20% change from sample to sample. Thus, the main source of error at sub μgL^{-1} phosphate concentration arises from the subtraction of the spectrum obtained for the blank particulates. Therefore, multiple spectra were recorded for each blank sample to obtain an average blank intensity for subtraction.

To further lower the detection limit, more than 12 mL of suspension could be passed through the membrane to increase the mass loading of the PAMB particles. However, there are practical limitations with the number of particulates that can be loaded onto the membrane while retaining uniform distribution as shown in Figure 2.7. Using a larger diameter membrane would increase the membrane area, which would allow more than 12 mL PAMB suspension to pass through the membrane while maintaining a uniform particle distribution. However, increasing the membrane area to process a larger volume of PAMB suspension does not lead to a lower detection limit, as the mass per area of the membrane also decreases while the area of the membrane increases. For example, if the diameter of the membrane is doubled to 25 mm

instead of 13 mm, the processed volume of suspension will have to be 4 times more to obtain the same intensity for 700 nm (Equation 2.2). Thus, we did not use larger diameter membranes for this study.

For the standard molybdenum blue method, detection in the range of 10-100 μgL^{-1} phosphate requires the use of 5-10 cm pathlength cuvettes. Asaoka et al. achieved a lower detection limit of 0.80 μgL^{-1} by using solvent extraction and post concentrating method in combination with 5-10 cm pathlength cuvette[68]. In our approach, we achieve the same detection limit as Asaoka et al, without the need for an extraction process or long pathlength cuvettes[68]. On average, a 4-5 times more intense band at 700 nm is obtained for the membrane method compared to the standard method using a 1 cm cuvette (see Figure 2.3C and d). Thus, using a 1 cm pathlength, the molar extinction coefficient for the band at 880 nm is determined to be equal to 0.203±0.006 $cm^2/\mu g$ which is within 91% of the value of the extinction coefficient for the 700 nm band used in the membrane method. Therefore, the higher absorbance obtained for the membrane method is because we have 4-5 times more PAMB particles per area of the beam compared to the standard method.

2.3.2.3. Detection of arsenate using the membrane method

For the detection of arsenate, similarly, a Beer's law plot of band intensity at 700 nm versus the captured mass of arsenate/per area of the membrane was constructed for 5-100 μgL^{-1} arsenate in water as shown in Figure 2.12. The slope of the linear regression gave the extinction coefficient, which is 0.198±0.009 $cm^2/\mu g$. The corresponding R^2 value of the least square regression was 0.998. The average relative standard deviation %RSD of the regression was 13%.

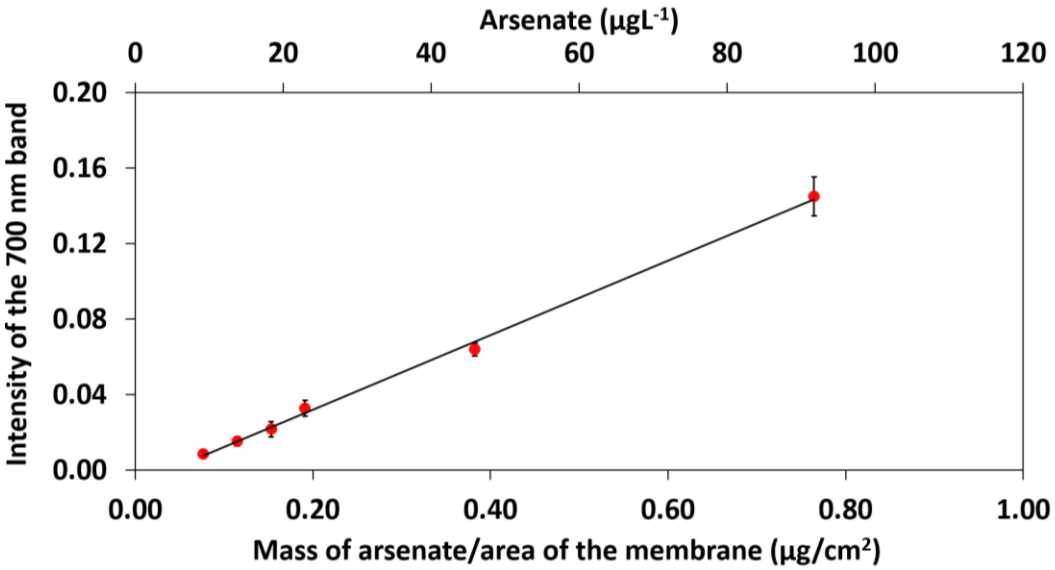

Figure 2.12. Beer's law plot of the 700 nm band intensity as a function of the mass of arsenate captured per area of a 13 mm membrane. The error bars are plotted as the standard deviation where n= 4. The secondary x-axis is the concentration of arsenate determined from the processed 6-12 mL of AsAMB suspension volume generated from 5-100 μgL^{-1} arsenate solution through the 13 mm membranes.

The concentration of arsenate in the Stillwater River and tap water was not measurable using the membrane method due to the phosphate interference. However, to determine the accuracy of the method for arsenate detection, a similar matrix spike analysis was performed using the River and tap water. The measured arsenate concentrations and arsenate % recovery in the matrices is given in Table 2.2. In Table 2.2 the average arsenate % recovery for the membrane method in the spiked samples is 104%. This high % recovery of arsenate validates the accuracy of the membrane method for the detection of arsenate in the real matrices. The detection of 10 μgL^{-1} of arsenate (low concentration spike) in the River and tap water fulfills the EPA limit of arsenic in drinking water.

Table 2.2 : Matrix spike analysis of the water samples collected from the Stillwater River and Orono Municipal tap.

Samples	Matrix Spike (μgL^{-1})	Membrane method (μgL^{-1})	% recovery	SD, membrane method (μgL^{-1})
Stillwater river	10	11	111	2
Tap water	10	12	115	2
Stillwater river	50	46	91	7
Tap water	50	51	103	6
Stillwater river	200	208	104	15
Tap water	200	206	103	5

For arsenate, the extinction coefficient of the membrane method was found to be 0.198±0.010 $cm^2/\mu g$. which is about 13% lower than the measured extinction coefficient of 0.223 $cm^2/\mu g$ for the phosphate. The detection limit for arsenate using the membrane method was 4.8 μgL^{-1} arsenate for 4 replicates with a 98% confidence interval. This detection limit for arsenate using the membrane method is calculated from the measured standard error of 4 replicates of 6 mL of a 15 μgL^{-1} AsAMB suspension passed through a 13 mm membrane. Processing a larger volume of suspension could lower the detection limit further but, as with phosphate, the blank intensity was subtracted for the arsenate to determine the band and it is the error in the blank subtraction that controlled the precision, and hence, the detection limit of the method was 4.8 μgL^{-1}.

Similarly, the method was tested for the detection of silicate in water, as well. Silicate is an interferent and, when present during the standard molybdenum blue method, the silicate forms blue sillicomolybdate ions that have a band at 880-890 nm. However, the formation of these blue ions was not observed at silicate concentrations below 5 mgL^{-1}. Furthermore, at concentrations below 5 mgL^{-1}, the addition of CTAB leads to the formation of solid white CTAB particles, instead of blue particles. Therefore, the interference due to the silicate has no effect over the detection range below 100 μgL^{-1} phosphate or arsenate for both the standard and the membrane method.

2.4. Method robustness

2.4.1. Effect of temperature

The method, as reported, was designed for laboratory-based use, and thus, we did not fully explore sample temperature as a parameter. However, we recognize that the membrane-based method could potentially be used for field-based operation where ambient temperatures would vary, and therefore, the effect of the reaction temperature on particulate formation warrants investigation**.** For field-based detection of phosphate in freshwaters using the membrane method, the PAMB solutions should form particles with CTAB in the ambient (10-30°C) temperature range.

The reaction temperature is also an important factor to consider when using the standard molybdenum method. In the standard method, the development of the blue color of the PAMB solution varies from 10-60 min, depending on the temperature and the concentration of the phosphate in the solution[37]. Below 15^{o}C, the development of the blue color requires more than

10 minutes to occur for all phosphate concentrations. The slow rate of PAMB formation could lead to underestimation of phosphate at a low temperature (10-20°C) if a Visible spectrum is recorded after the recommended development time of 5-10 min.

The question remains as to what effect does reaction temperature has on the formation of the PAMB particles. Thus, the formation of PAMB particles at two concentrations of phosphate (10 and 100 μgL^{-1}) and two temperatures of 15 and 35^{o}C was investigated and compared to the results obtained at room temperature, 21 ^{o}C. The formation of the PAMB ions was carried out at room temperature following the standard method and then, the solutions were transferred into an ice-water bath (15°C) and heated on a hot plate (35°C) before adding the CTAB solution. The suspensions were made by adding 0.25 mL and 1 mL 0.1 w/v% CTAB in water to a 25 mL PAMB solution of 10 μgL^{-1} and 100 μgL^{-1} phosphate. After the addition of CTAB at 15, 21, and 35°C, PAMB particles in the suspension were observed after stirring for 30-35, 15-20, and 10-15 min, respectively. After stirring a total time of 45 min from the addition of the CTAB to the solution to ensure complete particulate formation, 3-6 mL of the suspensions were then extracted into syringes and passed through membranes to collect the PAMB particles. Then a Visible spectrum was recorded through the membrane at room temperature. As shown in Figure 2.13, the intensity of the 700 nm band for PAMB particles generated at 15°C and 35°C were equal in absorbance value to those obtained at 21°C. Thus, while an increase in reaction temperature reduces the time for formation and aggregation of the PAMB particles in the suspension, it did not change the quantification of the amount of phosphate in the solution. In general, we recommend for field-use at temperatures in the 15-20°C range, recording of a Visible spectrum

should be performed at least 45 min after the addition of CTAB to the PAMB solutions to ensure that all PAMB ions form particles with CTAB.

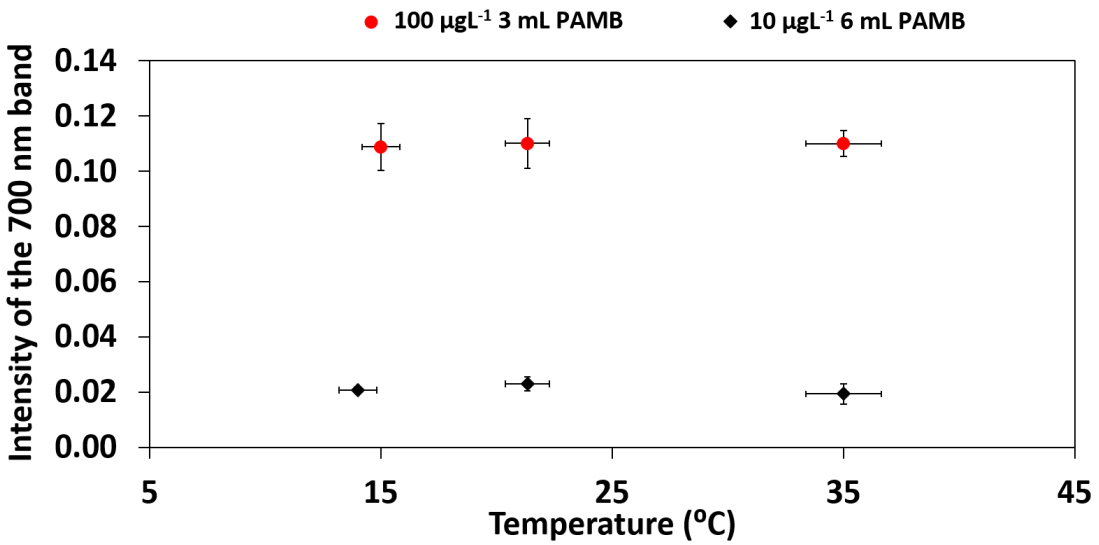

Figure 2.13**.** The intensity of the 700 nm band recorded directly through the membrane by passing 3-6 mL of PAMB suspension made at 15°C, 21°C, and 35°C. The spectra were recorded at room temperature.

2.4.2. Particle stability

In the standard molybdenum blue method, the PAMB solution is stable for several hours [13][38][39]. However, when the PAMB solution does not contain an excessive amount of reductant, the dissolved oxygen present in the solution oxidizes the PAMB species and thus, a Visible spectrum should be recorded as soon as possible [40]. As the oxidation can lead to an underestimation of the amount of phosphate present in the sample. This contrasts with the PAMB particles generated in this work. Therefore, we investigated the stability of the blue color of the PAMB particles in suspension by collecting the particles on the membrane and recording the Visible spectra to determine the band intensity at numerous intervals for 36 h.

Figure 2.14, shows the intensity of the 700 nm band of the PAMB particles on the membrane as a function of time, recorded at room temperature. Suspension of the PAMB particles was prepared by adding 0.5 mL 0.1 w/v% CTAB in water into multiple 50 mL of 10 μgL^{-1} phosphate solutions. Then 6 mL of suspension was extracted from the continuous stirred solution using a syringe and passed through the membrane to collect the particles on the membrane. A Visible spectrum was then recorded 30 min after the addition of CTAB to measure the intensity of the 700 nm band. Similarly, 6 mL samples were extracted at various intervals (0.5-14 h later) up to 36 h and then collected on a membrane where a Visible spectrum was recorded directly through the membrane. As shown in Figure 2.14, the intensity measured at 700 nm did not change for 36 h after the addition of CTAB to the PAMB solution. Thus, the charge-neutral PAMB particles are not readily oxidized, and thus, measuring a Visible spectrum is not under a time constraint as found for the standard molybdenum method.

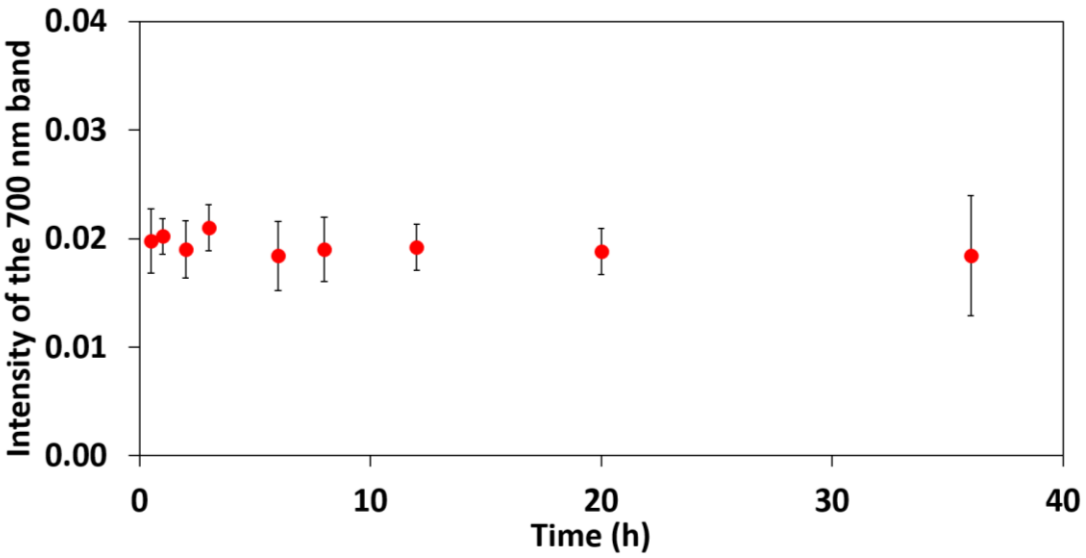

Figure 2.14. The intensity of the 700 nm band as a function of time recorded directly through the membrane, starting from 0.5 h to 36 h after the addition of CTAB to the PAMB solution. The error bars represent the standard deviation (n=5).

2.5. Conclusion

In this work, we have demonstrated a new, fast, and inexpensive method of detecting trace level phosphate and arsenate in water based on the molybdenum blue method. Using this method, we achieved a detection limit of 0.64 μgL^{-1} phosphate and 4.8 μgL^{-1} of arsenate in water with a 98% confidence interval. When compared to the standard molybdenum blue method for phosphate detection, the membrane method showed exceptional linearity (R^2= 0.997) from 100 μgL^{-1} to 500 μgL^{-1} and a slope of 0.997, showing that equivalent values to the standard method were achieved. Furthermore, matrix spikes with the environmental sample, such as the Stillwater River, Orono, Maine, and the Orono Municipal tap water, showed an average 95% recovery of phosphate and 104% recovery of arsenate. The high percent recovery of the method in the matrix spike test shows that the method can successfully be applied for environmental sample analysis. The method is also robust in the ambient temperature range (15-35 ^oC) for the detection of phosphate and arsenate even up to 36 h.

Another advantage of our method is that it enables the use of Visible spectrometers that do not require extended wavelength ranges. In the standard method, the band appears at 880-890 nm, close to the cutoff of 900 nm at a low cost.

CHAPTER 3: A SIMPLE SOLUTION TO THE PROBLEM OF SELECTIVE DETECTION OF PHOSPHATE AND ARSENATE BY THE MOLYBDENUM BLUE METHOD

3.1. Introduction

The molybdenum blue method (MBM) is the standard APHA (APHA 4500 PE) approved method for the detection of phosphate in drinking and freshwater [59]. Since the first use of the MBM in 1962 [48], it has been the subject of many improvements in the detection limits, increasing reaction rates, and simplifying the methodology [22,60,64]. However, the fundamental limitation of the MBM continues to be the interference from arsenate for the detection of phosphate.

In the MBM, the phosphate and arsenate react with a solution of molybdenum (VI) under acidic conditions to form the Keggin structured heteropoly acid complexes 12-molybdophosphoric acid (12-MPA, Reaction 3.1) and 12-molybdoarsenoric acid (12-MAsA, Reaction 3.2). Both 12-MPA and 12-MAsA are then reduced to a phosphomolybdenum blue (PMB, Reaction 3.3) and an arsenomolybdenum blue (AsMB, Reaction 3.4) species. The blue colored solution is then transferred to a 1 or 5 cm pathlength cuvette, and a visible spectrum is recorded. Based on the type of reductant, the PMB or AsMB gives rise to an intense IVCT band in the range of 700-900 nm, with a molar extinction coefficient for the PMB and AsMB reported in the range of 10000-28000 L mol^{-1} cm^{-1} [49].

$$PO_4^{3-} + 12MoO_4^{2-} + 27H^+ \rightarrow H_3PO_4(MoO_3)_{12} + 12H_2O \qquad 3.1$$

$$12 - \text{MPA}$$

$$H_3PO_4(MoO_3)_{12} + \text{Reductant} \rightarrow [H_4PMo(VI)_8Mo(V)_4O_{40}]^{3-} \quad 3.2$$

PMB

$$AsO_4^{3-} + 12MoO_4^{2-} + 27H^+ \rightarrow H_3AsO_4(MoO_3)_{12} + 12H_2O \quad 3.3$$

$12 - \text{MAsA}$

$$H_3AsO_4(MoO_3)_{12} + \text{Reductant} \rightarrow [H_4AsMo(VI)_8Mo(V)_4O_{40}]^{3-} \quad 3.4$$

AsAMB

The standard MBM has a detection limit of 30 µg L^{-1} phosphate (10 µg L^{-1} phosphorus) in freshwater when using a 5 cm cuvette. Thus, the main hurdles to overcome for the MBM are to develop approaches to achieve selectivity between arsenate and phosphate and to lower the detection limit for arsenate [63,64,86,87].

A widely used approach for differentiating between phosphate and arsenic is to reduce the arsenate to arsenite [88]. The arsenite does not form a blue heteropolymolybdate complex and thus, does not produce a band in the visible region of the spectrum. In this approach, the total dissolved arsenic is quantified by determining the difference in intensity of the band at 700-900 nm from a spectrum of a sample where arsenite is oxidized into arsenate (absorbance due to P and total As) and a second spectrum for a sample where arsenate was reduced to (absorbance from P only) arsenite. While this approach enables selective detection of phosphate and arsenate, a pre-concentration step of the phosphate and arsenate is required to achieve the required APHA detection limit of phosphate and arsenic in water.

A second common approach to achieve selectivity by the MBM is to first remove the phosphate by passing the sample through an ion exchange column of calcium carbonate. For example, Kuramitz et al. developed an onsite testing method where a portable device equipped with a $CaCO_3$ column was used to remove phosphate interference [67]. To then improve the arsenate detection limit, the AsAMB ions were converted into a solid precipitate with a cationic surfactant and captured over a membrane for visual detection of the blue-colored AsAMB precipitates. While quantification by inspection by eye was imprecise, Kuramitz et al. reported a detection limit of 10 μg L^{-1} arsenate in water. Okazaki et al. also improved the detection limits for both phosphate and arsenate by precipitating the AsAMB and PAMB ions and collecting the particles onto a membrane. The particles were then extracted into an organic solvent and a spectrum was recorded through the solution measured, using a cuvette. Using this method, Okazaki et al. achieved a detection limit of 10 μg L^{-1} arsenic in water [89].

Recently, we developed a simple, fast, and solvent-free method that matches the accuracy of the standard APHA method for the detection of phosphate [82]. As with the Asaoka et al. method, the PAMB and AsAMB ions in solution form blue particles by charge neutralizing with CTAB, and the particles are then captured on a membrane [68]. However, in our case, the membrane is transparent in the visible region of the spectrum and thus, a visible spectrum can be recorded directly through the membrane in transmission mode [82]. This method eliminates the need for extraction of the particles from the membrane using an organic solvent, as is the case with the Asoaka et al. method [68]. Furthermore, the intensity of the band is due to the mass loading of the PAMB and the AsAMB particles on the membrane and hence, the detection limit is dictated by the volume passed through the membrane. Using this approach, we have

achieved a detection limit of 0.64 μg L^{-1} phosphate and 4.8 μg L^{-1} arsenate in water. While this approach provided a simple approach for achieving the APHA detection limit of 10 μg L^{-1} phosphate and arsenate without the need for long pathlength cuvettes, it did not address the fundamental limitation of the selective detection of phosphate and arsenate by the MBM [82].

In this chapter, we report a very simple extension of our method to achieve selective detection of arsenate and phosphate in water. The method does not involve the laborious and established pretreatment procedures of passing a sample through an ion exchange column or using oxidation/reduction of the arsenate or any additional sample pretreatment steps. The elements of the approach are shown in Figure 3.1. The key to this method resides in the membrane being transparent in both the visible and infrared spectral regions. As a result, the same membrane, containing both the PAMB and AsAMB particles that were used to record a visible spectrum, is simply dried and then used to record an infrared spectrum in transmission mode. The intensity of an IR band unique to arsenate is used to measure the arsenate concentration in the sample mixture. Once the arsenate concentration is determined, the contribution of arsenate to the overall intensity of the band at 700 nm in the visible spectrum can be calculated. The difference in intensity of the 700 nm band is then used to compute the concentration of phosphate in the sample. Thus, by recording a visible and infrared spectrum directly through the same membrane, we achieve the advantage of lower detection levels by concentrating the phosphate and arsenate directly in the beam of the spectrometer, as well as obtaining the selective measurement of phosphate and arsenate concentrations.

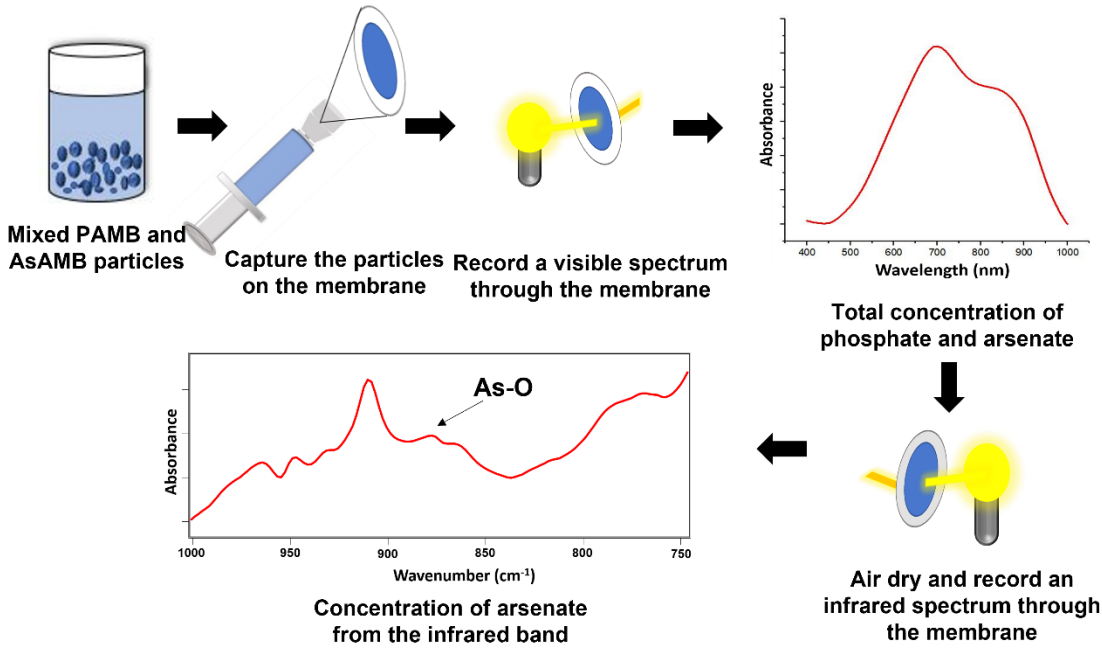

$$\text{Total concentration of phosphate and arsenate} - \text{Concentration of arsenate} = \text{Concentration of phosphate}$$

Figure 3.1. The Vis/IR method for the selective detection of phosphate and arsenate in water by the MBM.

3.2. Experimental section

3.2.1. Materials

All glassware and polyethylene volumetric flasks were washed with phosphate-free (Tergajet) detergent powder and deionized water (18 MΩ), then acid-washed with a warm 10% HCl solution and dried in the oven at 105°C for 20 minutes before use. Reagent grade ammonium molybdate heptahydrate $(NH_4)_6Mo_7O_{24}$, potassium antimonyl tartrate ($C_8H_{10}K_2O_{15}Sb_2$), L-ascorbic acid, cetyltrimethylammonium bromide (CTAB) (364.45 g/mol), analytical grade ≥99.0% monopotassium dihydrogen phosphate (KH_2PO_4), and 99.99% sodium arsenate dibasic heptahydrate ($Na_2HAsO_4 \bullet 7H_2O$) were purchased from Sigma Aldrich. The membranes (0.45 µm/13 mm) used were transparent across the infrared and visible regions of the spectrum and were obtained from Orono Spectral Solutions Inc.

3.2.2. Standard phosphate and arsenate solutions

Polyethylene volumetric flasks were used to prepare the phosphate and arsenate standard solutions. Stock solutions of 100±3 mgL^{-1} phosphate and arsenate were prepared by dissolving 0.143±0.005 g of monobasic potassium dihydrogen phosphate and 0.221±0.005 g of sodium arsenate dibasic heptahydrate into 1000±3 mL of deionized water in a volumetric glass flask. A 1.00±0.006 mL aliquot of the stock solution was drawn using a micropipette and transferred to a 100.0±0.8 mL volumetric flask and then filled up to the mark with DI water to obtain a 1.00±0.03 mgL^{-1} stock solution. Then, 50.00±0.50 mL of 10.0±0.4-500.0±3.3 µg L^{-1} phosphate and arsenate solutions were prepared by serial dilution of the 1 mgL^{-1} stock solution. All solutions were stored at room temperature.

3.2.3. Formation of PAMB and AsAMB ions in the solution

The experimental procedures to generate the PAMB and AsAMB ions are given elsewhere [82]. In brief, a greenish-yellow reagent solution was prepared by mixing 50 mL of 2.5 M H_2SO_4 with 5 mL of potassium antimonyl tartrate ($C_8H_{10}K_2O_{15}Sb_2$) for 45 seconds and then adding 0.60 g of ammonium molybdate heptahydrate ($(NH_4)_6Mo_7O_{24}$) dissolved in 15 mL of water. This was followed by the addition of 30 mL of 0.10 M L-ascorbic acid. The solution was stored at room temperature and stable for 4 hours [59]. The formation of the PAMB and AsAMB suspension was carried out by adding 2 mL of the greenish-yellow reagent to the freshly prepared 50 mL standard phosphate and arsenate solutions. The combined solution was stirred at 21°C for 20 minutes, leading to the formation of the PAMB and AsAMB anionic species. Likewise, a blank solution was prepared by adding 2 mL of the greenish-yellow reagent into 50 mL DI water. Formation of PAMB and AsAMB particles.

3.2.4. Formation of PAMB and AsAMB particles

The formation of the PAMB and the AsAMB particles in solution was carried out by the addition of CTAB to the PAMB and AsAMB solutions of known concentrations of phosphate and arsenate [82]. A 0.025 w/v% CTAB solution was made by adding 0.025 g of CTAB in 100 mL of DI water. Then, 1.0 mL of the 0.025 % w/v CTAB solution was added to 50 mL of PAMB, AsAMB, mixtures of AsAMB and PAMB, and blank solutions. The blank suspension was required for recording the reference in the visible spectrum. The PAMB and the AsAMB particles in suspension were sonicated for 20 min and diluted 10-fold for measuring the average particle size on a Malvern 3000 HSA Zetasizer.

3.2.5. Environmental sample preparation

Water samples were collected from the Orono municipal tap water and the shallows of the Stillwater River, Orono, Maine from June to September 2020. The samples were passed through a 47 mm dia. (0.45 µm pore size) polyvinylidene membrane to remove any undissolved particulate matter from the water. A 2 mL aliquot of the greenish yellow solution was added to 50±0.5 mL of the tap and river water samples to form the blue PAMB and AsAMB ions in the solution. This was followed by the formation of blue colloidal particles by adding 1 mL of 0.025 w/v% CTAB to the water, followed by 20 minutes of sonication at room temperature. Matrix spikes were also performed with the river and tap water samples. These include spiking 25±0.25-50±0.50 mL of the water with 50 µg L^{-1} phosphate and 100 µg L^{-1} arsenate, 50±0.5 mL of the water with 50 µg L^{-1} phosphate and 25 µg L^{-1} arsenate, and 50±0.5 mL of the water with 50 µg L^{-1} phosphate and 50 µg L^{-1} arsenate.

3.2.6. Recording a visible spectrum through the membrane

The factors controlling particle size, collection of the PAMB and AsAMB particles on the transparent membranes, and the procedures for recording a visible spectrum in transmission mode are described in detail in Chapter 2[82]. In brief, a 3-12 mL sample was extracted from a stirred PAMB or AsAMB suspension using a Luer lock syringe. The syringe was then connected to the Luer lock of the membrane filter assembly. The assembly was held vertically and the suspension in the syringe was pushed upward by hand through the assembly at a rate of 1-2 mL/min. Pushing the suspension vertically through the membrane from below resulted in a uniform distribution of the PAMB and AsAMB particles on the fully wetted membrane surface. A visible spectrum in transmission mode was then recorded through the Luer lock of the membrane assembly [14]. The reference spectrum was recorded through a fully wetted membrane containing a uniform distribution of blank particles [82].

3.2.7. Recording an IR spectrum through the membrane

After recording the visible spectrum, the membrane was air-dried by blowing dry air through the Luer lock of the membrane assembly. Typically, 2-3 min of gentle airflow led to a uniformly distributed layer of dried particles on the membrane. The IR spectra were recorded in transmission mode through the assembly following established procedures [14]. The spectra of the PAMB, AsAMB, and blank particles were recorded using a membrane as a reference. All the spectra were recorded at 8 cm^{-1} resolution using an ABB-Bomem FTLA 2000 FTIR spectrometer equipped with a DTGS detector.

3.3. Results and discussion

3.3.1. Qualitative aspects of the method

The visible spectra of the PAMB, AsAMB, and polymolybdate particles (known as the blank) captured on separate membranes are shown in Figure 3.2. All three spectra show the same band centered at 700 nm with a shoulder near 850-870 nm. The rising slope around 400-500 nm is not a band but a continuous increasing background due to the scattering of the visible light by the solid particles. The spectra in Figure 3.2 highlight the selectivity issue between phosphate and arsenate with the MBM, as it is not possible to delineate the contribution of PAMB and AsAMB to the overall intensity of the peak at 700 nm. Even the combined total amount of arsenate and phosphate cannot be determined because the extinction coefficient at 700 nm for arsenate is different from that of phosphate [82]. The selectivity is further complicated because the polymolybdate clusters also produce the same band at 700 nm. In the MBM, the number of molybdenum ions added is typically 500-45000 times higher than the total phosphate and arsenate ions present in the sample. This excess is to ensure that all the phosphate and arsenate in the solution are converted into PAMB and AsAMB ions. However, the excess molybdenum ions result in the formation of polymolybdate (blank) clusters in the solution, along with the PAMB and AsAMB ions. These blank clusters also produce particles when CTAB is added and the visible spectrum of the blank particles on the membrane shows an identical, albeit much weaker, band at 700 nm, as in the spectra obtained with the PAMB and AsAMB particles (see Figure 3.2a). Since the concentration of the blank particles is known, the contribution of the blank to the overall intensity of the band at 700 nm is typically accounted for by recording a reference of a membrane containing blank particles [82].

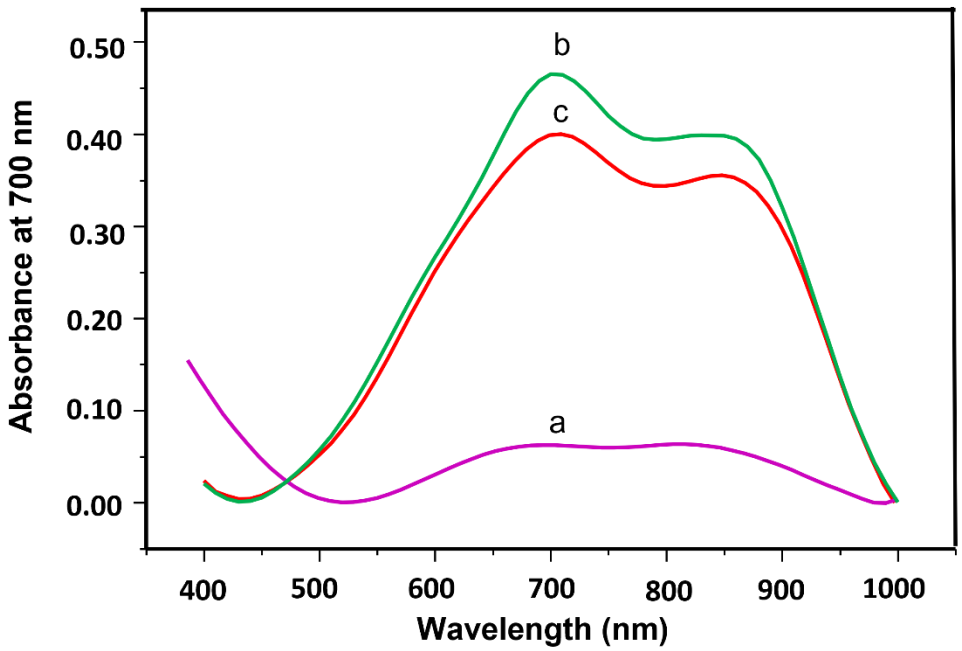

Figure 3.2. Visible spectra in the transmission mode of (a) blank polymolybdate particles captured on a membrane by passing 12 mL of a blank suspension generated using 1.0 mL of 0.1% w/v CTAB in water, (b) PAMB particles captured on a membrane by passing 3 mL of the PAMB suspension generated from a 500 µg L^{-1} phosphate solution, and (c) AsAMB particles captured on a membrane by passing 3 mL of the AsAMB suspension generated from a 500 µg L^{-1} arsenate solution.

Figure 3.3 shows the corresponding IR spectra of the samples used to measure the visible spectra in Figure 3.2. The only processing step was to air dry the membranes after recording the visible spectra. The IR spectra are opaque in the region between 1130 and 1270 cm^{-1}, due to the strong C−F modes of the polytetrafluoroethylene-based membrane. Other key bands are the strong peaks at 2920 and 2850 cm^{-1}, along with multiple peaks in the 1100-800 cm^{-1} region. The bands at 2920 and 2850 cm^{-1} are the $-CH_2$ asymmetric and symmetric stretching vibrations of the long alkyl tail of the CTAB molecule [90]. The band at 911 cm^{-1} is the ν(C−N) stretching vibration mode of the CTAB head group [90]. The ν_{as}(Mo−O) mode appears at 1045 cm^{-1} and the corresponding symmetric ν_s (Mo−O) mode has a strong band at 964 cm^{-1} [91].

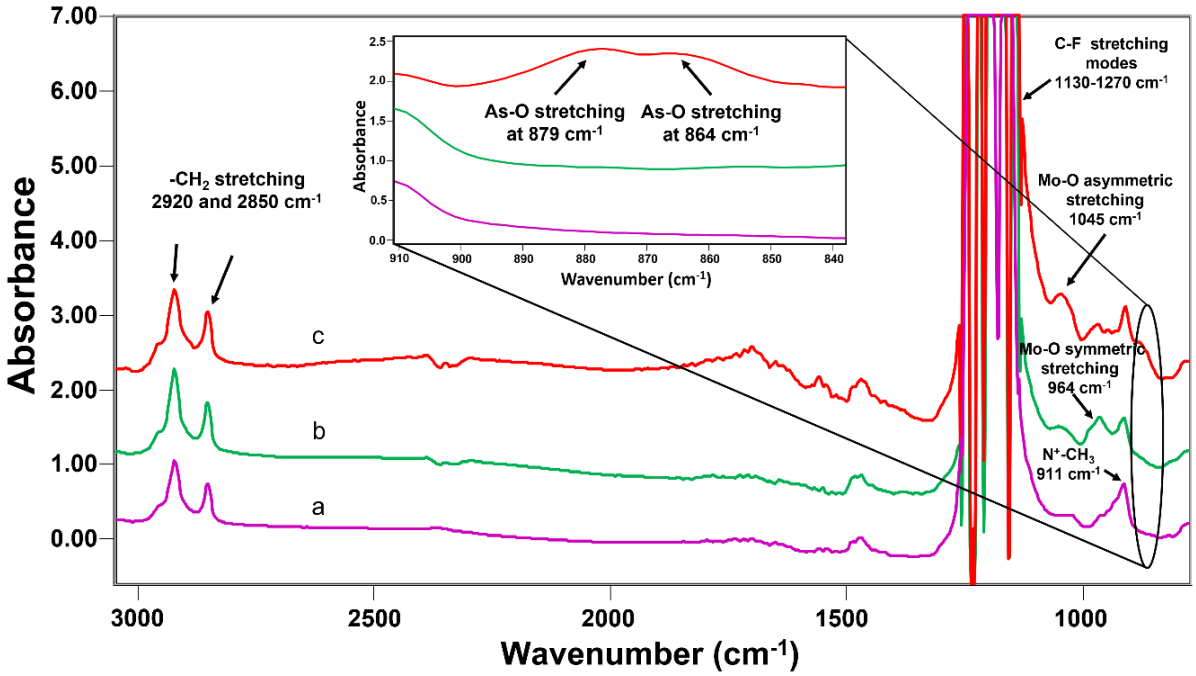

Figure 3.3. The infrared spectra of the same samples used to record the visible spectra are shown in Figure 3.2. The spectra are for (a) blank polymolybdate particles, (b) PAMB particles, and (c) AsAMB particles captured on a 13 mm membrane. The ordinate scale is for the curve labeled (a). Curves (b) and (c) are offset for clarity. A two-point linear baseline correction from 840 to 890 cm^{-1} has been applied to the spectra shown in the inset.

At first glance, there does not appear to be any difference in the IR spectra obtained after collecting the PAMB, AsAMB, or blank particulates on a membrane. However, upon closer inspection, the region between 840-900 cm^{-1} shows unique bands at 879 and 864 cm^{-1} in the spectrum obtained for the AsAMB particles (see inset, Figure 3.3c). These two bands at 879 and 864 cm^{-1} are As-O stretching modes of arsenate and do not appear in the spectra obtained for the blank or PAMB particles (see inset, Figure 3.3a, b) [92].

The two arsenate bands are relatively weak and appear in a narrow featureless region, albeit one that is a sloping background, between 890 to 840 cm^{-1} and are adjacent to a strong ν(C–N) headgroup mode of the CTAB at 911 cm^{-1}. As shown in the inset of Figure 3.3, it is this

featureless background region that is important for performing a baseline correction that enables measurement of the intensity of the arsenate band at 879 cm^{-1} which in turn, is used to determine the arsenate concentration. However, obtaining a featureless background was problematic during the initial development of the method as a weak broad feature centered around 864 cm^{-1} in the background region appeared randomly about 50% of the time (for example, see Figure 3.4a). This broad feature at 864 cm^{-1} was not an As-O mode because it was not accompanied by the stronger peak at 879 cm^{-1}. This was the main hurdle encountered during the development of our method as the appearance of this broad feature prevented the measurement of the arsenate bands intensities when they were less than 0.02 absorbance units. For typical volumes passed through the membrane, this translated to an inability to measure arsenate concentrations below 100 ug L^{-1}.

When first developing our method, we added a higher amount of the CTAB (1 mL of 0.025%w/v CTAB) to 25 ml of the sample as this amount of CTAB was shown to result in PAMB and AsAMB particles with an average diameter of 1-5 µm in size [82]. At this size range, 100% of the particles were captured on the 0.45 µm membranes. In the work reported here, we add a lower amount of the CTAB (1 mL of 0.025%w/v CTAB) to a 50 mL sample because it resolved the issue associated with the appearance of a broad feature at 864 cm^{-1}.

Figure 3.4 shows the spectra obtained for 1 mL of 0.1 % w/v CTAB and 1 mL of 0.025% w/v CTAB added to a 50 mL mixed solution of 25 µg L^{-1} arsenates and 50 µg L^{-1} phosphate. When using 0.1 % w/v CTAB solution, the *ν*(C–N) band of the CTAB head group at 911 cm^{-1} was more intense and accompanied by another weak band at 864 cm^{-1}. When using 0.025% w/v CTAB, the

band at 911 cm^{-1} was lower in intensity and the broad band at 864 cm^{-1} did not appear. In this case, the intensity of the As-O at 879 cm^{-1} can be measured. Therefore, it was necessary to reduce the amount of CTAB added into the mixed solution to obtain a flat background in the region containing the As−O band at 879 cm^{-1}.

We have traced the origin of the broad feature at 864 cm^{-1} to a subtle change in the architecture of the CTAB surrounding the PAMB and AsAMB particles. The appearance of the broad feature at 864 cm^{-1} was always accompanied by an increase in the intensity of the *v*(C–N) headgroup mode of CTAB at 911 cm^{-1} relative to the $-CH_2$ modes of the alkyl tails of CTAB at 2920 and 2850 cm^{-1}. The position and intensity of the $-CH_2$ bands are insensitive to the surrounding environment and thus, their intensities are solely dependent on the adsorbed amount of CTAB on the PAMB and AsAMB particles [93][94]. In contrast, the *v*(C–N) mode at 911 cm^{-1} is structure sensitive and its intensity increases when an opposite change is in the direction of the transition dipole moment [95]. Thus, the relative increase in the intensity ratio for the 911/2850 cm^{-1} bands in Figure 3.4 obtained at the higher CTAB concentration is indicative of a higher fraction of the CTAB molecules bound more perpendicular to the surface of the anionic PAMB and AsAMB particles [95]. By lowering the amount of CTAB by a factor of 4 in this work, we reduced the adsorbed amount of CTAB on the particles (as determined by the intensity of the $-CH_2$ band at 2920 cm^{-1}) by 10%. By reducing the adsorbed amount of CTAB, the CTAB molecules are less densely packed on the surface and hence, adopt a flatter configuration leading to a reduction in the 911 cm^{-1} band and broad feature at 864 cm^{-1}.

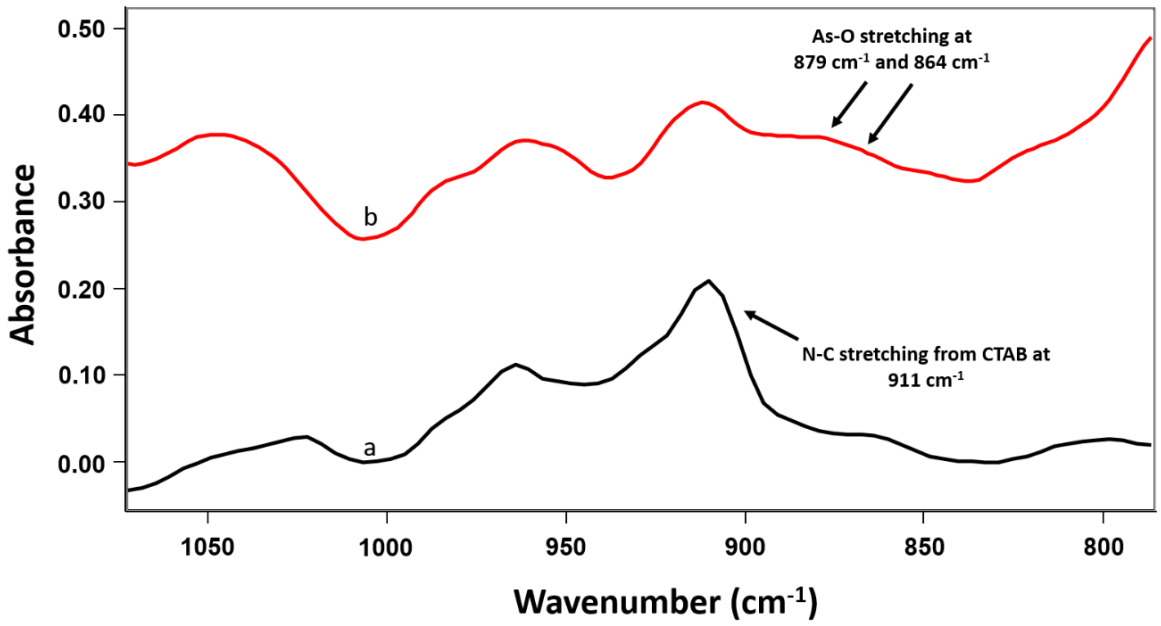

Figure 3.4. The infrared spectra of the particles captured on a 13 mm membrane by passing 12 mL suspension of an (a) 1 mL 0.1% w/v CTAB and (b) 1 mL 0.025% w/v CTAB added to a mixed solution of AsAMB and PAMB ions of 25 µg L^{-1} arsenate+ 50 µg L^{-1} phosphate.

However, reducing the CTAB concentration from 0.1 %w/v to 0.025 %w/v CTAB is not without consequences. This resulted in a 40-45% decrease in the intensity of the 700 nm band in the visible spectrum for the PAMB and AsAMB particles when measured through the membrane. Hence, we were no longer capturing 100% of the particles. By reducing the CTAB amount to 1 mL of 0.025 %w/v CTAB, we found that the average AsAMB particle size dropped from 1-5 µm to 0.5-1.0 µm. Thus, a fraction of the particles pass through the 0.45 µm membrane. This was confirmed by measuring the average particle size on the effluent, after passing a 6-12 mL sample through a 0.45 µm membrane. The average particle size in the effluent was in the range between 0.25- 0.35 µm.

One potential solution to capture a higher fraction of the smaller particle is to use a smaller pore size membrane. Figure 3.5 shows the results obtained when using a 0.10 µm/13 mm

membrane to capture the particles, compared to using a 0.45 µm/13 mm membrane. Using the 0.10 um membrane resulted in only a 5-10% increase in particles captured over the 0.45 um membrane, which translated to about 65-70% capture of the total particles. Since we did not obtain 100% capture of the particles with the 0.10 um membranes, and the increase in particle capture was marginal over the 0.45 µm membrane, we used the 0.45 µm/13 mm membrane throughout this work because the 0.45 µm membrane can tolerate higher flow rates of 3-5 mL/min versus 1-2 mL/min for the 0.10 µm membrane.

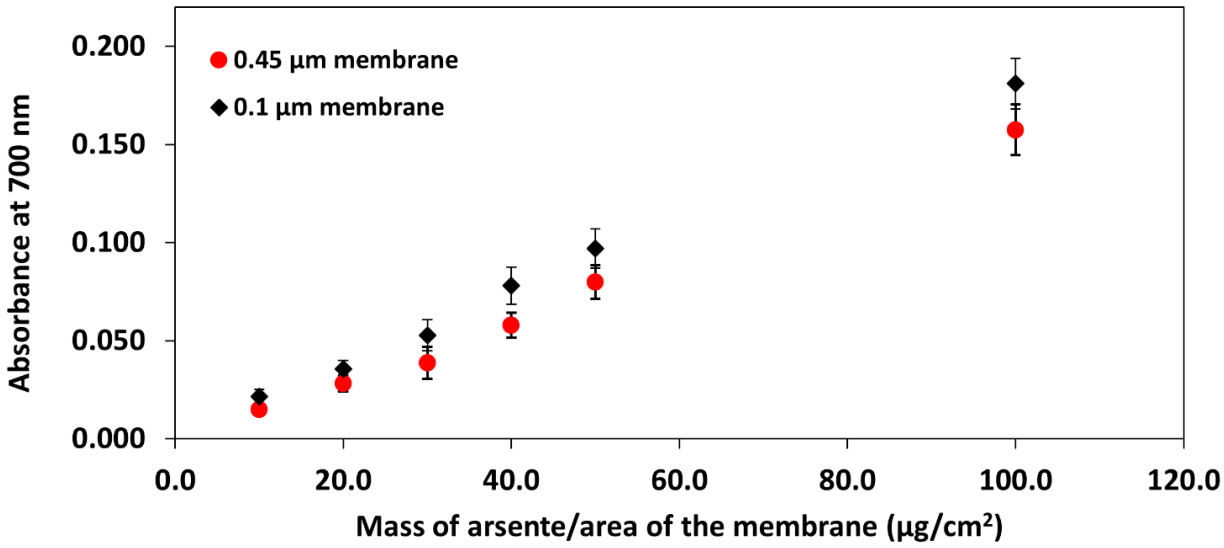

Figure 3.5. The plot of the intensity of the 700 nm band versus the mass of arsenate captured per area for the 0.10 µm and 0.45 µm pore membranes. Spectra were obtained after passing 12 mL of AsAMB suspensions prepared using 10-100 µg L^{-1} of arsenate solutions through the 0.10 µm and 0.45 µm membranes.

Our attempt to identify unique peaks in the infrared spectrum due to the PAMB particles was not successful. While bands unique to AsAMB appear in a region with a flat featureless background, the same is not the case for PAMB. P-O stretching vibrations for known salts of phosphates appear in the 1200-950 cm^{-1} range and are masked by the stronger Mo–O bands in

this region [91][92]. Thus, the essential elements of the approach to achieve selective detection of arsenate and phosphate, using the MBM, involves measuring both the visible and infrared spectra.

3.3.2. The quantitative aspect of the membrane method

3.3.2.1. Determination of arsenate concentration

Details regarding the quantitative aspects of a membrane-based approach for the visible region of the spectrum are described elsewhere [82] and are applicable for analysis in the infrared region. When using a membrane, the peak intensity in absorbance units is proportional to the concentration of the analyte times the pathlength (*c* * *l*), which is the mass of the analyte per area of the membrane and has units of µg / cm^2, as shown in the Equation 3.1.

$$Abs = \varepsilon \times (\frac{\mu g}{cm^2}) \quad 3.1$$

Thus, the detection range and limit depend on the diameter of the membrane and the mass deposited, which in turn, depends on the volume of the suspension passed through the membrane. For example, we recently reported a detection range from 1 to 10,000 ug L^{-1} for water in oil, and this 5 orders detection range was achieved by varying the amount of solution passed through the membrane [14].

In Equation 3.1, ε is the extinction coefficient and was applicable when we captured 100% of the particles. At the reduced CTAB amount used in the work, we do not obtain 100% capture of the particles, and a calibration curve is generated where the slope is the calibration constant (k) rather than the extinction coefficient. We note that once the arsenate concentration is

determined, one could prepare a second sample following the procedures at the higher CTAB concentrations in Reference [13] and collect 100% of the particles to determine the phosphate concentration. However, there is an element of elegance with simply measuring arsenate and phosphate using the same membrane. Hence, calibration plots are required for the detection of arsenate in both the visible and IR spectra and phosphate in the visible spectrum. These calibration plots are shown in Figs. 3.5-7. The calibration plots were generated using a minimum of 4 different membranes for each point in the plots.

Figure 3.6 shows the IR spectra obtained after passing 12 mL of AsAMB suspension through 13 mm diameter membranes of various AsAMB suspensions prepared using arsenate solutions ranging from 25 to 250 µg L^{-1}.

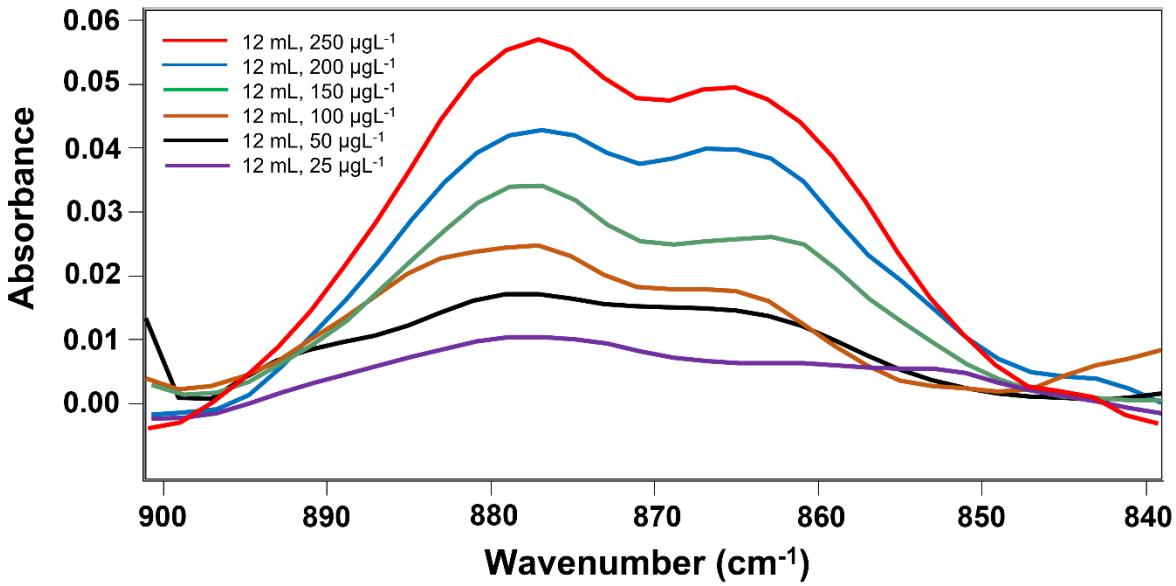

Figure 3.6. IR spectra of the AsAMB particles collected on the membrane for arsenate concentrations ranging from 25 to 250 µg L^{-1}. Baseline corrected from 895 cm^{-1} to 840 cm^{-1}.

A calibration plot of the peak height of the band at 879 cm^{-1}, versus the mass of arsenate/per area of the membrane for concentrations used in generating the spectra, in Figure

3.7. Using a statistically weighted linear regression, we obtain a value for the calibration constant (k_{879}) of 0.0106±0.0005 $cm^2/\mu g$ with a 95% confidence interval. The curve shows excellent linearity with an R^2 value of 0.996 over the range of 25 to 250 µg L^{-1} of arsenate. The plotted error bars are the standard error (n=4) and the average % relative standard deviation (%RSD) of 7 different concentrations was found to be 22%.

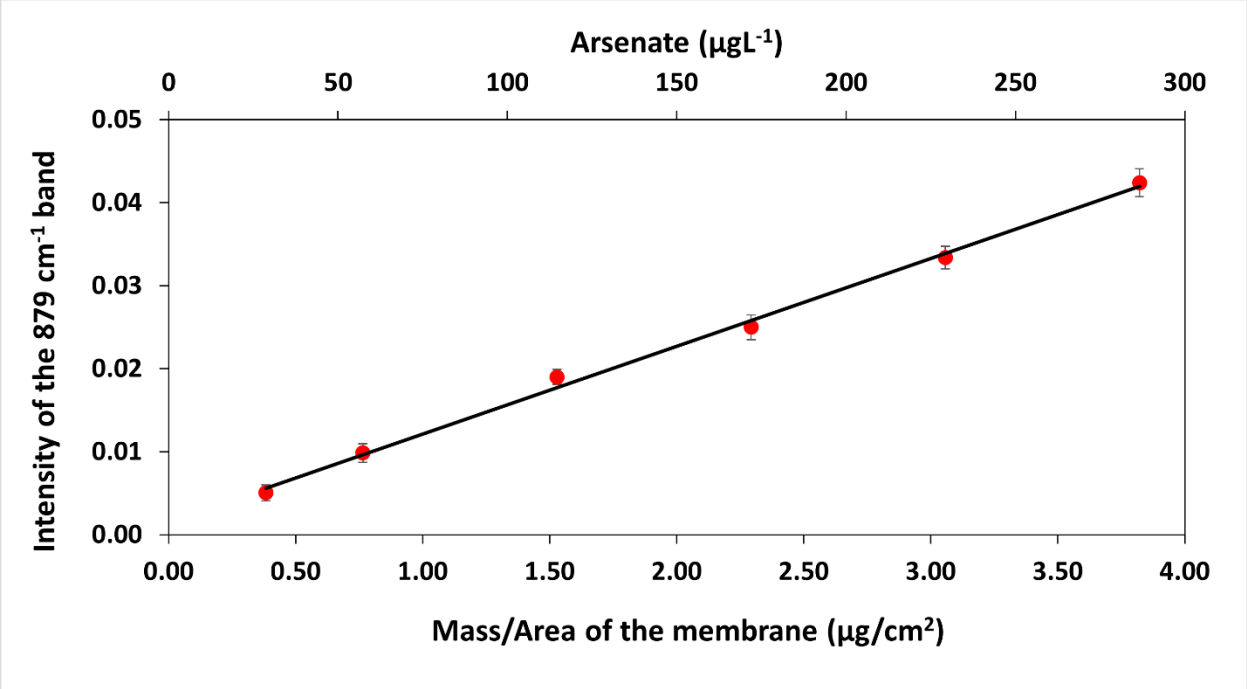

Figure 3.7. The plot of the intensity of the band at 879 cm^{-1} as a function of the captured mass of arsenate per area of the 13 mm membrane was obtained using the membrane method. The error bars indicate standard error (SE) where n= 4. The secondary x-axis is the concentration of arsenate defined by passing 12 mL of the AsAMB suspension, generated from 25-250 µg L^{-1} arsenate solution, through the membrane.

Using the calibration constant for the IR band at 879 cm^{-1} (k_{879}) and the intensity of the band at 879 cm^{-1} in the IR spectrum (Abs_{879}), the mass of the arsenate (M_{arsenate}) collected on the membrane for an unknown sample is calculated as shown in Equation 3.2:

$$M_{arsenate} = \frac{Abs_{879} \times \ area\ of\ the\ membrane\ (cm^2)}{k_{879}(\frac{cm^2}{ug})} \quad 3.2$$

In our work, we used a 13 mm diameter membrane, and the active diameter is 10 mm due to the use of a Teflon™ O-ring as a seal inside the membrane housing. Thus, the active area of the membrane was 0.785 cm^2. The concentration of arsenate in the solution is then calculated in terms of µg L^{-1}, using Equation 3.3:

$$C_{arsenate} = \frac{M_{arsenate(\mu g)}}{V\ (mL)} \quad 3.3$$

where V is the volume of the AsAMB suspension passed through the membrane.

The method detection limit (MDL) of arsenate for the IR method was calculated as 13.9 µg L^{-1} with a 95% confidence interval. The calculation of the MDL is based on using three 50.00 ± 0.50 mL of 75±2.5 µg L^{-1} arsenate solutions. Suspensions of the AsAMB particles were generated and 12 ml of each suspension was passed through 3 different 13 mm membranes. The MDL was calculated from 3x the standard error (SE) following EPA guidelines. The linearity in detection from 25-250 µg L^{-1}, combined with a detection limit of 13.9 µg L^{-1}, shows that the membrane-based IR method could be used to achieve the EPA-required detection limit of arsenate in drinking water via the MBM without the interference of phosphate.

3.3.2.2. Determination of arsenate and phosphate concentrations

Once the amount of arsenate was determined, using Equation. 3, the contribution of arsenate to the 700 nm band in the visible was calculated. This required development of the calibration constant, which was determined from the plot shown in Figure 3.8. Figure 3.8 is the calibration plot of the peak height of the band at 700 nm versus the mass of arsenate/per area

of the 13 mm membrane using concentrations of 25 -100 µg L^{-1} arsenate. The membranes used to generate this curve were the same membranes used for generating the calibration curve for the band at 879 cm^{-1} in the infrared spectrum. Using a statistically weighted linear regression, we obtain a value of 0.106±0.010 cm^2/µg for the calibration constant ($k_{700,As}$) with a 95% confidence interval. The curve shows linearity with the R^2 value of 0.994 over the range of 10 to 100 µg L^{-1} arsenate. The plotted error bars are the standard error (n=4) and the %RSD for 6 different concentrations was found to be 8%.

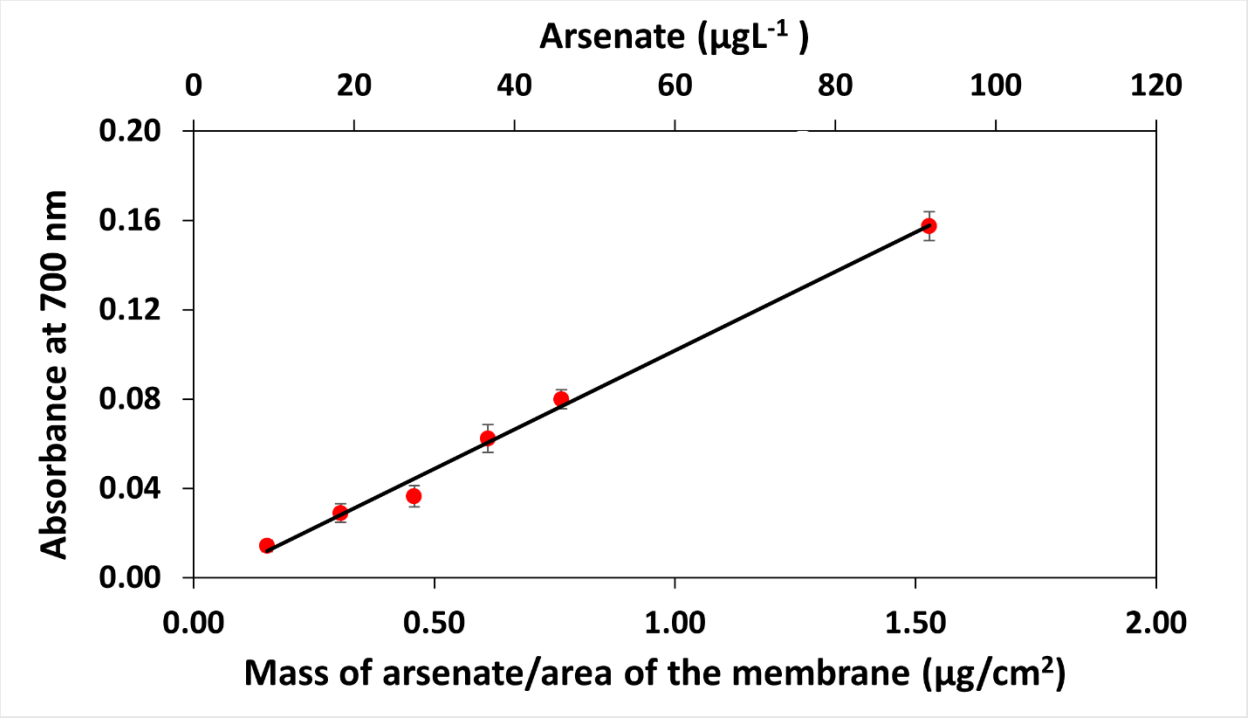

Figure 3.8. The plot of the intensity of the band at 700 nm, as a function of the captured mass of arsenate per area of the 13 mm membrane, was obtained using the membrane method. The error bars are the standard error (SE), where n=4. The secondary x-axis is the concentration of arsenate, defined by passing 12 mL of the AsAMB suspensions through the membrane. The AsAMB suspensions were generated using 10-100 µg L^{-1} arsenate solutions.

The final information needed to quantify both arsenate and phosphate is the calibration constant for phosphate. Figure 3.9 shows the calibration plot using phosphate concentrations of 10-100 µg L^{-1} to determine the calibration constant ($k_{700,\ P}$). A statistically weighted linear

regression was used to obtain a value of 0.135±0.016 $cm^2/\mu g$ for $k_{700,\,P}$, with a 95% confidence interval. The curve shows excellent linearity with the R^2 value of 0.990 over the range of 10 to 100 µg L^{-1} phosphate. The plotted error bars are the standard error (n=4) and the %RSD for 6 different concentrations was found to be 7%. Using the same protocols for determining the MDL for arsenate, we obtained an MDL of 0.86 µg L^{-1} phosphate in water.

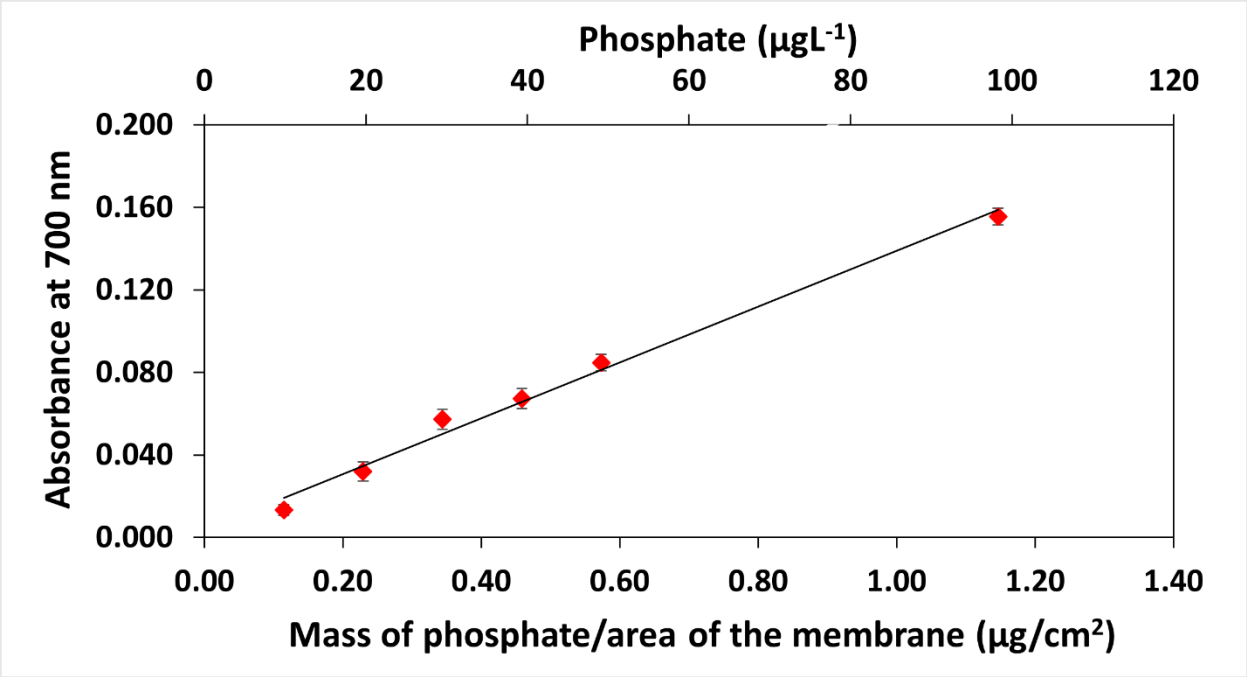

Figure 3.9. The plot of the intensity of the band at 700 nm, as a function of the captured mass of phosphate per area of the 13 mm membrane, was obtained using the membrane method. The error bars are the standard deviation (SD), where n= 4. The secondary x-axis is the concentration of phosphate defined by passing 9 mL of the PAMB suspension generated from 10-100 µg L^{-1} phosphate solution through the membrane.

Once the mass/cm^2 of arsenate was determined from Equation 3.2 using $k_{879,}$ the contribution of arsenate to the band at 700 nm ($Abs_{700,\,As}$) was determined using Equation. 3.4:

$$Abs_{700,As} = \frac{c_{700,As}\ (\frac{cm^2}{\mu g})}{k_{879}\ (\frac{cm^2}{\mu g})} \times Abs_{879} \qquad 3.4$$

The intensity of the peak at 700 nm due to phosphate ($Abs_{700,P}$) is then determined by subtracting the $Abs_{700,AS}$ from the Abs_{P+As} of the 700 nm band.

$$Abs_{700,P} = Abs_{P+As} - Abs_{700,As} \quad 3.5$$

The concentration of phosphate, $C_{phosphate}$ is then determined using Equations.3. 6 and 3.7.

$$M_{phosphate} = \frac{Abs_{700,P} \times area\ of\ the\ membrane\ (cm^2)}{k_{700,P}(\frac{cm^2}{ug})} \quad 3.6$$

$$C_{phopshate} = \frac{M_{phopshate(\mu g)}}{V\ (mL)} \quad 3.7$$

To test the method, samples were prepared with known concentrations of standard phosphate and arsenate solutions. Volumes ranging from 6 to 12 ml were processed through the membranes and using the Vis/IR method, the % recovery of arsenate in the spiked samples was 108% over the range of 25-100 µg L^{-1} arsenate in water and the % recovery for phosphate was 95% (see Table 3.1).

Table 3.1. Measured values obtained using the Vis/IR method for the water samples containing both arsenate and phosphate.

Phosphate (µg L^{-1})	Arsenate (µg L^{-1})	Arsenate measured by IR (µg L^{-1})	Phosphate measured by Visible method (µg L^{-1})	% Recovery Arsenate	% Recovery Phosphate	SD, IR method (Arsenate) (µg L^{-1})
100	25	**27**	106	107	106	8
100	50	**56**	95	112	95	12
100	100	**108**	85	108	85	14

3.3.2.3. Analysis of the environmental samples

The utility of this approach then rests on measurements with real matrices. Using ICP-MS, the concentrations of arsenate (assuming complete oxidation) were 0.83 ± .02 and 1.04 ± .04 µg L^{-1}, in the Stillwater River and Orono tap water respectively, and the corresponding concentration values for phosphate were 23.7 ± 0.9 and 23.0 ±0.6 µg L^{-1}.

The arsenate and phosphate concentrations in the tap and river water samples were then measured using the Vis/IR method and the values obtained are given in Table 3.2. The arsenate gave a non-detect (ND) value as the concentrations were below the detection limit whereas, the phosphate values were within 90-95% of the values obtained by ICP-MS.

Matrix spikes were then performed on samples collected from the Stillwater River and Orono municipal tap water to determine the % recovery of phosphate and arsenate using the method. Three 50 mL samples were spiked with three different spiking concentrations (25, 50, and 100 μg L^{-1}) of arsenate. The phosphate spike in all the samples was fixed at 50 μg L^{-1}. These spiking concentrations were selected based on the concentration of arsenate and phosphate in the natural waters. Table 3.2 shows the results of the matrix spikes of the river and tap water samples. Excellent recoveries were obtained for all samples. The average % recovery for phosphate was 106% for the tap water and 101% for the river sample. The corresponding average % recovery for arsenate was 111% and 105% for the tap and river water samples, respectively.

Table 3.2. Measured phosphate and arsenate concentrations in Stillwater River and Orono municipal tap water (n=3).

Samples	Matrix spike with arsenate (µg L^{-1})	Matrix spike with phosphate (µg L^{-1})	Arsenate measured using the IR method (µg L^{-1})	Total phosphate measured (µg L^{-1})	SD, IR method arsenate	% Recovery arsenate	% Recovery phosphate
Stillwater River	-	-	**ND**	**22**	-	-	**93**
Tap water	-	-	**ND**	**21**	-	-	**91**
Stillwater River	25	50	**29**	**70**	6	112	96
Stillwater River	50	50	**47**	**79**	8	93	115
Stillwater River	100	50	**112**	**68**	16	111	91
Tap water	25	50	**30**	**77**	8	114	112
Tap water	50	50	**54**	**75**	6	105	108
Tap water	100	50	**115**	**70**	12	115	98

Because we have reduced the level of CTAB, the maximum concentration exhibiting linear detection should not exceed 250 µg L^{-1} of total phosphate, arsenate, or a mixture. Above this total concentration a lower capture level of phosphate and arsenate on the membrane. This is because the amount of CTAB is insufficient to precipitation all the AsAMB and PAMB ions as

particles. As a result, the dynamic range of the Vis/IR method for a mixed phosphate and arsenate solution is 25-250 μg L^{-1}. If the solution concentration exceeds 250 μg L^{-1}, we recommend using the higher CTAB concentrations used in our previous work [11].

3.4. Conclusion

We have developed a new and fast method for selective detection of phosphate and arsenate in water using the MBM in combination with Vis/IR spectroscopy. Using this approach, we achieved a detection limit of 0.86 μg L^{-1} phosphate and 13.9 μg L^{-1} arsenate in water. Using matrix spikes with samples from the river and tap water showed phosphate and arsenate average % recovery of 105% and 108%, respectively, over the concentration range of 25 to 250 μg L^{-1}. The % recovery s for the Vis/IR method in the matrix spike test shows that this method can be used to detect phosphate and arsenate in environmental samples.

CHAPTER 4: QUANTIFICATION OF FREE AND WEAKLY BOUND CYANIDE IN WATER USING INFRARED SPECTROSCOPY

4.1. Introduction

Cyanide is a highly poisonous compound having a maximum allowed concentration of 0.2 mgL^{-1} in drinking water in the United States and 0.05 mgL^{-1} in the European Union [69]. In mineral water, the limit is 0.07 mgL^{-1}[70][71], which is also the limit established by the World Health Organization [72]. In natural waters, the acceptable limit for cyanide is lower than in drinking water. The permissible limit of cyanide in freshwater is 0.035 mgL^{-1} on a 24-hour average and should never exceed 0.052 mgL^{-1} at any time[73]. A lower limit in freshwater is because severe toxicity to marine life can occur when the concentration exceeds 0.03 mgL^{-1} [73,96,97].

The above regulations refer to free cyanide (CN^-) in water as cyanide can form many complexes with other species present in the water. Cyanides form strong complexes with cations, such as Fe^{3+}, Au^{2+}, and Co^{2+} and weak acid dissociate (WAD) cyanides with cations, such as Cu^{2+}, Ni^{2+} and Zn^{2+}[98][99]. Thus, the amount of free CN^- in water varies with the number and type of cations present in the matrix. The amount can also vary with pH[100][101]. For example, the pKa of HCN is 9.2 and thus, loss of the volatile HCN can occur under acidic conditions[102]. Each of these complexes have their own toxicity, but by far, the most toxic form of cyanide for humans and aquatic life is the CN^-[74].

The complex nature of the cyanide species in water have led to numerous methods to measure total cyanide, WAD cyanide and CN^- and these methods often require elaborate sample pretreatment steps[103–106]. For example, in APHA 4500- CN^- method C, HCN gas is liberated

from a continuous stream of a sample at pH 6.0[103], which is then absorbed using a NaOH scrubber to separate the CN^- from the HCN. In APHA 4500- CN^- method E, quantification of the CN^- is accomplished using semi-automated colorimetry, where the CN^- is converted into cyanogen chloride by reacting it with chloramine-T. This cyanogen chloride then reacts with pyridine and barbituric acid to produce a red-colored complex in the solution with a band at 590-610 nm[75][107]. The dynamic range of detection for EPA 4500- CN^- method E is from 0.005 to 0.5 mgL^{-1}[103].

Another common approach to measure CN^- is APHA 4500-CN^- method D. In this case, the CN^- is titrated using silver nitrate to form a stable $Ag(CN)_2^-$ complex (a WAD cyanide) in solution (see Reaction 4.1)[103]. Once all the CN^- is bound with Ag^+, the excess Ag^+ then forms a complex with p-dimethylaminobenzylidene rhodanine, resulting in a change in color from yellow to light pink (Reaction 4.2). Before forming the complex, the rhodanine indicator exhibits an absorbance peak at 450 nm, and after reaching the end point, the band shifts to 490 nm. Thus, from the amount of silver nitrate added to reach the endpoint, the concentration of the CN^- is determined. Further addition of the Ag^+ results in the formation of AgCN precipitate in the solution as shown Reaction 4.1 and 4.2.

$$Ag^+ + 2CN^- \rightarrow Ag(CN)_2^- \quad (4.1)$$

$$Excess\ Ag^+ + Rhodanine\ (Yellow) \rightarrow Ag^+ - Rhodanine\ complex\ (Pink)$$

$$450\ nm \qquad\qquad 490\ nm$$

$$Ag^+ + Ag(CN)_2^- \rightarrow 2AgCN \quad (4.2)$$

$$K_{sp} = 2 \times 10^{-8}\ mol\ L^{-1}$$

The method has a detection limit of 1.0 mgL^{-1} CN^- in water[103]. However, the accuracy of this method in measuring CN^- in an unknown sample is highly matrix specific and vulnerable to interference at all pH values. Apart from the interference of cations that complex the CN^-, which is a problem for measuring total cyanide, the method is also susceptible to interference due to the presence of anions. such as S^{2-} and $S_2O_3^{2-}$, in the sample[108]. This is because the method relies on the fate of the Ag^+ ion and both S^{2-} and $S_2O_3^{2-}$ form Ag_2S and $Ag_2S_2O_3^{2-}$ precipitates with the Ag^+ in solution. Ag_2S is a dark black precipitate which masks the pink color of the Ag^+-Rhodanine complex, making it impossible to obtain the band at 490 nm as shown in Reaction 4.3 and 4.4.

$$2Ag^+ + S^{2-} \rightarrow Ag_2S_{(s)} \quad 4.3$$

$$Ag^+ + 2S_2O_3^{2-} \rightarrow Ag(S_2O_3)_2^{3-}{}_{(aq)} \quad 4.4$$

Similarly, $S_2O_3^{2-}$ reacts with the silver ions in the solution to form an $Ag(S_2O_3)^{3-}{}_2$ complex in the solution and causes over estimation of cyanide in the samples, as shown in Reaction 4.5 . As a result, cyanide solutions must be pre-treated with Pb(II) to remove the S^{2-} or $S_2O_3^{2-}$ ions from the solution before the rhodanine titration method can be used[99].

The approach described in this chapter capitalizes on the underlying chemistry of the APHA method 4500-CN^- D (see Figure 4.1). Specifically, our approach is not based on a titration with Ag^+ to reach an endpoint, but rather the formation of an AgCN precipitate with the addition of excess Ag^+ ions. The AgCN precipitates are then captured onto an IR transparent membrane by passing a fixed volume of sample through a membrane assembly. The membrane is then air dried and an infrared spectrum is recorded in transmission mode. The captured AgCN particles

produce a strong and narrow CN stretching mode at 2165 cm^{-1} and from the intensity this band, the concentration of the CN^- in the water is determined.

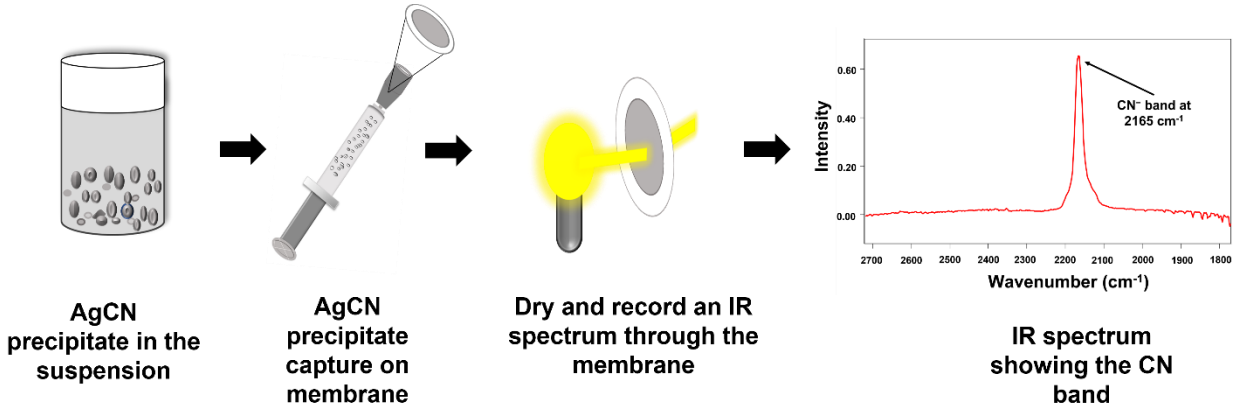

Figure 4.1. The method used for determining the free CN^- concentration in water using a membrane and IR spectroscopy.

Reaction 4.5: Formation of silver cyanide precipitate in the solution with silver nitrate.

$$NaCN_{(aq)} + AgNO_{3(aq)} \rightarrow NaNO_{3(aq)} + AgCN \downarrow \qquad 4.5$$

One of the major advantages of the membrane method over the APHA method 4500-CN^- D is that the chemistry is not predicated on the fate of the Ag^+ ion. Thus, it can be used to analyze samples that contain high concentrations of anions, such as sulfide, sulfite, thiosulfate, chloride and hydroxide, which form precipitates with Ag^+ ions. For example, in the presence of excess Ag^+ ions, formation of the black Ag_2S precipitate does not interfere with the formation of AgCN in the suspension. Both the Ag_2S and the AgCN are captured on the membrane. When an IR spectrum is recorded through the membrane, the Ag_2S does not interfere with detection of the CN band at 2165 cm^{-1} and hence, determination of the concentration of CN^-. Moreover, we have found that by purposely adding S^{2-} ions to a sample, detection of both the CN^- and the WAD

cyanide fraction is possible. The addition of Na_2S to a sample forms a salt with the cations in the WAD cyanide, releasing the CN^- from the WAD cyanide for reaction with the Ag^+ ions.

Another important aspect of the membrane method is the use of $^{13}CN^-$ to improve the detection limit of CN^- in water. At low CN^- concentrations (< 0.2 mgL^{-1}), the particles formed in solution are below 100 nm in diameter and are not captured onto the 0.1 µm membrane. By adding 5 mgL^{-1} of $^{13}CN^-$, the total CN^- concentration leads to particles of a sufficient size so that they are captured on the membrane. Quantification is possible because the $Ag^{12}CN$ and $Ag^{13}CN$ are distinguished by different IR bands. Using $^{13}CN^-$ enabled a limit of detection (LOD) of 0.036 mgL^{-1}, which is 28 times lower than the reported LOD for APHA method 4500-CN^- D and equal to the detection limit of APHA 4500- CN^- method E. Hence, the membrane method meets the required detection limits for both drinking water and freshwater sources.

4.2. Experimental

4.2.1. Materials

All glassware were washed with deionized water (18 MΩ), then acid washed with warm 10% HCl solution and dried in the oven at 105°C for 20 minutes before use. All chemicals were purchased from Sigma Aldrich. These include reagent grade sodium cyanide (97% purity), anhydrous silver nitrate beads (99.998% purity), silver cyanide (99%), sodium hydroxide (ACS reagent, ≥97.0%), sodium thiosulfate pentahydrate (ACS reagent, ≥99.5%), and reagent grade disodium sulfide. The infrared transparent membranes (0.45 and 0.1 µm /13 mm diameter) were obtained from Orono Spectral Solutions Inc.

4.2.2. Standard solutions of samples

Stock solution of 1000.0±10.3 mgL^{-1} cyanide $CN^-$and $^{13}CN^-$ were prepared by dissolving 0.20±0.02 g of sodium cyanide and 0.25±0.03 g of potassium cyanide ($K^{13}CN$) in 100 mL volumetric glass flasks and adjusting the pH 12.0 using 0.25 M NaOH. Then, 100±0.8 mL of 100, 10, 5, 1, 0.5, and 0.2 mgL^{-1} CN^- and $^{13}CN^-$ solutions were prepared by serial dilution of the 1000 mgL^{-1} stock solution. The pH of the solutions were maintained at pH 12.0 and were reduced to pH 7.5-8.5 using 0.25 M HCl just prior to use (i.e., addition of the Ag^+ solution). A 50±0.5 mL stock solution of 5.04 gL^{-1} Ag^+ was prepared by dissolving 0.40±0.02 g of $AgNO_3$ in a 50 mL volumetric flask. A 100 mL stock solution of 1000 mg L^{-1}, S^{2-}, SO_3^{2-} and $S_2O_3^{2-}$ were prepared by dissolving 0.55 mL of $Na_2S•9H_2O$, 0.16±0.05 mg of Na_2SO_3 and 0.16±0.05 mg of $Na_2S_2O_3•5H_2O$ in DI water. The stock solution of the 1000 mgL^{-1} S^{2-} was adjusted to pH 9.00 to avoid the formation of H_2S in the solution. All solutions were stored at room temperature (21°C).

4.2.3. Formation of AgCN

A 25-40 times molar excess Ag^+ solution was added to each CN^-sample of 0.1 mgL^{-1} to 100 mgL^{-1}. The time required to form a precipitate varied with the concentration of the CN^-. Within 1-5 mgL^{-1} CN^-, visible precipitates formed after 2-5 minutes stirring whereas, above 100 mgL^{-1}, precipitate formation was instantaneous. A brownish white precipitate was observed in the solution within 2-5 minutes after adding the $AgNO_3$. The average size of the particles in the suspension were measured using the dynamic light scattering on a Malvern 3000 HSA Zetasizer. The suspension was diluted 10 times with DI water before the measurements.

4.2.4. Recording the IR spectrum of the membrane

Details of the membrane, the membrane assembly, and the procedures for recording a spectrum through the membrane assembly are described in detail in Chapters 2 and 3. In brief, 3-12 mL of the stirred suspension was extracted using a syringe and passed through the Luer™ lock of the membrane assembly. The membrane was then air-dried by attaching Tygon™ tubing to the Luer™ lock and gently blowing dry air for 2-3 minutes through the assembly. IR spectra were recorded in transmission mode through the Luer™ lock of the membrane assembly following an established procedure[12]. A reference spectrum was recorded in transmission mode through an unused membrane assembly. All the spectra were recorded at 8 cm^{-1} resolution using an ABB-Bomem FTLA 2000 FTIR spectrometer equipped with a DTGS detector.

4.2.5. Samples containing sulfur compounds

100 mL samples containing S^{2-}, SO_3^{2-} and $S_2O_3^{2-}$ at concentrations of 0.5-10.0 mgL^{-1} were prepared by addition of Na_2S, Na_2SO_3 and $Na_2S_2O_3$ to 100 ml of DI water adjusted to pH7.5- 8. The pH of the S^{2-} spiked samples increased to almost 8.2-8.5, due to the presence of excess OH^- ions. However, the pH of the SO_3^{2-} and the $S_2O_3^{2-}$ remained in the range of 7.5-8.0. The solutions were stirred for 5 minutes and then spiked with NaCN to prepare solutions with a final concentration of 1.0 or 5.0 mgL^{-1} CN^-. After addition of the CN^-, the pH of all solutions were in the range of 8.5- 9.0. Then 32-40 times molar excess of Ag^+ over the CN^- was added to each sample solution and the beaker was stirred for 20 minutes. The S^{2-} solutions turned into a dark black suspension right after the addition of the Ag^+ due to formation of the Ag_2S particles. The SO_3^{2-} and the $S_2O_3^{2-}$ suspensions were brownish in color.

4.2.6. Environmental samples

Water samples were collected from the Orono municipal tap water and the shallows of the Stillwater River, Orono, Maine from June to October 2021. To eliminate any undissolved particulate matter from the water samples, the samples were passed through a 47 mm dia. (0.45 m pore size) polyvinylidene membrane. The pH of these samples was in the range of 7.5 to 7.9 and samples were stored in a dark glass container at room (2°C) temperature. Each of the river and tap water samples were further split into two samples for a total of 4 samples. One sample of each matrix was spiked with 10 mgL^{-1} of S^{2-}. Then all 4 samples were spiked with either 1 or 5 mgL^{-1} CN^- (a total of 8 different samples) and stirred for 5 minutes. Then, 32-40 times molar excess of Ag^+ ions over CN^- were added to each solution resulting in a final volume was in the range of 100-102 mL. The solutions were stirred for 20-30 minutes to ensure sufficient time to form particulate suspensions. After the addition of the Ag^+, the suspensions containing S^{2-} turned dark black immediately, due to formation of the Ag_2S precipitate, whereas, those samples not containing S^{2-} remained brown due to formation of AgOH. The formation of the Ag_2S showed that the S^{2-} was added in excess above the concentration of the WAD cyanide in the sample. Then, a 3-6 mL aliquot was extracted from each stirred suspension using a syringe and passed through the membrane assemblies containing 13 mm diameter/0.1 µm membranes. The membranes were air dried and IR spectra were recorded directly through the assembly. Each S^{2-} treated sample was measured 3 times with 3 different 13mm/0.1 µm membranes. During the early stages of the method development, we varied the concentration of S^{2-} from 1 to 10 mgL^{-1} and found that the CN band increased with the amount of S^{2-} added for both river and tap water samples. Above 10 mgL^1, there was no further increase in the band intensity.

4.3. Results and discussion

4.1.1. IR spectra of AgCN particles deposited onto the membrane

Figure 4.2 shows the IR spectrum of the collected precipitate onto a membrane recorded in transmission mode through the membrane assembly. The regions between 1270- 1130 cm^{-1} and 530-480 cm^{-1} are opaque because of the strong CF modes of the polytetrafluoroethylene-based membrane. In the region between 2300-2000 cm^{-1} (see inset), a sharp band at 2165 cm^{-1} was observed, which is the C-N stretching mode of cyanide. This relatively strong and narrow band appears in a featureless region on a flat background. There is some effect of dispersion in the shape of this band resulting from recording a transmission spectrum with micron sized particles. While this manifests in some asymmetry on the low wavelength side of the CN band, it has a negligible effect in the determination of the CN^- concentration. The low level of dispersion is the result of partial refractive index matching between the AgCN (n=1.68) particles embedded in the membrane (n=1.31).

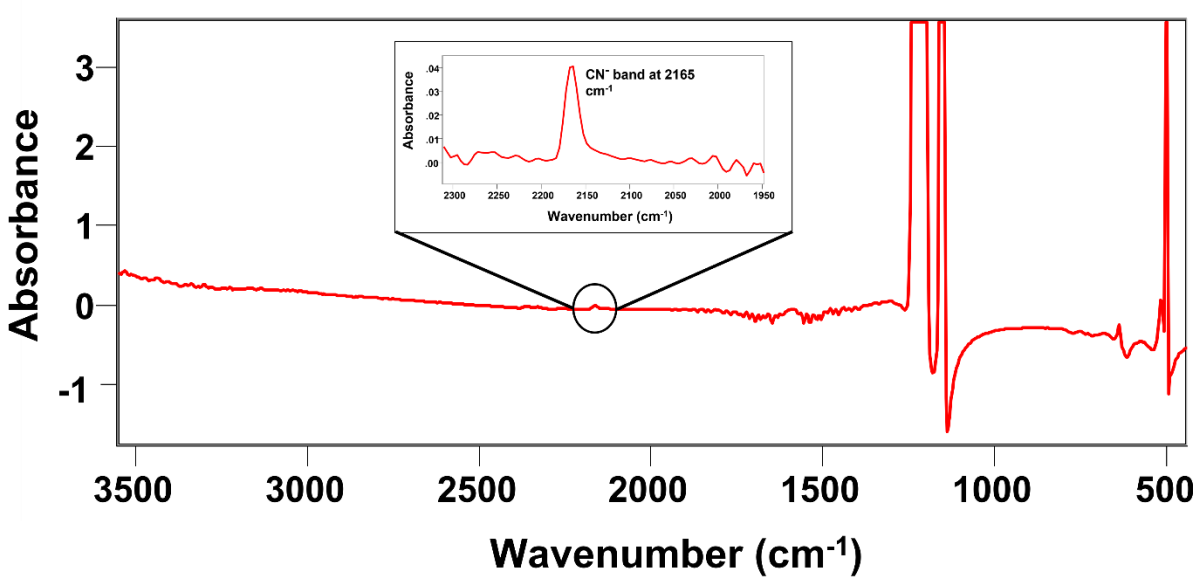

Figure 4.2. IR spectrum of the AgCN precipitate captured on a 13 mm/0.45 µm membrane. The AgCN suspension was prepared by adding 1.0 mL of a 500 mg L^{-1} Ag^{+} solution to 100 mL of a 1.0 mgL^{-1} cyanide solution and 6 ml of this suspension was passed through the membrane assembly.

4.1.2. Quantification of the CN band

Details regarding the quantitative aspects of the membrane-based approach are described in Chapters 2 and 3. For CN^{-} detection, the intensity of the 2165 cm^{-1} band in absorbance units is directly proportional to the concentration of the cyanide times the pathlength ($c \times l$), which, for particles captured on a membrane, converts to the mass of the cyanide per area of the membrane, as shown in Equation 4.1.

$$Abs = k_{2165} \times \left(\frac{mass}{area}\right) \qquad 4.1$$

Therefore, the dynamic range of detection and the detection limit of the method depend on the diameter of the membrane and the mass of the cyanide deposited. The latter, in turn, depends on the volume of the particulate suspension passed through the membrane.

Using the calibration constant for the IR band at 2165 cm^{-1} (K_{2165}) and the measured intensity of the band at 2165 cm^{-1} in the IR spectrum (Abs_{2165}), the mass of the cyanide ($M_{cyanide}$) collected on the membrane for an unknown sample is then calculated as shown in Equation 4.2:

$$M_{cyanide} = \frac{Abs_{2165} \times \ area\ of\ the\ membrane\ (cm^2)}{k_{2165}(\frac{cm^2}{mg})} \qquad 4.2$$

In our work, we used a 13 mm diameter membrane, and the active diameter is 10 mm due to the use of a Teflon™ O-ring as a seal inside the membrane housing [109]. Thus, the active area of the membrane was 0.785 cm^2. The concentration of CN^- in the solution is then calculated in terms of mgL^{-1}, using Equation 4.3:

$$C_{cyanide} = \frac{M_{cyanide(mg)}}{V\ (mL)} \qquad 4.3$$

where V is the volume of the $AgCN$ suspension passed through the membrane.

4.1.3. Calibration Plot

The first step was to generate a calibration curve to determine K_{2165}. CN^- solutions of 100 mL of 0.05-5.0 mgL^{-1} were prepared and 40-50 times molar excess of Ag^+ to the amount of CN^- ions were added to each sample solution to precipitate out the AgCN. After stirring for 2-30 minutes, various amounts (3-12 mL) of the suspension were collected from the stirred beaker using a syringe and this volume was passed through the membrane assembly containing either a 13 mm/0.45 or 0.1 µm membrane. The membranes were air dried, and IR spectra were then recorded (see Figure 4.4).

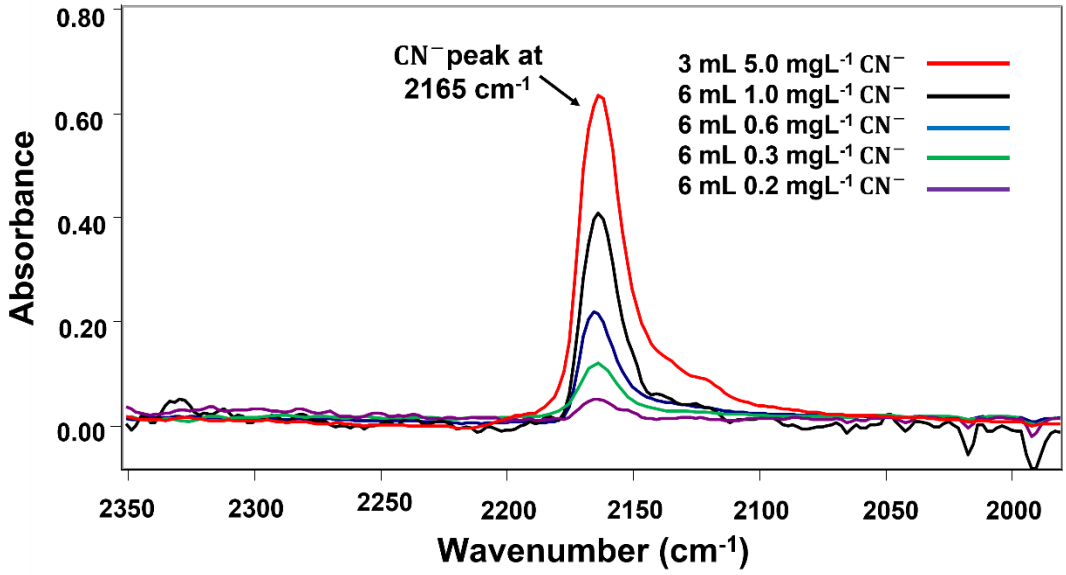

Figure 4.3. IR spectra recorded through a membrane assembly after passing 3-6 mL of 0.2-5 mgL^{-1} CN^- as AgCN suspensions through 13 mm/0.1 µm membranes.

IR spectra were recorded for each cyanide concentration a minimum of 3 times using 3 different membranes. A calibration plot of the peak height of the CN^- band at 2165 cm^{-1} versus the captured mass of cyanide/per area of the membrane for concentrations of 0.2 -5.0 mgL^{-1} cyanide is shown in Figure 4.4. A linear Beer's Law relationship was obtained and the extinction coefficient, using a statistically weighted linear fit, has a value of 4.74±0.12 cm^2/mg. The error in the extinction coefficient is given as the standard error. The calibration curve shows high linearity with an R^2 value of 0.998 over the range of 0.05 mgL^{-1} to 5.0 mgL^{-1} CN^-. The average percent relative standard deviation (%RSD) for the nine different concentrations was 22%.

The statistical analysis above was done in triplicate using three separate beakers spiked with CN^- that were prepared at different times during the day. Since the IR beam passing through the Luer™ lock of the membrane assembly is about 4 mm in diameter, we are under sampling the active area of the membrane.

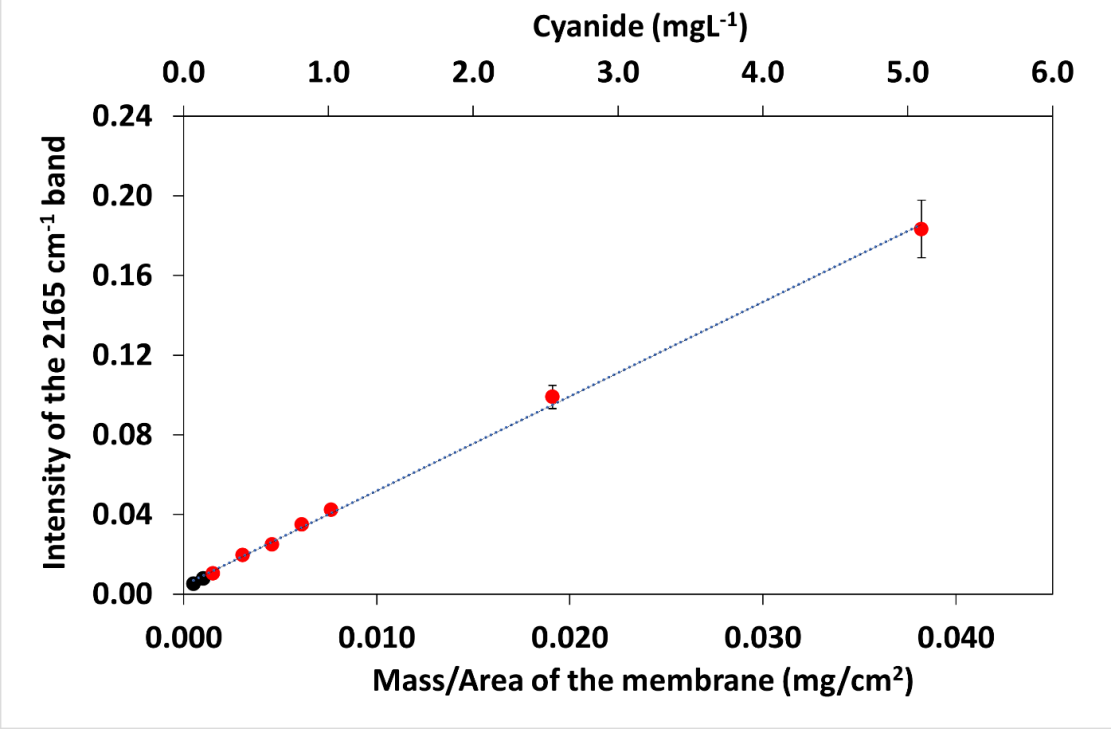

Figure 4.4. A plot of the intensity of the band at 2165 cm^{-1} verses the captured mass of cyanide per area of a 13 mm diameter membrane. The error bars indicate standard error (SE) where n= 3. The secondary x-axis is the concentration of cyanide defined by passing 6-12 mL of the AgCN suspension through the membrane that were generated using 0.05-5 mg L^{-1} cyanide solutions.

Figure 4.4 has red and black data points. For concentrations of 0.2 mgL^{-1} and above (red data points), a linear relationship with the intensity of the band at 2165 cm^{-1} and the captured mass of CN^- was obtained. However, when the concentration of CN^- was 0.1 mgL^{-1}, we did not observe a band at 2165 cm^{-1}. This was not dictated by the signal to noise ratio of the infrared spectrometer but rather by the drop in the percent capture of particles because they are too small to be collected onto the 0.10 µm membrane. When the concentration of CN^- was 0.1 mgL^{-1}, the average particle size as measured by dynamic light scattering was 90-120 nm. Thus, lowering the detection limit below 0.2 mgL^{-1} would require increasing the size of the AgCN particles in the suspension so that they could be captured using either the 0.1 µm or 0.45 µm membrane.

A.1. Factors Affecting the size of the AgCN particles in the suspension

The size of the AgCN particles in the suspension are dependent on multiple factors, such as the dynamics of AgCN formation, concentration of the CN^-, amount of Ag^+ added to the solution, pH, the presence of nucleation sites for particles to aggregate, and the concentration of the interfering counter ions in the matrix sample. For example, when 0.5 mL of 5 mgL^{-1} of Ag^+ solution was added to a 100 mL of 1.0 mgL^{-1} cyanide solution at pH 8.0, the average size of the particles obtained was 500-600 nm (see Figure 4.5). Thus, the AgCN particles at 1.0 mgL^{-1} can be easily captured using a 0.45 µm membrane and the resulting effluent shows a clear solution with no particles. However, there still could be some fraction of AgCN particles in the effluent that are too small to be detected by eye. We then passed the same solution through a 0.1 µm membrane and obtained the same intensity of the CN band as with a 0.45 µm membrane. This shows that the 0.45 µm membrane captured nearly 100% of the particles. The relatively large AgCN particles are due to the high concentration of CN^- (1.0 mgL^{-1}) and Ag^+ ions in solution. However, when the concentration of the CN^- decreases to the range of 0.10-1.0 mgL^{-1}, the size of the particles formed are 100-350 nm (see Figure 4.5). As a result, only 60-70% of the AgCN particles are captured onto the 0.45 µm membrane with the remaining fraction passing through the membrane. At this concentration range, the 0.10 µm membranes were used to generate the linear plot in Figure 4.4. Hence, the 0.10 µm membranes were chosen for all quantitative work. However, this did not solve the problem of lowering the LOD because the particles passed

through the 0.10 µm membranes when the CN^- concentration was below 0.2 mgL^{-1}.

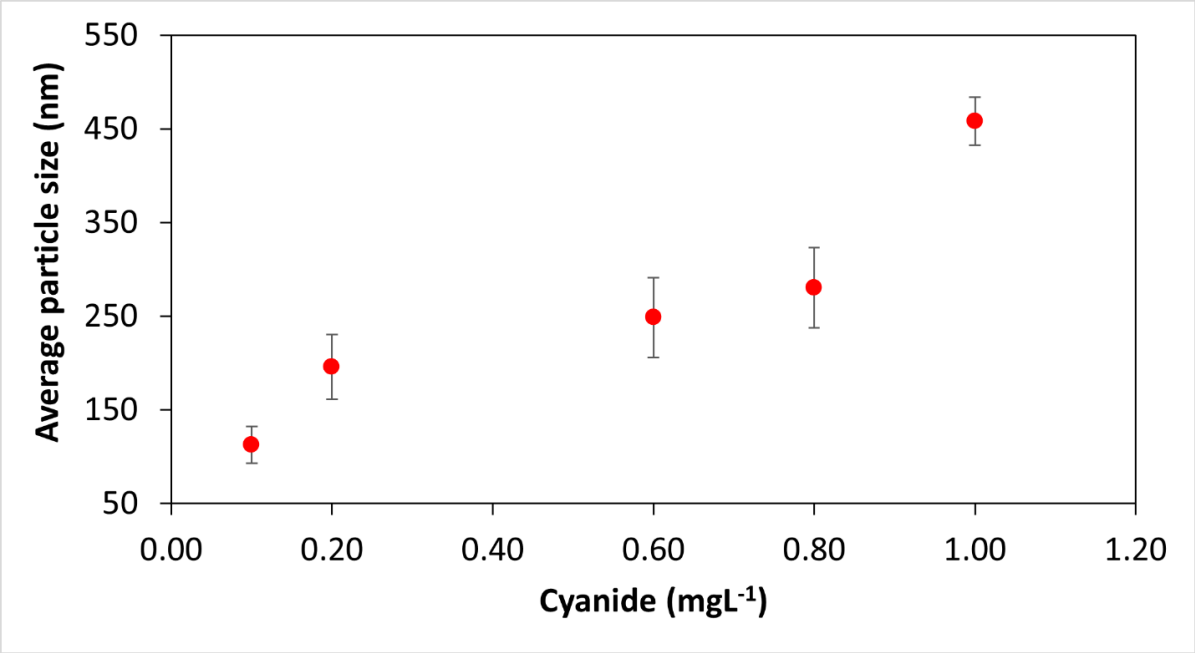

Figure 4.5. The size of the AgCN particles at different cyanide concentrations, measured after adding 25 times molar excess Ag^+ ions in the solution. The error bars are the standard deviation of 3 measurements.

We tried several approaches to increase the size of the AgCN particles when the CN^- concentration was below 0.2 mgL^{-1}. One approach was to have coprecipitation of simple salts with the AgCN. In this case, NaCl was first added to the sample before addition of the Ag^+ solution. The hypothesis was that the coprecipitation of AgCl and AgCN in the solution would lead to AgCN embedded in the larger AgCl particles. However, this attempt was unsuccessful. Even though the average size of the particles in the suspension was 300-400 nm for 0.1 mgL^{-1} CN^- solution, no band at 2165 cm^{-1} was observed when this suspension was passed through a membrane. This is because the AgCl and AgCN particles formed independently of each other. In another approach, we seeded the sample with AgCl particles. Since the Ksp of AgCN is 10^6 orders in magnitude lower than AgCl, the hypothesis was that the CN^- would displace the Cl and create

AgCN on the outer crust of the AgCl particle. However, this exchange was slow and did not occur to a level for detection of CN bands.

The approach we used was to increase the concentration of total free CN^- ion in the solution by spiking the CN^- solution with isotopically labeled $^{13}CN^-$. The amount of $^{13}CN^-$ added (0.1-1 mg/L) ensured that the minimum overall concentration of CN ($^{13}CN^- + CN^-$) exceeded this value. As shown in Figure 4.6, at this minimum overall concentration, the particle size is sufficient to be captured on the 0.10 µm membrane. The $Ag^{13}CN$ stretch appears at 2120 cm^{-1} and thus, is separate from the AgCN peak at 2165 cm^{-1} (see Figure 4.6).

DI water was pH adjusted to 7.5-8.0 and spiked with 3 different CN^- concentrations (0.70, 0.90 and 0.95 mg L^{-1}) using a 1000 mgL^{-1} CN^- stock solution and, then the solutions were stirred for 1-2 minutes. Then $^{13}CN^-$ was added to the solution to bring the total concentration of ($CN^- + ^{13}CN^-$) to 1 mg L^{-1}. For example, 100 mL of a 0.9 mgL^{-1} CN^- solution was spiked with a 0.1 mgL^{-1} of $^{13}CN^-$ to have the total concentration of the cyanide $CN^- + ^{13}CN^-$ in the solution equal 1 mgL^{-1}. During development of the method, we opted to spike low concentration of $^{13}CN^-$ into higher concentrations of CN^- solutions to preserve the supply of the more costly ^{13}CN. When 0.5 mL of a 5 mg L^{-1} Ag^+ solution was added to the sample at pH 8-8.5, mixed AgCN /$Ag^{13}CN$ particles formed in the sample with a measured average diameter of 540 nm. In all cases, the measured size of the AgCN particles were in the range of 450-600 nm and easily captured on a 0.1 µm membrane. The spectra obtained after collecting the particles onto membranes are shown in Figure 4.6. These were obtained by passing 12 mL of the above suspensions through 13 mm/0.1 µm membranes. The IR spectra shows two distinct C-N peaks at 2165 and 2121 cm^{-1} which are the

^{12}CN and ^{13}CN stretching modes. Also note that the intensity of the band at 2121 cm^{-1} is linear with the concentration of the $^{13}CN^-$ and the appearance of a band at 2121 cm^{-1} shows that detection below 0.2 mgL^{-1} CN^- is achieved.

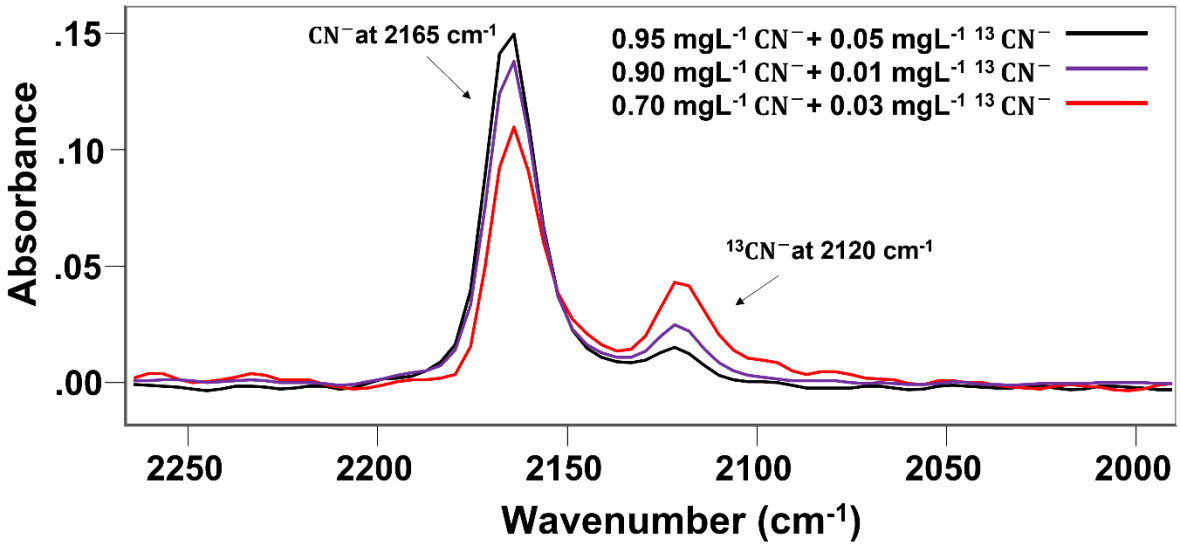

Figure 4.6. Infrared spectra of AgCN and $Ag^{13}CN$ particles collected onto 13 mm/0.1 µm membranes after passing 12 mL of each suspension.

4.1.4. Detection limit

Following EPA guidelines, the method detection limit (MDL) was 0.036 mgL^{-1}, as determined by 3 times the standard error (SE) using three separately prepared 0.15 mg L^{-1} CN^- solutions. The DI water samples were pH adjusted in the range of 7.5-8.0 and then spiked with 0.85 mgL^{-1} $^{13}CN^-$ and 0.15 mgL^{-1} CN solutions to bring the total (CN^- + $^{13}CN^-$) concentration to 1 mgL^{-1}. Next, 0.5 mL of 5 mgL^{-1} of Ag^+ solution was added to each solution to bring the final sample volume to 100 mL. The solutions were stirred for 20 minutes to form the AgCN and $Ag^{13}CN$ particles in the suspension. Then, 6 mL aliquots were extracted from each stirring suspension and passed through different 0.1 µm/13 mm diameter membranes to capture the

particles on the membrane surface. The membranes were then air dried and IR spectra were recorded in transmission mode.

The amount of ^{13}CN used per sample added <5 cents to the cost of running each sample. It was the use of ^{13}CN that enabled the two black data points in Figure 4.4, which in turn, led to the lowering of the detection limit . It is also noted that addition of $^{13}CN^-$ to all samples also simplified the process with analyzing an unknown. By adding $^{13}CN^-$, we ensure the overall CN^- concentration is in the 1 -5 mgL^{-1} range, which defines a single amount of Ag^+ to add to the sample, the operating range of pH of 7-9, and the use of the 0.10 µm membrane. It is this approach we would recommend using a 0.10 µm membrane when running an unknown sample.

4.1.5. pH of the solution.

Under acidic conditions, the CN^- forms HCN which evaporates from the solution. Thus, it is standard practice to maintain the pH of the CN^- stock solutions at 11-12 pH to avoid any loss of CN^- ions from the solution. However, at pH 12, the OH^- concentration is 10^{-3} M and addition of Ag^+ ions lead to the immediate formation of particles due to the precipitation of AgOH (see Reaction 4.6), K_{sp} of AgOH is 2* 10^{-8} mol L^{-1}, see Reaction 4.1). While, in principle, this should not affect the detection of the AgCN by infrared spectroscopy, the amount of excess Ag^+ needed to react with both the OH and CN^- becomes excessive. Moreover, the number of AgOH particles present clog the pores and limit the total volume that can be passed through the membrane.

$$\mathrm{NaOH_{(aq)} + NaCN_{(aq)} + 2AgNO_{3\,(aq)} \rightarrow\ 2NaNO_{3\,(aq)} + AgCN\downarrow + AgOH\downarrow} \qquad 4.6$$

Thus, to limit the amount of AgOH precipitate while limiting the evaporation of HCN, we adjust the pH of the sample to 7-8.5 just prior to addition of the Ag^+ solution. This lowers the

amount of AgOH formed to a manageable amount that allows for 20-30 mL of suspension to be passed through the membrane and at the same time, does not require an excessive amount of Ag^+ to be added to the sample. For example, when 0.5 mL of a 5.0 mgL^{-1} Ag^+ is added to 100 mL solution of 1.0 mgL^{-1} CN^- at pH 8.5, the amount of Ag^+ ions left in solution after forming AgOH is almost 45 times higher the total concentration of the CN^- ions, ensuring complete precipitation of the CN^-.

Spectroscopically, the AgOH precipitate does not pose a problem for the method as AgOH does have any IR band in the region of interest. Moreover, when the concentration of the CN^- is sufficiently high in the solution (0.5-1 mgL^{-1}), the method requires to pass a small amount of suspension volume (3-6 mL) through the membrane to obtain a measurable band for the cyanide at 2165 cm^{-1}. Therefore, the presence of the excess AgOH on the membrane does not interfere with the method around 0.5-1.0 mgL^{-1} cyanide in water. However, when the concentration of the cyanide in the solution is in the range of 0.05-0.5 mgL^{-1}, the formation of the excess AgOH precipitate in the solution is problematic for practical reasons. For example, at pH 8.0 and 0.2 mgL^{-1} cyanide in water, 3-6 mL of sample volume can be passed at a rate of 0.3-0.5 mL/min through a 0.1 µm membrane. When an IR spectrum was recorded, a band at 2165 cm^{-1} was observed with an average intensity of 0.01 absorbance unit. But as the concentration of the cyanide in the solution was further decreased down to 0.1 mgL^{-1}, the additional AgOH precipitate made it difficult to pass more than 6 mL of sample with a 0.10 µm membrane as the membrane is plugged with excess AgOH precipitate. As a result, it is not possible to obtain the band at 2165 cm^{-1} with a sufficient signal to noise ratio for quantification. To circumvent this issue, the 0.45

µm pore size membrane was used, as it can tolerate a flow rate of 1-2 mL/min which enables 12-24 mL of sample to be easily passed through the membrane.

4.1.6. Concentration of the Ag^+ ions in the solution

In principle, the amount of Ag^+ added should simply exceed the upper limit of the CN^- detection range. From a thermodynamic perspective, the K_{sp} for AgCN is $1.2 * 10^{-16}$ mol L^{-1} at 25°C, and thus, to achieve the target detection limit of 0.05 mgL^{-1}, adding 10-fold excess Ag^+ (i.e., 0.5 mgL^{-1}) would result in precipitation of essentially all CN^- at the detection limit into particles. However, the amount of excess Ag^+ affects the particle size. Too high an excess(100-fold of the concentration at the upper end of the range – 5 mgL^{-1}), leads to many nucleation sites, resulting in smaller particles that are not captured on the membrane. Furthermore, at this high Ag^+ concentration, other anions in freshwaters, such as Cl^- , also form precipitates. However, at too low an excess(2-3 fold), there is a risk of adding insufficient Ag^+ to account of other anions (OH^-, S^{2-}, etc.) that can also form precipitates with Ag^+. From our studies, we find that the use of 20-30 times molar excess Ag^+ ions over the CN^- concentration range of 0.05-5 mgL^{-1} is sufficient to capture 100% of the AgCN particles on the membrane. However, since we also have formation of AgOH along with the AgCN in the solution, we added 40-50 times molar excess Ag^+ ions to the total number of (CN^- + OH^-) ions in the solution at pH 7.0-8.5. During the development of the method, we periodically checked that the Ag^+ added was in excess by examining for Ag^+ in the effluent. For example, adding 0.5 mL of 5 mgL^{-1} Ag^+ ions into a 100 mL of 1.0 mgL^{-1} CN^- solution at pH 8.5 results in the formation of a brownish white suspension. After passing 6 mL of this stirred suspension through a 0.10 µm membrane, the effluent collected into a separate beaker was clear. When additional CN^- ions were added to the clear effluent collected

in the beaker, again, a brownish white precipitate was formed, indicating that there was excess Ag^+ ions in the effluent.

A.2. Sulfur containing anions

A major advantage of our method is that anions, such as S^{2-} and $S_2O_3^{2-}$, do not interfere with CN^- detection. Figure 4.7 shows the IR spectra obtained for excess Ag^+ added to solutions containing 1.0 mgL^{-1} CN^- with 0.5-1.0 mgL^{-1} S^{2-}, SO_3^{2-} and $S_2O_3^{2-}$. The intensity of the CN band without the presence of any of the sulfur containing ions was 0.044 absorbance units. For the spectra obtained in the presence of the sulfur containing anions, the average intensity of the CN band for 1.0 mgL^{-1} CN^- samples was 0.042 with a standard deviation of 0.0046 (n=3). Thus, this shows that the membrane method can be used to quantify the amount of CN^- in the presence of sulfur- based interferents found with the Ag^+ titration method, APHA 4500-CN^- D.

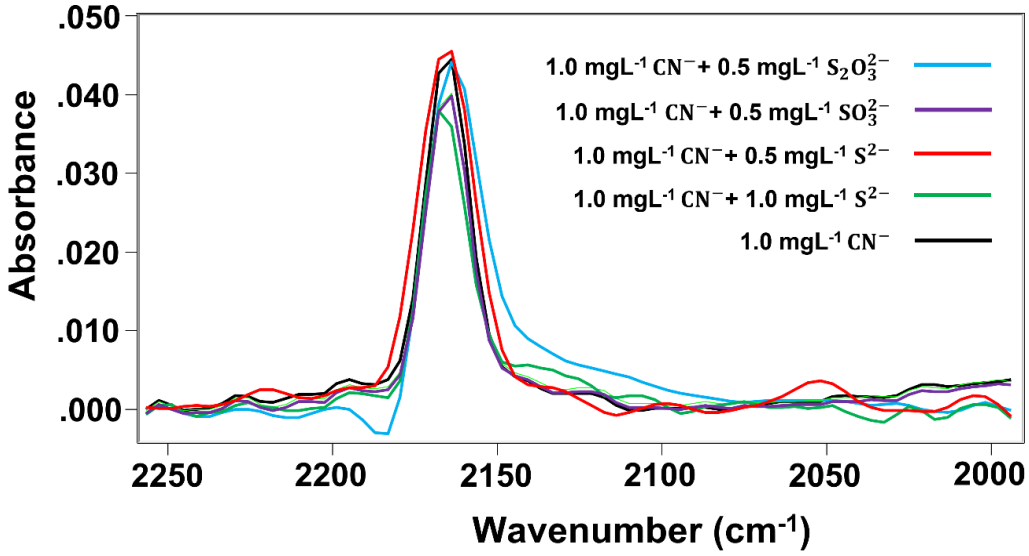

Figure 4.7. Infrared spectra after passing 6 mL of the AgCN suspensions produced by addition of excess Ag^+ to solutions containing 1.0 mgL^{-1} CN^- with 0.5-1.0 mgL^{-1} S^{2-}, SO_3^{2-} and $S_2O_3^{2-}$.

A.3. Environmental samples and WAD Cyanide

The general applicability of this approach rests on testing the method with real matrices. However, the traditional approach of measuring % recoveries of CN^- using matrix spikes with real samples will be negatively biased due to formation of WAD and strongly bound cyanide. Hence, we compared our values for matrix spiked Stillwater River water and the Orono tap water with the values obtained from a commercial laboratory, using EPA method OIA 1677-09. Method OIA 1677-09 measures the available cyanide in water which is defined as CN^- + WAD cyanide. A ligand exchange is preformed to release the CN^- from the WAD cyanide, followed by flow injection analysis using amperometric detection. S^{2-} is a known positive interferent in method OIA 1677-09, as it produces a signal at the silver electrode. We selected this method for comparison because we hypothesized that addition of S^{2-} to our samples would enable the measurement of the WAD cyanide$^-$ fraction.

The approach we have developed to measure the WAD cyanide is by addition of S^{2-} to the sample to form metal sulfides with those cations that form cyano-complexes with zinc, copper cadmium, nickel, and silver (i.e, the WAD cyanide). Removal of metal ions from solution occurs rapidly with addition of S^{2-} over a wide pH range[110][111]. As we showed in Figure 4.7, the presence of S^{2-} does not interfere with the formation of AgCN and has no effect on the measured concentration of CN-. Thus, we predicted that a measurement of the sample prior to S^{2-} addition would yield the CN^- and after S^{2-} addition, the CN^- + WAD cyanide. From the difference between these two measurements, the WAD cyanide is determined.

The results obtained for our membrane method and from the commercial lab using method OIA 1677-09 are given in Table 4.1 Both methods had non-detect (ND) values for the river and tap water samples as the CN^- + WAD cyanide, if present, was at concentrations below the detection limits. Next, we performed a matrix spike into the two samples. River and tap water were spiked with 1 mgL^{-1} CN^-, adjusted to pH 12, and then split into two samples. One sample was placed into a 100 mL sample bottle (provided by the commercial lab). The concentration values of available cyanide (CN^- + WAD cyanide) measured at the commercial lab were 0.85± 0.02 and 0.84 ±0.02 µg L^{-}, for river and tap water samples, respectively.

The IR spectra of river samples spiked with 5 mgL^{-1} are shown in Figure 4.8. The intensity of the CN band at 2165 cm^{-1} is 0.06 absorbance units for the sample without any S^{2-} spike which corresponds to 65% recovery of CN^-. This low % recovery is negatively biased due to formation of the WAD and strongly bound CN^- complexes. Evidence to support this point is from the increase in intensity of the CN band to 0.087 absorbance units in the IR spectrum obtained for the sample spiked with 10 mgL^{-1} S^{2-}. This translates to a 92% recovery in the spiked sample and that 19% of the total cyanide was due to WAD cyanide. This was confirmed from comparison of the values obtained from our method with those obtained from the commercial lab. For the 1 mgL^{-1} CN^- spiked samples, a 66% and 63% recovery was obtained for the tap and river water samples, respectively, which is lower than the 84% and 85% recoveries obtained for the commercial samples. A lower % recovery is expected, given that we measure only the free CN^- and not the WAD cyanide. More importantly, the S^{2-} spiked river and tap water samples gave 95% and 102% recovery of available CN^- , which is well in agreement with the available CN^-

measured by the commercial lab. This shows that it is possible to measure both CN^- and WAD cyanide with the membrane-based method.

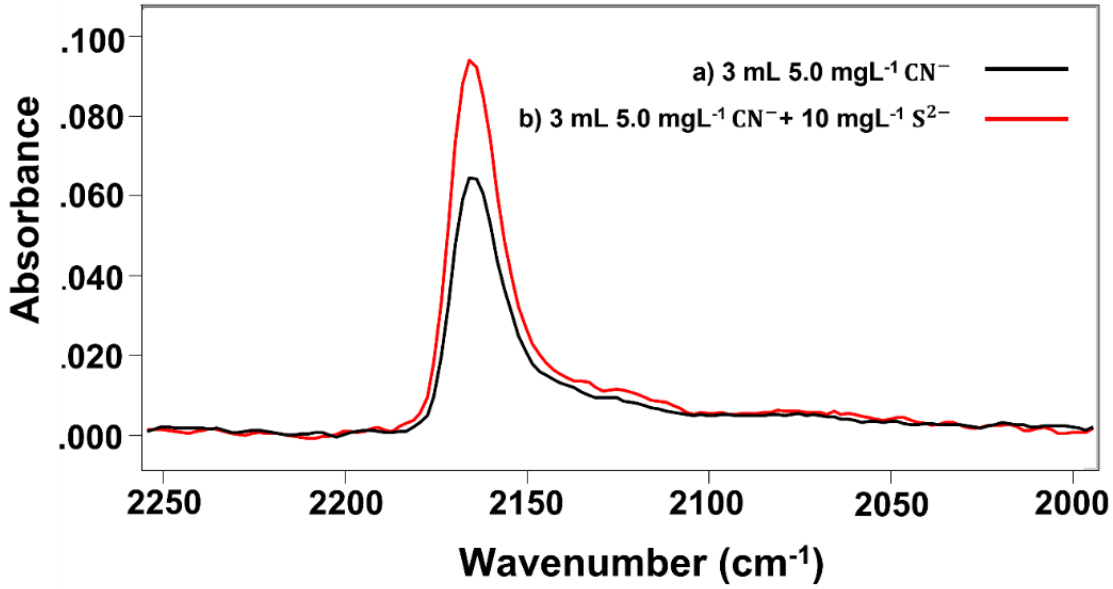

Figure 4.8. Infrared spectra after passing 3 mL of a suspension containing excess Ag^+ added to the river water sample spiked with 5.0 mgL^{-1} CN^- solution a) prior to addition of S^{2-} and b) with 10 mgL^{-1} S^{2-}.

Table 4.1. The Concentration of free and WAD CN^- measured in Stillwater river and Orono tap water sample using APHA method OIA 1677-09 and the membrane method.

Samples Sources	CN^- Spike mgL^{-1}	CN^- Spike measured commercially mgL^{-1} (Free +WAD)	CN^- without adding S^{2-} mgL^{-1}	CN^- after adding 10 mgL^{-1} S^{2-} mgL^{-1}	Standard deviation (SD) n=3 mgL^{-1}	% Recovery after S^{2-} spike
tap water	5.0	-	3.33	4.6	0.25	92%
tap water	1.0	0.84	0.66	0.86	0.13	102%
River water	5.0	-	2.85	4.4	0.33	88%
River water	1.0	0.85	0.63	0.81	0.11	95%

A.4. Conclusion

We have developed a new and fast method for selective detection of CN^- and WAD cyanide in water using an infrared transparent membrane and IR spectroscopy. The approach involves precipitating the CN^- with Ag^+ and capturing the particles on a membrane. The WAD cyanide is determined by the addition of Na_2S to the sample as the S^{2-} liberates the CN^- from WAD metal cyanide complexes. Using this approach, we achieved a detection limit of 0.15 mg L^{-1} CN^- in water. This detection limit is obtained by seeding the sample with ^{13}CN to obtain particles of sufficient size to be captured on the membrane.

CHAPTER 5: A FABRICATION METHOD TO GENERATE P- AND N-TYPE BISMUTH TELLURIDE NANOPARTICLES FOR USE IN THERMOELECTRIC GENERATORS

5.1. Introduction

5.1.1. Thermoelectric power conversion

Thermoelectric materials (TE) are a class of materials that can be used to build thermoelectric generators (TEGs) which can directly convert heat energy into electricity or vice versa[112][113]. These materials are packaged into a compact solid-state device that can work as refrigerators or heat pumps without the use of any mechanical moving parts. The potential of this technology as an alternative source of energy has sparked much research in academia and in industry. However, the application of a temperature differential to generate electricity was not practical until the development of semiconductor materials that have high electrical and low thermal conductivity. Since the development of semiconductor materials with these unique properties, the use of thermoelectric devices to power space stations or for space explorations has been the norm[114]. There are space probes using thermoelectric power have been operating for more than 20 years in space, which is a testament to the reliability of this technology.

The most common application of TEGs is in cooling and temperature control of semiconductor lasers, as seat coolers in cars, as solid state coolers in compact refrigerators, and as power sources in wrist watches which run on the heat dissipated from humans [115][116]. More impactful applications have been postulated, such as their use in converting the waste heat from a car or ship's exhaust into useful energy[117]. However, use of thermoelectric technology

is still far from being part of everyday life. This is because TEGs have very low efficiency and generate minimal power output relative to the mechanical cycle. The engineering challenges to design and construct TEGs with better efficiencies will require advancements in thermoelectric materials and device fabrication techniques.

5.1.2. Principal of thermoelectric energy conversion

The Seebeck (heating) and Peltier (cooling) effects are at the center of thermoelectricity and thermoelectric energy conversion. In the case of heating, a thermoelectric device is created by combining a p-type and an n-type semiconductor in a closed electrical contact. Figure 5.1 shows the principles underlying power generation or active cooling. A voltage difference is produced when a temperature gradient is established between the hot and cold sides of the semiconductor material. This voltage is referred to as the Seebeck voltage, and it is proportional to the temperature gradient. As a result of this Seebeck effect, a proportionality constant known as the Seebeck coefficient is obtained.

The Peltier cooling is the reverse phenomenon of the Seebeck effect. Here, an electrical current is passed through the p- and n-type material, which is placed into a closed electrical contact and a temperature gradient is obtained because of heat absorbed or emitted by the materials at the junction. The Peltier coefficient measures how much heat is carried by per unit of charge in the junction.

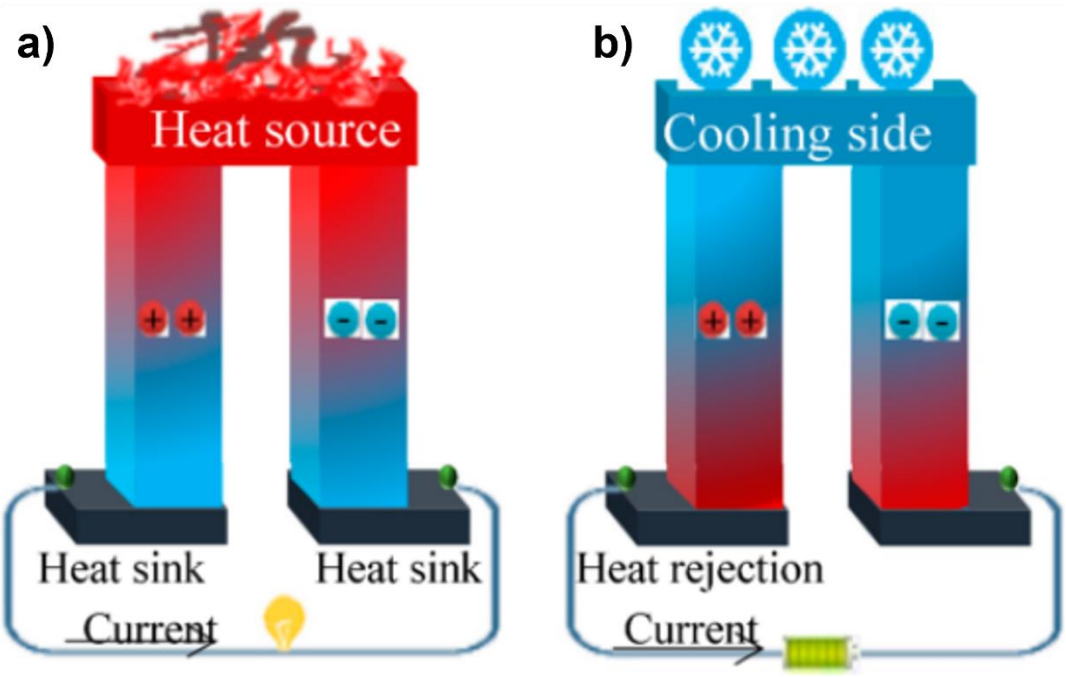

Figure 5.1. A thermoelectric device a) Seebeck effect (power generation) and b) Peltier effect (refrigeration). Q is the heat flow from the hot side of the junction to the cold side and I is flow of the current through the closed loop. Reproduced with permission from MDPI [118].

The p- and n-type semiconductor materials are created by doping with impurities that create excess holes or positive charge carriers (p-type) or excess negative electrons (n-type) in the material, and each pair of p-n type semiconductor material forms a thermoelectric couple. The heat and charge are carried by free electrons or holes. If the free charges are positive (p-type), a positive charge will accumulate on the cold end, resulting in a positive potential. Negative free charges (n-type material) will also produce a negative potential at the cold end for the Seebeck effect, as shown in Figure 5.1a. Likewise, when a DC current is applied, the holes and the electrons travel to the positive and the negative terminals, carrying heat along to create a cold side and a hot side (see Figure 5.1b).

Because the ability of a device to generate power or cool depends on both the thermal and electrical conductivity of the semiconductor material in use. Thus, in principle, the material should be of high electrical and low thermal conductivity. As a result, the semiconductor materials are divided into various classes based on their ability to generate power at various temperature ranges of applications and the efficiency of the semiconductor materials are described in terms of a dimensionless unit called the Figure of merit or ZT as shown in Equation 5.1, 5.2, and 5.3[119][117].

$$ZT = \frac{\alpha S^2 T}{k} \quad 5.1$$

$$= \frac{S^2 T}{k_\rho} \quad 5.2$$

$$= \frac{S^2 T}{(k_e + k_l)\rho} \quad 5.3$$

Where, S, σ, T and k are the Seebeck coefficient, electrical conductivity, temperature, and thermal conductivity, respectively. The thermal conductivity has two parts, lattice thermal conductivity (k_l) and electronic thermal conductivity (K_e). To obtain high thermoelectric efficiency, the ZT must be large. The power efficiency of the thermoelectric device can be described as,

$$= \frac{T_H - T_C}{T_H}\left[\frac{(1+ZT)^{\frac{1}{2}} - 1}{(1+ZT)^{\frac{1}{2}} + \left({}^{T_C}/_{T_H}\right)}\right] \quad 5.4$$

where, Tc and T_H are the cold and hot side temperatures. Thus, a large Δ T is necessary for high efficiency[120].

5.1.3. Bismuth telluride

Bismuth telluride and its related nanocomposites are the most studied thermoelectric materials [121] and the most commonly used in TEGs for commercial Peltier-cooled thermal sensors[117][122]. Bismuth telluride is a low temperature thermoelectric material and the maximum ZT value of bismuth telluride is somewhere between 1-2 at the temperature range of 300 to 500 K [123]. From Equation 5.1., improving the efficiency (i.e., increasing ZT) is achieved by increasing the electrical conductivity or decreasing the thermal conductivity. It has been demonstrated that selective doping with sulfur leads to an increase in ZT for bismuth telluride. Sulfur doping of the bulk n- type bismuth telluride improved the electrical conductivity of the materials by 20-80% leading to an improvement in the ZT [124]. Wang et al. used amorphous silicon dioxide as dopant for bulk p- type bismuth telluride and obtained ZT values of 1.12 and 1.27 at 303 K and 363 K, respectively[125].

Another approach to increasing ZT has been to synthesize well-defined porous bismuth telluride nanoparticles[126–130]. In these nanostructured materials, quantum confinement leads to an increase in the density of states near the fermi level which increases the thermoelectric power efficiency[131–133]. It has also been shown that the presence of well-defined pores in the nanostructure can scatter the thermal phonons much more efficiently which leads to a reduction in the thermal conductivity without compromising carrier mobility and

electrical conductivity[132]. Thus, nanostructured materials have better thermoelectric efficiencies than their bulk material counterpart[134].

Both top-down approach and bottom-up approaches have been used to form nanostructured bismuth telluride nanocomposites. The tops-down approach involves grinding bulk materials into nanostructured composites whereas, the bottoms-up approach employs the process of assembling nanostructures. In some cases, both methods are used, which is referred to as hybrid production.

Several methods, such as solvothermal or hydrothermal reaction, water–based chemical reduction, chemical oxidation, wet chemical method, and large–scale zone melting have been used to generate nanostructured materials to improve the thermoelectric efficiencies of TEG [135–142]. The solvothermal and hydrothermal methods produce bismuth telluride nanostructured single crystals. However, there are safety concerns with the reaction process as the aqueous reaction mixtures are heated up above the boiling point of the water under high pressure which can pose various health risks if not handled with caution. The water–based chemical reduction process is simple in design but control of the particle size is difficult. Moreover, it is not possible to obtain the low dimensional grain and crystalline size of the particles as the particle size is above 300 nm[138]. For the chemical oxidation technique, obtaining totally oxide- free material is not possible and hence, the electrical properties cannot be improved by employing this technique[136]. The wet chemical method uses toxic ethylene glycol to prepare the solution for the disproportionation reaction crucial for the formation of the

bismuth telluride [143]. Large–scale zone melting is used for production of the bismuth telluride ingot and not for nanoparticle generation[144].

The tops-down approach has mainly involved classical mechanical ball milling of the bulk bismuth telluride. Typically, ingots of bismuth telluride are added to steel shot and milled for a specified time. The resulting particles have wide size distributions that oscillate in size with the milling time, due to flocculation/deflocculation processes, and range in particle diameters between 50 nm to several microns [145][146]. The materials are then hot pressed, or plasma sintered into pellets for making TEG devices. The resulting nanocomposite device has large grain boundaries that can reduce the lattice thermal conductivity and increase the ZT[147]. The compacting of bismuth telluride nanoparticles for device fabrication is a low-cost method to obtain large amount of material needed for the thermoelectric power generation[148][149].

5.1.4. Thermoelectric research program at the university of Maine

Our project to improve the power efficiency of thermoelectric materials began in 2015 at the Frontier Institute for Research in Sensor Technologies (FIRST) in collaboration with Maine Maritime Academy (MMA). Because thermoelectric materials can recover waste heat and convert it into useful electricity, the technology is beneficial to Maine's marine industry. The thermoelectric research program at MMA began in 2008. Initially, a feasibility study was conducted to investigate the use of TEGs in marine propulsion systems to generate usable electricity for on-board lighting. Commercial prototype thermoelectric units were installed on lobster boats to test the design's mechanical feasibility. The design and implementation of the TEG’s were successful, and the performance obtained was better than the manufacturer's data.

When applied to a hybrid vessel, however, the output power was insufficient to be a critical component of the vessel system. Aside from that, the high thermal conductivity of the material made it difficult to maintain a thermal gradient between the hot and cold sides of the device.

Aside from waste heat recovery, the marine industry in Maine is facing increased costs because of the Main International Convention for the Prevention of Pollution from Ships regulations (MARPOL). The marine vessels are required to reduce their emission levels over a specified time period[150]. There is a need for marine vessels to operate in the affected areas to reduce the level of NO_x, SO_x, and the particulate matters to improve the port quality and to protect the environment[151]. TEG could be used for this purpose, as a portion of the waste heat from marine diesel engines could be recovered and stored in high power density batteries. This power could then be used for an electric drive system, reducing the load on the diesel engine and resulting in lower emissions. As a result, a pilot study to improve the material property of bismuth telluride was proposed as collaboration work between FIRST and the Marine Engine Testing & Emissions Laboratory (METEL) at MMA.

One practical challenge in TEG technology is the need to generate sufficient material to fabricate a device. Typical pile heights of both p- and n- type materials are 0.5 to 1 cm to achieve a sufficient temperature gradient across the device. While there has been many publications on fabrication of new exotic materials with high ZT, these typically are very thin films (<100 nm) and operate over a narrow temperature range[147]. Thus, our efforts have focused on using the readily available bismuth telluride found in commercial TEGs. The concept that we pursue in our research was derived from the bottoms-up fabrication of nanoparticulate bismuth telluride

particles and the introduction of porosity into the sintered structure to increase scattering of thermal phonons. However, a bottoms-up approach is challenging because of the need to generate both p- and n- type materials with a precise control over the level of dopants. In this regard, only p-type nanoparticles of bismuth telluride, synthesized using a bottoms-up approach, have been reported.

The specific goal of the project was to develop a top-down ball milling procedure to generate nano-particulates of both p- and n- type bismuth telluride particles less than 100 nm in diameter with narrow size distribution. The advantage of the ball milling is that no material synthesis is required, as commercial ingots of p- and n- type bismuth telluride could be used. Advanced ball milling procedures were used to create n- and p-type bismuth telluride nanoparticles which were stabilized in water using a cationic polymer. Adsorption of the polymer onto the fresh particle surface created during the milling process led to charge stabilization, preventing reaggregation of the bismuth telluride in suspension.

Using this approach, we have developed methods to achieve particles with diameter less than 100 nm. Dynamic light scattering was used to measure the average size and size distribution of the nanoparticles. The surface morphology and size of the crystalline grain were determined using SEM and XRD, respectively. Electrical resistivity, thermal conductivity and Seebeck coefficient of the nanomaterials were measured. We also hypothesized that sintering the particles under pressure at temperatures below the melting point of 586°C would both eliminate the polymer and lead to partial sintering of the particles. This in turn, would introduce pores of sufficient size to scatter thermal phonons, leading to TEG devices with higher efficiencies. While

our fabricated pellets had reduced electrical conductivity, we do observe decrease in thermal conductivity and hence, this approach could offer a new route to improving efficiencies in the design of materials for TEGs.

5.2. Experimental

5.2.1. Materials and instruments

Bulk n-type ($Bi_2Te_{2.7}Se_{0.3}$,99.99%) and p-type ($Bi_{0.5}Sb_{1.5}Te_3$,99.99%) of 44 microns in diameter were purchased from American Elements and were supplied in an airtight container. The materials were stored inside a nitrogen glove box to avoid the formation of the bismuth telluride oxide. The glove box was purged with N_2 gas initially for five minutes to remove the air. After 5 minutes of purging, the bulk sample containers were transferred into the glove box and the door was closed tight. Then the glove box was purged with N_2 gas for 5 more minutes to make sure that the glove compartment was free of air. We also used bismuth telluride materials extracted from a commercial module, HZ14, obtained from Hi-Z Technologies. Antimony triiodide (SbI_3 98%) was obtained from Sigma Aldrich and was stored in an airtight bottle at room temperature. Polydiallyldimethylammonium chloride (PDADMAC) with average Mw of 200,000-350,000 supplied as 20 wt.% in H_2O was purchased from Sigma Aldrich and stored at room temperature.

A planetary Micro Mill PULVERISETTE 7 was purchased from FRITSCH Milling and Sizing Inc. The micro-mill consists of two zirconia oxide sample bowls and zirconia oxide grinding shots of 0.1 mm or 1.0 mm diameter.

5.2.2. Ball milling procedure

The ball milling of the p- and n-type bismuth telluride was performed using two separate zirconia bowls and separate sets of 1.0 mm and 0.1 mm shots to avoid any cross-contamination between the p- and n-type materials. For grinding purposes, 15-17 g of 1.0 mm zirconia oxide shot was added to a zirconia oxide bowl. Then, 1-2 g of p-type or n-type bulk bismuth telluride, weighed inside the glove box under nitrogen purge, was added to a zirconia oxide bowl on top of the zirconia shot. For the n-type bismuth telluride, 1% w/w antimony triiodide was added to the zirconia bowl.

Through a series of trial-and-error experiments, we developed protocols for generating 40, 100 and 300 nm diameter particles. For 40 nm particles, 40 %w/w PDADMAC was mixed with 6 mL of deionized water in a separate beaker and stirred for 30 minutes. The polymer-water mixture was added to each zirconia bowl containing the bulk samples and the bowls were then loaded into the micro mill for ball milling. The samples were ball-milled for 30 minutes at 1100 rpm to generate the suspension of 40 nm nanoparticles. For 100 and 300 nm particles, 30 %w/w and 35 %w/w PDADMAC were mixed with 6 mL of deionized water, respectively. The polymer-water mixture was added to the zirconia bowl with the bulk sample and ball milled at 1100 rpm for 30 minutes. After ball milling, the zirconia shots were filtered out with a 0.45-micron membrane, and the sample suspension was dried in an oven at 80-100°C for 12-16 hours to obtain nanoparticles in the form of a powder. The nanoparticles were then stored at room temperature in an airtight vial located in the glove box.

5.2.3. X-Ray Diffraction

The powder X-ray diffraction of the bulk and nano particles was performed using a PANalytical XPert PRO MRD XL #DY2409 instrument with a fixed divergence slit. The target anode material was Cu, the K-Alpha1 wavelength was 1.5440598 Å and the K-Alpha2 wavelength was 1.544426 Å. The bulk powder was taped onto a glass slide with a single sided tape. The ball milled samples were pressed into pellets at 300°C and the XRD data was collected along the direction of hot pressing.

5.2.4. Hot and cold pressing of the nanoparticles into a pellet

The p- and n-type ball-milled nanoparticles were hot pressed into a cylindrical pellet using a pellet dye and a hydraulic press under 500 psi at 200, 250, and 300^{o}C (see Figure 5.2). The pressed pellets were 5 mm in diameter and had a height of 3 to 4 mm. A barrel jacket heater surrounding the pellet dye was used to heat the dye up to 300°C without applying any pressure. To control the temperature ramp, the jacketed pellet dye was attached to a home built PID controller. The temperature was monitored using a type K thermocouple that was inserted between the heater and the dye. The jacketed dye was insulated to keep the temperature constant while hot pressing and a constant nitrogen gas was flowed inside the dye through the purging hole to prevent the oxidation of the material while hot pressing. A temperature ramp rate of 5-10°C per minute was used. Once the dye reached the desired temperature, it was held constant at that temperature for 1 hour to remove the PDADMAC polymer used in ball milling the material. After 1 hour, the sample was then hot pressed at 500 psi for 5-10 minutes using the hydraulic press while maintaining the temperature at 300°C. The pressure and temperature were then gradually released over 20 minutes under constant nitrogen gas flow . Then the pellet

was removed from the press and stored in an airtight container inside the nitrogen glove box. In another approach, nanoparticles were cold pressed at 500 psi into a pellet at room temperature under steady nitrogen flow, then post annealed to 200, 250, 300, and 400°C at a ramp rate of 10°C/min until the hot-pressing temperature was reached. The pressure was reduced slowly, and the sample was allowed to come down to room temperature naturally under the nitrogen flow. This second procedure was used to determine if post sintering altered the electrical and thermal conductivity of the materials, compared to hot pressing.

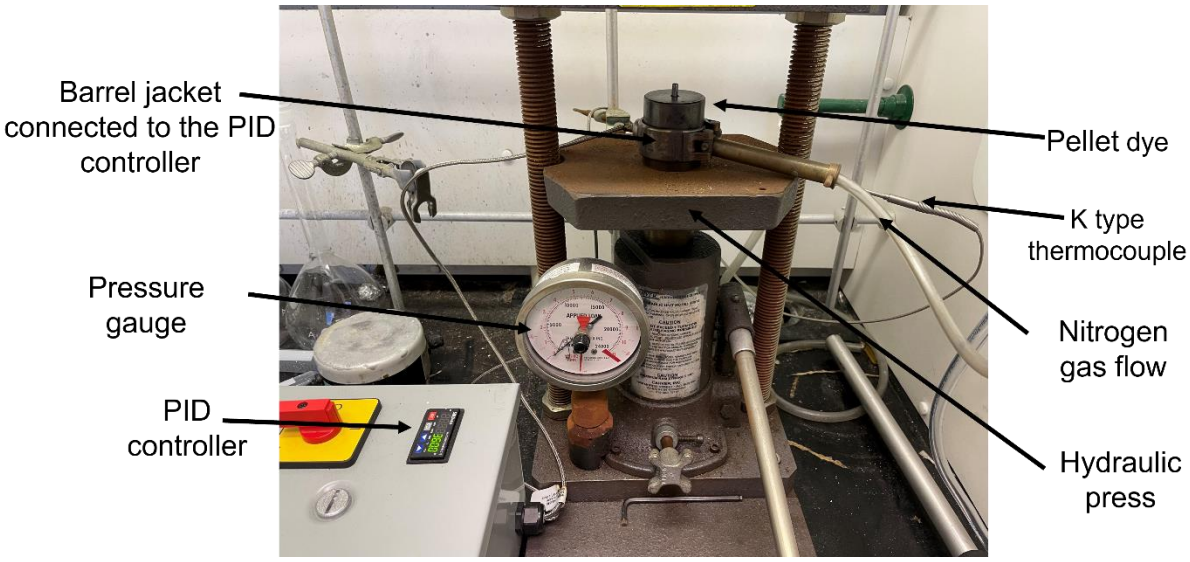

Figure 5.2. The setup for hot pressing of the bismuth telluride nanoparticles into a pellet using a heated dye on a hydraulic press, controlled using a home built PID controller.

5.2.5. Electrical resistivity

The electrical resistivity of the bulk and ball milled p-type material was measured for the cold pressed and hot pressed 13 mm diameter pellets using a four-point probe, as shown in Figure 5.3. Approach for measuring the electrical conductivity of the p-type bismuth telluride pellets inside a high-temperature muffle furnace in real-time, using a homebuilt four-point probe

connected to a multiplexer and a Keithley source measure unit. This setup was used to measure the sheet resistance to calculate the bulk resistivity of the pellets using a modified 4-point probe that can be inserted inside a high temperature furnace to measure the resistivity of the samples at elevated temperatures. As shown in Figure 5.3a, a 13 mm p- type bismuth telluride sample was mounted on the 4-probe sample holder, such that the tip of the probe holds the sample mounted on top of the ceramic plate. The probe tips are made of nichrome wires. Two of the probes measure the current passed across the sample and the other two probes measure the corresponding voltage across the sample. The probe tips were coated with conductive silver paint to decrease the ohmic contact resistance. Figure 5.3b shows the end of the probe connected to a Keithley source measure unit to measure the current and voltage over time. The multiplexer is also connected to the source meter and hooked up with a computer (not shown in Figure 5.3) to record the data. Figure 5.3c shows the probe with the sample inserted inside a narrow glass tube that sits inside the muffle tube furnace. The glass tube has a locking mechanism on both ends to make sure temperature remains constant over time. The probe head is positioned in the middle of the furnace to unsure uniform heating. The temperature was measured using a K type thermocouple inserted in the ceramic material of the tube furnace that sits below the sample.

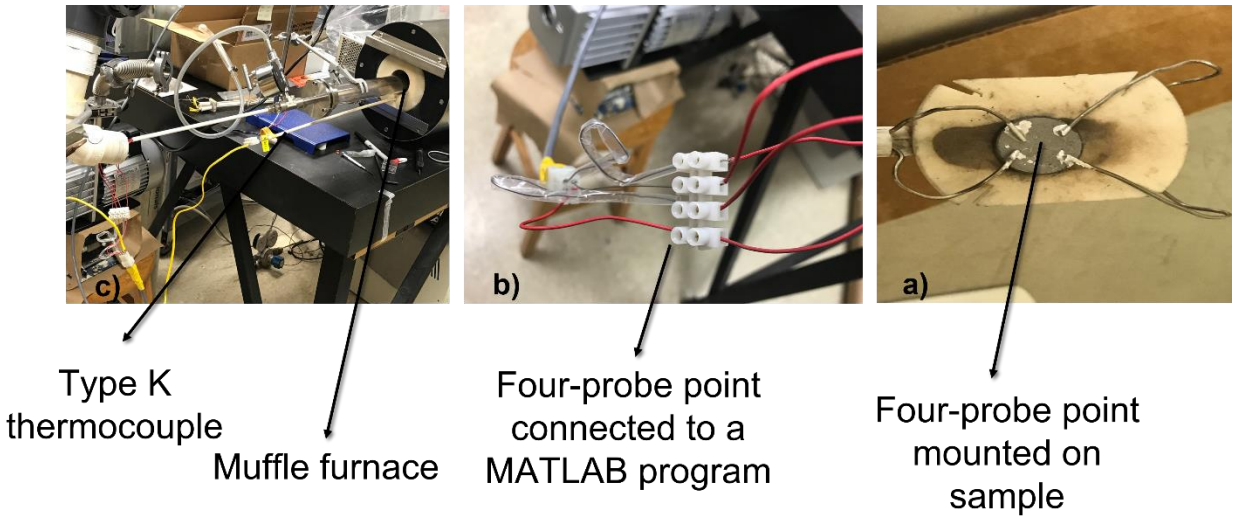

Figure 5.3. Approach for measuring the electrical conductivity of the p-type bismuth telluride pellets inside a high-temperature muffle furnace in real-time, using a homebuilt four-point probe connected to a multiplexer and a Keithley source measure unit.

Once the sample was loaded, the glass tube was purged with a 10 mL/min nitrogen gas flow to remove any trapped oxygen. The sheet resistance of the sample is then measured over time at room temperature and recorded using a MATLAB data acquisition program. The sheet resistance was also measured as a function of increasing temperature using a PID controller, as shown in Figure 5.4. Once a stable resistance reading was obtained, the temperature was increased in ramp mode (2^{o}C/min) up to 400°C while remaining isothermal at 100°C, 200°C, and 300°C for at least 30 minutes to obtain a uniform sheet resistance value.

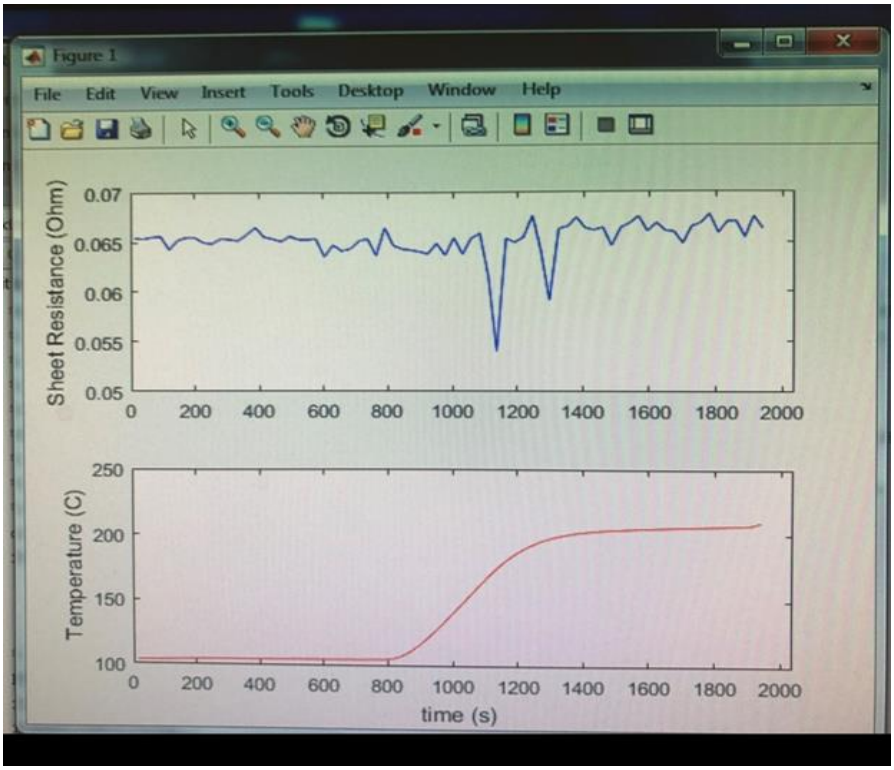

Figure 5.4. Output from the MATLAB program showing the sheet resistance of a 13 mm p- type bulk bismuth telluride, measured in real time as a function of temperature using a 4-point probe. The pellet was hot pressed at 300°C. The temperature was ramped at a rate of 2°C/min using a PID controller.

Similarly, the sheet resistance of ball milled p-type nanoparticles was determined using 13 mm diameter hot pellets hot pressed at 300°C. After the data was collected, the sample was allowed to cool down to room temperature and the sample's sheet resistance was measured during the cooling process. It required about 8-10 hours to measure the sheet resistance of a single sample because the ramping and cooling process was slow at 2°C/min.

5.3. Results and discussion

5.3.1. Characterization of the bismuth telluride bulk and nanoparticles

5.3.1.1. Particle size distribution

After ball milling, a small amount of the suspension from the zirconia bowl was extracted using a micropipette and diluted 10-fold to measure the average particle size distribution on a Malvern 3000 HSA Zetasizer. The average size distribution of the "as received" bulk p-type bismuth telluride powder was 610±103 nm (see Figure 5.5). Once the samples were ball milled in the presence of 30, 35, and 40 %w/w PDADMAC, the size distribution of the particles was 316±45 nm, 129±23 nm, and 60±15 nm, respectively.

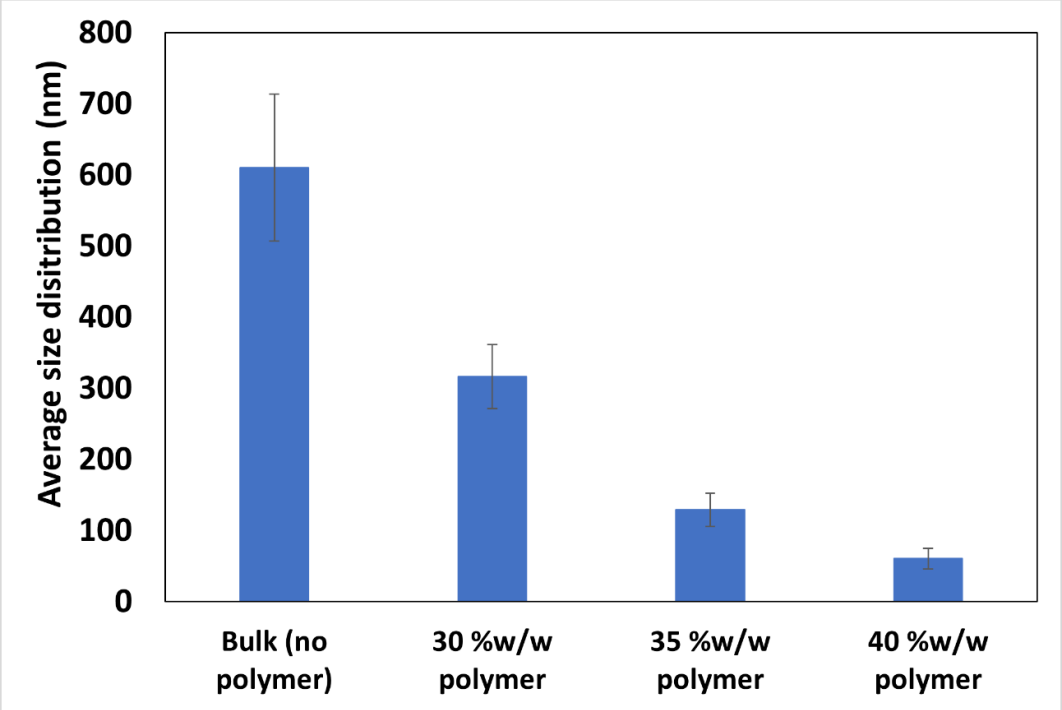

Figure 5.5. Average particle size distribution of the bulk p-type bismuth telluride, before and after ball milling with different % w/w PDADAMAC in water.

5.3.1.2. Scanning electron microscopy (SEM)

The SEM of the ball milled p- and n-type nanoparticles were performed to determine the size distribution of the ball milled nanoparticles and observe the microscopic void in the materials. Figure 5.6a and Figure 5.6b shows the SEM images of the p- type bismuth telluride nanoparticles after ball milling in presence of the 40 %w/w PDADMAC. Figure 5.6c and Figure 5.6d shows the SEM images of the n type bismuth telluride nanoparticles after ball milling in presence of the 40 %w/w PDADMAC.

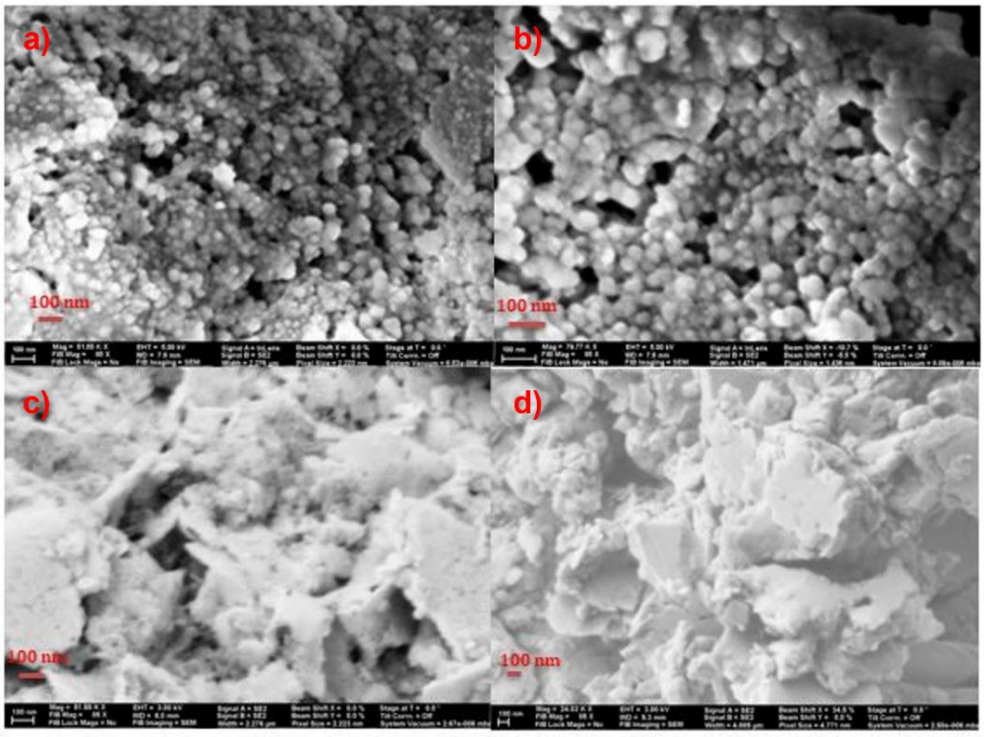

Figure 5.6: SEM image of the p-type bismuth telluride (a and b) and n- type bismuth telluride (c and d) nanoparticles. The images were taken after drying the nanoparticles at 80°C for 12 hours.

Figure 5.6 shows that uniform distribution of the bismuth telluride nanoparticles and presence of microscopic porosity. In the case of n- type materials, the particles tend to aggregate into bigger clusters but individual particles with different shapes were observed. While collecting

the SEM images, different random locations were chosen, and the size of the individual nanoparticles was measured, as shown in Figure 5.7, and the obtained numbers were consistent with the DLS measurement results shown in Figure 5.5.

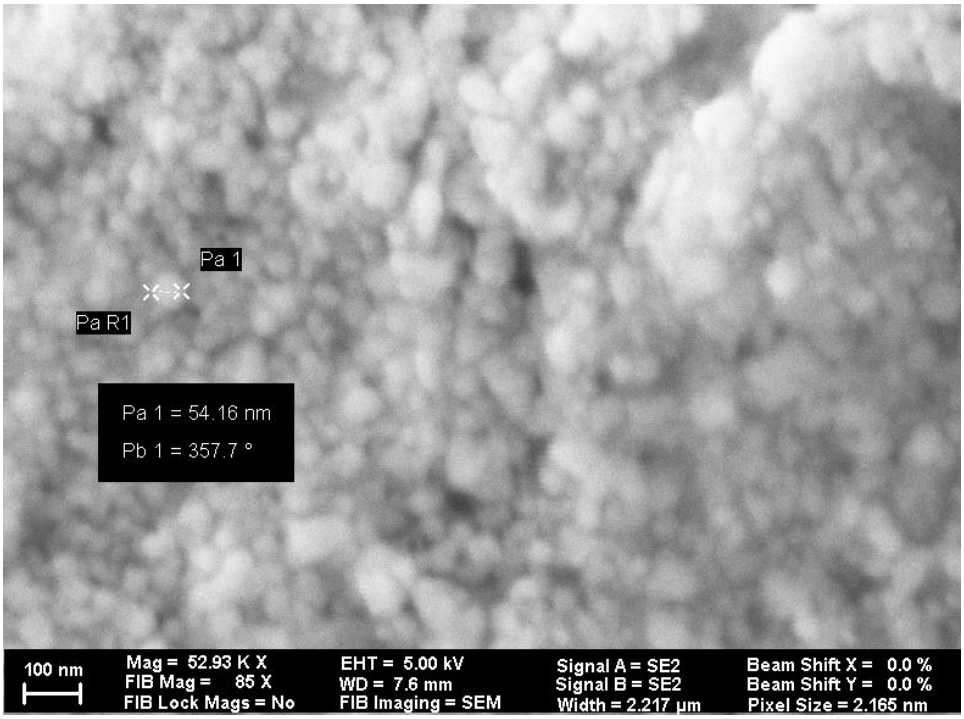

Figure 5.7. SEM image of the p-type bismuth telluride nanoparticles prepared by ball milling in presence of 40 %w/w PADAMAC, showing the size of the individual nanoparticle measured from edge to edge.

Figure 5.8a and 5.8b shows the SEM images of the p- type bismuth telluride nanoparticles after ball milling in presence of 35 and 30 %w/w PDADMAC. The average size of the particles in the 35 %w/w PDADMAC sample was in the range of 80-130 nm whereas the average size of the particles in the 30 %w/w PDADMAC sample was in the range of 280-350 nm. Thus, the SEM images suggest that with increasing %w/w of polymer, the size of the nanoparticles decreased in the suspension due to the electrostatic stabilization of the negatively charged nanoparticles with adsorption of opposite charged polymer on their surface[152].

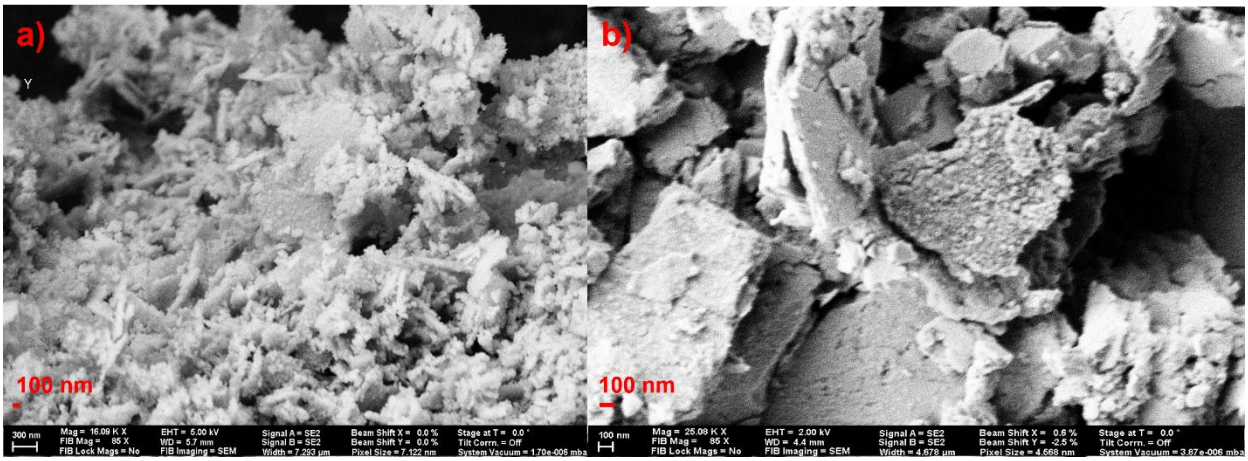

Figure 5.8. SEM images of the p-type bismuth telluride samples ball milled in presence of a) 35 and b) 30 %w/w PADAMAc in water solution. The images were taken after drying the suspension at 80°C for 12 hours

The main reason we hot pressed the pellets at 300°C was to ensure that microscopic voids are present in the hot-pressed samples so that the thermal conductivity would be lowered. The presence of voids is shown in Figure 5.9 for a pellet made with 40 nm particles hot pressed at 300°C. The SEM images of the pellet cross section shows that the porosity remains even after hot pressing the sample at 300°C. The shape of the nanoparticles were mostly irregular, as shown in Figure 5.9, and the particles were partially sintered together while retaining a level of porosity.

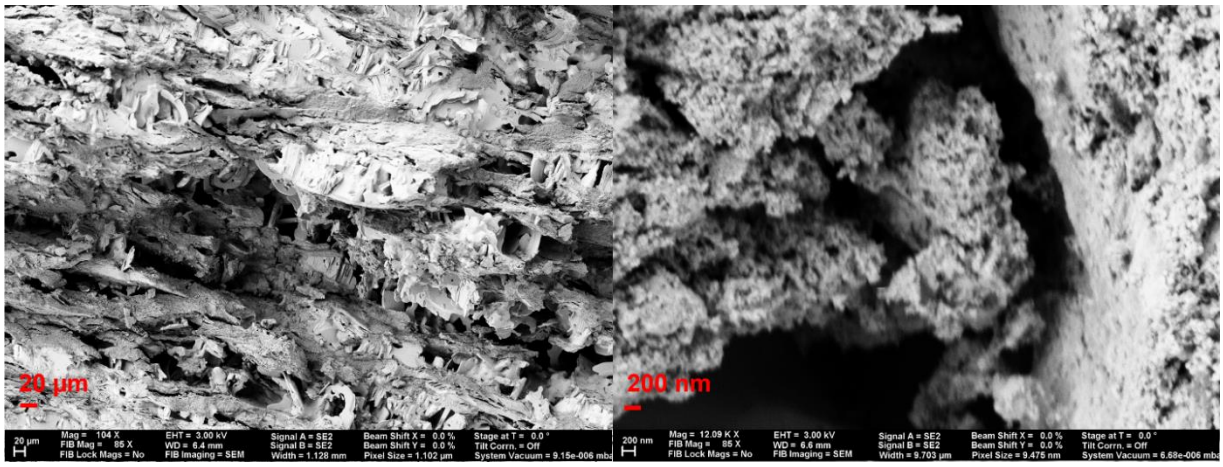

Figure 5.9. A cross-section SEM image of a p- type pellet made of 40 nm particles hot pressed at 300°C.

5.3.1.3. Thermogravimetric analysis (TGA)

TGA of the bulk p- type and the bulk n-type material was performed and compared with the ball milled nanoparticles to determine the amount of PDADMAC remaining after hot pressing at 200, 250, and 300^{o}C. In Figure 5.10, the TGA plot shows one peak at 220°C due to removal of the PDADMAC and a second peak at around 320 °C, suggesting the complete oxidation of the PADAMAC. Figure 5.10c and Figure 5.10d show the TGA curves for the p- type 40 nm particles hot pressed at 500 psi into a 5 mm pellet at 200, 250 and 300°C. A peak due to PADAMAc is observed in Figure 5.10c. However, in Figure 5.10d, the TGA shows that the peak due to PDADMAC removal is not observed when the sample was hot pressed at 300°C. Hence, we conclude that heating in the range of 300-350°C is sufficient to remove all PDADMAC from the sample. Similar TGA curves were obtained for the n-type bismuth telluride. Thus, both the p-type and the n-type nanoparticles were hot-pressed around 300-350^{o}C to remove the polymer from the material surface. Hot pressing at a higher temperature, such as 400^{o}C, was not implemented because this would reduce the micro voids necessary to lower the thermal conductivity of the material.

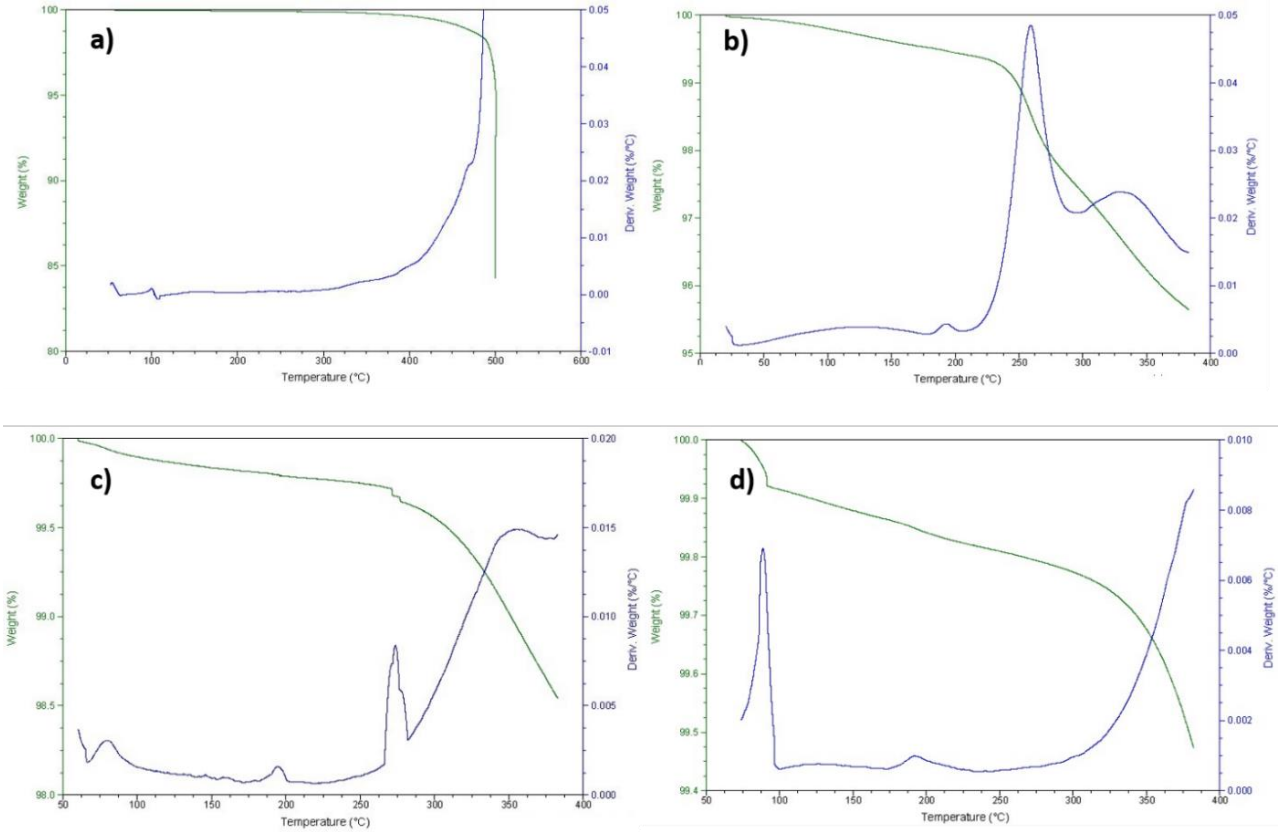

Figure 5.10. TGA of the p-type bismuth telluride a) as received, and 40 nm particles hot pressed at b) 200, c) 250, and d) 300°C.

Cold pressed 40 nm particle pellets were post annealed at 300, 350, and 400^{o}C, and TGA analysis was performed to investigate if post annealing of the pellets can be used as an alternative to hot pressing. Cold pressing the samples did reduce the formation of the cracks within the pellets. However, the TGA of the post annealed sample (see Figure 5.11) shows that the polymer removal starts around 200^{o}C and continues up until 400^{o}C.

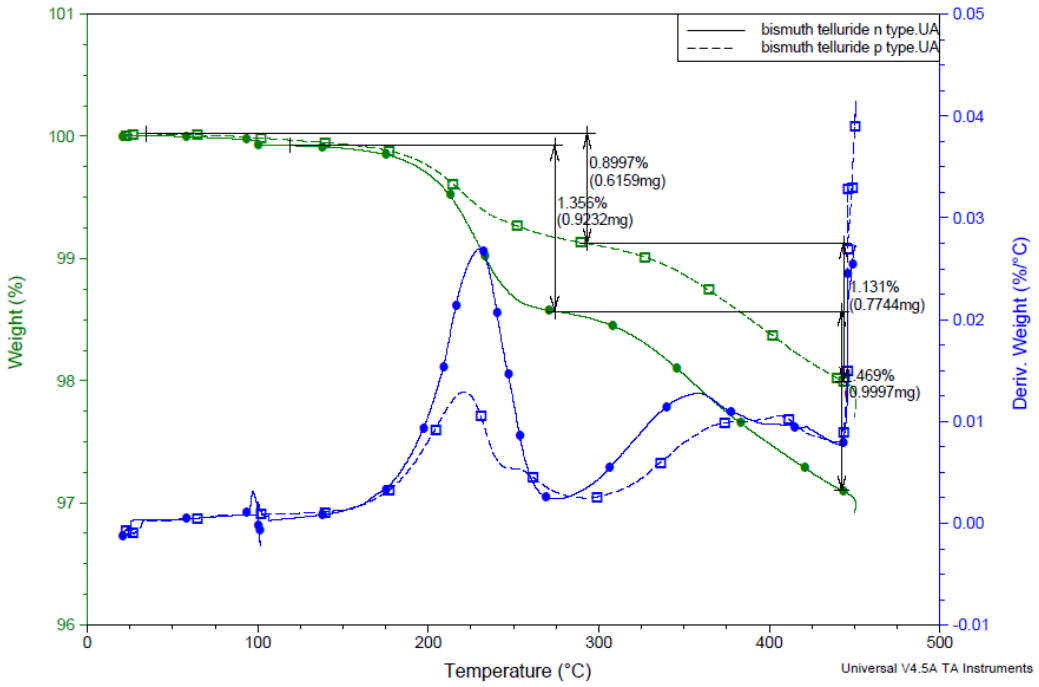

Figure 5.11. TGA of the cold pressed bulk p- and n-type bismuth telluride.

5.3.1.4. Powder X-Ray diffraction (XRD)

The XRD pattern of the ball milled p-type materials after hot pressing the nanoparticles at 300°C is shown in Figure 5.11. All of the ball milled samples had a rhombohedral crystal structure (R3m), which is consistent with the standard PDF #01-080-6665 for p-type bismuth telluride.

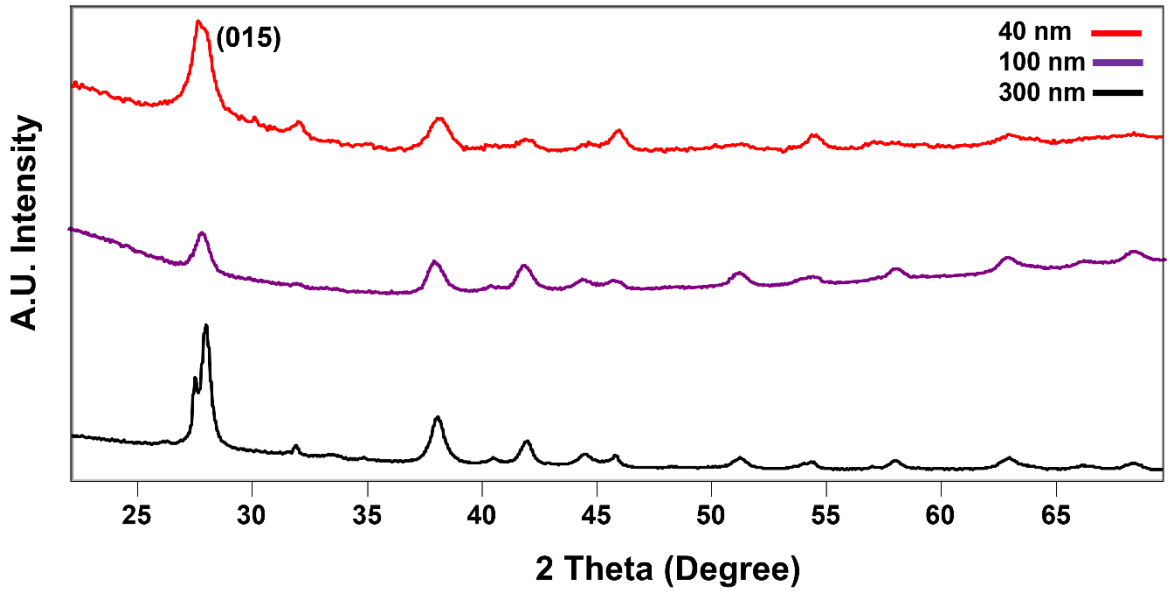

Figure 5.12: XRD of p- type bismuth telluride pellets along the perpendicular direction of hot pressing at 300°C.

The average crystallite size was measured using the Scherrer Equation,

$$t = K\lambda/(\mathrm{B}\cos\theta) \qquad 5.5$$

where t denotes the average crystallite size, K is the Scherrer constant, λ is the X-ray wavelength, and B is the peak FWHH (in radians) found at 2Θ. Using this equation, the average crystallite size for the 300 nm particles was 183 nm, whereas the average crystallite size for the 100 nm particles was about 38 nm. The average crystallite size of the 40 nm particles was 29 nm. This shows that the particles are polycrystalline in nature.

5.3.1.5. Energy-dispersive X-ray spectroscopy (EDS)

EDS on the ball milled n-type samples were performed before and after hot pressing at 300^{o}C ^{o}C to determine the fraction of oxygen and carbon present in the samples. The oxidation of the bismuth telluride reduces electrical conductivity of the bismuth telluride which, in turn,

lowers the Seebeck voltage, resulting in a lower power output. Furthermore, the presence of the organic polymer in the ball milled samples can reduce the electrical conductivity of the material.

Figure 5.13 shows the EDS spectrum of the 40 nm n-type bismuth telluride pellet before and after hot pressing at 300^{o}C in which both carbon and oxygen are present in the samples after ball milling. The wt.% of carbon in the sample was 19.66 % and oxygen was 3.13 %. This means some of the bismuth telluride oxidized but the oxidized fraction is less than 5 wt.% of the total sample. After hot pressing the sample at 300^{o}C, EDS analysis showed no carbon in the sample. However, the wt.% oxygen increased from 3.13% to 5.59%. Thus, the hot pressing at 300^{o}C leads to an increase in oxidation of the material but the extent of this oxidation was minimized due to nitrogen purging of the samples during the hot press.

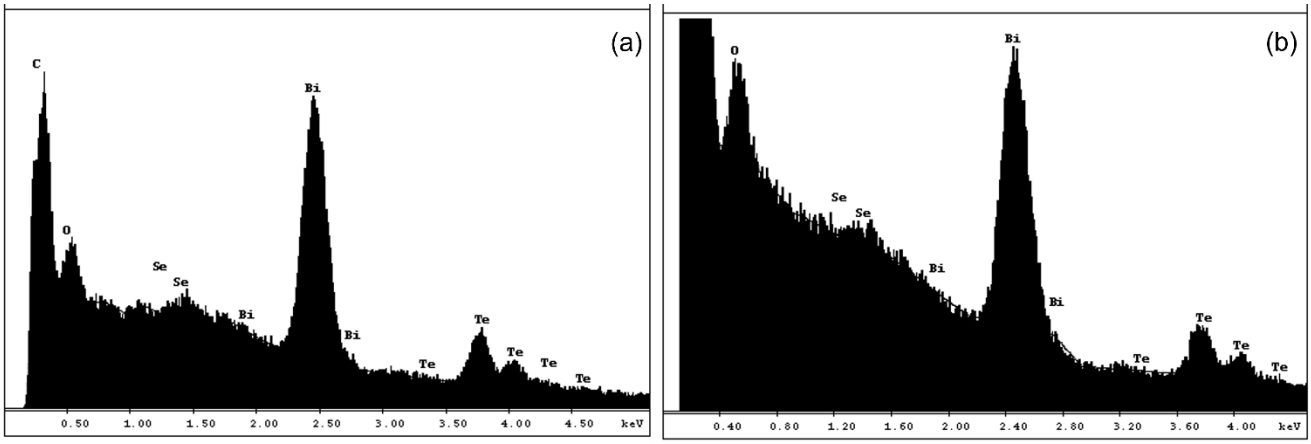

Element	Wt %	At %
C K	19.96	72.22
O K	3.13	8.51
SeL	1.62	0.89
BiM	54.68	11.37
TeL	20.60	7.02
Total	100.00	100.00

Element	Wt %	At %
O K	5.59	39.55
SeL	1.78	2.55
BiM	70.13	37.96
TeL	22.49	19.94
Total	100.00	100.00

Figure 5.13. The EDS and the elemental analysis of the ball milled n-type bismuth telluride (a) before hot press and (b) after hot press at 300°C.

5.3.1.6. Void fraction

The void fraction formed was calculated before and after annealing a 13 mm diameter pellet for both the p- and n-type bismuth telluride. The "as received" p- and n- type bismuth telluride had a measured bulk density of 7.58 and 7.63 g/cm^3, respectively. In contrast, when 40 nm p- and n-type particles were pressed into a pellet, the packing densities were 5.02 and 5.33 g/cm^3 prior to hot pressing. The difference between the bulk and packing densities is due to the void fraction. Thus, by measuring the volume of the pellet and its weight, the void fraction is determined. Therefore, a void fraction of 34% and 30% were obtained for p- and n-type bismuth telluride for the pressed pellets. After annealing the pellets at 300°C for 1 hour, the packing density of the same p- and n-type pellet increased to 5.70 g/cm^3 and 5.97 g/cm^3, resulting in a drop in the void fraction to 27% and 22%, respectively. This overall 11-12% decrease in the void fraction is caused by the high temperature surface sintering of the sample at 300°C.

5.3.2. Thermoelectric properties of the p- and n-type nanoparticles

5.3.2.1. Electrical resistivity

The electrical resistivity of the bulk or ball milled bismuth telluride was measured for the 5 mm or 13 mm diameter pellets of the hot and cold pressed p- and n- type bismuth telluride powders. Different sample preparation conditions and numerous methods and setups were used to determine the factors that affect the electrical conductivity of the bismuth telluride. Most of the electrical resistivity measurements were performed using the p-type material because it was less susceptible to oxidation compared to the n-type material.

$$\rho = {RA}/{l}$$

The electrical resistivity of the bulk p-type bismuth telluride is shown in Figure 5.14 Figure 5.14a shows the measured electrical resistivity of a 13 mm bulk cold pressed and a 13 mm bulk hot-pressed sample at 300°C. Figure 5.14b shows the electrical resistivity of the bulk p-type bismuth telluride measured by 7 different labs to obtain a standard resistivity value of the bulk bismuth telluride. Thus, we decided to compare the resistivity of our bismuth telluride with those from different labs.

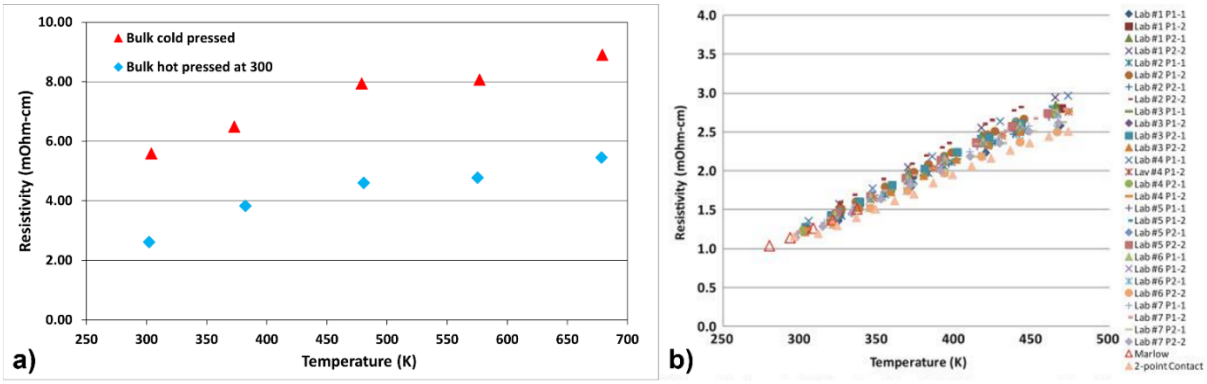

Figure 5.14. Electrical resistivity of bulk p-type bismuth telluride materials a) measured using our 4 probe point setup and b) measured by seven different labs [153].

The electrical resistivity of the cold pressed and hot pressed (at 300°C) sample were measured at 25°C and the values were 5.59 and 2.61 mOhm-cm, respectively.25°C Whereas, the resistivity of the bulk sample measured at other labs (see Figure 5.14b) were in the range of 1.4-1.5 mOhm-cm at 100°C. Thus, the measured resistivity for the cold pressed sample is almost 4.5 times higher, whereas the resistivity of the hot-pressed sample is only a factor of 1.5 higher than the bulk values. This high resistivity is caused by the porosity and partly due to contact resistance between the tips of the probe and the sample.

The probe was designed to measure the sheet resistance of a thin film and not the bulk resistance of a thick disk. We could not physically attach the tips of the probe to the sample and,

as a result, resorted to the use of conductive silver paste on the tips of the probe to minimize contact resistance between the probe and the sample. Nevertheless, the difference in resistance between the hot and cold pressed samples shows that the presence of voids does lead to a reduction in the electrical conductivity and that surface sintering increases the contact between the particulates and hence, lowers the resistance of the pressed disk at 300°C.

We then measured the electrical resistivity of the ball milled p-type samples hot pressed at 300°C and the data is shown in Figure 5.15. The electrical resistivity of the pressed samples were 7.9, 10.3, and 9.1 mOhm-cm for the 40, 100, and 300 nm particulate disks, respectively. Comparing these values with literature values (see Figure 5.14b), we find that the resistivity of the ball milled samples are almost 6-8 times higher than the bulk resistivity. This increase in the electrical resistivity is expected, as we are creating voids in the material by ball milling and hot pressing at about half-way to the melting point temperature (586°C).

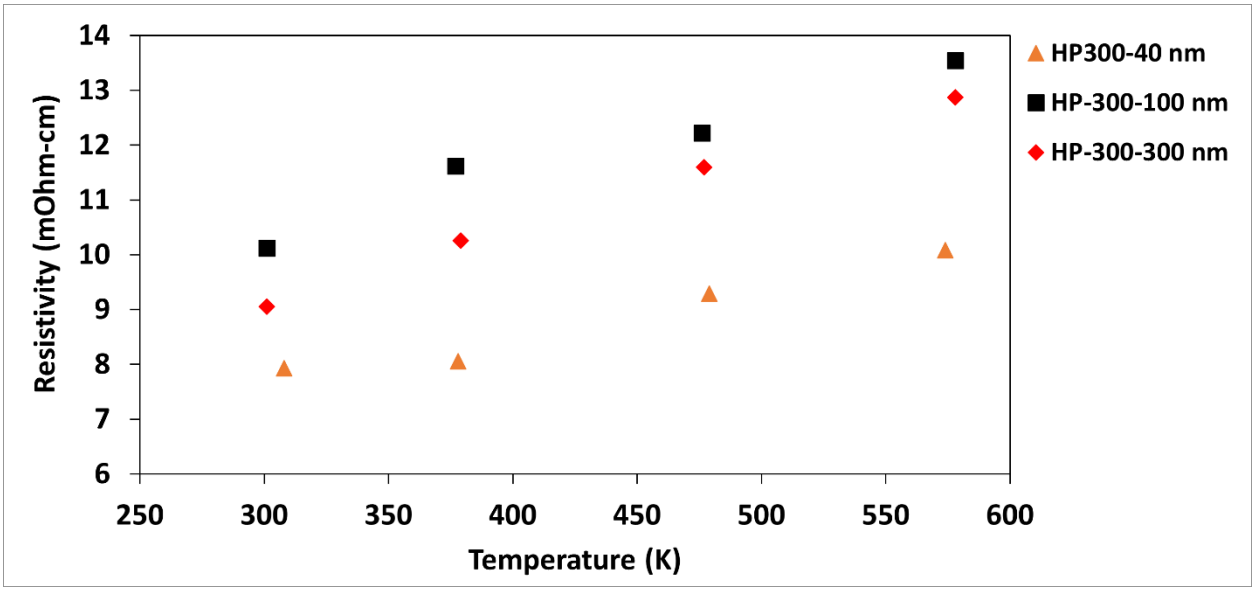

Figure 5.15. The electrical resistivity of the p-type bismuth telluride pellet as a function of temperature. The pellets were hot pressed at 300°C.

Initially, we thought that part of the higher electrical resistance could be due to the oxidation of the bismuth telluride with the dissolved oxygen present in the DI water. If this oxidation of the sample during the ball milling can be reduced, then this could lower the resistivity of the hot-pressed nanoparticles. Thus, we used deoxygenated DI water to ball mill the p-type bismuth telluride and hot press them at 300°C to measure the resistivity of the sample.

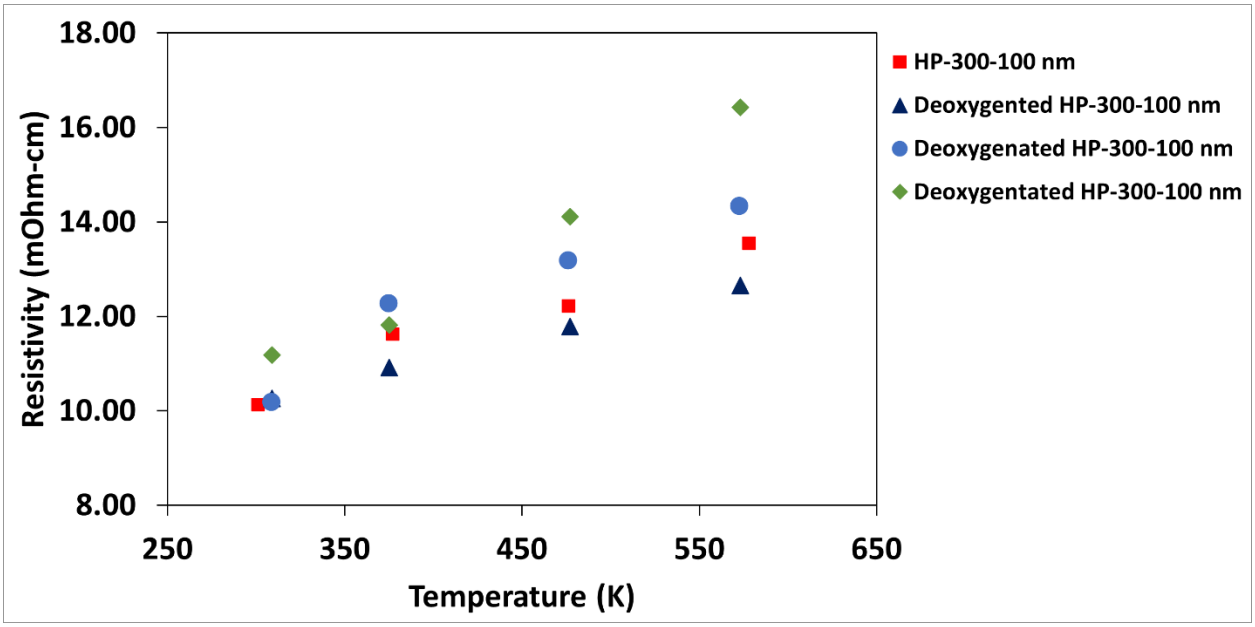

Figure 5.16. Resistivity of the p-type bismuth telluride pellets hot pressed at 300°C measured as a function of temperature using a four-point probe.

Figure 5.16 shows that ball milling of the sample in deoxygenated water is a minor factor in the measured resistance of the p-type bismuth telluride. For example, the resistivity of the 100 nm particle size sample was 10.1 mOhm-cm. When the deoxygenated water was used for ball milling, the resistivity of the 100 nm samples ball milled with deoxygenated water and then hot pressed at 300°C were 10.2, 10.3, and 11.3 mOhm-cm at 25°C. Furthermore, the resistivity of the deoxygenated samples is almost 5-10% higher, compared to the samples ball milled in DI water and hot pressed at 300°C.

5.3.2.2. Thermal conductivity and Seebeck Coefficient

The thermal conductivity and Seebeck coefficient data were collected at Cornell University. Figure 5.17 shows that the thermal conductivity of the bulk sample hot pressed at 300°C was 1.21 W/K m at ambient temperature and changed little between 7°C to 107°C. The bulk material will contain voids since we hot pressed the bulk (as received) material well below the melting point of bismuth telluride. The reported thermal conductivity of the p type bulk bismuth telluride pressed into disks after melting above the melting point are between 1.45 to 1.5 W/K m at 50-100°C [154]. Hence, even hot pressing the bulk material at 300°C introduces void within the material that reduces the thermal conductivity to 1.2 W/K m which is about a 20% reduction in thermal conductivity.

The thermal conductivity obtained for hot pressed pellets varied with the size of the nanoparticle, with values of 0.8 , 0.59 and 0.22 W/K m for 40, 300 nm and 100 nm particles measured at 27°C , respectively. Increasing the temperature to 107°C resulted in little change in the thermal conductivity values of any of the nanoparticle-based pellets. A higher thermal conductivity for 40 nm particles is most likely due to a “too small a void size” leading to reduced phonon scattering. However, the thermal conductivity value of the 40 nm particle sample was almost 2 times lower than the reported bulk values at 100°C. The thermal conductivity of the 300 nm particles was almost 2.5 times lower than the reported bulk values at 100°C. The 100 nm particles showed the lowest thermal conductivity value out of all four samples. The thermal conductivity of the 100 nm particles was between 0.20-0.22 W/K m within 27- 107°C, which is almost 6.7 times lower than the bulk reported values at 50- 100°C range. As a result, we

concluded that the 100 nm diameter particles lead to the pore structure that best scattered the thermal phonons.

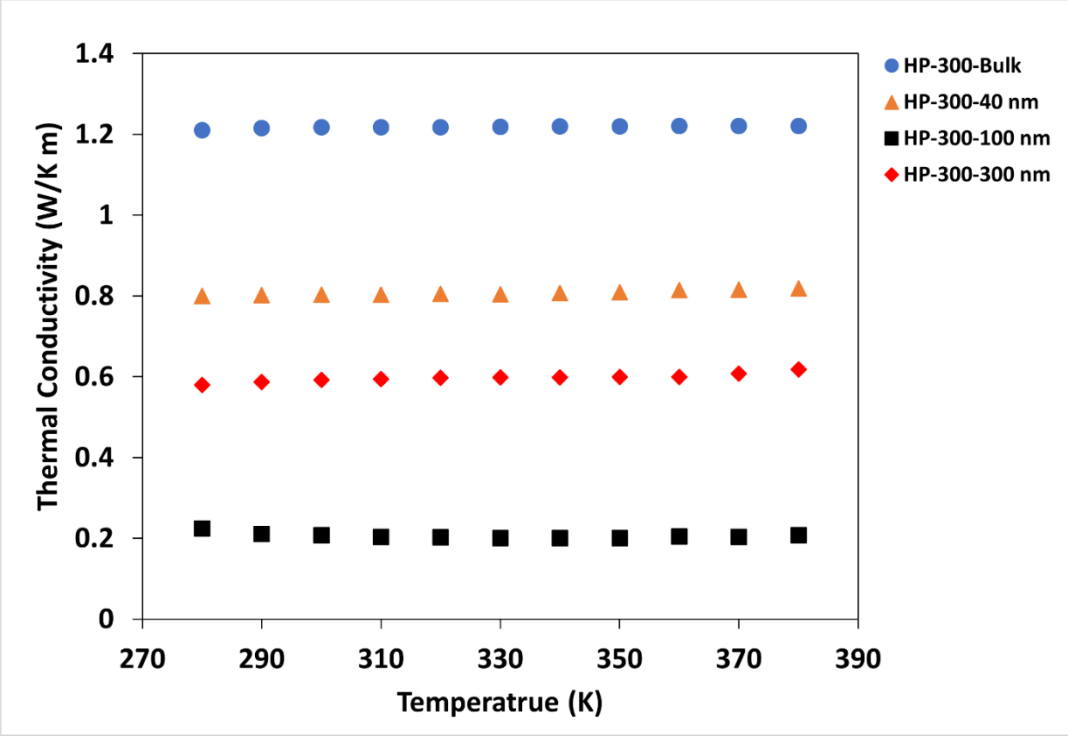

Figure 5.17. The thermal conductivity of the p- type bismuth telluride material as a function of measuring temperature. The pellets were hot pressed (HP) into 5 mm diameter pellets under nitrogen gas flow at 300°C.

Figure 5.18 shows the Seebeck coefficient values for p- type bulk and nanoparticles hot pressed at 300°C and measured from 280 K to 380 K. The Seebeck values increased with temperature for all samples. The porous bulk material hot pressed at 300°C had the lowest Seebeck value of 195 µV/K at ambient temperature and increased to 206 µV/K at 107°C (380 K). The reported Seebeck coefficient value for bulk p- type bismuth telluride is about 230-240 µV/K at 100°C and decreases with increase of the temperature[153][154]. A decrease in the Seebeck coefficient is understandable, as the presence of microscopic void reduces the charge transport from the hot side to the cold side. The Seebeck values of the hot-pressed nanoparticles were

slightly higher than those of the porous bulk material. For example, the Seebeck coefficient for the 40 nm particles was in the range of 210 µV/K at 107°C. For 100 nm particles, the values ranged between 200 and 220 µV/K and was around 235 µV/K at 107°C for 300 nm particles. Overall, the ball milling and hot pressing of the nanoparticles only showed a 5-8% decrease in the Seebeck coefficient value at 107 ° C.

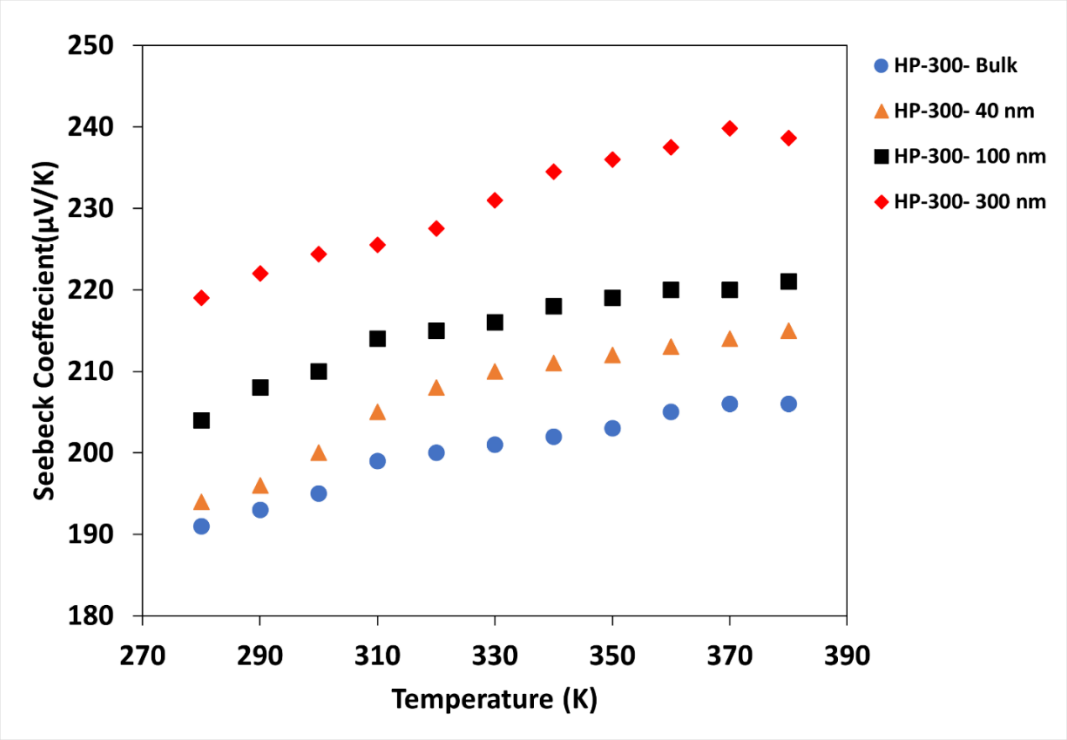

Figure 5.18. The Seebeck coefficient of the p- type bismuth telluride material as a function of measuring temperature. The pellets were hot pressed (HP) into 5 mm diameter pellets under nitrogen gas flow at 300°C.

The thermal conductivity and Seebeck coefficient of n-type bismuth telluride bulk and 40 nm particles hot pressed at 300°C are shown in Figure 5.19 and Figure 5.20. Due to a problem with the instrument at Cornel, the thermal conductivity and Seebeck coefficient values at 100 nm and 300 nm were not measured. The thermal conductivity of the selenium doped bulk n- type bismuth telluride ($Bi_{2.15}Te_{2.55}Se_{0.3}$) is 1.65 W/K m at room temperature[155]. A thermal

conductivity of 2.5 W/K m at 100°C has also been reported by Hegde et al. for the $Bi_2Te_{2.70}Se_{0.3}$ [156]. Thus, the thermal conductivity of the bulk $Bi_{2.15}Te_{2.55}Se_{0.3}$ hot pressed at 300°C was measured to be 2.15 W/K m at 27°C, rising to 2.45 W/K m at 107°C, which is consistent with the reported values of the n- type material. For the 40 nm particles, the value was 0.45 W/K m at 27°C and increased to 0.79 W/K m, which is nearly 3.2 times lower than the porous bulk material values obtained at 100°C. As a result, unlike the p-type counterparts, the thermal conductivity of the porous bulk n- type used showed no improvement. However, when compared to its p-type counterpart, the 40 nm n- type particles decreased more rapidly in thermal conductivity with increasing temperature. At 107°C, the thermal conductivity of the p- type 40 nm particles decreased 1.5 times compared to a 3 times reduction for the 40 nm n type nanoparticles.

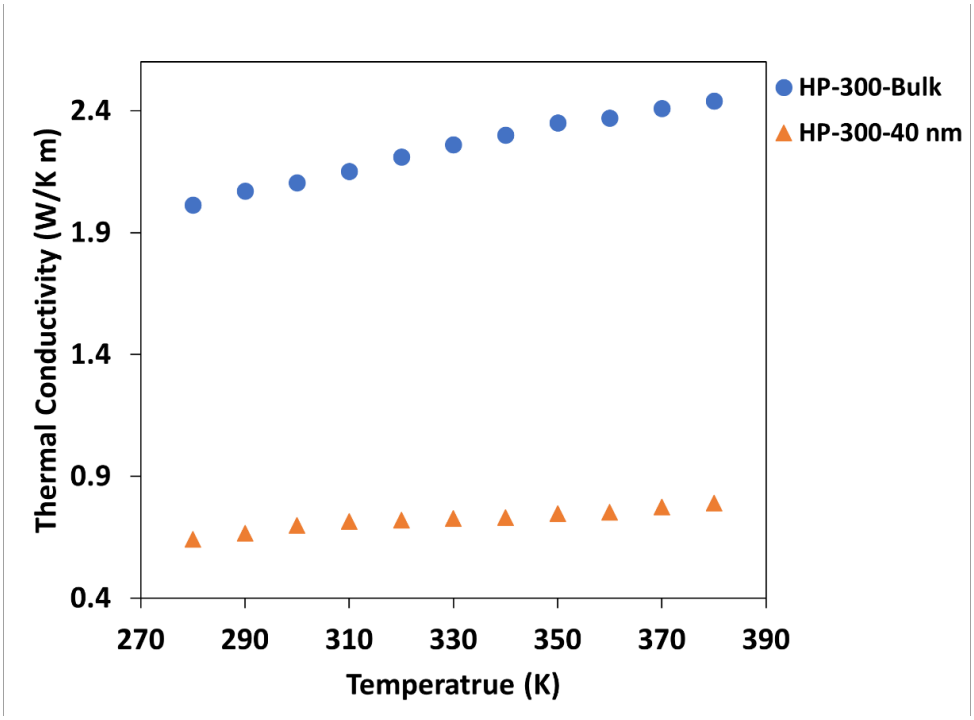

Figure 5.19. Thermal conductivity of the n type bismuth telluride material as a function of temperature. The pellets were hot pressed (HP) into 5 mm diameter pellets under nitrogen gas flow at 300°C.

Figure 5.20 shows the Seebeck coefficient of the porous bulk and 40 nm n type particles hot pressed at 300°C. The Seebeck value of the bulk material was -45 µV/K at 25°C and increased up to -52 µV/K at 107°C. For the 40 nm particles, it was -58 µV/K at 25°C and went up to -68 µV/K at 105°C The Seebeck coefficient value of the n type bismuth telluride material depends on the composition and level of selenium dopant present in the material[140]. Addition of selenium dopant increases the electron concentration of the n- type material, which in turn, increases the Seebeck coefficient value and contributes to the overall improvement of the ZT[157]. In this study, we have used $Bi_{2.15}Te_{2.55}Se_{0.3}$ (99.99%) as n- type material, which has a reported Seebeck coefficient of -60 to -80 µV/K at 100°C [140]. Thus, our porous bulk material showed a slight decrease in the Seebeck coefficient at 100°C, compared to the reported bulk values. The Seebeck coefficient value of the 40 nm particles were similar to reported bulk values at 100°C and performed better than the porous bulk materials hot pressed at 300°C (see Figure 5.20).

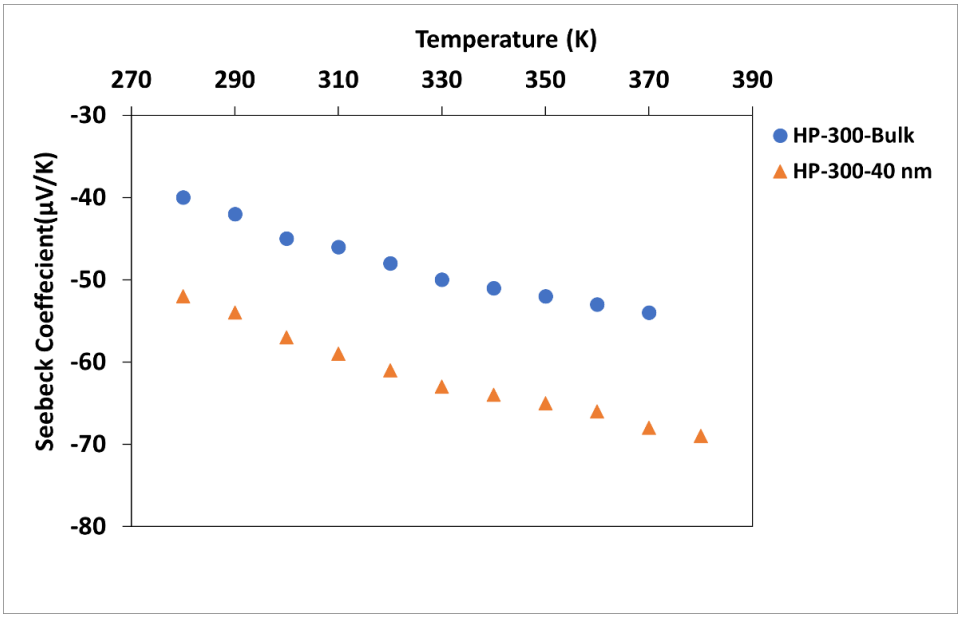

Figure 5.20. Seebeck coefficient of the n- type bismuth telluride material as a function of temperature. The pellets were hot pressed (HP) into 5 mm diameter pellets under nitrogen gas flow at 300°C.

5.3.2.3. Figure of merit, ZT

Figure 5.21 shows the ZT of the p- type porous bulk and nanoparticles hot pressed at 300°C. The ZT was calculated using the values obtained from Figure 5.14Figure 5.15,

Figure 5.17 and Figure 5.18. The bulk p- type hot pressed at 300°C had a ZT of 0.37 at 25°C and dropped to 0.34 at 105°C.

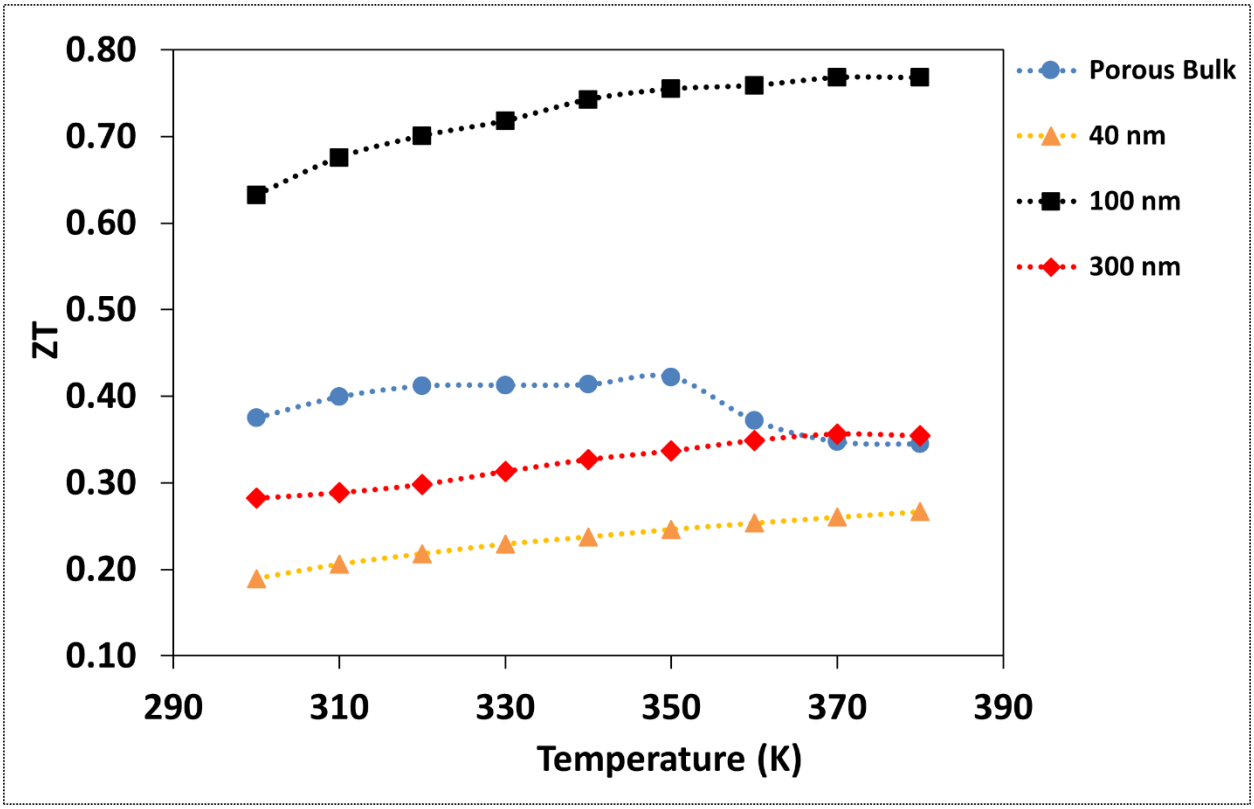

Figure 5.21. ZT of the p- type bismuth telluride hot pressed at 300°C as a function of measuring temperature.

This ZT value is much lower than the ZT value of bulk bismuth telluride material in the literature[154][153]. For example, p-type $Bi_{0.5}Sb_{1.5}Te_3$ synthesized by zone melting has a ZT of 1.0 at room temperature[158][159]. As our bulk material was hot pressed at a temperature well

below the melting point of bismuth telluride, whereas the reported ZT values are for material melted into a pellet and do not contain voids.

At 105°C, the ZT of the 40, 100, and 300 nm particles was 0.27, 0.77, and 0.35, respectively, as shown in Figure 5.21. The 100 nm particles showed the highest ZT value at 105°C and Figure 5.21 shows that the ZT value is increasing further with the increase of temperature. A peak ZT for p- type bismuth telluride is reported at 100-110°C for bulk material[154] and a similar trend is also observed for the nanostructured materials[117]. Above these temperatures, the ZT decreases. In our case, the ZT of the 100 nm particles is still about 23% lower than the reported ZT value of 1 for bulk bismuth telluride at 100°C. Even though we lowered the thermal conductivity of the 100 nm particles by a factor of 6.7 compared to the bulk material, the electrical resistivity of the 100 nm particles is almost 8 times higher than the reported bulk values at 100°C[153][154]. One interesting aspect is that the ZT appears to plateau above 100°C for our nanoparticulate materials, which differs from that reported for nonporous materials which peak and then decrease at or near this temperature. Since the goal is to work at temperatures of 200 to 300 C with engines, further studies at these higher temperatures are warranted. As a result, 100 nm particles appear to be a promising contender for device development in the future.

We also spent considerable time and effort on device fabrication, Peltier cooling, and Seebeck power generation. And these studies have been described in the dissertation of Dr. Travis Wallace. We also published an article on the method of a device fabrication and validation of the measuring of the Seebeck power output for individual p- and n- type couples of bismuth telluride. The article is provided in the Appendix to this thesis.

5.4. Conclusion

In this chapter, we have described a top-down approach of synthesizing different size of p- and n- type bismuth telluride nanoparticles with well-defined pore structures. The method involves ball milling the bulk material in presence of a cationic polymer PADAMAC. The cationic PADAMAC adsorbs on a freshly created surface generated during the ball milling and prevents reaggregation of the particles. By altering the concentration of the PADAMAC relative to the bismuth telluride, we were also able to control the size of the nanoparticles in the suspension. When hot pressed at temperatures of 300°C, the presence of pores scatters more thermal phonons, compared to their nonporous counterparts. A maximum thermal conductivity reduction of 6.7 times at 107°C was achieved for p-type 100 nm particles, compared to the reported bulk values at 100°C. However, the electrical conductivity of the pressed disks were 8 times lower, leading to an overall decrease in ZT. Nevertheless, we demonstrate that tuning the particle size and sintering temperature is a potential strategy in the development of TE materials.

CHAPTER 6: FUTURE WORK

The approach described in Chapters 2 and 3 use the standard molybdenum blue method to detect phosphate and arsenate in water. One possible extension of this work would be to use a different and much simpler method of detecting both phosphate and arsenate without using the complex molybdenum blue method. One straightforward approach would be to form phosphate and arsenate salts via a precipitation reaction using copper chloride instead of molybdenum blue, as shown in reactions 6.1 and 6.2.

$$2PO_4^{3-} + 3Cu^{2+} \rightarrow Cu_3(PO_4^{3-})_2 \downarrow \quad 6.1$$

$$2AsO_4^{3-} + 3Cu^{2+} \rightarrow Cu_3(AsO_4^{3-})_2 \downarrow \quad 6.2$$

The precipitate then can be captured on the membrane and IR spectra can be recorded through the membrane as shown in Figure 6.1.

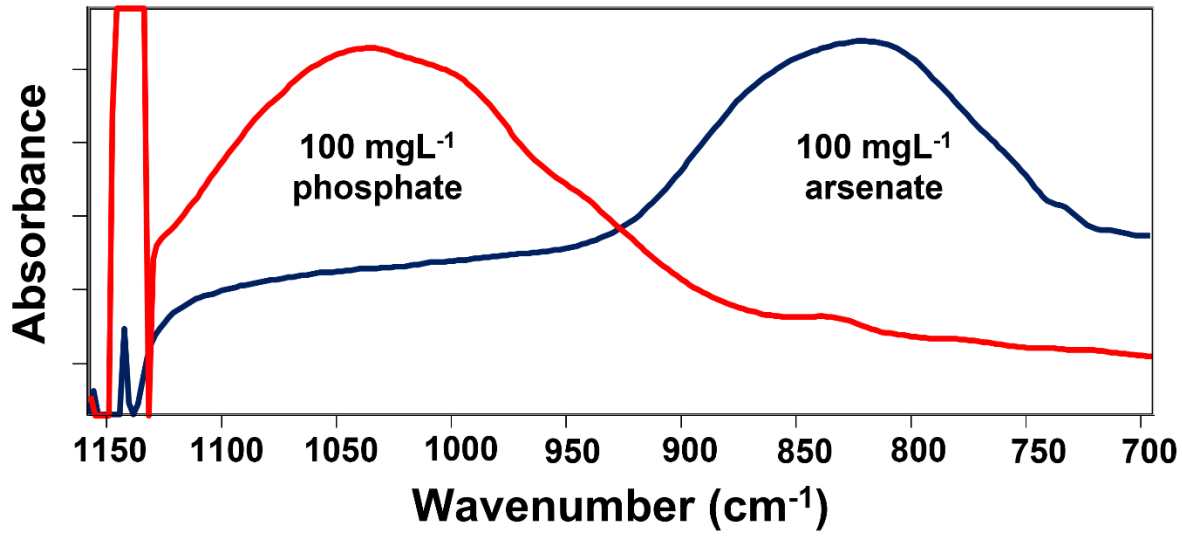

Figure 6.1. The IR spectra of copper phosphate and copper arsenate recorded directly through the membrane showing distinct stretching bands for P-O and As-O at different frequencies.

In Figure 6.1 The P-O and As-O produce bands at different wavenumbers. As a result, using the copper chloride precipitation reaction and the protocol described in Chapter 4, a method for detecting phosphate and arsenate could be developed. The advantage of using the salt formation method is that both the phosphate and arsenate IR bands can be observed in this method. This contrasts to the molybdenum blue and CTAB method described in Chapter 3, in which the P-O band is obscured due to the presence of strong Mo-O located around 1050 cm^{-1}. As a result, the amount of phosphate was measured indirectly using the combination of the visible and IR spectroscopy. We hypotheses that copper chloride method would be a more simpler approach where the amount of phosphate and arsenate both could be measured from the intensity of the IR bands as shown in Figure 6.1. The kinetics of the precipitation reaction to form the particles and methods to control the size of the particles in the suspension, as described in Chapter 4, would have to be developed for the copper chloride method.

The work described in Chapter 4 will be expanded in the future by performing a series of control experiments to confirm that the CN^- ions can be released from the WAD compounds by adding S^{2-} to the solution. Thus, DI water will be spiked with various concentrations of Cu^{2+}, Zn^{2+}, Ca^{2+}, and Ag^+. Then the solution will be spiked with 1-5 mgL^{-1} of CN^- so that the WAD cyanide compounds can form. Then 32-40 times Ag^+ will be added to the solution so that any fraction of unbound Free CN^- can form the AgCN precipitate in the solution. Then, in the same manner, a second solution will be prepared by adding the cations and spiking it with the same concentration CN- to form the WAD cyanide compounds. After that the solution will be further spiked with 10 mgL^{-1} S^{2-} so that CN- can be liberated from the WAD compounds. Then Ag^+ will be added to the

solution to form the AgCN particles. Thus, the equation 1 will be used to determine what fraction of WAD cyanide was released by the addition of the S^{2-} in the solution.

$$CN^{-}\ realeased\ (mg\ L^{-1}) = \ CN^{-}\ with\ S^{2-}spike(mg\ L^{-1}) - \ CN^{-}\ witohut\ S^{2-}(mg\ L^{-1}) \qquad 6.3$$

Multiple improvements are suggested for the work described in Chapter 5, which are listed below.

1. Longer period of ball milling (1-2 hours) to make nanoparticles with well-defined grain boundaries to further increase the thermal phonon scattering.

2. A robust hot-pressing system is required to avoid the crack formation on the nano pellets. Thus, for that reason a rectangular shaped dye should be built.

3. Hot press the nanoparticles at elevated temperatures (400 °C) to improve the electrical properties should be investigated.

4. Approaches to obtain more accurate electrical resistivity values for the p and n type nanoparticles are needed .

REFERENCES

[1] O. of G.W. and D.W. U.S. EPA, Method Development for Unregulated Contaminants in Drinking Water : Public Meeting and Webinar, (2018) 1–104.

[2] U.S. Environmental Protection Agency, Method 120 . 1 : Conductance (Specific Conductance , µmhos at 25°C) by Conductivity Meter, (1982).

[3] J.W. O'Dell, Determination of Turbidity By Nephelometry, Methods Determ. Met. Environ. Samples. (1996) 378–387. https://doi.org/10.1016/b978-0-8155-1398-8.50021-5.

[4] J.D. Pfaff, Determination of Inorganic Anions By Ion Chromatography, Methods Determ. Met. Environ. Samples. (1996) 388–417. https://doi.org/10.1016/b978-0-8155-1398-8.50022-7.

[5] Environmental Protection Agency, Method 1664B: n-Hexane Extractable Material and Silica Gel Treated n-Hexane Extractable Material by Extraction and Gravimetry, United States Environ. Prot. Agency. (2010).

[6] U.S. Environmental Protection Agency, Method 150.2: pH, Continuous Monitoring (Electrometric) by pH Meter, (1982) 2–6. www.epa.gov.

[7] EPA, Method 352.1: Nitrogen, nitrate (colorimetric, brucine) by spectrophotometer, Methods Chem. Anal. Water Wastes. (1983) 365–367.

[8] U.S.E.P. Agency, Measurement of Purgeable Organic Compounds in Water By, 0 (1995).

[9] USEPA, Method 525.2 Determination of Organic Compounds in Drinking Water by Liquid-Solid Extraction and Capillary Column Gas Chromatography / Mass Spectrometry Determination of Organic Compounds Rev 2.0, (1991) 60.

[10] V.N. Epov, I.E. Vasil'eva, V.I. Lozhkin, E.N. Epova, L.F. Paradina, A.N. Suturin, Determination of Macroelements in Baikal Water Using Inductively Coupled Plasma Mass Spectrometry, J. Anal. Chem. 54 (1999) 837–842.

[11] Determination of Trace Elements By Stabilized Temperature Graphite Furnace Atomic Absorption, Methods Determ. Met. Environ. Samples. (1996) 146–186. https://doi.org/10.1016/b978-0-8155-1398-8.50012-4.

[12] E.G. Roy, C. Jiang, M.L. Wells, C. Tripp, Determining Subnanomolar Iron Concentrations in Oceanic Seawater Using a Siderophore-Modified Film Analyzed by Infrared Spectroscopy, Anal. Chem. 80 (2008) 4689–4695. https://doi.org/10.1021/ac800356p.

[13] A. Chandrasoma, A.A.A. Hamid, A.E. Bruce, M.R.M. Bruce, C.P. Tripp, An infrared spectroscopic based method for mercury(II) detection in aqueous solutions., Anal. Chim. Acta. 728 (2012) 57–63. https://doi.org/10.1016/j.aca.2012.03.047.

[14] S.H. Saleh, C.P. Tripp, A Reagentless and Rapid Method to Measure Water Content in Oils,

Talanta. (2020) 121911. https://doi.org/10.1016/j.talanta.2020.121911.

[15] S.O. Procedure, Orono Spectral Solutions , Inc . for ASTM Method D7575 , Oil and Grease in Water, (2014) 1–20.

[16] S.H. Saleh, C.P. Tripp, Measurement of water concentration in oils using CaO powder and infrared spectroscopy, Talanta. 228 (2021) 122250. https://doi.org/10.1016/j.talanta.2021.122250.

[17] S.H. Saleh, C.P. Tripp, A new approach for measuring water concentration in oil using copper sulfate powder and infrared spectroscopy, Spectrochim. Acta Part A Mol. Biomol. Spectrosc. 262 (2021) 120107. https://doi.org/10.1016/j.saa.2021.120107.

[18] K.A. Bakeev, Process analytical technology: Spectroscopic tools and implementation strategies for the chemical and pharmaceutical industries, John Wiley & Sons, 2010.

[19] D.F. Swinehart, The Beer-Lambert law, J. Chem. Educ. 39 (1962) 333–335. https://doi.org/10.1021/ed039p333.

[20] D. Calloway, Beer-Lambert Law, J. Chem. Educ. 74 (1997) 744. https://doi.org/10.1021/ed074p744.3.

[21] A. Public, H. Association, APHA: Standard Methods for the Examination of Water and Wastewater, Am. Public Heal. Assoc. Water Work. Assoc. Environ. Fed. 552 (1998).

[22] L.J. Gimbert, P.M. Haygarth, P.J. Worsfold, Determination of nanomolar concentrations of phosphate in natural waters using flow injection with a long path length liquid waveguide capillary cell and solid-state spectrophotometric detection, Talanta. 71 (2007) 1624–1628. https://doi.org/10.1016/j.talanta.2006.07.044.

[23] S. Karadağ, E.M. Görüşük, E. Çetinkaya, S. Deveci, K.B. Dönmez, E. Uncuoğlu, M. Doğu, Development of an automated flow injection analysis system for determination of phosphate in nutrient solutions., J. Sci. Food Agric. 98 (2018) 3926–3934. https://doi.org/10.1002/jsfa.8911.

[24] D.L. Correll, The Role of Phosphorus in the Eutrophication of Receiving Waters: A Review, J. Environ. Qual. 27 (1998) 261–266. https://doi.org/10.2134/jeq1998.00472425002700020004x.

[25] J. Manuel, Nutrient pollution: A persistent threat to waterways, Environ. Health Perspect. 122 (2014) A304–A309. https://doi.org/10.1289/ehp.122-A304.

[26] P.M. Glibert, From hogs to HABs: Impacts of industrial farming in the US on nitrogen and phosphorus and greenhouse gas pollution, Biogeochemistry. 150 (2020) 139–180. https://doi.org/10.1007/s10533-020-00691-6.

[27] N.R. Nicomel, K. Leus, K. Folens, P. Van Der Voort, G. Du Laing, Technologies for Arsenic Removal from Water: Current Status and Future Perspectives, Int. J. Environ. Res. Public

Health. 13 (2015). https://doi.org/10.3390/ijerph13010062.

[28] R.N. Ratnaike, Acute and chronic arsenic toxicity, Postgrad. Med. J. 79 (2003) 391–396. https://doi.org/10.1136/pmj.79.933.391.

[29] H. Mochizuki, Arsenic Neurotoxicity in Humans, Int. J. Mol. Sci. 20 (2019) 3418. https://doi.org/10.3390/ijms20143418.

[30] T.S.Y. Choong, T.G. Chuah, Y. Robiah, F.L. Gregory Koay, I. Azni, Arsenic toxicity, health hazards and removal techniques from water: an overview, Desalination. 217 (2007) 139–166. https://doi.org/10.1016/j.desal.2007.01.015.

[31] G. Duffy, I. Maguire, B. Heery, C. Nwankire, J. Ducrée, F. Regan, PhosphaSense: A fully integrated, portable lab-on-a-disc device for phosphate determination in water, Sensors Actuators B Chem. 246 (2017) 1085–1091. https://doi.org/10.1016/j.snb.2016.12.040.

[32] D.M. Anderson, A.D. Cembella, G.M. Hallegraeff, Progress in understanding harmful algal blooms: paradigm shifts and new technologies for research, monitoring, and management., Ann. Rev. Mar. Sci. 4 (2012) 143–176. https://doi.org/10.1146/annurev-marine-120308-081121.

[33] B.L. Turner, M.J. Papházy, P.M. Haygarth, I.D. McKelvie, Inositol phosphates in the environment., Philos. Trans. R. Soc. London. Ser. B, Biol. Sci. 357 (2002) 449–469. https://doi.org/10.1098/rstb.2001.0837.

[34] H. Chen, L. Zhao, F. Yu, Q. Du, Detection of phosphorus species in water: Technology and strategies, Analyst. 144 (2019) 7130–7148. https://doi.org/10.1039/c9an01161g.

[35] K. Lin, J. Pei, P. Li, J. Ma, Q. Li, D. Yuan, Simultaneous determination of total dissolved nitrogen and total dissolved phosphorus in natural waters with an on-line UV and thermal digestion., Talanta. 185 (2018) 419–426. https://doi.org/10.1016/j.talanta.2018.03.085.

[36] P.J. Worsfold, L.J. Gimbert, U. Mankasingh, O.N. Omaka, G. Hanrahan, P.C.F.C. Gardolinski, P.M. Haygarth, B.L. Turner, M.J. Keith-Roach, I.D. McKelvie, Sampling, sample treatment and quality assurance issues for the determination of phosphorus species in natural waters and soils., Talanta. 66 (2005) 273–293. https://doi.org/10.1016/j.talanta.2004.09.006.

[37] P. Monbet, I.D. McKelvie, P.J. Worsfold, Dissolved organic phosphorus speciation in the waters of the Tamar estuary (SW England), Geochim. Cosmochim. Acta. 73 (2009) 1027–1038. https://doi.org/10.1016/j.gca.2008.11.024.

[38] P. Worsfold, I. McKelvie, P. Monbet, Determination of phosphorus in natural waters: A historical review, Anal. Chim. Acta. 918 (2016) 8–20. https://doi.org/10.1016/j.aca.2016.02.047.

[39] P.M. Haygarth, G.S. Bilotta, R. Bol, R.E. Brazier, P.J. Butler, J. Freer, L.J. Gimbert, S.J. Granger, T. Krueger, C.J.A. Macleod, P. Naden, G. Old, J.N. Quinton, B. Smith, P. Worsfold,

Processes affecting transfer of sediment and colloids, with associated phosphorus, from intensively farmed grasslands: an overview of key issues, Hydrol. Process. 20 (2006) 4407–4413. https://doi.org/10.1002/hyp.6598.

[40] S. Simon, H. Tran, F. Pannier, M. Potin-Gautier, Simultaneous determination of twelve inorganic and organic arsenic compounds by liquid chromatography–ultraviolet irradiation–hydride generation atomic fluorescence spectrometry, J. Chromatogr. A. 1024 (2004) 105–113. https://doi.org/10.1016/j.chroma.2003.09.068.

[41] P.L. Smedley, D.G. Kinniburgh, A review of the source, behaviour and distribution of arsenic in natural waters, Appl. Geochemistry. 17 (2002) 517–568. https://doi.org/10.1016/S0883-2927(02)00018-5.

[42] M. Pettine, M. Camusso, W. Martinotti, Dissolved and particulate transport of arsenic and chromium in the Po River (Italy), Sci. Total Environ. 119 (1992) 253–280. https://doi.org/10.1016/0048-9697(92)90268-W.

[43] P. Seyler, J.M. Martin, Distribution of arsenite and total dissolved arsenic in major French estuaries: Dependence on biogeochemical processes and anthropogenic inputs, Mar. Chem. 29 (1990) 277–294. https://doi.org/10.1016/0304-4203(90)90018-8.

[44] W.R. Cullen, K.J. Reimer, Arsenic speciation in the environment, Chem. Rev. 89 (1989) 713–764. https://doi.org/10.1021/cr00094a002.

[45] C. Neal, M. Neal, H. Wickham, Phosphate measurement in natural waters: two examples of analytical problems associated with silica interference using phosphomolybdic acid methodologies, Sci. Total Environ. 251–252 (2000) 511–522. https://doi.org/10.1016/S0048-9697(00)00402-2.

[46] L. Drummond, W. Maher, Determination of phosphorus in aqueous solution via formation of the phosphoantimonylmolybdenum blue complex Re-examination of optimum conditions for the analysis of phosphate., 2670 (1995). https://doi.org/10.1016/0003-2670(94)00429-P.

[47] J.W. O'Dell, Method 365.1 - Determination of phosphorus by semi-automated colorimetry., in: E.M.S. Laboratory (Ed.), Methods Determ. Met. Environ. Samples, William Andrew Publishing, Westwood, NJ, 1996: pp. 479–495. https://doi.org/10.1016/B978-0-8155-1398-8.50027-6.

[48] J. Murphy, J.P. Riley, A modified single solution method for the determination of phosphate in natural waters, Anal. Chim. Acta. 27 (1962) 31–36. https://doi.org/10.1016/S0003-2670(00)88444-5.

[49] E.A. Nagul, I.D. Mckelvie, P. Worsfold, S.D. Kolev, Analytica Chimica Acta The molybdenum blue reaction for the determination of orthophosphate revisited : Opening the black box, Anal. Chim. Acta. 890 (2015) 60–82. https://doi.org/10.1016/j.aca.2015.07.030.

[50] C.G. Bochet, T. Draper, B. Bocquet, M.T. Pope, A.F. Williams, 182Tungsten Mössbauer spectroscopy of heteropolytungstates, Dalt. Trans. (2009) 5127–5131. https://doi.org/10.1039/B904101J.

[51] A. Müller, E. Krickemeyer, J. Meyer, H. Bögge, F. Peters, W. Plass, E. Diemann, S. Dillinger, F. Nonnenbruch, M. Randerath, C. Menke, $[Mo_{154}(NO)_{14}O_{420}(OH)_{28}(H2O)_{70}]^{(25 \pm 5)-}$: A Water-Soluble Big Wheel with More than 700 Atoms and a Relative Molecular Mass of About 24000, Angew. Chemie Int. Ed. English. 34 (1995) 2122–2124. https://doi.org/10.1002/anie.199521221.

[52] K. Murata, S. Ikeda, Studies on polynuclear molybdates in the aqueous solution by laser Raman spectroscopy, Spectrochim. Acta Part A Mol. Spectrosc. 39 (1983) 787–794. https://doi.org/10.1016/0584-8539(83)80018-X.

[53] I.D. Mckelvie, D.M.W. Peat, P.J. Worsfold, Techniques for the Quantification and Speciation of Phosphorus in Natural-Waters, Anal. Proc. 32 (1995) 437–445. https://doi.org/Doi 10.1039/Ai9953200437.

[54] J.F. KEGGIN, Structure of the Molecule of 12-Phosphotungstic Acid, Nature. 131 (1933) 908–909. https://doi.org/10.1038/131908b0.

[55] A.Y. El-Sayed, Y.Z. Hussein, M.A. Mohammed, Simultaneous determination of phosphate and silicate in detergents and waters by first-derivative spectrophotometry, Analyst. 126 (2001) 1810–1815. https://doi.org/10.1039/B103159G.

[56] T. Fontaine, Spectrophotometric Determination of Phosphorus, Ind. Eng. Chem. Anal. Ed. 14 (1942) 77–78. https://doi.org/10.1021/i560101a038.

[57] V.W. Truesdale, C.J. Smith, P.J. Smith, Transformation and decomposition of β-molybdosilicic acid, Analyst. 102 (1977) 73–85. https://doi.org/10.1039/AN9770200073.

[58] A. Sjösten, S. Blomqvist, Influence of phosphate concentration and reaction temperature when using the molybdenum blue method for determination of phosphate in water, Water Res. 31 (1997) 1818–1823. https://doi.org/10.1016/S0043-1354(96)00367-3.

[59] American Public Health Association (APHA), standard method for examination of water and wastewater, American Public Health Association (APHA), Washington, DC, 23rd edition, 2017, pp. 4500-P–4-164.

[60] S. Asaoka, Y. Kiso, T. Oomori, H. Okamura, T. Yamada, M. Nagai, An online solid phase extraction method for the determination of ultratrace level phosphate in water with a high performance liquid chromatograph, Chem. Geol. 380 (2014) 41–47. https://doi.org/10.1016/j.chemgeo.2014.04.025.

[61] 3500-As ARSENIC (2017), in: Stand. Methods Exam. Water Wastewater, American Public Health Association, 2018. https://doi.org/doi:10.2105/SMWW.2882.051.

[62] APHA, AWWA, WEF, 3120 B. Iductively Coupled Plasma (ICP) Method, Stand. Methods

Exam. Water Wastewater, Am. Public Heal. Assoc. (2017) 1–5.

[63] D.L. Johnson, Simultaneous determination of arsenate and phosphate in natural waters, Environ. Sci. Technol. 5 (1971) 411–414. https://doi.org/10.1021/es60052a005.

[64] S. Tsang, F. Phu, M.M. Baum, G.A. Poskrebyshev, Determination of phosphate/arsenate by a modified molybdenum blue method and reduction of arsenate by $S_2O_4^{2-}$, Talanta. 71 (2007) 1560–1568. https://doi.org/10.1016/j.talanta.2006.07.043.

[65] S. Taguchi, E. Ito-Oka, K. Masuyama, I. Kasahara, K. Goto, Application of organic solvent-soluble membrane filters in the preconcentration and determination of trace elements: spectrophotometric determination of phosphorus as phosphomolybdenum blue, Talanta. 32 (1985) 391–394. https://doi.org/10.1016/0039-9140(85)80104-1.

[66] C. Matsubara, Y. Yamamoto, K. Takamura, Rapid determination of trace amounts of phosphate and arsenate in water by spectrophotometric detection of their heteropoly acid-malachite green aggregates following pre-concentration by membrane filtration, Analyst. 112 (1987) 1257–1260. https://doi.org/10.1039/AN9871201257.

[67] T. Okazaki, W. Wang, H. Kuramitz, N. Hata, S. Taguchi, Molybdenum blue spectrophotometry for trace arsenic in ground water using a soluble membrane filter and calcium carbonate column, Anal. Sci. 29 (2013) 67–72. https://doi.org/10.2116/analsci.29.67.

[68] S. Asaoka, Y. Kiso, H. Okamura, Analytical Methods A membrane extraction method for trace level, Anal. Methods. 7 (2015) 9268–9273. https://doi.org/10.1039/C5AY02019K.

[69] J.A. Brisbin, Cyanide Clarification of Free and Total Cyanide Analysis for Safe Drinking Water Act (SDWA) Compliance, Revision 1.0, (2020).

[70] T.H.E. Council, O.F. The, E. Union, Council Directive 98/83/EC of 3 November 1998 on the quality of water intended for human consumption, Doc. Eur. Community Environ. Law. (2010) 865–878. https://doi.org/10.1017/cbo9780511610851.055.

[71] C.D. 2003/40/EC, Establishing the list, concentration limits and labelling requirements for the constituents of natural mineral waters and the conditions for using ozone-enriched air for the treatment of natural mineral waters and spring waters, L 126/34 EN Off. J. Eur. Union. 2 (2003) 34–39.

[72] Y. Sayato, WHO Guidelines for Drinking-Water Quality, Eisei Kagaku. 35 (1989) 307–312. https://doi.org/10.1248/jhs1956.35.307.

[73] EPA, EPA Ambient Water Quality Criteria for Endosulfan, (1980).

[74] A.A. Salkowski, D.G. Penney, Cyanide poisoning in animals and humans: A review, Vet. Hum. Toxicol. 36 (1994) 455–466. http://europepmc.org/abstract/MED/7839575.

[75] J.W. O 'Dell, Method 335.4 Determination of Total Cyanide By Semi-Automated

Colorimetry Determination of Total Cyanide By Semi-Automated Colorimetry, Environ. Monit. Syst. Lab. Off. Res. Dev. U.S. Environ. Prot. Agency. 1 (1993) 1–16.

[76] R.J. Diaz, R. Rosenberg, Spreading Dead Zones and Consequences for Marine Ecosystems, Science (80). 321 (2008) 926 LP – 929. https://doi.org/10.1126/science.1156401.

[77] J.L. Barringer, P.A. Reilly, Arsenic in groundwater: a summary of sources and the biogeochemical and hydrogeologic factors affecting arsenic occurrence and mobility, in: P.M. Bradley (Ed.), Curr. Perspect. Contam. Hydrol. Water Resour. Sustain., InTech, Rijeka, Croatia, 2013: pp. 83–116. https://doi.org/10.5772/55354.

[78] A. Gomez-Caminero, P.D. Howe, M. Hughes, E. Kenyon, D.R. Lewis, M. Moore, A. Aitio, G.C. Becking, J. Ng, I.P. on C. Safety, W.H.O.T.G. on E.H.C. for A. and A. Compounds, Arsenic and arsenic compounds, (2001). https://apps.who.int/iris/handle/10665/42366.

[79] N. US EPA, OCSPP, OPPT, Chemical Contaminant Rules _ Drinking Water Requirements for States and Public Water Systems _ US EPA, (2016) 1–6.

[80] H. Katano, T. Ueda, Spectrophotometric determination of phosphate anion based on the formation of molybdophosphate in ethylene glycol-water mixed solution, Anal. Sci. 27 (2011) 1043–1047. https://doi.org/10.2116/analsci.27.1043.

[81] A. Najafi, M. Hashemi, Vortex-assisted supramolecular solvent microextraction based on solidification of floating drop for preconcentration and speciation of inorganic arsenic species in water samples by molybdenum blue method, Microchem. J. 150 (2019) 104102. https://doi.org/10.1016/j.microc.2019.104102.

[82] Nayeem K. Ibnul, Carl P. Tripp, A solventless method for detecting trace level phosphate and arsenate in water using a transparent membrane and visible spectroscopy, Talanta. (2021) 122023. https://doi.org/10.1016/j.talanta.2020.122023.

[83] D.A. Links, B. Botar, A. Ellern, Mapping the formation areas of giant molybdenum blue clusters : a spectroscopic study, (2012)8951–8959. https://doi.org/10.1039/c2dt30661a.

[84] P. Gouzerh, M. Che, From Scheele and Berzelius to Müller: Polyoxometalates (POMs) revisited and the “missing link” between the bottom up and top down approaches, Actual. Chim. (2006) 9–22.

[85] M. Hatta, C.I. Measures, J. (Jarda) Ruzicka, Determination of traces of phosphate in sea water automated by programmable flow injection: Surfactant enhancement of the phosphomolybdenum blue response, Talanta. 191 (2019) 333–341. https://doi.org/10.1016/j.talanta.2018.08.045.

[86] L. Borgnino, V. Pfaffen, P.J. Depetris, M. Palomeque, Continuous flow method for the simultaneous determination of phosphate/arsenate based on their different kinetic characteristics, Talanta. 85 (2011) 1310–1316. https://doi.org/10.1016/j.talanta.2011.06.001.

[87] K. Morita, E. Kaneko, Spectrophotometric Determination of Trace Arsenic in Water Samples Using a Nanoparticle of Ethyl Violet with a Molybdate−Iodine Tetrachloride Complex as a Probe for Molybdoarsenate, Anal. Chem. 78 (2006) 7682–7688. https://doi.org/10.1021/ac061074h.

[88] D.L. Johnson, M.E.Q. Pilson, Spectrophotometric determination of arsenite, arsenate, and phosphate in natural waters, Anal. Chim. Acta. 58 (1972) 289–299. https://doi.org/10.1016/S0003-2670(72)80005-9.

[89] T. Okazaki, H. Kuramitz, N. Hata, S. Taguchi, K. Murai, K. Okauchi, Visual colorimetry for determination of trace arsenic in groundwater based on improved molybdenum blue spectrophotometry, Anal. Methods. 7 (2015) 2794–2799. https://doi.org/10.1039/C4AY03021D.

[90] R.B. Viana, A.B.F. da Silva, A.S. Pimentel, Infrared Spectroscopy of Anionic, Cationic, and Zwitterionic Surfactants, Adv. Phys. Chem. 2012 (2012) 903272. https://doi.org/10.1155/2012/903272.

[91] A.J. Bridgeman, Computational study of the vibrational spectra of α- and β-Keggin, Chem. - A Eur. J. 10 (2004) 2935–2941. https://doi.org/10.1002/chem.200305781.

[92] J. Tofan-Lazar, H.A. Al-Abadleh, Kinetic ATR-FTIR studies on phosphate adsorption on iron (Oxyhydr)oxides in the absence and presence of surface arsenic: Molecular-level insights into the Ligand exchange mechanism, J. Phys. Chem. A. 116 (2012) 10143–10149. https://doi.org/10.1021/jp308913j.

[93] D.R. Scheuing, J.G. Weers, A Fourier transform infrared spectroscopic study of dodecyltrimethylammonium chloride/sodium dodecyl sulfate surfactant mixtures, Langmuir. 6 (1990) 665–671. https://doi.org/10.1021/la00093a023.

[94] D.R. Scheuing, Fourier Transform Infrared Spectroscopy in Colloid and Interface Science, in: Fourier Transform Infrared Spectrosc. Colloid Interface Sci. American Chemical Society, 1990. https://doi.org/doi:10.1021/bk-1990-0447.ch001.

[95] C. Jiang, A. Gamarnik, C.P. Tripp, Identification of Lipid Aggregate Structures on TiO2 Surface Using Headgroup IR Bands, J. Phys. Chem. B. 109 (2005) 4539–4544. https://doi.org/10.1021/jp046042h.

[96] A. Redman, R. Santore, Bioavailability of cyanide and metal–cyanide mixtures to aquatic life, Environ. Toxicol. Chem. 31 (2012) 1774–1780. https://doi.org/10.1002/etc.1906.

[97] J.O. Egekeze, F.W. Oehme, Cyanides and their toxicity: A literature review, Vet. Q. 2 (1980) 104–114. https://doi.org/10.1080/01652176.1980.9693766.

[98] C.A. Young, T.S. Jordan, Cyanide remediation: current and past technologies, (1995) 104–129.

[99] P.L. Breuer, M.I. Jeffrey, D.M. Hewitt, Mechanisms of sulfide ion oxidation during

cyanidation. Part I: The effect of lead(II) ions, Miner. Eng. 21 (2008) 579–586. https://doi.org/10.1016/j.mineng.2007.11.010.

[100] R. Eisler, S.N. Wiemeyer, Cyanide hazards to plants and animals from gold mining and related water issues, Rev. Environ. Contam. Toxicol. (2004) 21–54.

[101] C.A. Johnson, The fate of cyanide in leach wastes at gold mines: An environmental perspective, Appl. Geochemistry. 57 (2015) 194–205.

[102] N. Kuyucak, A. Akcil, Cyanide and removal options from effluents in gold mining and metallurgical processes, Miner. Eng. 50–51 (2013) 13–29. https://doi.org/10.1016/j.mineng.2013.05.027.

[103] APHA, APHA Method 4500-CL: Standard Methods for the Examination of Water and Wastewater, 552 (1992).

[104] L.S. Bark, H.G. Higson, A review of the methods available for the detection and determination of small amounts of cyanide, Analyst. 88 (1963) 751–760. https://doi.org/10.1039/AN9638800751.

[105] H.B. Singh, N. Wasi, M.C. Mehra, Detection and Determination of Cyanide—A Review, Int. J. Environ. Anal. Chem. 26 (1986) 115–136. https://doi.org/10.1080/03067318608077109.

[106] J. Ma, P.K. Dasgupta, Recent developments in cyanide detection: A review, Anal. Chim. Acta. 673 (2010) 117–125. https://doi.org/10.1016/j.aca.2010.05.042.

[107] A. Method, W.A. Dissociable, W.A. Dissociable, A. Codes, W.A. Dissociable, M. Summary, Analysis of Cyanide (Total, Weak Acid Dissociable, and Free) - PBM, Inorganics (DRAFT). 2017 (2017).

[108] P.L. Breuer, C.A. Sutcliffe, R.L. Meakin, Cyanide measurement by silver nitrate titration: Comparison of rhodanine and potentiometric end-points, Hydrometallurgy. 106 (2011) 135–140. https://doi.org/10.1016/j.hydromet.2010.12.008.

[109] N.K. Ibnul, C.P. Tripp, A simple solution to the problem of selective detection of phosphate and arsenate by the molybdenum blue method, Talanta. (2021) 123043. https://doi.org/10.1016/j.talanta.2021.123043.

[110] T.P. Mokone, R.P. van Hille, A.E. Lewis, Effect of solution chemistry on particle characteristics during metal sulfide precipitation, J. Colloid Interface Sci. 351 (2010) 10–18. https://doi.org/10.1016/j.jcis.2010.06.027.

[111] A.H. Nielsen, T. Hvitved-Jacobsen, J. Vollertsen, Effects of pH and iron concentrations on sulfide precipitation in wastewater collection systems., Water Environ. Res. a Res. Publ. Water Environ. Fed. 80 (2008) 380–384. https://doi.org/10.2175/106143007x221328.

[112] P.A. Finn, C. Asker, K. Wan, E. Bilotti, O. Fenwick, C.B. Nielsen, Thermoelectric Materials:

Current Status and Future Challenges, Front. Electron. Mater. 1 (2021). https://doi.org/10.3389/femat.2021.677845.

[113] E. Stiller, March06.intro, 31 (2010) 1–42. papers2://publication/uuid/404677AC-FC6C-4F43-8A36-3280346ED166.

[114] C. Candolfi, S. El Oualid, D. Ibrahim, S. Misra, O. El Hamouli, A. Léon, A. Dauscher, P. Masschelein, P. Gall, P. Gougeon, C. Semprimoschnig, B. Lenoir, Thermoelectric materials for space applications, CEAS Sp. J. 13 (2021) 325–340. https://doi.org/10.1007/s12567-021-00351-x.

[115] Z. Soleimani, S. Zoras, B. Ceranic, S. Shahzad, Y. Cui, A review on recent developments of thermoelectric materials for room-temperature applications, Sustain. Energy Technol. Assessments. 37 (2020) 100604. https://doi.org/10.1016/j.seta.2019.100604.

[116] D. Zhao, G. Tan, A review of thermoelectric cooling: Materials, modeling and applications, Appl. Therm. Eng. 66 (2014) 15–24. https://doi.org/10.1016/j.applthermaleng.2014.01.074.

[117] H.J. Goldsmid, Bismuth Telluride and Its Alloys as Materials for Thermoelectric Generation, Mater. (Basel, Switzerland). 7 (2014) 2577–2592. https://doi.org/10.3390/ma7042577.

[118] Y. Zhang, Y.-J. Heo, M. Park, S.-J. Park, Recent Advances in Organic Thermoelectric Materials: Principle Mechanisms and Emerging Carbon-Based Green Energy Materials, Polym. . 11 (2019). https://doi.org/10.3390/polym11010167.

[119] S. Twaha, J. Zhu, Y. Yan, B. Li, A comprehensive review of thermoelectric technology: Materials, applications, modelling and performance improvement, Renew. Sustain. Energy Rev. 65 (2016) 698–726. https://doi.org/10.1016/j.rser.2016.07.034.

[120] G.J. Snyder, T.S. Ursell, Thermoelectric efficiency and compatibility, Phys. Rev. Lett. 91 (2003) 148301/1-148301/4. https://doi.org/10.1103/PhysRevLett.91.148301.

[121] M. Culebras, B. Uriol, C.M. Gómez, A. Cantarero, Controlling the thermoelectric properties of polymers: application to PEDOT and polypyrrole, Phys. Chem. Chem. Phys. 17 (2015) 15140–15145. https://doi.org/10.1039/C5CP01940K.

[122] S. D Patil, K. Devade, Review on Thermoelectric Refrigeration: Applications and Technology, Int. J. Mod. Trends Eng. Res. 2 (2015) 119–129.

[123] H.L. Ni, T.J. Zhu, X.B. Zhao, Thermoelectric properties of hydrothermally synthesized and hot pressed n-type Bi_2Te_3 alloys with different contents of Te, Mater. Sci. Eng. B. 117 (2005) 119–122. https://doi.org/10.1016/j.mseb.2004.11.001.

[124] Devender, P. Gehring, A. Gaul, A. Hoyer, K. Vaklinova, R.J. Mehta, M. Burghard, T. Borca-Tasciuc, D.J. Singh, K. Kern, G. Ramanath, Harnessing Topological Band Effects in Bismuth Telluride Selenide for Large Enhancements in Thermoelectric Properties through

Isovalent Doping, Adv. Mater. 28 (2016) 6436–6441. https://doi.org/10.1002/adma.201601256.

[125] Y.C. Dou, X.Y. Qin, D. Li, L.L. Li, T.H. Zou, Q.Q. Wang, Enhanced thermopower and thermoelectric performance through energy filtering of carriers in $(Bi_2Te_3)_{0.2}(Sb_2Te_3)_{0.8}$ bulk alloy embedded with amorphous SiO_2 nanoparticles, J. Appl. Phys. 114 (2013) 44906. https://doi.org/10.1063/1.4817074.

[126] F. Serrano-Sánchez, M. Gharsallah, N.M. Nemes, N. Biskup, M. Varela, J.L. Martínez, M.T. Fernández-Díaz, J.A. Alonso, Enhanced figure of merit in nanostructured $(Bi,Sb)_2Te_3$ with optimized composition, prepared by a straightforward arc-melting procedure, Sci. Rep. 7 (2017) 6277. https://doi.org/10.1038/s41598-017-05428-4.

[127] V. Stavila, D.B. Robinson, M.A. Hekmaty, R. Nishimoto, D.L. Medlin, S. Zhu, T.M. Tritt, P.A. Sharma, Wet-Chemical Synthesis and Consolidation of Stoichiometric Bismuth Telluride Nanoparticles for Improving the Thermoelectric Figure-of-Merit, ACS Appl. Mater. Interfaces. 5 (2013) 6678–6686. https://doi.org/10.1021/am401444w.

[128] H.J. Goldsmid, Improving the thermoelectric Figure of merit, Sci. Technol. Adv. Mater. 22 (2021) 280–284. https://doi.org/10.1080/14686996.2021.1903816.

[129] L.-P. Hu, T.-J. Zhu, Y.-G. Wang, H.-H. Xie, Z.-J. Xu, X.-B. Zhao, Shifting up the optimum figure of merit of p-type bismuth telluride-based thermoelectric materials for power generation by suppressing intrinsic conduction, NPG Asia Mater. 6 (2014) e88–e88. https://doi.org/10.1038/am.2013.86.

[130] A.J. Minnich, M.S. Dresselhaus, Z.F. Ren, G. Chen, Bulk nanostructured thermoelectric materials : current research and future prospects, (2009) 466–479. https://doi.org/10.1039/b822664b.

[131] S.K. Bux, J.-P. Fleurial, R.B. Kaner, Nanostructured materials for thermoelectric applications, Chem. Commun. 46 (2010) 8311–8324. https://doi.org/10.1039/C0CC02627A.

[132] J.R. Szczech, J.M. Higgins, S. Jin, Enhancement of the thermoelectric properties in nanoscale and nanostructured materials, J. Mater. Chem. 21 (2011) 4037–4055. https://doi.org/10.1039/C0JM02755C.

[133] M.S. Dresselhaus, G. Chen, M.Y. Tang, R.G. Yang, H. Lee, D.Z. Wang, Z.F. Ren, J.-P. Fleurial, P. Gogna, New Directions for Low-Dimensional Thermoelectric Materials, Adv. Mater. 19 (2007) 1043–1053. https://doi.org/10.1002/adma.200600527.

[134] B. Poudel, Q. Hao, Y. Ma, Y. Lan, A. Minnich, B. Yu, X. Yan, D. Wang, A. Muto, D. Vashaee, X. Chen, J. Liu, M.S. Dresselhaus, G. Chen, Z. Ren, High-thermoelectric performance of nanostructured bismuth antimony telluride bulk alloys., Science. 320 (2008) 634–638. https://doi.org/10.1126/science.1156446.

[135] L. Yang, Z.-G. Chen, M. Hong, G. Han, J. Zou, Enhanced Thermoelectric Performance of Nanostructured Bi_2Te_3 through Significant Phonon Scattering, ACS Appl. Mater. Interfaces. 7 (2015) 23694–23699. https://doi.org/10.1021/acsami.5b07596.

[136] R.R. Urkude, P.T. Patil, S.B. Kondawar, U.A. Palikundwar, Synthesis, Characterization and Electrical Properties of a Composite of Topological Insulating Material: Bi_2Te_3-PANI, Procedia Mater. Sci. 10 (2015) 205–211. https://doi.org/https://doi.org/10.1016/j.mspro.2015.06.042.

[137] S. Wang, H. Li, R. Lu, G. Zheng, X. Tang, Metal nanoparticle decorated n-type Bi_2Te_3-based materials with enhanced thermoelectric performances, Nanotechnology. 24 (2013) 285702. https://doi.org/10.1088/0957-4484/24/28/285702.

[138] C. Kim, D.H. Kim, Y.S. Han, J.S. Chung, S. Park, H. Kim, Fabrication of bismuth telluride nanoparticles using a chemical synthetic process and their thermoelectric evaluations, Powder Technol. 214 (2011) 463–468. https://doi.org/10.1016/j.powtec.2011.08.049.

[139] G. Schierning, A review on bismuth telluride (Bi_2Te_3) nanostructure for thermoelectric applications Related papers, (n.d.).

[140] A. Nozariasbmarz, J.S. Krasinski, D. Vashaee, N-Type Bismuth Telluride Nanocomposite Materials Optimization for Thermoelectric Generators in Wearable Applications, Materials (Basel). 12 (2019). https://doi.org/10.3390/ma12091529.

[141] W.-T. Chiu, C.-L. Chen, Y.-Y. Chen, A strategy to optimize the thermoelectric performance in a spark plasma sintering process, Sci. Rep. 6 (2016) 23143. https://doi.org/10.1038/srep23143.

[142] Z. Zhang, P.A. Sharma, E.J. Lavernia, N. Yang, Thermoelectric and transport properties of nanostructured Bi2Te3 by spark plasma sintering, J. Mater. Res. 26 (2011) 475–484. https://doi.org/DOI: 10.1557/jmr.2010.67.

[143] P. Srivastava, K. Singh, Structural and thermal properties of chemically synthesized Bi_2Te_3 nanoparticles, J. Therm. Anal. Calorim. J Therm Anal Calorim. 110 (2012) 523–527. https://doi.org/10.1007/s10973-012-2553-6.

[144] S. Wang, H. Li, R. Lu, G. Zheng, X. Tang, Metal nanoparticle decorated n-type Bismuth telluride based materials with enhanced thermoelectric performances, Nanotechnology. 24 (2013) 285702. https://doi.org/10.1088/0957-4484/24/28/285702.

[145] M.K. Keshavarz, D. Vasilevskiy, R.A. Masut, S. Turenne, P-type bismuth telluride-based composite thermoelectric materials produced by mechanical alloying and hot extrusion, J. Electron. Mater. 42 (2013) 1429–1435. https://doi.org/10.1007/s11664-012-2284-2.

[146] J.Y. Yang, X.A. Fan, R.G. Chen, W. Zhu, S.Q. Bao, X.K. Duan, Consolidation and thermoelectric properties of n-type bismuth telluride based materials by mechanical alloying and hot pressing, J. Alloys Compd. 416 (2006) 270–273.

https://doi.org/10.1016/j.jallcom.2005.08.054.

[147] F.M. El-Makaty, H.K. Ahmed, K.M. Youssef, Review: The effect of different nanofiller materials on the thermoelectric behavior of bismuth telluride, Mater. Des. 209 (2021) 109974. https://doi.org/10.1016/j.matdes.2021.109974.

[148] W. Xie, J. He, H.J. Kang, X. Tang, S. Zhu, M. Laver, S. Wang, J.R.D. Copley, C.M. Brown, Q. Zhang, T.M. Tritt, Identifying the Specific Nanostructures Responsible for the High Thermoelectric Performance of (Bi,Sb)2Te3 Nanocomposites, Nano Lett. 10 (2010) 3283–3289. https://doi.org/10.1021/nl100804a.

[149] W. Xie, X. Tang, Y. Yan, Q. Zhang, T.M. Tritt, High thermoelectric performance BiSbTe alloy with unique low-dimensional structure, J. Appl. Phys. 105 (2009) 113713. https://doi.org/10.1063/1.3143104.

[150] N. American, E. Control, R. Emissions, Designation of North American Emission Control Area to Reduce Emissions from Ships, US Environ. Prot. Agency. (2010).

[151] J.J. Winebrake, J.J. Corbett, E.H. Green, A. Lauer, V. Eyring, Mitigating the Health Impacts of Pollution from Oceangoing Shipping: An Assessment of Low-Sulfur Fuel Mandates, Environ. Sci. Technol. 43 (2009) 4776–4782. https://doi.org/10.1021/es803224q.

[152] J. Hierrezuelo, A. Sadeghpour, I. Szilagyi, A. Vaccaro, M. Borkovec, Electrostatic Stabilization of Charged Colloidal Particles with Adsorbed Polyelectrolytes of Opposite Charge, Langmuir. 26 (2010) 15109–15111. https://doi.org/10.1021/la102912u.

[153] H. Wang, International Round-Robin on Transport Properties of Bismuth Telluride, (2011) 1–19.

[154] K.R. Reyes-Gil, J. Whaley, R. Nishimoto, N. Yang, Development of transport properties characterization capabilities for thermoelectric materials and modules, Mater. Res. Soc. Symp. Proc. 1774 (2015) 7–12. https://doi.org/10.1557/opl.2015.578.

[155] X. Yan, B. Poudel, Y. Ma, W.S. Liu, G. Joshi, H. Wang, Y. Lan, D. Wang, G. Chen, Z.F. Ren, Experimental studies on anisotropic thermoelectric properties and structures of n-type $Bi_2Te_{2.7}Se_{0.3}$, Nano Lett. 10 (2010) 3373–3378. https://doi.org/10.1021/nl101156v.

[156] G.S. Hegde, A.N. Prabhu, R.Y. Huang, Y.K. Kuo, Reduction in thermal conductivity and electrical resistivity of indium and tellurium co-doped bismuth selenide thermoelectric system, J. Mater. Sci. Mater. Electron. 31 (2020) 19511–19525. https://doi.org/10.1007/s10854-020-04383-7.

[157] L. Hu, T. Zhu, X. Liu, X. Zhao, Point Defect Engineering of High-Performance Bismuth-Telluride-Based Thermoelectric Materials, Adv. Funct. Mater. 24 (2014) 5211–5218. https://doi.org/10.1002/adfm.201400474.

[158] W.M. Yim, F.D. Rosi, Compound tellurides and their alloys for peltier cooling—A review, Solid. State. Electron. 15 (1972) 1121–1140. https://doi.org/10.1016/0038-

1101(72)90172-4.

[159] L.D. Ivanova, Y. V Granatkina, Thermoelectric properties of Bi_2Te_3-Sb_2Te_3 single crystals in the range 100–700 K, Inorg. Mater. 36 (2000) 672–677. https://doi.org/10.1007/BF02758419.

APPENDIX: LOW-COST SEEBECK POWER MEASUREMENT SYSTEM FOR CHARACTERIZATION OF THERMOELECTRIC JUNCTIONS AND MODULES

Travis T. Wallace [a] *, Nayeem K. Ibnul [b], Robert J. Lad [b], Carl P. Tripp [b]

[a]*Marine Engine Testing and Emissions Lab, Maine Maritime Academy, Castine, ME, USA*

[b]*Frontier Institute for Research in Sensor Technologies (FIRST), University of Maine, Orono, ME, USA*

A.1. Abstract

Development of thermoelectric materials and devices requires performance testing to assess improvements as compared against known control samples. Traditionally, this has been done by measuring the figure of merit. However, another important parameter for materials evaluation is the power output of a single P-N junction pair, typically performed by applying current to the circuit and measuring the Peltier temperature difference output. This approach often leads to errors due to contact resistive heating across interfaces within a device. An alternative approach is to evaluate a thermoelectric couple as a Seebeck generator that requires expensive meters ($20 k-$30 k) to measure milli-volt and milli-amp outputs. In order to enable materials evaluation without the need to use full device modules that are costly and time intensive to fabricate and test, this paper describes the development of low-cost (~$200) measurement circuit and shows data that validates the milli-volt and milli-amp outputs from a single thermoelectric couple.

A.2. Introduction

Thermoelectric (TE) devices and modules are a potential enabling technology that will allow routine extraction of usable energy from temperature gradients associated with any combustible

fuel source. Whether TE technology is applied to, for example, the shore-side power industry or the off-shore maritime shipping industry, there are potential cost savings in terms of energy use for these large-scale operations by reducing the amount of fuel combusted and potentially reducing the carbon footprint of a plant. In order to demonstrate the utility and cost-effectiveness of using a specific TE module, however, measurements must be made to show the electrical output capabilities, ranges, limitations, and efficiencies. The Seebeck effect manifests in an electrical power output when a temperature differential is established across a P-N junction comprised of TE materials. For traditional commercial TE modules, measurements of the power output from a complete module are performed and provided in specification data sheets. For researchers developing thermoelectric materials, measuring the Seebeck coefficient from a single P-N junction pair, known as a couple, is desirable compared to the module level, which is a combination of electrically connected couples in series. In terms of ease of testing, measurements at the module level are routine since the magnitudes of the voltage (V) and current (A) are in the range of 10 1 to 101 and can be measured by standard multi-meters. However, manufacturing of a complete functioning P-N thermoelectric module is a complex and costly process, which requires appropriate facilities and trained personnel. Thus, from a materials development perspective, electrical characterization of a single P-N couple instead of a full module is preferred. Measurements from a single P-N couple have outputs in the 10^{-3} to 10^{-6} range for both voltage (V) and current (A) where most off-the-shelf multimeters fail to precisely measure the required milli-range outputs due to poor signal-to-noise ratio. Off-the-shelf options for voltage and current source meters with milli- and nano- range scales are priced > $20 k, which can put a strain on research budgets. Several different types of measurement systems that can

determine the current and voltage outputs from TE junctions and modules have been reported in the literature. Petsagkourakis et al. [1] review a number of thermoelectric applications that show the importance of comparative testing of device power outputs. El-Genk and Saber [2] used I-V curves to compare and validate experimental data to a theoretical model for a segmented TE material couple in which differences between experiment and modeling is attributed to heat losses and contact resistances. Parveen et al. [3] report a test procedure for applying decreasing load resistances while increasing the heat source temperature to create a power profile for a manufactured module. Min et al. [4] used a computer-controlled potentiostat from a commercial vendor to control the load applied to a thermoelectric module to develop I-V power output curves. O'Halloran and Rodrigues [5] modified the Min's approach to use a known resistance and a rheostat to vary the load applied to a thermoelectric module in order to develop voltage and power output curves. This last method may be considered to be the lowest cost method, but it is appropriate only for testing an entire module output. Sarihk et al. [6] discuss the development of a pulse width modulation loading device using MOSFETs for characterizing photovoltaic devices that produce up to 8.2A and 30.8 V at maximum power output. For this application, the MOSFETs are used as a variable resistor to provide the load for the output measurements. The circuit described in this paper is able to measure smaller voltage and current outputs than the published measurement capabilities of the circuit described in Sarihk et al. Rivai et al. [7] discuss a low cost I-V measurement circuit for use in evaluating photovoltaic cells. The circuit described in their measurement uses a capacitor as the load instead of a resistor bank. Van Dyk et al. [8] uses a resistor bank with relays to evaluate 100 and 101 range I-V output from an array of PV cells, but the circuit described in this work employs switches and MOSFETs as resistor triggers, is capable

of measuring 10^{-3} to 10^{-6} range for both voltage (V) and current (A). In this paper, we describe a I-V testing circuit capable of measuring the output current and voltages from complete TE modules, as described in Parveen [3], Min [4], and O'Halloran [5], and the low voltage and current outputs in the milli-volt and milli-amp scale from an individual TE couple. Using this approach, the I-V curves can be generated at minimal cost. The functionality of the circuit is demonstrated using a P and N type bismuth telluride based couple and commercially available modules (HZ-2, Hi-Z Technologies). The cost of the equivalent circuit to the source meter is approximately $200, depending on test specific customizations.

A.3. Experimental setup

A measurement circuit was designed and constructed with the capability of measuring millivolt to volt outputs and milliamp to amp output, via an analog voltage data output, from either a TE module or an individual TE couple. The circuit also has the capability to vary the amount of electrical load applied to the thermoelectric device to ascertain te optimal power output from the unit at a given temperature between 20°C and 250°C. The circuit board within the measurement system shown in Figure A.1 is designed with a variable resistor load bank containing discrete selectable values. This load bank uses power resistors over a user-defined range to provide different unique load values to apply to the thermoelectric generator of interest. Discreet resistors were used in order to provide a consistent, customizable, and repeatable I-V result.

A potentiometer that provides a variable resistive load was not used because the potentiometer introduces noise into the measurement due to the potentiometer acting as an

electromagnetic antenna [7]. The use of a potentiometer would also reduce the precision of the experiment due to the unreproducablility of resistive values for each repeated experiment. A rheostat which varies the load in discrete increments was not used because the unique loading required for differing TE couples would require differently rangedrheostats due to differing TE internal resistances. The use of individual resistors provided an increased adaptability of the circuit.

In the circuit shown in Figure A.1, each resistor is selected by the user via a toggle switch. The toggle switch was used because of its ease of use and implementation for the first generation circuit. These could easily be upgraded to solid state relays in the next iteration. The toggle switch triggers a MOSFET device (IRFB7437PBF, Infineon Technologies) connected to each resistor to close that particular conductor path, thus providing the load connected in parallel with the thermoelectric generator.

The potential difference for each load setting was measured using two different methods: (i) directly measuring the potential across the circuit using a data acquisition package or alternatively by (ii) measuring the linear analog voltage output of a Hall sensor (HLSR 20-P, LEM) monitoring the current through the load. The circuit was powered by a 60 Hz 120VAC input, 24 VDC output power supply (PW2-24, C-Ton Industries) rated for 1 W linear output, and uses 10 VDC and 5 VDC voltage regulators for the MOSFET and Hall sensor power, respectively.

The thermoelectric test rig, shown in Figure A.1, uses a benchtop 350 W laboratory hot plate (HP2305BQ, Thermo Scientific) for the heat source. The heat sink uses a 2.5-gallon water bath at 20°C circulated at 11.67 LPM through an aluminum plate heat exchanger using a water

pump (Universal Pump 185, Hydor). The thermoelectric materials were placed between the hot plate and the heat sink heat exchanger. An important component not shown in Figure A.1 is the boron nitride thermal paste applied between the heat sink and respective copper bar, between the copper bars and the ceramic plates, and between the ceramic plates and the module or couple.

Copper blocks, measuring 3.81 cm by 3.81 cm, were used as a base plate for both the hot side and cold side of the thermoelectric materials to aid temperature stability and to provide more uniform thermal conductivity across the contact surfaces. A thermocouple wire (K-type, Omega Engineering) was inserted into the copper pads via holes drilled 0.079 cm from the surface of the pad in order to measure the heat source and sink temperatures for the thermoelectric material at the contact surface. Alumina wafers were used to electrically isolate the thermoelectric couples and modules from the copper baseplates.

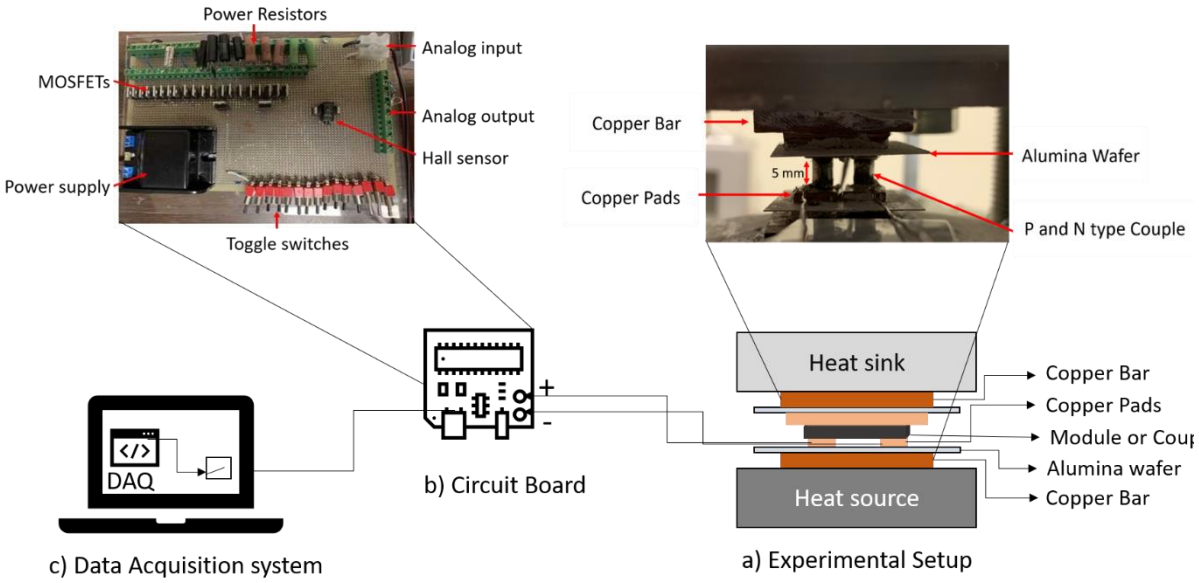

Figure A.1. a) The experimental setup showing the P-N couple inside the test rig, b) The circuit built for measuring current and voltage output, and c) The data acquisition system.

Thermal paste was applied to thermally conductive contact surfaces to ensure uniform heat transfer through the system. Microscopic surface roughness creates a non-uniform surface that only makes contact across asperities, which decreases the thermal conductivity of the system. This, in turn, decreases the efficiency of the thermoelectric device, as this energy transfer drives the output of the device. As the amount of thermal energy decreases, the amount of thermoelectric output decreases. For repeatable measurements in the 10^{-3} range of voltage and current output from the TE couples, the thermal paste is of paramount importance.

However, there is no thermal paste between the individual P and N junctions and the copper contact pads, as boron nitride is an electrical insulator. To ensure good thermal and electrical conduction through the copper contact pads and the P and N TE junctions, two different metallic resins of two-part epoxies was used to reduce the contact resistance. The resin was used without the hardener to allow for the use of the same copper pads. As a result, the TE couples

were not permanently bonded together. Three studies were conducted to ascertain this contact resistance impact, one without any epoxy resin, the second with nickel (Ni) epoxy resin (AA-DUCT 903, Atom Adhesives), and the third with silver (Ag) epoxy resin (H20E Epo-Tek, Ted Pella, Inc.).

A data acquisition (DAQ) software package (LabView, National Instruments) was developed to display the I/V measurements in real-time and record the data for further post-processing. The voltage signals from the direct potential difference and the Hall sensor voltage output were transmitted to the DAQ using an analog voltage differential card (NI 9205, National Instruments). The thermocouple signals were transmitted to the DAQ with a thermocouple analog card (NI 9213, National Instruments). Both cards were inserted into a common chassis (NI 9174, National Instruments) for data transmission to the DAQ software and computer. The data rate used was a 3000 measurements per second at 100 averaged samples per measurement. It was recognized that this data rate is 40 times higher than the published data rate of the NI 9213 card used for thermocouples but was used to capture any dynamic variation of voltage and/or current output at any given temperature.

The TE measurement system is extremely economical and uses off-the-shelf electronic components costing ~$200 and an additional ~ $400 for the other parts in the test rig. The heat source and heat sink equipment are required for any thermoelectric experimentation, therefore the approximate cost was decoupled from the circuit cost.

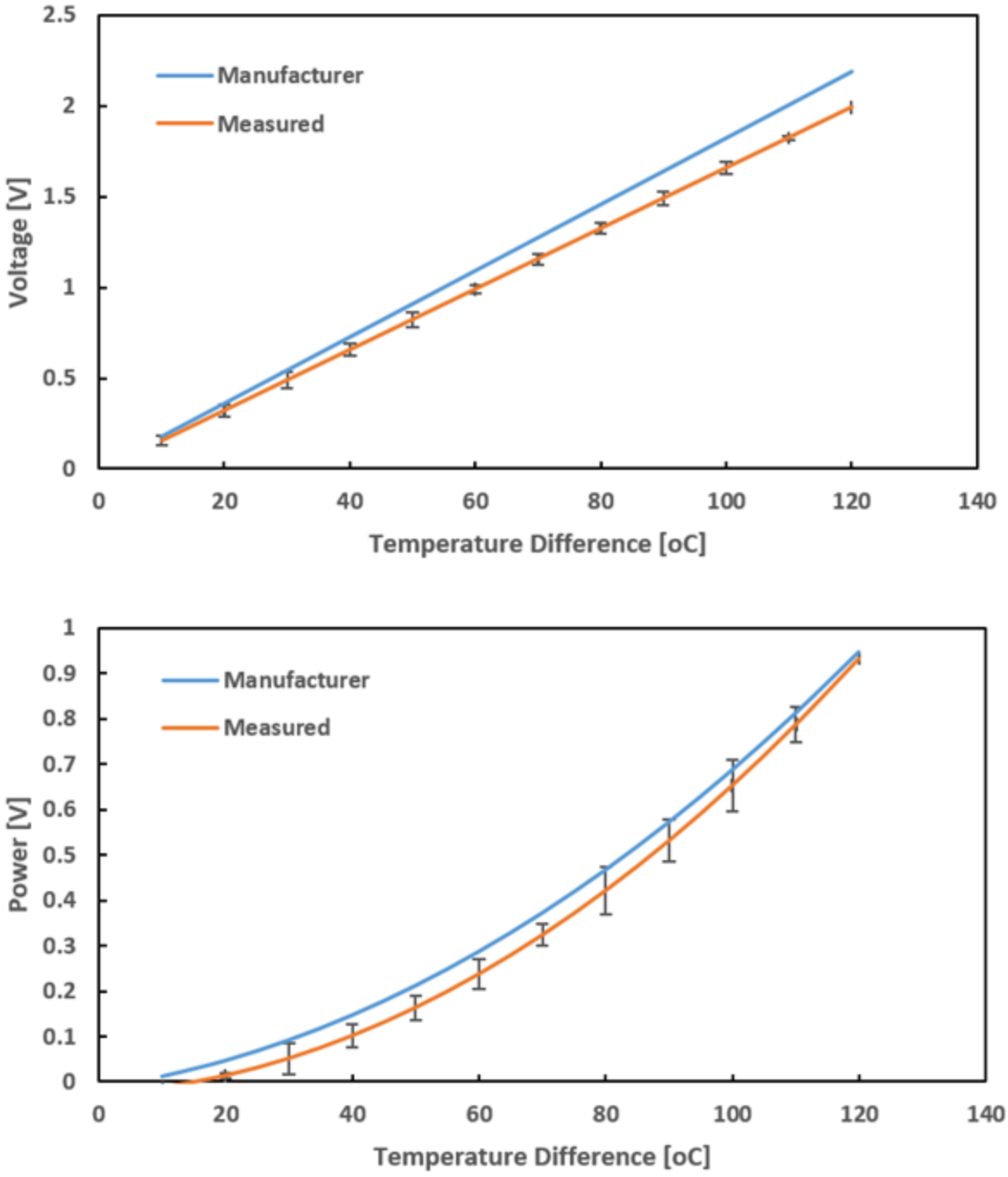

Figure A.2. Measured voltage and power output data points for module #1 shown against the manufacturer's published data [9] Error bars are the standard deviation. (n = 3).

A.4. Device validation

The circuit measurements were validated against published manufacturer performance data of a commercial module (HZ2, Hi-Z Technologies, Inc). This module was selected as it has the same P and N type BiTe materials as was used in the contact resistance study and it fit within the experimental setup. The circuit was set at a known resistance to load match the internal resistance of the thermoelectric modules. The hot side temperature was raised from 20°C to 150°C at a rate of ~15°C per minute using a hot plate heat source, and the cold side temperature was maintained at 19°C . Figure A.2 shows the measured voltage and power outputs versus temperature measured with the circuit as compared to the manufacturer specifications [9].

In Figure A.2, both the measured voltage and power output of the commercial module track the data trends of the manufacturer data. However, there was an observable difference in the voltage output data whereas the power output was within one standard deviation. The standard deviations (n = 3) were calculated to be 0.021 V and 0.015 W. The manufacturer's value of 4 Ω for the internal resistance of module #1 was assumed to be a steady-state value and was used as the load in the circuit. However, the internal resistance of thermoelectric materials does vary with the increasing temperature differential, therefore the measured data can vary due to differences between the load resistance and the internal resistance of the module. It was not known whether the manufacturer used a single constant resistive load or adjusted the load resistance with temperature.

A.5. Thermoelectric couple measurement results

The overall goal of our experimental design was to evaluate individual TE couples using a variety of TE material types. In order to evaluate the effectiveness of the setup and circuit, a baseline control experiment was performed using a single bismuth telluride P-N junction couple that was extracted from a commercially available module (HZ14, Hi-Z Technologies). This couple maintained the manufacturer's structural support and contact pads and was placed into the test rig with boron nitride thermal paste applied to all surfaces to ensure thermal conduction. All measurements involving TE couples were compared to the control data set.

The individual P and N junctions were separated from the manufacturer packaging, by stripping the contact pads and thermoplastic. Copper contact pads were used to bridge between the two junctions and act as the contacts for the leads. The top copper pad used to electrically bridge the junctions measured 2.15 mm thick, 18 mm long, and 9.5 mm wide. The bottom copper pads used for the individual P and N junction was 2.15 mm thick, 14 mm long, and 9.5 mm wide. A 20 AWG bare copper conductor was attached to each contact pad at the base of each individual junction using a silver epoxy (H20E Epo-Tek, Ted Pella, Inc.).

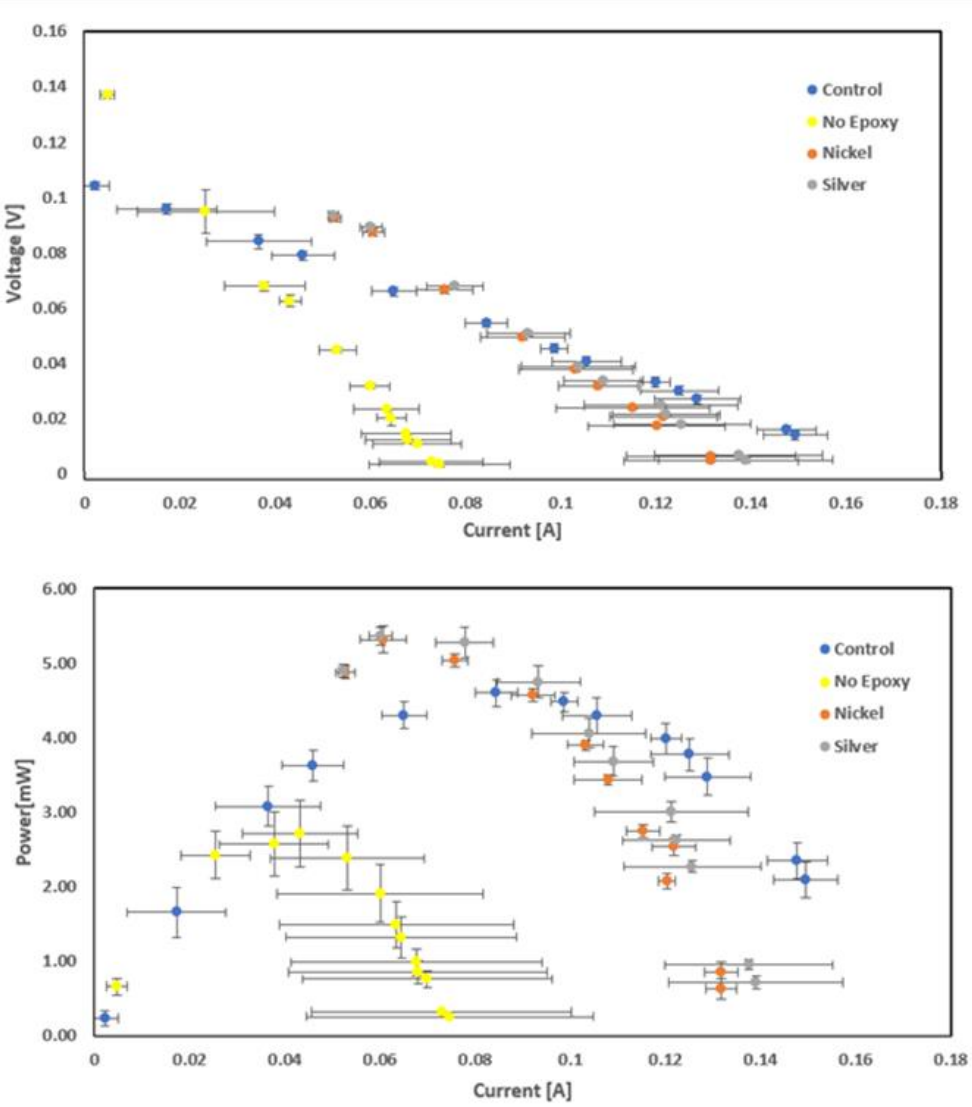

Figure A.3. Circuit voltage (top) and power (bottom) plotted against circuit current at a varying load for an individual BiTe P-N couple at a temperature differential of 150 ◦C using Ni, Ag, and no epoxy resin measured against the manufacturer baseline prepackaged couple. Error bars are the standard deviation. (n = 3).

Figure A.3 shows the measured voltage and power output for the bismuth telluride P-N junction couple. The test procedure involves holding a constant heat sink temperature of 20°C and increasing the heat source temperature from 20°C to 170°C at distinct resistive loads. The resistive load values are given in Table A.1. This range ensures that the data collected spans from open-circuit voltage, with minimal current flow, to the short-circuit condition, with minimal

voltage difference. Each experiment was performed three times. The error bars are two times the standard deviation of the measurements to yield a 95% confidence interval. The data in Figure A.3 was calibrated using a 0.15 Ω resistance in the circuit and a source meter (2400, Keithley). The slope of the calibration line was used as a correction factor for the measured data. Figure A.3, top, shows the measured voltage output for the couple using dry, Ni, and Ag contact epoxy resins as compared to the control couple. There was no difference in voltage output between the two epoxy cases (Ni and Ag), and the control sample in the optimal load range from 0.08A to 0.12A. In the dry case where there was no epoxy resin, the current output decreased by approximately 50% as compared to the control couple. This difference in voltage output can be attributed to an increase in roughness on the contact surfaces between the individual junctions in the couple and their respective copper contact pads leading to an increase in contact resistance. Based on the error bars associated with the voltage and current data, there is no difference between the two epoxy samples and the control data set.

Table A.1. Load bank resistor values.

Load setting	**Resistance [Ω]**	**Load Setting**	**Resistance [Ω]**
1	0.001	8	0.1
2	0.004	9	0.15
3	0.015	10	0.25
4	0.03	11	0.5
5	0.04	12	1
6	0.05	13	5
7	0.075		

Figure A.3, bottom, shows the power output obtained using the same load settings. The power output from the two epoxy resin and control lie within a common range of power output and differ from the dry case. The Ni and Ag cases show an approximate 20% increase in peak power output in the current range of 0.05A and 0.08A. This difference is attributed to variations in the sheet contact resistances of the epoxies leading to a different contact resistance, as compared to the aluminum contact pad of the commercial baseline couple. Outside of this range, however, there was no statistical difference between the baseline power output and the Ni and Ag epoxy data The dry epoxy case had an approximate 40% reduction in peak power output as compared to the control. This reduction can be attributed to the difference in the current output seen in Figure A.3. To account for the differences in contact resistances, baseline measurement offsets for voltage, current, and calculated power were measured at room temperature and are given in Table A.1. A contact resistance difference for the Ag and Ni epoxies from the control arises from the increased internal resistance of the couple as evidenced by the higher power output peak of the Ag and Ni epoxy cases at load settings of 11, 12, and 13 from Table A.1 versus the peak load of the control at load 9. The Ni and Ag cases are shown to be similar in the power results in Figure A.2, showing no difference for these two epoxies once the contact resistance offset was taken into account.

Table A.2. Voltage and current offsets measured at room temperature for Ag and Ni expoxy TE couple tests.

Epoxy	Voltage Offset [V]	Current Offset [A]	Calculated Power [mW]
Ag	0.0588	-3.021	-177.62
Ni	0.05764	-3.053	-175.95

A.6. Measurement limits

The present setup is limited both in terms of allowed TE couple sizes and operating temperature. The operating temperature is current-limited to a maximum heat source temperature of 180°C, which is less than the documented 250°C limit of the TE material. This temperature limit was chosen to minimize out-gassing of unsafe volatile organic compounds used as the binding agent in the thermal contact epoxy resins. In addition, this is the temperature limit for achieving a stable heat sink temperature. As a means to overcome this temperature limit, a larger water bath volume could be used with an increased coolant flow rate.

A limit on the TE couple height of 1.25 mm is caused by the height of the electrical conductor width combined with the thickness of the silver epoxy used to cement the conductor onto the base contact pad. This limit only applies to testing of individual TE couples rather than modules, as the copper contact pads are not required for module testing.

A.7. Conclusion

This paper describes a versatile TE measurement system with a circuit capable of testing individual TE couples as well as entire TE modules. The setup is also capable of comparative testing of contact resistances that occur at the interfaces between the TE materials and the

conductive pads. The ability of acquiring I/V measurements in both the 0.1 to 10 range as well as the 10^{-3} to 10^{-6} range by changing the resistor load range of the circuit using commercial low-cost off-the-shelf electronic components makes the testing system unique and beneficial. The evaluation of the experimental setup and material protocol showed that there was no statistical difference between the commercially manufactured control couple and the laboratory manufactured P and N pellets, as they were made of the same BiTe based TE materials.

Possible future upgrades to the system can include better control logic and expanded capabilities of the experimental setup discussed in the previous section. Automated control of the load setting for the circuit using solid-state relays and more advanced data acquisition software would increase the repeatability of the tests. The relays require a control voltage to trigger the closing of the load circuit, therefore the addition of an analog voltage output card(s) would be necessary, such as a National Instruments NI-9264 analog voltage output card. This card has a 16-channel output ability with a range of +/- 10 V output, allowing for the control of all 16 channels of the load circuit with one card. The MOSFETs could also be upgraded to TFETs once they are commercially available. This would allow for quicker load switching, making the load sweep more time efficient. The TFETs switch on at lower voltages and the drain current relationship has a larger slope, potentially making the circuit more electrically efficient as well. [10] Another obvious upgrade concerns the control of the heat source. It is presently under manual control, and a control device would maintain a more consistent heat source temperature.

A.8. Credit authorship contribution statement

Travis T. Wallace: Conceptualization, Methodology, Software, Validation, Investigation, Writing – original draft, Resources, Data curation, Formal analysis, Visualization. **Nayeem K. Ibnul:** Writing – original draft, Resources, Methodology, Investigation, Visualization. **Robert J. Lad:** Writing - review & editing, Supervision. **Carl P. Tripp:** Writing - review & editing, Supervision, Funding acquisition.

A.9. Declaration of Competing Interest

The authors declare that they have no known competing financial interests or personal relationships that could have appeared to influence the work reported in this paper.

A.10. Acknowledgments

The authors would like to acknowledge DOT grant DTRT13-G-UTC43 under METEL of Maine Maritime Academy and Research Reinvestment funds at UMaine for funding the project. The authors also would like to acknowledge Seth Murray and ElectroTechnical Services for their help in circuit design and advice.

A.11. References

[1] I. Petsagkourakis, K. Tybrandt, X. Crispin, I. Ohkubo, N. Satoh, T. Mori, Thermoelectric materials and applications for energy harvesting power generation, Sci. Technol. Adv. Mater. 19 (1) (2018) 836–862.

[2] M.S. El-Genk, H.H. Saber, High efficiency segmented thermoelectric unicouple for operation between 973 and 300 K, Energy Conversion Manage. 44 (2003) 1069–1088.

[3] S. Parveen, V. Vedanayakam, R.P. Suvarna, Measurement of power by varying load resistance – thermoelectric generator, ISOR J. of Appl. Phy. 10 (1) (2018) 18–22.

[4] G. Min, T. Singh, J. Garcia-Canadas, R. Ellor, Evaluation of Thermoelectric Generators by I-V Curves, J. Electron. Mater. 45 (3) (2016) 1700–1704.

[5] S. O'Halloran, M. Rodrigues, Power and efficiency measurement in a thermoelectric generator, ASEE Annu. Conf. Expo. Conf. Proc. no (2012) 2000.

[6] S. Sarikh, M. Raoufi, A. Bennouna, A. Benlarabi, B. Ikken, Implementation of a plug and play I-V curve tracer dedicated to characterization and diagnosis of PV modules under real operating conditions, Energy Conversion Manage. 209 (2020) 112613, https://doi.org/10.1016/j.enconman.2020.112613.

[7] A. Rivai, N.A. Rahim, M.F.M. Elias, J. Jamaludin, Multi-channel photovoltaic current–voltage (I–V) curve tracer employing adaptive-sampling-rate method, IET Sci. Measurement Technol. 14 (8) (2020) 969–976.

[8] Van Dyk, E. E., A. R. Gxasheka, and E. L. Meyer. "Monitoring current-voltage characteristics of photovoltaic modules." In Conference Record of the Twenty- Ninth IEEE Photovoltaic Specialists Conference, 2002., pp. 1516-1519. IEEE, 2002.

[9] Hi-Z Technologies, Inc, HZ-2 Thermoelectric Module.HZ-2 Datasheet, 2019.

[10] G. Nazir, A. Rehman, S.-J. Park, Energy-efficient tunneling field-effect transistors for low-power device applications: challenges and opportunities, ACS Appl. Mater. Interf. 12 (42) (2020) 47127–47163.

BIOGRAPHY OF THE AUTHOR

Mohammed Nayeem Ibnul is born and raised in Dhaka, Bangladesh on September 12th, 1991. He attended the University of Dhaka and graduated in 2014 with a bachelor's degree in Applied Chemistry and Chemical Engineering. After finishing his bachelor's. He entered the graduate program of the Department of Chemistry at the University of Maine in the fall of 2015 to pursue a doctorate degree in Chemistry. He joined Dr. Carl Tripp research group in spring 2016 to work on his thesis on the developing methods for the detection of analytes in water using a membrane and optical spectroscopy.

During his PhD he also worked on a multidisciplinary collaboration project between the Frontier Institute for Research in Sensor Technologies (FIRST) and the Maine Maritime Academy (MMA). Where his goal was to develop a fabrication method to generate p- and n-type bismuth telluride nanoparticles for use in thermoelectric generators.

Related Publications:

- **Nayeem K. Ibnul**, Carl P. Tripp, A simple solution to the problem of selective detection of phosphate and arsenate by the molybdenum blue method, Talanta. (2021) 123043.
- Travis T. Wallace, **Nayeem K. Ibnul**, Robert J. Lad, Carl P. Tripp, Low-cost Seebeck power measurement system for characterization of thermoelectric junctions and modules, Measurement. 183 (2021) 109889.
- **Nayeem K. Ibnul**, Carl P. Tripp, A solventless method for detecting trace level phosphate and arsenate in water using a transparent membrane and visible spectroscopy, Talanta. (2021) 122023.

Nayeem is a candidate for the Doctor of Philosophy degree in Chemistry from the University of Maine in May 2022.